

UNIVERSITY OF STRATHCLYDE

Development and characterisation studies of a type III fibronectin domain pair

By

Lisa McIntosh

A Thesis submitted to the University of Strathclyde in fulfilment of the
requirement for degree of Doctor of Philosophy

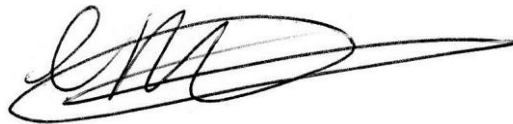
2014

DECLARATION OF AUTHENTICITY AND AUTHOR'S RIGHTS

This thesis is the result of the author's original research. It has been composed by the author and has not been previously submitted for examination which has led to the award of a degree.

The copyright of this thesis belongs to the author under the terms of the United Kingdom Copyright Acts as qualified by University of Strathclyde Regulation 3.50. Due acknowledgement must always be made of the use of any material contained in, or derived from, this thesis.

Signed:

A handwritten signature in black ink, consisting of several loops and a long horizontal stroke extending to the right.

Date: 20/04/2014

ACKNOWLEDGEMENTS

I would first like to thank my supervisors Doctor Christopher van der Walle, Doctor Christine Dufès and Professor Clive Wilson. I am forever grateful to Chris for the opportunity to carry out this work, his invaluable guidance, continued support and patience. My thanks go to Christine for her advice when writing this thesis. Lastly, thank you Clive for motivating me to keep going and inspiring me to give my all.

A number of people assisted me throughout this project and I would like to thank them all: Dr James Beattie of the University of Leeds for aiding me in the SPR studies; Dr Lindsay Cole of Applied Photophysics Ltd, (Leatherhead UK) for allowing me the use of the ACD prototype and Dr Steven Holt of ANSTO (Australia) and formally of ISIS (Oxford, UK) for sharing his knowledge of NR and performing the analysis for me. From the University of Strathclyde, I would like to thank Dr Micheala Kreiner for providing the multimeric FIII9'10 proteins, Tong Zhang (Alex) for running my mass spec samples, David Blatchford for his expertise in immunofluorescence and Christine Whitelaw for maintaining the cell cultures. I would also like to thank the technical, workshop and secretarial staff for all their help. Finally, I would like to thank the University of Strathclyde for funding this project.

I have made a number of friends during my PhD, I would like to thank them for their unrelenting support and their amazing ability to help find the joy when times looked bleak. My thanks go to you: Gracie, Joe, Ruairidh, Munerah, Jen L, Jen M, Shonagh, Gemma, Stewart, Kelly and Michelle. I cannot begin to measure the enormous

impact you all have made on my life. Each of you are an inspiration in your own special, unique way.

Finally, my biggest thanks go to my family. Without your constant encouragement and love I would not have made it this far. To my parents, Maggie and Tony, you have supported me at every point of my life and in every decision I have undertaken. My sister and my best friend Cassie and my little brother Shawn, you are both shining lights in my life and a constant source of entertainment and fun. Last but not least, my dear partner Peter, you have seen me through the bad days and the good with equal enthusiasm and still have not quit. Your patience amazes me.

When I first embarked on this work, I thought a PhD was a solitary task undertaken in isolation. With the help of the people mentioned here and many others I have learned the importance of, and the strength that comes with working as part of a team towards a shared goal. Without the help and support of the people around me I could not have completed this thesis.

CONTENTS

ACKNOWLEDGEMENTS	ii
LIST OF ABBREVIATIONS	vii
LIST OF FIGURES.....	xii
LIST OF TABLES	xix
ABSTRACT.....	xxi
CHAPTER 1. Introduction.....	1
1.1 The extracellular matrix (ECM)	1
1.2 Integrin receptors.....	3
1.3 Key protein components of the ECM.....	8
1.3.1 Vitronectin.....	8
1.3.2 Collagen	8
1.3.3 Laminin	9
1.3.4 Fibronectin	10
1.4 The insulin-like growth factor axis.....	13
1.4.1 Insulin-like growth factors	14
1.4.2 Insulin-like growth factor receptors (IGFR)	16
1.4.3 Insulin-like growth factor binding proteins (IGFBP).....	16
1.4.4 IGFBP binding to fibronectin.....	21
1.4.5 Effects of IGFBP binding to fibronectin.....	23
1.5 Mimicking the extracellular matrix for biomaterials.....	25
1.5.1 Cell attachment and the ‘RGD’ motif	26
1.5.2 Self-assembling peptides and proteins	29
1.5.3 Non-specific <i>versus</i> directed protein adsorption.....	29
1.5.4 Multimeric clustered ligands and “nanopatterning”	32
1.5.5 Coiled-coil protein systems.....	35
1.5.6 Investigating protein adsorption at the solid liquid interface.....	36
1.6 Research aims and hypothesis	39
CHAPTER 2. Expression and purification of proteins	41
2.1 Introduction	41
2.2 Materials	44
2.3 Buffers and reagents	44
2.4 Methods	46
2.4.1 FIII9’10 mutants and recombinant expression.....	46
2.4.2 Protein characterisation.....	58
2.5 Results	64

2.5.1	Mutation and expression of FIII9'10 proteins	64
2.5.2	Protein characterisation	68
2.6	Discussion.....	78
2.6.1	Plasmid DNA mutation and replication	78
2.6.2	Protein manufacture	79
2.6.3	Protein expression	79
2.6.4	Protein characterisation.....	80
2.6.5	Circular dichroism.....	81
2.7	Summary.....	82
CHAPTER 3. Biophysical and functional characteristics of FIII9-10 mutants...		83
3.1	Introduction	83
3.2	Materials	84
3.3	Buffers and reagents	85
3.4	Methods	85
3.4.1	Binding of FIII9-10 to IGFBP-5	85
3.4.2	Physical stability of FIII9-10 based proteins	91
3.5	Results	96
3.5.1	Interactions between IGFBP-5 and FIII9'10-GGC mutants	96
3.5.2	Equilibrium chemical denaturation measured by fluorescence	99
3.5.3	Automated circular dichroism data	102
3.6	Discussion.....	109
3.6.1	Surface Plasmon resonance.....	109
3.6.2	Unfolding by GdmCl denaturant.....	110
3.6.3	Extended circular dichroism analysis.....	111
3.7	Summary.....	112
CHAPTER 4. Surface adsorption and biological activity of FIII9-10 mutants.		114
4.1	Introduction	114
4.2	Materials	116
4.3	Buffers and reagents	117
4.4	Methods	119
4.4.1	Probing protein adsorption onto surfaces.....	119
4.4.2	Surface mapping using neutron reflectometry	126
4.4.3	Functional analysis of mutated proteins.....	135
4.5	Results	140
4.5.1	Conformation of proteins on surfaces of varying wettability	140
4.5.2	Protein adsorption studies by neutron reflectivity	148

4.5.3	Functional analysis of the FIII9-10 mutants	164
4.6	Discussion.....	172
4.6.1	Surface wettability effects on protein conformation.....	172
4.6.2	Protein adsorption to titania surfaces	175
4.6.3	Functional analysis of proteins.....	179
4.7	Summary.....	182
CHAPTER 5.	Exploring multimeric integrin ligands	184
5.1	Introduction	184
5.2	Materials.....	186
5.3	Buffers and reagents	187
5.4	Methods	188
5.4.1	Conformational analysis by circular dichroism	188
5.4.2	Surface mapping of multimers on gold using neutron reflectometry	189
5.4.3	Cell adhesion study of multimeric ligands on gold surfaces.....	192
5.5	Results	193
5.5.1	Conformation analysis of multimeric ligands following storage	193
5.5.2	Protein adsorption studies by neutron reflectivity	203
5.5.3	Cell adhesion to multimeric proteins on gold surfaces	208
5.6	Discussion.....	212
5.6.1	Conformational analysis.....	212
5.6.2	Multimeric $\alpha 5\beta 1$ ligands on gold support	215
5.7	Summary.....	217
CHAPTER 6.	Conclusions and future work	219
References	223
Appendix A	245
Appendix B	249

LIST OF ABBREVIATIONS

11-MUD	11-mercaptoundecanol
ACD	automated circular dichroism
AFM	atomic force microscopy
ANSTO	Australian Nuclear Science and Technology Organisation
APS	ammonium persulphate
APTMS	(3-aminopropyl)trimethoxysilane
Au	gold
Au/11-MUD	gold/11-mercaptoundecanol
BHK	baby hamster kidney
BSA	bovine serum albumin
CAG	contact angle goniometry
CBD	cell binding domain
CD	circular dichroism
cDNA	complementary deoxyribonucleic nucleic acid
cFN	cell associated fibronectin
CH ₃ COOH	acetic acid
CH ₃ OH	methanol
Conc.	concentration
D ₂ O	deuterium oxide
Da	Dalton
d-FIII9'10	deuterated type III fibronectin domains 9 to 10 including substitution of proline for leucine ¹⁴⁰⁸
d-FIII9''10 H2P	deuterated type III fibronectin domains 9 to 10 including substitution of proline for leucine ¹⁴⁰⁸ and proline for histidine ¹³⁷⁷
DMEM	Dulbecco's Modified Eagle Medium
DMF	<i>N, N</i> - dimethylformamide
dNTP	deoxynucleoside triphosphatates
DNA	deoxyribonucleic acid
DTT	dithiotheitol
E1364A	primer- Ala substituted for Glu ¹³⁶⁴

EB	enzyme-linked immunosorbent assay buffer
<i>E.coli</i>	<i>Escherichia coli</i>
ECM	extracellular matrix
EDA	extra domain A
EDB	extra domain B
EDTA	ethylenediaminetetraacetic acid
ELISA	enzyme-linked immunosorbent assay
EnSCs	human endometrial stromal cells
FIII1-11	type III fibronectin domains 1 to11
FIII7	7 th type III fibronectin domain
FIII7-10	type III fibronectin domains 7 to10
FIII8	8 th type III fibronectin domain
FIII8-v15	type III fibronectin domains 8 to 15
FIII9	9 th type III fibronectin domain
FIII9-10	type III fibronectin domains 9 to 10
FIII9'10	type III fibronectin domains 9 to 10 including substitution of proline for leucine ¹⁴⁰⁸
FIII9'10-GGC	type III fibronectin domains 9 to 10 including substitution of proline for leucine ¹⁴⁰⁸ and addition of tripeptide GGC
FIII9'10-GGC E2A	type III fibronectin domains 9 to 10 including substitution of proline for leucine ¹⁴⁰⁸ and substitution of alanine for glutamin acid ¹³⁶⁴ and addition of tripeptide GGC
FIII9'10-GGC I2A	type III fibronectin domains 9 to 10 including substitution of proline for leucine ¹⁴⁰⁸ and substitution of alanine for isoleucine ¹⁴¹⁰ and addition of tripeptide GGC
FIII9''10 T2P	type III fibronectin domains 9 to 10 including substitution of proline for leucine ¹⁴⁰⁸ and proline for threonine ¹³⁵³
FIII9''10 H2P	type III fibronectin domains 9 to 10 including substitution of proline for leucine ¹⁴⁰⁸ and proline for histidine ¹³⁷⁷
FIII10	10 th type III fibronectin domain
FN	fibronectin
FPLC	fast protein liquid chromatography system

FBS	foetal bovine serum
GdmCl	guanidine hydrochloride
GH	growth hormone
GMW	gold matched water
GST	glutathione S-transferase
H1377P	primer- His substituted for Pro ¹³⁷⁷
h	hour
HABA	4'-hydroxyazobenzene-2-carboxylic acid
H/D exchange	hydrogen/deuterium exchange
I1410A	primer- Ala substituted for Ile ¹⁴¹⁰
IEF	isoelectric focusing
IGF	insulin like growth factor
IGFBP1-6	insulin like growth factors binding proteins 1 to 6
IGF-I and IGF-II	insulin like growth factors
IGF-IR and IGF-IIR	insulin like growth factors cell surface receptors
IgG	immunoglobulin G
IMAC	immobilised metal affinity chromatography
IPTG	isopropyl β -D-thiogalactoside
K _{av}	partition coefficient
LAP-TGF- β	latency associated peptide transforming growth factor
MALS	multi-angle light scattering
mES	mouse embryonic cells
Min	minute
MFG-E8	milk fat globule EGF factor 8
mPEG-silane	methoxy-polyethylene glycol-silane
M _r	relative molecular mass
mRNA	messenger ribonucleic acid
MRW	mean residue weight
MWCO	molecular weight cut-off
N/A	not applicable
NaCl	sodium chloride
NaH ₂ PO ₄	monosodium phosphate

NaOH	sodium hydroxide
NMR	nuclear magnetic resonance
NR	neutron reflectivity
OD ₅₀₀	optical density at 500 nm
PBS	phosphate buffered saline
PCR	polymerase chain reaction
PEO	poly(ethylene oxide)
PFA	paraformaldehyde
pFN	plasma FN
PFTOS	1H, 1H, 2H, 2H-perfluorooctyltriethoxysilane
<i>Pfu</i>	<i>Pyropcccus furiosus</i>
PHSRN	proline-histidine-serine-arginine-asparagine
pI	isoelectric point
RGD	arginine-glycine-aspartic acid
SAM	self-assembling monolayer
SDS	sodium dodecyl sulphate
SDS-PAGE	sodium dodecyl sulphate polyacrylamide gel electrophoresis
SEC	size exclusion chromatography
SLD	scattering length density
SPR	surface plasmon resonance
T1353P	primer- Pro substitution for Thr ¹³⁵³
TBE buffer	tris-borate-ethylenediaminetetraacetic acid buffer
TCEP	tris(2-carboxyethyl)phosphine
TCOS	trichlorooctylsilane
TEMED	N,N,N',N'- TetramethylethyleIndiamine
Ti	titanium
TiO ₂	titanium dioxide/titania
TIRF	total internal reflection fluorescence
Tm	thermal denaturation midpoint
Tris	tris(hydroxymethyl)aminomethane
UV	ultraviolet
V ₀	void volume of column (ml)

V_e elution volume of the sample (ml)
 V_t total volume of the column (ml)

LIST OF FIGURES

Figure 1-1 Schematic representation of some of the main features of the extracellular matrix. [Reproduced from Huxley-Jones et al. 2008].	2
Figure 1-2 Schematic representation of α (blue) and β (red) subunits of a typical integrin spanning the cell membrane (pink).	4
Figure 1-3 Schematic representation of the rested (bent) and activated (straightened) states of the ectodomain of integrin α IIb β 3. Domains including thigh, calf and epidermal growth factor-like (EGF) are labelled on the α (blue) and β (red) subunits. [Data from Xiong et al. 2001, Jianghai Zhu et al. 2008].	6
Figure 1-4 Schematic representation of a fibronectin monomer containing 3 repeating units, type I (blue), II (red) and III (green). Including alternatively spliced repeats (black): extra domain A (EDA), extra domain B (EDB) and variable region (V) which can contain different lengths of amino acids.	11
Figure 1-5 Ribbon diagram of FIII domains 9 and 10. β strands shown as ribbons (yellow) and the exposed loops PHSRN (FIII9) and RGD (FIII10) indicated. [Coordinates were obtained through Protein Database and the image produced using JMol (12.2.24)].	12
Figure 1-6 The IGF axis consist of IGF-I and IGF-II polypeptides (orange), six IGFBPs (various colours), a family of proteases (lilac) and cell-surface IGFBP receptor, IGF-IR and IGF-IIR (light grey). [Reproduced from Beattie et al. 2006].	14
Figure 1-7 Schematic representation of domain structure of the IGFBPs highlighting the similarity between IGFBP1-6. Cysteines indicated by red vertical lines and the disulphide linkages as red horizontal lines. IGF binding regions are contained in yellow boxes. [Reproduced from Bach et al. 2005].	18
Figure 2-1 Sequence alignment of mouse (Mus_Fn) and human (Hum_Fn) FIII9 domains. Every 10 th amino acid is noted with an upper dot along with the corresponding sequence number, according to Leahy et al. (1996).	42
Figure 2-2 Sequence alignment of mouse and human FIII9. The amino acids targeted for substitution are underlined.	43
Figure 2-3 Map of pRSET A vector from Invitrogen (Paisley, UK)	47
Figure 2-4 Illustration of QuikChange® site-directed mutagenesis protocol.	50
Figure 2-5 Flow diagram illustrating the steps involved in engineering mutated proteins.	55
Figure 2-6 Flow diagram outlining steps required for protein purification from <i>E. coli</i> cells.	58

Figure 2-7 Typical far UV spectra displaying various common secondary structures. Including α -helix (solid line), anti-parallel β -sheet (long dashed line), type I β -turn (short dashed line) and random coil (dotted line). [Reproduced from Kelly et al. 2005].	63
Figure 2-8 Agarose gel electrophoresis of cDNA, Hyperladder I lane 1. Left pane FIII9'10-GGC mutants E1364A lane 2, 3, 4, I1410A lane 5, 6, 7. Right pane FIII9'10 mutants T1353P lane 2 and 3, H1377P lane 4 and 5.	66
Figure 2-9 Typical chromatogram of FPLC purification of FIII9'10-GGC I2A. Important points indicated including initiation of flow through of cell lysates (A), washing of column with wash buffer (B), washing of column with 15 % elution buffer (C), protein peak (D) and elution buffer % composition (E).	67
Figure 2-10 Alignment of amino acid sequences for FIII9'10-GGC proteins, with the difference in the amino acid sequence highlighted.	70
Figure 2-11 Alignment of amino acid sequences for FIII9-10 proteins, with the difference in the amino acid sequence highlighted.	71
Figure 2-12 SDS-PAGE gel image of FIII9'10-GGC E2A (red rectangles), showing protein Mw marker (M), initial unpurified sample (A), flow through from sample injection (B), initial wash (C), 15 % elutant (D) and final sample (E).	72
Figure 2-13 SDS-PAGE gel image showing molecular weight marker (kDa) (M) and proteins FIII9-10 (A), FIII9'10 (B), FIII9''10 H2P (C), FIII0''10 T2P (D), FIII9'10-GGC (E), FIII9'10-GGC I2A (F) and FIII9'10-GGC E2A (G).	73
Figure 2-14 Example of chromatogram peaks from calibration of Superdex™ 75 10/300 GL column. Showing blue dextran (A), ovalbumin (B), FIII9-10 (C), myoglobin (D) and ribonuclease A (E).	74
Figure 2-15 Calibration curve for size exclusion chromatography calculations. Equation of line shown on figure.	75
Figure 2-16 Far UV CD spectra of FIII9-10 (black) and mutant variations FIII9'10 (red), FIII9'10-GGC I2A (green), FIII9'10-GGC E2A (purple), FIII9'10 H2P (blue) and FIII9''10 T2P (orange) in sodium phosphate buffer.	77
Figure 2-17 Near UV CD spectra of FIII9-10 (black) and mutant variations FIII9'10 (red), FIII9'10-GGC I2A (green), FIII9'10-GGC E2A (purple), FIII9'10 H2P (blue) and FIII9''10 T2P (orange) in sodium phosphate buffer.	77
Figure 3-1 Illustration of surface plasmon sensor light path and schematic of intensity and resonance signal. Analyte shown as red oval and ligand as yellow α [Reproduced from Butler, Biacore UK].	87

Figure 3-2 Photograph of modified Automated CD sample housing, important features are annotated.....	94
Figure 3-3 Illustration of typical 96 well plate auto sampler set up with buffer (grey) and protein incubated in specified conditions (black). Protein mutations were grouped together, separation indicated here by black line (Read A1 to H1 then A2 to H2 and so on).	95
Figure 3-4 Binding of IGFBP-5 to immobilised FIII9'10-GGC (red line), FIII9'10-GGC I2A (yellow line) and FIII9'10-GGC E2A (blue line).....	97
Figure 3-5 SPR binding spectra of IGFBP-5 and IGF-1 to immobilised FIII9'10-GGC (blue), FIII9'10-GGC I2A (purple) an FIII9'10-GGC E2A (red).	98
Figure 3-6 SPR binding spectra of integrin $\alpha 2\beta 1$ to immobilised FIII9'10-GGC (orange), FIII9'10-GGC I2A (green) and FIII9'10-GGC E2A (pink).	99
Figure 3-7 Chemical equilibrium denaturation using GdmCl of FIII9-10 (blue) and mutants FIII9'10 (red), FIII9''10 T2P (green) and FIII9''10 H2P (purple). The step-wise unfolding of each domain is indicated.	101
Figure 3-8 Far UV CD spectra of thermal denaturation for FIII9-10 protein fragments, FIII9-10 (A), FIII9'10 (B) and FIII9''10 H2P (C). Change in spectra indicates unfolding occurs at a temperature of above 55-60 °C.	103
Figure 3-9 Global analysis of CD spectra data for thermal denaturing of proteins FIII9-10 (A) FIII9'10 (B) and FIII9''10 H2P (C) showing average folded species (blue) and unfolded species (red). Left pane shows comparison of the different spectral shapes. Right pane shows concentration profile comparing the different species at 20 to 100 °C. Error bars represent the standard deviation of the mean of three runs.....	105
Figure 3-10 Far UV CD spectrum of FIII9-10 (A), FIII9'10 (B) and FIII9''10 H2P (C) following incubation in buffer with varying pH.	106
Figure 3-11 Far UV CD of FIII9-10 (A), FIII9'10 (B) and FIII9''10 H2P (C) following incubation with varying concentrations of GdmCl in 10 mM NaH ₂ PO ₄ , 50 mM NaCl, pH 6.0 buffer. Inset shows unfolding of protein indicating different species 1 (blue), 2 (red) and species 3 (green).	108
Figure 4-1 Contact angle (θ) of energies and forces at the interface of a solid surface, a liquid and a vapour.	121
Figure 4-2 Photograph of filtered water being deposited on to hydrophilic and hydrophobic surface. Different contact angles are created and highlighted in red. .	121
Figure 4-3 Photograph of the motorised rotating cell holder (left), developed at the University of Strathclyde and standard circular cell holder (right).Both are shown	

containing circular cells, the stoppers used for the rotating cell were modified to allow for free movement.....	123
Figure 4-4 Schematic representation of the basic set up for neutron reflectometry. Top image shows silicon substrate clamped in place with sample solution in blue. Lower image shows expanded point of contact of sample in solution and silicon substrate.....	127
Figure 4-5 Schematic depicting (I) integrin on surface, (II) protein binding to integrin, (III) antibody conjugate binding to protein and (IV) colorimetric change initiated by binding to horseradish peroxidase (HRP).	136
Figure 4-6 Far UV CD spectra for FIII9-10 adsorbed to beads with surfaces of increasing hydrophobicity: silica (red), mPEG-silane (purple), APTMS (green), PFTOS (orange) and TCOS (blue). Inset shows far UV CD spectrum for FIII9-10 in aqueous solution.....	144
Figure 4-7 Far UV CD spectra for FIII9'10 adsorbed to beads with surfaces of increasing hydrophobicity: silica (red), mPEG-silane (purple), APTMS (green), PFTOS (orange) and TCOS (blue). Inset shows far UV CD spectrum for FIII9'10 in aqueous solution.....	145
Figure 4-8 Far UV CD spectra for FIII9"10 H2P adsorbed to beads with surfaces of increasing hydrophobicity: silica (red), mPEG-silane (purple), APTMS (green), PFTOS (orange) and TCOS (blue). Inset shows far UV CD spectrum for FIII9''10 H2P in aqueous solution.....	146
Figure 4-9 Near UV CD spectra for FIII9-10 (A), FIII9'10 (B) and FIII9''10 H2P (C) in solution (yellow) and adsorbed to beads with surfaces of increasing hydrophobicity: silica (red), mPEG-silane (purple), APTMS (green), PFTOS (orange) and TCOS (blue).....	147
Figure 4-10 Mass increase as a function of the H/D exchange time (on a logarithmic scale) for FIII9-10 (■), FIII9'10 (▲) and FIII9"10 H2P (●).....	150
Figure 4-11 Schematic of neutron beam reflection pathway as it interacts with a protein bilayer formed at solid liquid interface between protein sample and TiO ₂ substrate surface.....	151
Figure 4-12 Reflectivity profile for FIII9'10 adsorbed to TiO ₂ coated silicon substrate surface at bulk concentrations of 10 (red), 30 (blue), 100 (green) and 200 (yellow) mg/L in D ₂ O phosphate buffer. Data points shown as empty circles with the fitted reflectivity profiles shown as solid lines of the same colour. For clarity, reflectivity profiles for increasing bulk concentrations are sequentially offset in the ordinate by a factor of log ₁₀ 0.5. Surface following washing (black) displayed with highest offset.	155

Figure 4-13 Schematic depicting the possible arrangement of FIII9'10 (grey ovals) adsorption following incubation with concentrations of 10 mg/L, 30 mg/L, 100 mg/L, 200 mg/L and following washing at the TiO₂ surface (shown as grey line)..... 157

Figure 4-14 Reflectivity profile for d-FIII9'10 adsorbed to TiO₂ coated silicon substrate surface at bulk concentrations of 10 (red), 30 (blue), 100 (green) and 200 (yellow) mg/L in H₂O phosphate buffer. Data points shown as empty circles with the fitted reflectivity profiles shown as solid lines in the same colour. For clarity, reflectivity profiles for increasing bulk concentrations are sequentially offset in the ordinate by a factor of log₁₀0.5. Surface following washing (black) displayed with highest offset. 158

Figure 4-15 Schematic depicting the possible arrangement of d-FIII9'10 adsorption following incubation with concentrations of 10 mg/L, 30 mg/L, 100 mg/L, 200 mg/L and following washing (top to bottom) at the TiO₂ surface (shown as grey line). 159

Figure 4-16 Reflectivity profile for FIII9"10 H2P adsorbed to TiO₂ coated silicon substrate surface at bulk concentrations of 10 (red), 30 (blue), 100 (green) and 200 (yellow) mg/L in D₂O phosphate buffer. Data points shown as empty circles with the fitted reflectivity profiles shown as solid lines in the same colour. For clarity, reflectivity profiles for increasing bulk concentrations are sequentially offset in the ordinate by a factor of log₁₀0.5. Surface following washing (black) displayed with highest offset. 160

Figure 4-17 Schematic depicting the possible arrangement of FIII9"10 H2P adsorption following incubation with concentrations of 10 mg/L, 30 mg/L, 100 mg/L, 200 mg/L and following washing (top to bottom) at the TiO₂ surface (shown as grey line). 162

Figure 4-18 Reflectivity profile for d-FIII9"10 H2P adsorbed to TiO₂ coated silicon substrate surface at bulk concentrations of 10 (red), 30 (blue), 100 (green) and 200 (yellow) mg/L in H₂O phosphate buffer. Data points shown as empty circles with the fitted reflectivity profiles shown as solid lines in the same colour. For clarity, reflectivity profiles for increasing bulk concentrations are sequentially offset in the ordinate by a factor of log₁₀0.5. Surface following washing (black) displayed with highest offset. 163

Figure 4-19 Schematic depicting the possible arrangement of d-FIII9"10 H2P adsorption following incubation with concentrations of 10 mg/L, 30 mg/L, 100 mg/L, 200 mg/L and following washing (top to bottom) at the TiO₂ surface (shown as grey line). 164

Figure 4-20 Binding of FIII9-10 (■), FIII9'10 (▲) and FIII9"10 H2P (●) to integrin α5β1 as measured by ELISA. Results are normalised and expressed as percentages of maximum binding activity. 165

Figure 4-21 BHK cell adhesion data for surfaces coated with FIII9-10 (■), FIII9'10 (▲) and FIII9''10 H2P (●). Error bars represent the sample standard deviation.	166
Figure 4-22 Immunofluorescence image showing BHK cell attachment onto untreated TiO ₂ substrate stained for vinculin (blue), actin (pink), and the nuclei (yellow). Images are shown with colour inverted to aid contrast and were photographed at 20x magnification (left) and 63x magnification (right).	168
Figure 4-23 Immunofluorescence image showing BHK cell attachment onto TiO ₂ substrate coated with either 100 µg/ml FIII9-10 (A), FIII9'10 (B) or FIII9''10 H2P (C). Cells were stained for vinculin (blue), actin (pink), and the nuclei (yellow). Images are shown with colour inverted to aid contrast and were photographed at 20x magnification (left) and 63x magnification (right).	171
Figure 5-1 Schematic of the ligands FIII9'10-GGC (A), FIII9'10-dimer (B), FIII9'10-trimer (C) and FIII9'10-tetramer (D). Each “portion” of the multimeric ligand is described and dashed lines are a visual aid to help distinguish between sections. For simplicity the coiled-coils are drawn as one block.	185
Figure 5-2 Schematic of surface layers of Au magnetic contrast NR substrate, including 11-MUD passivation layer interpenetrated with protein in D ₂ O buffer...	191
Figure 5-3 Far UV CD spectra of the dimer (dashed line), trimer (solid line) and tetramer (dotted line) in 10 mM NaH ₂ PO ₄ , 300 mM NaCl, pH 7.0.....	194
Figure 5-4 Far UV CD spectra for multimeric ligands dimer (A), trimer (B) and tetramer (C) in 10 mM NaH ₂ PO ₄ , pH 7 buffer following incubation with varying salt concentrations from 50 to 500 mM.	196
Figure 5-5 Far UV CD spectra of thermal denaturation of multimeric ligands dimer (A), trimer (B) and tetramer (C) in 10 mM NaH ₂ PO ₄ , 300 mM NaCl, pH 7 buffer.	198
Figure 5-6 Global analysis of CD spectra data for thermal denaturing of multimers dimer (A) trimer (B) and tetramer (C) showing folded species (blue), intermittent step (red) and unfolded species (green). Left pane shows comparison of the different spectral shapes. Right pane shows concentration profile comparing the different species at 20 to 100 °C.....	200
Figure 5-7 Far UV CD spectrum of multimeric ligands, dimer (A), trimer (B) and tetramer (C) following incubation with varying concentrations of GdmCl in 10 mM NaH ₂ PO ₄ , 300 mM NaCl, pH 7 buffer.....	202
Figure 5-8 Reflectivity profile showing up-spin (triangles) and down-spin (circles) for magnetic Au surface coated with self-assembling monolayer of 11-MUD (empty shapes) and proteins (filled shapes) layer one (black) layer two (grey): FIII9'10-GGC (A), trimer (B) and tetramer (C). Data points shown as empty/filled circles/triangles with the fitted reflectivity profiles shown as solid lines of the same	

colour. For clarity, reflectivity profiles for up-spin have been offset in the ordinate by a factor of \log_{10}204

Figure 5-9 Fitted SLD for reflectivity data corresponding to the fits of all polarisation data for FIII9'10 GGC, trimer and tetramer adsorbed to Au/11-MUD substrate from solution in 10 mM NaH_2PO_4 , 50 mM NaCl, pH 7.4 for FIII9'10-GGC and 10 mM NaH_2PO_4 , 300 mM NaCl, pH 7.4 for trimer and tetramer prepared with D_2O . Profiles are shown as the distance from the Silicon/ SiO_2 substrate interface and labels are used as a guide for the SLD of each layer. Solid line shows “up” spin and dotted line corresponds to “down” spin.207

Figure 5-10 Immunofluorescence image showing BHK cell attachment onto Au/11-MUD substrate stained for vinculin (blue), actin (pink), and the nuclei (yellow). Images are shown with colour inverted to aid contrast and were photographed at 20x magnification (left) and 63x magnification (right).208

Figure 5-11 Immunofluorescence image showing BHK cell attachment onto Au/11-MUD substrate coated with FIII9'10-GGC, stained for vinculin (blue), actin (pink), and the nuclei (yellow). Images are shown with colour inverted to aid contrast and were photographed at 20x magnification (A and B) and 63x magnification (C and D).....209

Figure 5-12 Immunofluorescence image showing BHK cell attachment onto Au/11-MUD substrate coated with trimer, stained for vinculin (blue), actin (pink), and the nuclei (yellow). Images are shown with colour inverted to aid contrast and were photographed at 20x magnification (A and B) and 63x magnification (C and D)...210

Figure 5-13 Immunofluorescence image showing BHK cell attachment onto Au/11-MUD substrate coated with tetramer, stained for vinculin (blue), actin (pink), and the nuclei (yellow). Images are shown with colour inverted to aid contrast and were photographed at 20x magnification (A and B) and 63x magnification (C and D)...211

LIST OF TABLES

Table 1-1 Integrins and their respective receptor family.	5
Table 1-2 Selection of RGD supporting ligands and their corresponding integrin binding partners. [Data from Humphries et al. 2006].	27
Table 2-1 Primer design for mutation of FIII9'10-GGC and FIII9'10.	48
Table 2-2 DNA values as calculated by GeneQuantII.	65
Table 2-3 Computed parameters for His tagged FIII9-10 proteins.	69
Table 2-4 Size exclusion chromatography calibration standards.	74
Table 2-5 Estimation and calculated M_r of the mutated proteins by size exclusion chromatography.	75
Table 3-1 SPR response for binding of integrin $\alpha 2\beta 1$ to FIII9'10-GGC mutants.	99
Table 3-2 Equilibrium chemical denaturation of FIII9-10 and mutants.	101
Table 3-3 Calculated transition values from temperature unfolding of FIII9-10 domain pairs.	104
Table 4-1 Running conditions for 18 cm Immobiline DryStrip on Ettan IPGphor Isoelectric focusing unit.	134
Table 4-2 Advancing contact angles of water on surfaces.	141
Table 4-3 Measurement of protein bands following isoelectric focusing.	149
Table 4-4 Calculated neutron reflectivity parameters for bare substrate surfaces. ...	152
Table 4-5 Neutron reflectivity parameters used for calculation of the surface coverage of protein at a range of bulk concentrations from 10 to 200 mg/L.	154
Table 4-6 Calculated neutron reflectivity parameters for FIII9'10 adsorbed to TiO_2 obtained from measurements in D_2O phosphate buffer.	155
Table 4-7 Calculated neutron reflectivity parameters for d-FIII9'10 adsorbed to TiO_2 obtained from measurements in H_2O phosphate buffer.	158
Table 4-8 Calculated neutron reflectivity parameters for FIII9"10 H2P adsorbed to TiO_2 obtained from measurements in D_2O phosphate buffer.	161
Table 4-9 Calculated neutron reflectivity parameters for d-FIII9"10 H2P adsorbed to TiO_2 obtained from measurements in H_2O phosphate buffer.	163

Table 5-1 Temperature unfolding of FIII9'10 GCC multimeric ligand calculated transition values.	199
Table 5-2 Layer thickness and component volume fractions from constrained fits to multiple data sets using Monte Carlo analysis.	205

ABSTRACT

This thesis presents an investigation into a 9th-10th type III fibronectin (FN) domain pair (FIII9-10) focused on the characterisation and functional activity of the protein.

Initial work attempted to establish whether there was a binding interaction between FIII9-10 and IGFBP-5. Surface plasmon resonance failed to demonstrate an interaction and so thereafter the programme examined the use of FIII9-10 as a protein scaffold for cell adhesion.

Surface-induced unfolding of proteins results in a loss of function. To improve the conformational stability of FIII9-10, Pro-Pro pairs were introduced. A previously developed multimeric FIII9'10 α 5 β 1 ligand was also studied.

FIII9-10 cDNA constructs were expressed in *E. coli*. Purity, fold and molecular weight were confirmed using SDS-PAGE, circular dichroism (CD) and mass spectrometry. Changes in conformational stability generated by the mutations were assessed by equilibrium chemical denaturation. An automated CD system was used to follow the secondary structure changes generated by thermal denaturation. Adsorption induced structural changes were investigated using a novel 'solid state' CD technique for a range of surface energies. Neutron reflectometry was employed to estimate the surface coverage and packing arrangement of the FIII9-10 mutants.

Calculation of the Gibbs free energy demonstrated a two-fold increase in stability compared to wild type with a 9-11°C increase in the T_m . The mutated proteins showed enhanced stability when adsorbed to silica, but lost structure as surface hydrophobicity increased. This loss was less than that for the wild-type. ELISA studies verified that the mutation of the FIII9-10 did not compromise the receptor

binding affinity. Immunofluorescence microscopy of baby hamster kidney on protein coated substrates displayed improved cell adhesion and spreading.

The enhanced structural stability of the FIII9-10 mutants showed promise for use in influencing and controlling the interactions between medical implants and host tissue, mimicking the role of the extracellular matrix and improving biocompatibility.

CHAPTER 1. Introduction

1.1 The extracellular matrix (ECM)

The extracellular matrix (ECM) is a complex, tissue-specific arrangement which influences and controls the physical environment and interactions of cells (Figure 1-1). It occupies the extracellular space and, although a significant proportion of the ECM is water, the two main structural components are proteoglycans and fibrous proteins. These two macromolecular families contribute to the diverse functions of the ECM and help to regulate tasks such as cell adhesion, migration and rigidity, which are strongly dependent on the surrounding physical environment. The ECM arrangement is involved in controlling and organising a range of cellular processes including cell attachment, wound healing, organ development, tissue regeneration and tumorigenesis. A greater insight of the ECM ability to control cellular processes *in vivo* could be translated to therapeutic technologies to improve wound healing or prevent progression of cancer and other diseases (Shin et al. 2003, Guo and Giancotti 2004, Berrier and Yamada 2007, Frantz et al. 2010).

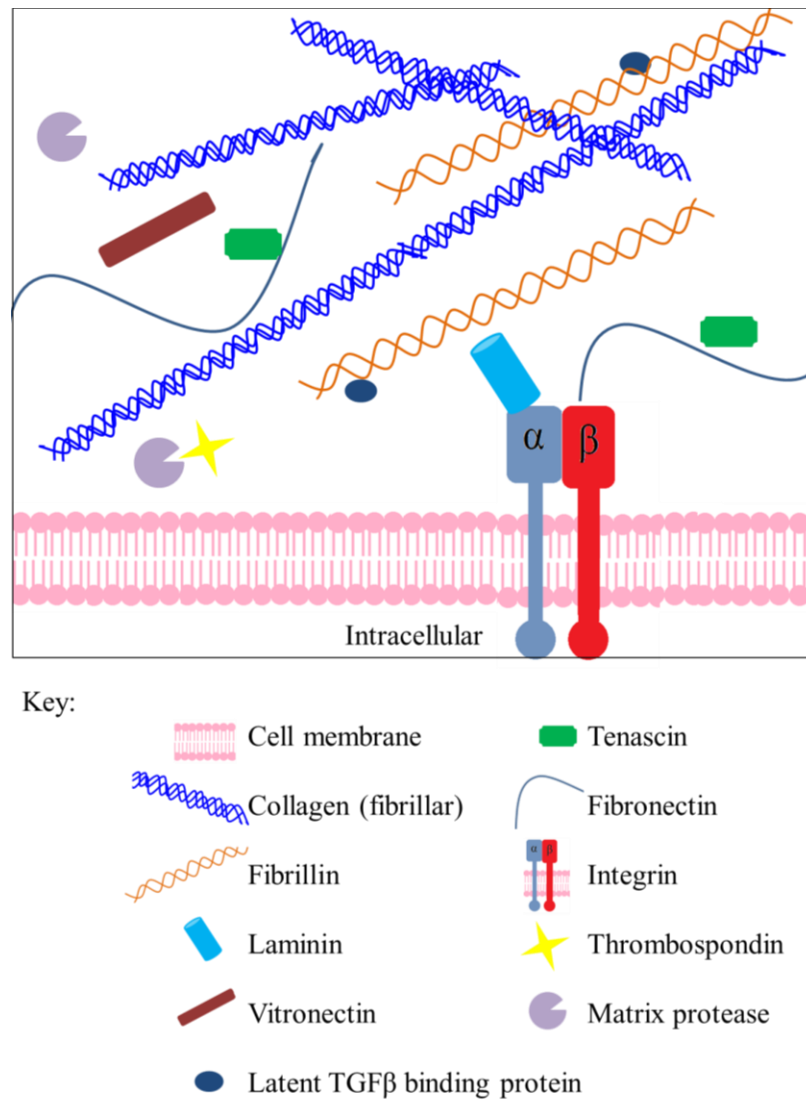


Figure 1-1 Schematic representation of some of the main features of the extracellular matrix. [Reproduced from Huxley-Jones et al. 2008].

An understanding of the structural components has become important with the generation of engineered ECM whose stiffness, orientation, ligand binding and morphology can be controlled (Frantz et al. 2010). As part the ECM arrangement there are several connective tissue components including several classes of collagen and the non-collagenous proteins laminin, vitronectin and fibronectin (FN). Cell

adhesion to the ECM is primarily mediated through integrin receptors which contribute to numerous physiological and pathological processes. Matrix adhesion sites contain integrin clusters which associate with the cell actin cytoskeleton allowing for dynamic changes in cell morphology which are essential for tissues to withstand shear stresses (Calderwood et al. 2000).

1.2 Integrin receptors

One of the most important types of cell surface adhesion and signalling receptor are the integrin receptors (Hynes 2002). Present in many cell types including smooth muscle, endothelium, platelets and osteoclasts (Samanen et al. 1997), this heterodimeric group of receptors consist of two non-covalently associated transmembrane α and β subunits which interact independently for correct ligand binding (Humphries 2000). Both α and β comprise of a large extracellular domains composed of a membrane distal, globular head (~ 700-1100 residues). The integrin subunits consist of large N-terminal extracellular domain and a short C-terminal cytoplasmic domain which, with specific stimulation, can facilitate biochemical and mechanical changes within the cell (Figure 1-2) (Luo et al. 2007).

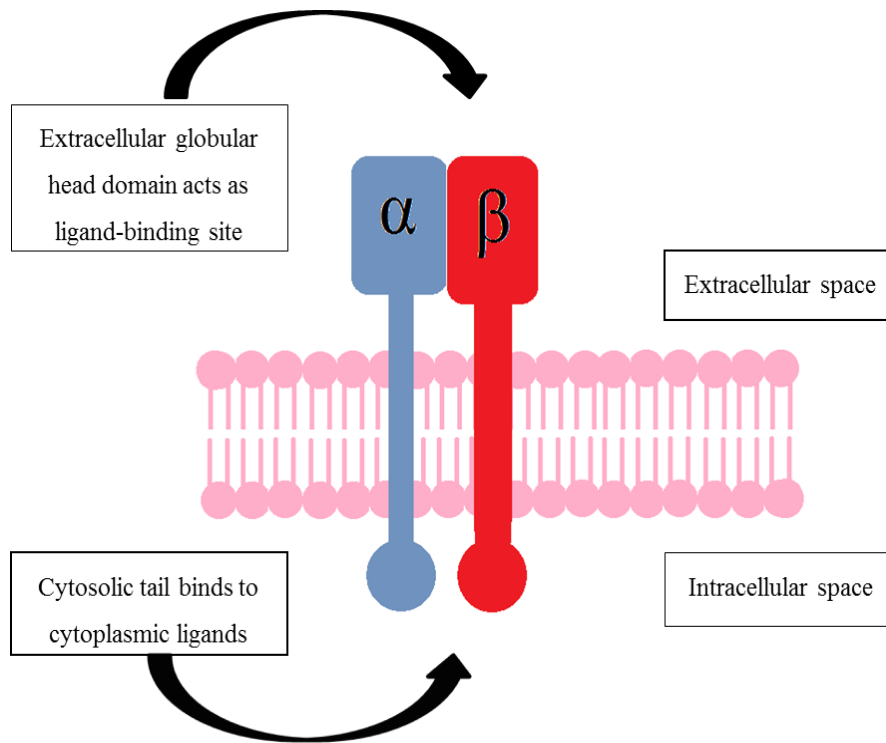


Figure 1-2 Schematic representation of α (blue) and β (red) subunits of a typical integrin spanning the cell membrane (pink).

Integrin mediated ECM adhesions can be said to have a dual function to both probe the surrounding area and facilitate attachment (Geiger and Bershadsky 2001). Interaction between integrins and ECM proteins trigger a sophisticated signalling process within the cell. This results in the formation of focal complexes and the activation of the cellular actin network to form cytoskeletal projections on the mobile edge of the cell, termed lamellipodium. In turn these lamellipodia protrusions outgrow the cell which “search” for further points for interaction thus driving the attachment and migration of the cell (Geiger and Yamada 2011).

Ligand specificity is determined by the combination of the α and β subunits, to date there have been eighteen α and eight β identified. There are at least 24 kinds of

dimeric combinations that have been identified in vertebrates each having distinct binding profiles to the various extracellular ligands (Beckerle 2001, Thomas et al. 2006). Several integrins can recognise the same ligands with varying affinity (Table 1-1).

Table 1-1 Integrins and their respective receptor family.

RGD receptors	Collagen receptors	Laminin receptors	Leukocyte-specific receptors
$\alpha 5\beta 1$	$\alpha 1\beta 1$	$\alpha 3\beta 1$	$\alpha 4\beta 1$
$\alpha 8\beta 1$	$\alpha 2\beta 1$	$\alpha 6\beta 1$	$\alpha 4\beta 7$
$\alpha IIb\beta 3$	$\alpha 10\beta 1$	$\alpha 6\beta 4$	$\alpha 9\beta 1$
$\alpha V\beta 3$	$\alpha 11\beta 1$	$\alpha 7\beta 1$	$\alpha X\beta 2$
$\alpha V\beta 5$	$\alpha Ib\beta 3$		$\alpha L\beta 2$
$\alpha V\beta 6$			$\alpha D\beta 2$
$\alpha V\beta 8$			$\alpha M\beta 2$
			$\alpha E\beta 7$

[Data from Plow et al. 2000, Barczyk et al. 2010].

Electron micrographs of the complete ectodomain (domain which extends into the extracellular space), which includes the headpiece with the ‘lower leg’ calf and epidermal growth factor domains of the α and β subunits, respectively, have been acquired for integrin $\alpha IIb\beta 3$ in its rested and activated state (J. Zhu et al. 2008). The integrin receptors have been shown to change from compact ‘bent’ form when inactive, which results in the head domains lying close to the cell membrane, and an extended ‘standing’ conformation when activated (Nishida et al. 2006). Figure 1-3 depicts a schematic representation of the compact and standing states of a typical integrin. Interestingly, studies of the crystal structures of an extracellular segment of $\alpha v\beta 3$ interacting with a FN fragment showed that the bent conformation could bind

with the arginine-glycine-aspartic acid tripeptide (RGD) site (Adair et al. 2005). This supports previous work which demonstrated that a cyclic RGD peptide could bind to the bent conformation of $\alpha V\beta 3$ (Xiong et al. 2002), thus highlighting the complex nature of integrin structure and function.

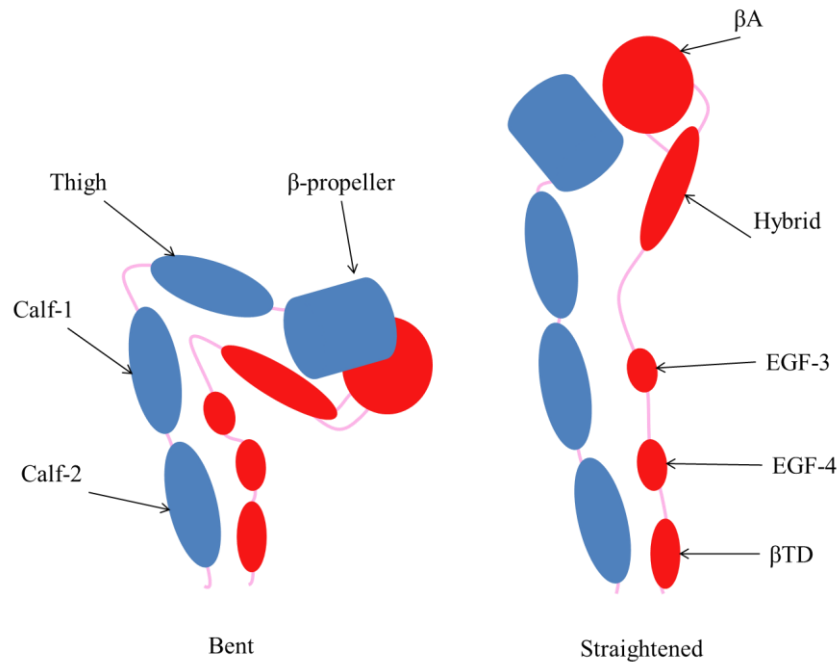


Figure 1-3 Schematic representation of the rested (bent) and activated (straightened) states of the ectodomain of integrin $\alpha IIb\beta 3$. Domains including thigh, calf and epidermal growth factor-like (EGF) are labelled on the α (blue) and β (red) subunits. [Data from Xiong et al. 2001, Jianghai Zhu et al. 2008].

The attachment and spreading of cells on ligands such as vitronectin, FN or collagen is organised by the integrin receptors into focal contacts that form at the end of actin filaments (Wayner et al. 1991). The binding of a ligand to an integrin receptor causes tyrosine phosphorylation of the β subunit cytosolic domain by v-src (Tapley et al. 1989). This in turn facilitates the binding of cell actin filaments and intermediary proteins (vinculin and talin) which form complexes associated with the focal

adhesion structures (Wayner et al. 1991). Thus, integrins are thought to exist on the cell surface in an inactive form and can be activated either by binding ECM (outside-in signalling), but also by intracellular signalling (inside-out signalling) (Takagi et al. 2002). Outside-in signalling involves cell adhesion, proliferation, migration, differentiation and apoptosis (Faull and Ginsberg 1996, Plow et al. 2000, Ling et al. 2003). Inside-out signalling involves, for example, platelet aggregate via α II β 3 activation leading to haemostasis (Shattil 1999). Integrin receptors may alternate between active and inactive states by conformational changes of the ligand binding sites from a high affinity state (active) to a low affinity state (inactive).

Integrin receptors are usually present at 10-100 fold higher concentrations on the cell surface than other non-adhesive receptors (Albers 1994). It is likely that the ECM binds a large number of integrins in a polyvalent manner, increasing binding affinity. However, tight regulation over integrin recruitment activation state and binding affinity must be maintained in order to facilitate transitional cell detachment during cell migration. It is known that ECM proteins stimulate the clustering of integrins, which is a key step in the assembly of cell focal adhesions. In association with the formation of focal adhesions, there is a force dependent “adhesion strengthening” process (Laukaitis et al. 2001, von Wichert et al. 2003, Wozniak et al. 2004).

1.3 Key protein components of the ECM

1.3.1 Vitronectin

The small multifunctional adhesive glycoprotein vitronectin is mostly present in the blood as a monomer, but can also be found in the ECM of various tissues and bodily fluids (up to 16mer) (Stockmann et al. 1993). The polypeptide chains often are in the form of two molecular species of around 60 and 75kDa of which up to 30 % is a result of glycosylation. The recognised cell binding domain sequence RGD is present and through this integrin binding is facilitated. Vitronectin is known to bind to the integrins $\alpha\beta3$ and $\alpha\beta5$ to support cell adhesion (Wayner et al. 1991). The formation of multimeric vitronectin clusters has been shown to increase heparin binding when compared to the monomeric form. These multimers can form by reducing the vitronectin with urea also following binding of the molecule to plasminogen activity inhibitor PAI-1 (Memmo and McKeown-Longo 1998). More recently, it has been shown that to achieve enhancement of cell adhesion and spreading, oligomerisation must be initiated, additionally that this process requires the heparin binding domain (Chillakuri et al. 2010).

1.3.2 Collagen

Collagen is a multichain glycoprotein constructed from three polypeptide units forming a unique triple-helix conformation. It is a major structural component of the ECM and the most abundant of the structural proteins. There are at least 20 different kinds of genetically distinct molecules which, based on structural features, can be

categorized as fibril-forming (types I, II, III, V and XI) and network-forming (types IV, VIII and X), with type I being the most common in the ECM. This key component of the ECM is a versatile substrate for supporting cell proliferation and differentiation (Friess 1998, Harley and Gibson 2008).

1.3.3 Laminin

Interactions via the basement membrane are mediated by the engagement of laminin with several integrins including $\alpha3\beta1$, $\alpha6\beta1$, $\alpha7\beta1$ and $\alpha6\beta4$. The structural conformation of laminin involves three non-identical polypeptide chains, α , β and γ which form cross-shaped molecules in mammals. There are five α , three β and three γ subunits identified which can combine to produce 15 isoforms. Their function is determined by the subunit combination which can be selective for multiple cell adhesive regions including the RGD motif which is located on the amino-terminal half of the α chains. It has been determined that integrin binding is specifically governed by α chains (Adams 2002, Nishiuchi et al. 2006). The full importance of laminin is still emerging; for example, direct interaction between laminin and retinal ganglion cells is required for full axon emergence and orientation *in vivo* (Randlett et al. 2011).

1.3.4 Fibronectin

FN plays an important role in both the biological function and the structural integrity of cells and tissues (Hynes and Yamada 1982). In humans the FN gene comprises of 46 exons within an 82 kb gene and is located on chromosome 2 (2q34). Due to extensive alternative splicing of FN pre-mRNA there are 20 potential isoforms of the protein leading to variants with different functions (White et al. 2008). The occurrence of splicing gives rise to insoluble cell associated FN (cFN) and soluble plasma FN (pFN). FN is one of many important ECM proteins engaged in wound healing and contributes to almost every stage. It is involved in platelet formation during the initial inflammation stage of healing and is also released by macrophages as a chemotactic factor to attract fibroblast cells to the injured area. It helps to promote cell proliferation by forming a provisional matrix with fibrin and collagen type V which enables migrating cells to anchor to the area. As part of the fibrin clot FN provides a supportive scaffold which enhances fibroblast activity and stimulates healing and wound contraction (J. Li et al. 2007).

FN usually exists as a dimer of about 500 kDa composed of two subunits linked by a disulphide bond near their C-terminus. Isopeptide bonds form between FN dimers in the N-terminal domain to form insoluble (cellular) cFN (Pankov and Yamada 2002). The association of FN with cell surface integrins is the main motivator behind this process (Mao and Schwarzbauer 2005). The FN monomers contain three types of repeating unit, termed type I, type II and type III (Figure 1-4). Each repeating unit has a different number of amino acid residues with type I usually consisting of about 40, type II comprising of approximately 60 and type III having the most with around

90 amino acids. Furthermore type I and II each have two intrachain disulfide bonds while type III does not contain any disulphides. Typically FN contains 12 type I repeats each with stacked β -sheets enclosing a hydrophobic core. There are two type II repeats comprising of disulfide bond linked perpendicular anti-parallel β -sheets. Type III repeats make up approximately 90% of the FN sequence with 15 to 17 repeats (Pankov and Yamada 2002, Mao and Schwarzbauer 2005).



Figure 1-4 Schematic representation of a fibronectin monomer containing 3 repeating units, type I (blue), II (red) and III (green). Including alternatively spliced repeats (black): extra domain A (EDA), extra domain B (EDB) and variable region (V) which can contain different lengths of amino acids.

There are at least 11 heterodimeric integrins which FN can bind to in a cell and tissue specific manner, the best characterised of these are integrin $\alpha 5\beta 1$ and $\alpha v\beta 3$. FN contains multiple binding sites for other ECM compounds including heparin (Hayashi et al. 1980) and collagen (Balian et al. 1980). The binding of FN to cell surface integrins thus providing a physical and biological link between cells and the ECM is important to these studies.

The short polypeptide sequence, RGD, located on the peptide loop in the 10th FN type III domain (FIII10) is the key attachment site for integrins (Pierschbacher and Ruoslahti 1984). In addition to this sequence, a “synergy site” proline-histidine-serine-arginine-asparagine (PHSRN) has been located to the 9th FN type III domain

(FIII9), which is required for maximum binding to integrin $\alpha 5\beta 1$ (Aota et al. 1994, Mardon and Grant 1994). Figure 1-5 shows the conformational positioning of the PHSRN and RGD motifs on the 9th and 10th type III FN repeats.

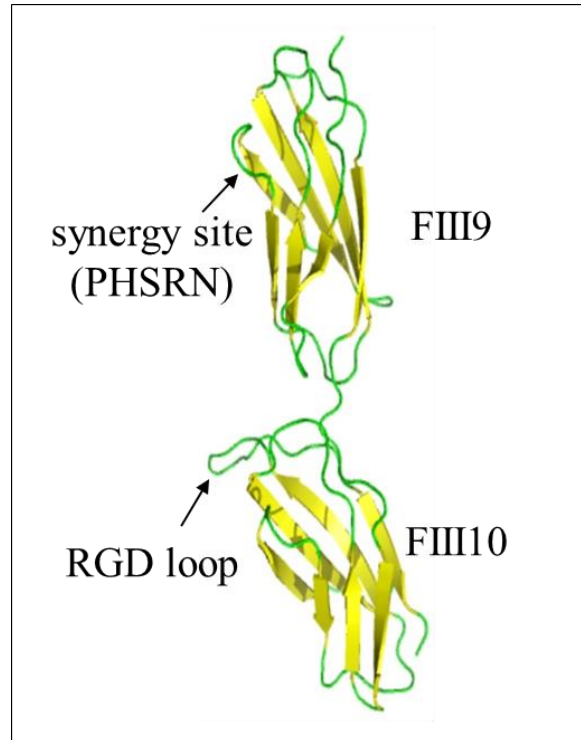


Figure 1-5 Ribbon diagram of FIII domains 9 and 10. β strands shown as ribbons (yellow) and the exposed loops PHSRN (FIII9) and RGD (FIII10) indicated. [Coordinates were obtained through Protein Database and the image produced using JMol (12.2.24)].

Conformational stabilisation of FIII9 occurs through interaction with its neighbouring domains, particularly the 8th type III FN domain (FIII8) (Altroff et al. 2001). The domain-domain mobility between FIII9 and FIII10 is unusually high; constricting this mobility by introducing an interdomain disulphide bridge brings about a change in the relative orientation between the RGD- and PHSRN-bearing loops and a decrease in $\alpha 5\beta 1$ binding affinity (Altroff et al. 2004). Thus, while cell adhesion and spreading can be controlled through site-directed mutation of key

residues in binding motifs, an alternative route would be to subtly alter the FIII9/FIII10 scaffold architecture. Integrin $\alpha 5\beta 1$ mediates osteoblast differentiation, angiogenesis, tumorigenesis and embryo implantation, thus FIII9 and FIII10 have a potential for use in tissue engineering, anti-cancer and implantation therapies.

1.4 The insulin-like growth factor axis

The insulin like growth factor (IGF) axis is an important group of molecules which play a vital part in the different stages of several varieties of cell life cycles (Lochrie et al. 2006). Numerous tissues are affected by the developmental and regulatory effects of these molecules (Beattie et al. 2006). The IGF axis is known to be involved in the differentiation and apoptosis of mammary epithelial cells (Lochrie et al. 2006) and, under specific circumstances may also play a role in tumorigenesis (X. Q. Li et al. 2007). The IGF axis, shown in Figure 1-6, consists of insulin like growth factors (IGF-I and IGF-II), the cell surface receptors IGF-IR and IGF-IIR, and six high affinity IGF binding proteins (IGFBP1-6) (Beattie et al. 2006). Components of the IGF axis are also known to interact with other biomolecules within the extracellular matrix, the effects of which have been the source of many sometimes conflicting studies. This present work will pay particular attention to the interactions between IGFBP-5 and FN owing to the possible affects it may have on breast cancer cell proliferation.

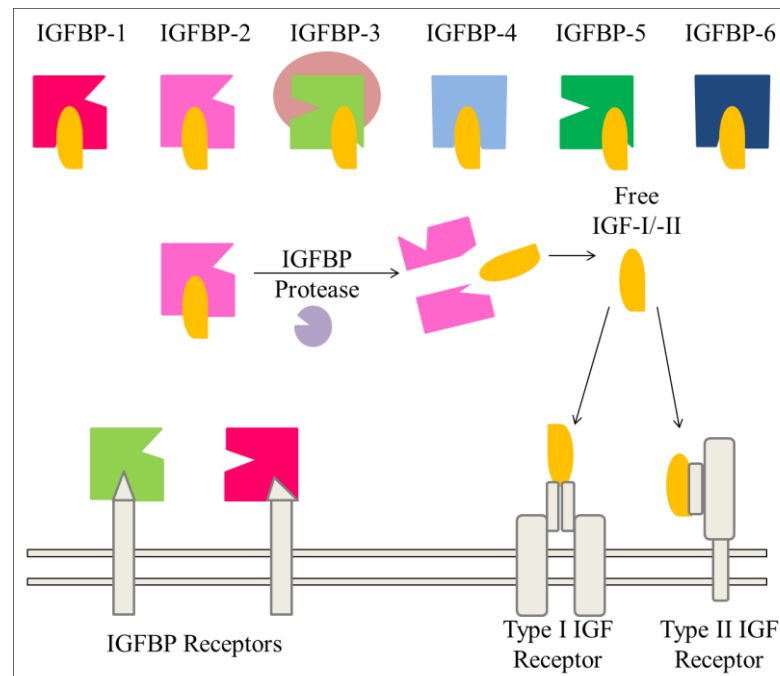


Figure 1-6 The IGF axis consist of IGF-I and IGF-II polypeptides (orange), six IGFBPs (various colours), a family of proteases (lilac) and cell-surface IGFBP receptor, IGF-IR and IGF-IIR (light grey). [Reproduced from Beattie et al. 2006].

1.4.1 Insulin-like growth factors

IGF-I and IGF-II are single-chain polypeptides of about 7 kDa in size (Sachdev and Yee 2001, Mohan and Baylink 2002) they are structurally and functionally similar to insulin (Yu and Rohan 2000, Sachdev and Yee 2001, Mohan and Baylink 2002, Beattie et al. 2006) and play an important part in the growth and differentiation of several tissues (Lochrie et al. 2006).

Many tissues are known to produce IGF-I, including the brain, muscle and bone however the greatest contributor to circulating IGF-I is the liver (Mohan and Baylink 2002, Beattie et al. 2006). It is thought that the action of IGF-II on growth and development occurs mostly during embryonic and foetal growth, a role which is then

replaced by IGF-I after birth. Circulating IGF-I concentrations vary with age, increasing slowly from birth then peaking during puberty and declining with age finally achieving around 100-200 ng/ml in adult life. The changing concentrations of IGF-I are regulated by growth hormone (GH). IGF-II concentrations remain fairly constant after birth; they are significantly higher than IGF-I and can reach up to 400-600 ng/ml in adults (Yu and Rohan 2000).

The expression of IGF-I is mainly stimulated by pituitary GH which is responsible for linear growth and development (Helle 2004). In normal humans, there is a negative feedback loop between these hormones in which a surplus of IGF-I suppresses the secretion of GH (Helle 2004). The expression of both IGF-I and IGF-II is dependent on cell and tissues type as they are expressed in a wide variety of cells (Beattie et al. 2006). Furthermore, IGF expression is also regulated by other growth factors including epidermal growth factor, fibroblast growth factor and platelet-derived growth factor as well as hormones such as follicle-stimulating hormone, luteinizing hormone and thyrotropin (Yu and Rohan 2000). It is well established that the IGFs are important mediators of physiological growth (Allan et al. 2006). They also regulate cell survival, proliferation, differentiation and migration (Yu and Rohan 2000, Marshman et al. 2003). Additionally IGFs can act as survival factors, protecting cells from apoptosis (Yu and Rohan 2000).

1.4.2 Insulin-like growth factor receptors (IGFR)

The IGF receptors present on the cell surfaces are involved in mediating intracellular activities of the IGFs, including growth. The main receptor is insulin-like growth factor I receptor (IGF-IR) which both IGF-I and IGF-II bind to, with IGF-I having a 2 to 15-fold higher binding affinity (Yu and Rohan 2000, Firth and Baxter 2002, Marshman et al. 2003). The IGF-IR is heterotetrameric and comprises of two α and two β subunits. It has structural similarities to the insulin receptor and is also able to bind with insulin with a much lower affinity (Yu and Rohan 2000, Marshman et al. 2003, Beattie et al. 2006).

1.4.3 Insulin-like growth factor binding proteins (IGFBP)

The majority of circulating IGFs are bound in a complex to insulin-like binding proteins 1-6 (IGFBP 1-6) (Helle 2004). The IGFBPs are a group of six extracellular binding proteins which exhibit a modulator effect on the mitogenic actions of the IGFs due to their greater binding affinity to the IGFs than that of the cell surface receptors. Their actions are dependent upon the tissue type, species, concentration of IGFBP and the presence of proteins such as heparin, osteopontin and FN in the ECM (Nam et al. 2000, Nam et al. 2002, Xu et al. 2004, Beattie et al. 2005, Flint et al. 2005).

The higher affinity of the IGFs for the IGFBPs may be a preventative measure to reduce any undesirable effects of the IGFs such as uncontrolled cell proliferation. The IGFs, however, must be released to allow interaction with the IGF receptor. One

such method is proteolytic degradation of the IGFbps by several specific proteases (Bunn and Fowlkes 2003). IGFbp-3 accounts for about 80-90% of the circulating IGFs and acts as a reservoir increasing the half-lives of the bound IGFs from 10 min to 15 h. The IGFbps bind to IGF-I and protect it from proteolytic degradation in biological fluids, hence controlling the bioavailability of IGF-I in the tissue (Grimberg and Cohen 2000).

The structures of the IGFbps are very similar and can be divided into three distinct domains. A cysteine-rich amino (N)-terminal domain and a cysteine-rich carboxyl (C)-terminal domain joined by a central non-conserved (L) region (Figure 1-7). The cysteine-rich domains contain the IGF binding sites and the central domain carries proteolytic degradation sites. The central domain is the site of post-translational modifications, proteolysis, acid-labile subunit and ECM associations. Differences in the central domain can account for variations in IGF degradation. There is a high level of conservation in both the N- and C- terminal domains. All IGFbps contain 6 cysteine residues in the C-terminal domain and the N-terminal domain of IGFbp1-5 contains 12 while IGFbp-6 has 10 (Allan et al. 2006, Sitar et al. 2006, Akkiprik et al. 2008).

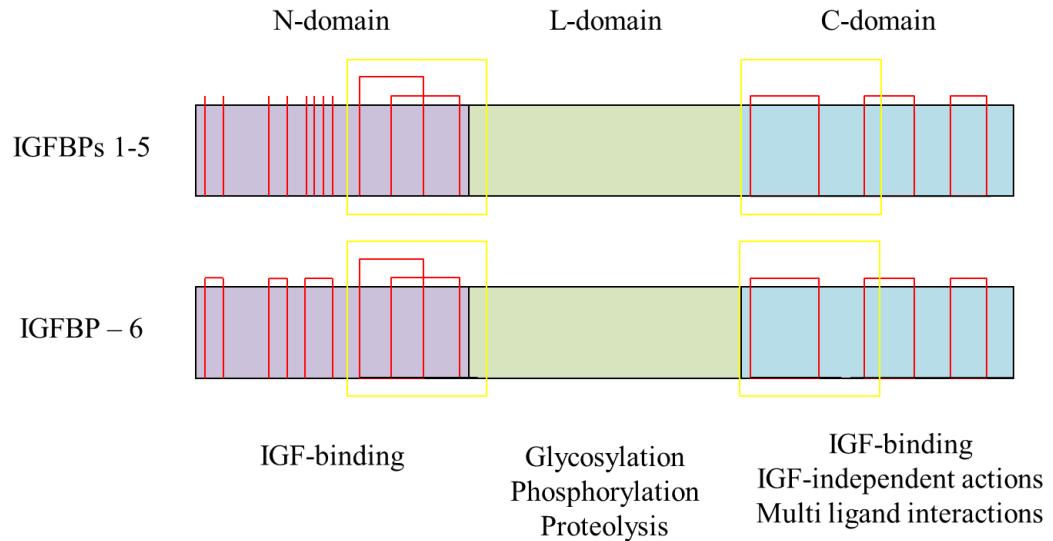


Figure 1-7 Schematic representation of domain structure of the IGFBPs highlighting the similarity between IGFBP1-6. Cysteines indicated by red vertical lines and the disulphide linkages as red horizontal lines. IGF binding regions are contained in yellow boxes. [Reproduced from Bach et al. 2005].

1.4.3.1 Role of IGFBPs in cancer

Extensive research has been carried out into uncovering the role of the IGFBPs with respect to cell proliferation, migration and attachment to the ECM. An area which has received particular interest is the role of IGFBP in cancer. There is conflicting evidence as to whether IGFBP-5 has inhibitory or enhancing effects on breast cancer cells (Perks et al. 1999, Perks et al. 2002, Butt et al. 2003, Butt et al. 2005).

Breast cancer cell growth has been shown to be inhibited in IGFBP-5 over-expressing cells compared to control vectors (cell lines transfected with vector not containing IGFBP-5 cDNA) (Butt et al. 2003). *In vitro* data found a decreased growth rate of tumours was found in mice injected with an IGFBP-5 expressing cells compared to mice injected with the control vector (Butt et al. 2003, Butt et al. 2005).

In contrast, IGFBP-5 has also been shown to give rise to enhanced cell survival in C-2 induced apoptosis. C2-ceramide (*N*-Acetyl-D-sphingosine) induced apoptosis is caused as the membrane structure is altered at the 4,5-*trans* double bond at concentrations between 20 and 35 μ M. The mechanism has yet to be elucidated (Ahn and Schroeder 2010). Perks and colleagues showed that IGFBP-5 could confer survival in cell lines by reducing C2-ceramide induced apoptosis. There was also evidence for an IGF-dependant mechanism. Using MCF-7 cells, which are IGF responsive, a non-IGF binding mutant IGFBP-5 displayed no survival effects on the cells. This suggested that, in such a circumstance, the IGF/IGFBP-5 complex enhances the actions of endogenous IGF by modulating the receptor interaction through preservation and slow release of IGF (Perks et al. 2002).

1.4.3.2 Binding of insulin-like growth factors to insulin-like growth factor binding proteins

The binding of the IGFs to the IGFBPs is thought to involve both the N-terminal and C-terminal domains of the IGFBPs (Bach et al. 2005, Allan et al. 2006, Sitar et al. 2006). Isolated N-terminal IGFBP fragments have shown a decreased binding affinity of 10-1000 fold lower to IGFs than full length IGFBP (Sitar et al. 2006). It was reported by Sitar and co-workers (2006) that the binding of IGF-I to IGFBP-4 involved a segment of IGF-I binding to a “thumb region” of the N-terminal IGFBP-4 composed of the amino acids 1-4, which then mask the IGF residues responsible for IGF-IR binding. Furthermore, this thumb region then interacts with a small number of residues of the C-terminal domain which also contributes to blocking IGF-IR

binding region of IGF-I. Nuclear magnetic resonance spectroscopy confirmed the central domain of full length IGFBP-4 to be unstructured and flexible, irrespective of binding with IGF-I (Sitar et al. 2006).

Although the central domain of IGFBP does not directly bind to IGF-I, it still plays an important part as this is the region which would first be degraded by proteolysis and so expose the bound IGF. However, it is suggested that as long as either the N-terminal “thumb” or C-terminal fragment remain intact, interaction between IGF-I and IGF-IR would still be inhibited. It is proposed that the central domain acts as a “mechanical flap” covering the IGF-I before it is encapsulated by the N- and C-terminal domains (Sitar et al. 2006). Information regarding the binding mechanism of the IGFBPs may lead to a better understanding of their interactions and therefore effect on the cell.

1.4.3.3 Binding of IGFBPs to extracellular matrix proteins

Interactions between the IGFBPs and ECM proteins are thought to be mediated by the C-terminal domain of IGFBP. This region is known to interact with several proteins and other significant molecules with the effect of mediating IGF-independent actions or modulating IGF-dependant actions (Bach et al. 2005). IGF-independent cell migration is mediated by IGFBP-1 binding to the integrin $\alpha 5\beta 1$ subtype via its C-terminal domain RGD sequence (Jones et al. 1993). Heparin is known to inhibit the interactions between both IGFBP-3 and IGFBP-5 with IGF-I (Arai et al. 1994). IGFBP-5 proteolysis has been shown to increase by binding to FN,

this in turn inhibits IGFBP-5 mediated potentiation of IGF-I induced migration (Xu et al. 2004). The binding of the IGFBPs to ECM proteins can have a stimulatory and inhibitory effect which can be IGF-dependant or IGF-independent resulting in stimulation or suppression of IGFBP actions.

1.4.4 IGFBP binding to fibronectin

IGFBP-5 has been shown to bind to both pFN and cFN by glutathione S-transferase pull-down assay and co-immunoprecipitation tests (Xu et al. 2004). Gel permeation chromatography and immunoprecipitation tests have also been utilised to confirm the presence of IGFBP-3/FN complexes in plasma (Gui and Murphy 2001). Studies suggest that the C terminal domain of IGFBP-5 is thought to be the area involved in binding with FN. This has been shown by binding assays using deletion mutants (Xu et al. 2004) and cumulative mutagenesis (Beattie et al. 2009). In the study by Beattie and co-workers (2009), a panel of IGFBP-5 mutants were investigated which included an N-terminal domain mutant with amino acid substitutions at points 68-70 and 73-74 and a series of five cumulative C-terminal mutants with selected residues from 201-218 substituted for alanine. These areas were selected because they correspond to a hydrophobic patch which is considered to be the major IGF binding site (Allan et al. 2006, Beattie et al. 2009). The accumulative effect of the increasing level of mutation in the C-terminal domain of IGFBP-5 displayed a decrease in binding to a FN derived protein fragment, suggesting that the C-terminal domain of IGFBP-5 is engaged in FN binding (Beattie et al. 2009).

Identifying the region of FN which binds to IGFbps has been the subject of many studies. A truncated FN region containing type I repeats 10 and 11 was found to bind with IGFBP-5, leading to the conclusion that the binding domain for FN and IGFBP-5 was located here (Xu et al. 2004). In the study by Xu and co-workers (2004), the binding domain was deduced from overlapping of sequence alignments from FN clones which did not include the RGD motif or the synergy site. However, the use of surface plasmon resonance (SPR) has shown that IGFBP-3 and IGFBP-5 both bind to a biotinylated derivative of the 9th and 10th type III FN domain which contain the synergy site and the RGD motif respectively (Beattie et al. 2009). This data conflicts with a yeast two-hybrid study which found that a 120 kDa fragment of FN containing the cell binding domain did not interact with IGFBP-3, and that a 40 kDa C-terminal fragment containing the heparin binding domain and fibrin binding domain bound to IGFBP-3 (Gui and Murphy 2001).

The difference in experimental techniques could be responsible for the disparity in the results from these three studies. As previously mentioned, the research performed by Xu and colleagues (2004) did not include the cell binding domain in the truncated FN fragments the binding was concluded to be near the 10th and 11th type I repeats which form part of the fibrin binding domain. This would appear to confirm the findings by Gui and Murphy (2001) as the fibrin binding domain is present in the 40 kDa FN fragment. The lack of binding in the 120 kDa cell binding domain containing fragment could be due to low detection limits of the blotting and solid phase binding methods used by Gui and Murphy (2002) for complexes displaying high dissociation (Beattie et al. 2009). A further reason for the differences in results could be due to a structural difference in the conformation of the FN fragments used.

In the study by Beattie and co-workers (2009) mutations of the FN RGD motif, located on the 10th type III FN repeat, were shown to have reduced ability of both IGFBP-3 and IGFBP-5 to bind to a FN derivative, indicating that this area is important for binding. Furthermore, analysis of mutagenesis of the synergy site located on the 9th type III FN repeat suggests that this region is also important for the binding of FN to both IGFBPs. Insert mutations which may change the conformation of FN showed reduced binding (Beattie et al. 2009). It is unsurprising that the structural conformation of the 9th and 10th type III FN domains is important in binding with the IGFBPs as it is also essential for the high affinity binding of FN to other ligands (Grant et al. 1997, Altroff et al. 2004).

1.4.5 Effects of IGFBP binding to fibronectin

1.4.5.1 Cell migration

IGFBP-5 has been shown to dominate the IGF-I action in FN null mouse embryonic (mES) cells but not in wild type. The proliferation of FN null mES cells (which are unable to produce their own FN but still able to assemble a FN matrix when provided exogenous FN) seen on addition of IGFBP-5 and IGF-I to culture media was significantly greater than for addition of IGF-I alone. However, the addition of exogenous IGFBP-5 to wild type mES cells had no effect on IGF-I induced migration. The binding of FN to IGFBP-5 has been shown to eliminate the dominate action of IGFBP-5 over IGF-I induced cell migration (Xu et al. 2004). Furthermore migration of FN null mES cells was measured in the presence and absence of exogenous FN and it was concluded that the addition of FN abolished the dominant

action of IGFBP-5 in IGF-I induced migration. Implying that IGFBP-5 interacts with FN (Xu et al. 2004).

1.4.5.2 Cell attachment

The breast cancer cell line Hs578T does not produce a functional IGF-I receptor and contains negligible amounts of IGF-I and IGF-II. Hence, any effect of the IGFBPs on the cell attachment would be considered to be IGF-independent. The effects of the treatment by different IGFBPs on the attachment of this cell line to FN was measured and found to have varying results. A decrease in cell attachment was seen on addition of IGFBP-2, IGFBP-5 and IGFBP-6. Additionally, no effect was seen for IGFBP-1, and an increase in cell attachment was found for IGFBP-3 and IGFBP-4 (McCaig et al. 2002). It has been postulated that the decrease in cell attachment may be involved in apoptosis of breast cancer cells by removal of cells from the adjacent extracellular matrix (Beattie et al. 2009). The up-regulation of IGFBP-5 during cellular apoptosis in the mammary gland both *in vivo* and *in vitro* further strengthens this concept (Boutinaud et al. 2004, Lochrie et al. 2006). The resulting physiological significance of these results remains to be determined, however it showed that integrin function is affected by the action of IGFBPs at the cell surface (McCaig et al. 2002).

1.5 Mimicking the extracellular matrix for biomaterials

Implanted medical devices have many different uses such as dental implants, vascular stents and metal pins to assist the healing of bone fractures. When a biomaterial is inserted into the body, the surface will come into contact with bodily fluids, such as blood. As a result, the protein components of the blood will interact with the surface. These interactions will then influence the essential cell functions: adhesion, growth and differentiation. There are three interconnected factors to consider when generating a biomedical substrate: (i) the surface of the device, (ii) protein interactions and (iii) subsequent cell responses.

There is great potential for biomaterials which allow control of cell adhesion to deliver tissue engineering solutions for a wide variety of needs in regenerative medicine. Synthetic substrates which mimic the ECM to support cell adhesion, self-renewal and differentiation could be designed towards improving wound healing to promote cell growth in a directed approach. FN is a critical component of the ECM for both structural integrity and biological function; hence, FN-based ECM scaffolds present a promising candidate for use in creating bioactive surfaces. Full length FN does not offer sufficient ligand specificity to be an optimal biomaterial agent. However, FN-based fragments provide an easy to assemble option which can allow for integrin-targeted interactions (Roy and Hocking 2013). Promisingly developments using FN derived matrix mimics have shown to promote bone marrow stromal cell adhesion when functionalised to implants within artificially created rat tibia cortical defects (Petrie et al. 2008).

1.5.1 Cell attachment and the 'RGD' motif

Organisation of FN fibrils in the ECM presents a polyvalent display of ligands to cell surface integrin receptors. Previous work has shown that integrin-driven polymerisation of soluble FN is dependent on extension of the FN monomer in order to expose self-associating sites (Mao and Schwarzbauer 2005). The resultant fibrils are able to undergo extension/contraction over a four-fold change in length, yielding an elastic matrix (Ohashi et al. 1999). Such dynamic movements within the cell matrix inevitably change both the matrix rigidity and the spatial arrangement of the ligand display 'seen' by the cell. Interestingly, fibroblasts have been shown to probe the elasticity of their supporting matrix, responding to greater elasticity with increased motility and protruding lamellipodia but decreased 'spread' morphology (Pelham and Wang 1997).

A vast amount of biomaterials research has focussed on the use of the RGD motif as a target ligand as it is probably the most recognised peptide sequence associated with cell adhesion. Found in FN and multiple other ECM proteins RGD is therefore a predictable target for simulated cell adhesion to surfaces. The affinity of binding to the several integrin receptors which recognise the sequence may be modulated by the conformation of the RGD loop and the surrounding amino acids within the protein (Hersel et al. 2003). A selection of RGD binding integrins and their corresponding ligands are shown in Table 1-2.

Table 1-2 Selection of RGD supporting ligands and their corresponding integrin binding partners. [Data from Humphries et al. 2006].

Integrin binding ligands	RGD binding integrins							
	$\alpha V\beta 3$	$\alpha V\beta 6$	$\alpha V\beta 1$	$\alpha V\beta 5$	$\alpha V\beta 8$	$\alpha IIb\beta 3$	$\alpha 5\beta 1$	$\alpha 8\beta 1$
Bone sialoprotein	✓			✓				
Fibrillin	✓							
Fibrinogen	✓					✓		
Fibronectin	✓	✓	✓			✓	✓	✓
LAP-TGF-β	✓	✓	✓		✓			
MFG-E8	✓			✓				
Osteopontin	✓	✓	✓	✓			✓	✓
Tenascin	✓							✓
Thrombospondin	✓					✓		
Vitronectin	✓			✓		✓		✓
von Willebrand factor	✓					✓		

MFG-E8 (Milk fat globule EGF factor 8), LAP-TGF- β (latency associated peptide transforming growth factor)

The interaction of RGD with the biomaterial surface is an important aspect of engineering biomaterials. Molecular modelling is a useful technique to elucidate the complex interactions between a surface and a peptide or protein. Song and colleagues (2010) utilised modelling in an attempt to clarify the non-specific adsorption of RGD to TiO₂ surfaces presenting either nanotopography or a “perfect” flat surface. The results suggested that prior to RGD interaction, a surface hydration layer forms and, it is then through this that RGD can interact with the TiO₂ surface via electrostatic interactions and van der Waals forces. The topography of the surface was a key factor with RGD interacting more rapidly to a surface presenting nanotopography (Song et al. 2010). More controlled methods of substrate pre-treatment with RGD have been achieved, one such example involved the formation

of a self-assembling monolayer of (3-mercaptopropyl)trimethoxysilane onto glass surfaces which was then incubated with gold beads which would bind via the sulphur group. Finally to this, they added a cyclic pentapeptide presenting RGD which was able to support cell attachment in a specific manner only on surfaces presenting the RGD “anchors” (Abdelghani-Jacquín et al. 2002).

There have been recent challenges to the extent to which peptides like RGD can accurately mimic the local cellular environment, despite creative engineering approaches (Barker 2011). One concern is the ability of peptides to selectively bind the different integrin subtypes. Protein fragments provide an alternative route as they have been shown to distinguish between integrin $\alpha 5\beta 1$ subtypes and selectively engage different integrin receptors (Altroff et al. 2004, Roy and Hocking 2013)

The RGD motif is present on the 10th type III repeat of FN has been the subject of many studies and has been shown to be a key attachment site. The synergistic PHSRN site on the 9th type III repeat has repeatedly been shown to modulate binding to integrin $\alpha 5\beta 1$. Cell adhesion and spreading on FN is strongly dependent on maintaining the native spatial relationship between RGD and PHSRN and can be improved by making a key substitution of proline for leucine-1408 in FIII9 to increase its conformational stability. This introduces a Pro-Pro pair which restricts local flexibility of the protein backbone. The recombinant FN, termed FIII9’10 resulted in increased cell spreading and attachment compared to wild type FN type III domain 9-10 (FIII9-10). Furthermore, bridging the domain interface with a disulphide bond severely restricts interdomain tilt and mobility, diminishing integrin binding affinity and cell spreading (Aota et al. 1994, van der Walle et al. 2002).

1.5.2 Self-assembling peptides and proteins

Ideally, the self-assembly of proteins would involve the independent formation of an organised stable structure through non-covalent forces such as hydrogen bonds, ionic bonds and van der Waals interactions. The application of self-assembling proteins is diverse and has included the pH induced formation of a self-assembled artificial protein hydrogels. Application to biomimetic peptide and protein structures has also been explored by the compiling of helical coiled-coils for di-, tri- and tetra- helical multimers. The stability and order of the structures formed are encouraging for application towards functional biomaterials (Zhang et al. 2002).

1.5.3 Non-specific *versus* directed protein adsorption

Non-specific adsorption of a protein to a surface usually involves the incubation of the desired surface in a protein solution. The protein adsorbs to the surface through non-specific hydrophobic and electrostatic interactions. Directed protein adsorption through covalent surface modification involves the attachment of suitable mechanisms to the ligand display. These can be in the form of polymer side chains, self-assembling monolayers or components of a lipid bilayer (Dillow 2002).

The surface adsorption of FN to a mildly hydrophilic gold substrate was investigated using atomic force microscopy (AFM) and time-of-flight secondary ion mass spectrometry (ToF-SIMS) (Giamblanco et al. 2012). Pure FN layers were found to adsorb with domain III predominantly exposed on the surface, thus allowing the RGD and PHSRN regions to interact with cells. However, when co-adsorbed in an

equimolar solution with human serum albumin, the FN was rearranged in a way in which domain I was presented on the surface, essentially obscuring the common binding domain of FN (Giamblanco et al. 2012). This is of concern because often cell culture assays probing the cell attachment properties of adsorbed proteins will use serum free media and as a consequence may be obtaining amplified results. The competitive adsorption of proteins from a mixture is commonly called the “Vroman effect” named after Leo Vroman who first observed it in the late 1960s (Noh and Vogler 2007, Hirsh et al. 2013). It is generally understood that in a mixture of proteins those with a smaller molecular weight (< 50 kDa) will adsorb preferentially to the larger proteins (Noh and Vogler 2007). More recent studies have suggested that the mixture will initially form layers. The adsorbed layer forms a “transient complex” with can move allowing the other protein to adsorb. If the second protein has a higher affinity for the surface it can extend and effectively force the initially adsorbed protein off the surface (Hirsh et al. 2013).

Computer modelling has been utilised to evaluate the adsorption of FN in “explicit water” to poly (ethylene glycol) and a castor oil copolymer of hexamethylene diisocyanate -based polyurethane surfaces (PEG-HDI and CO-HDI, respectively) (Panos et al. 2012). The surfaces represented different wetting abilities, with PEG-HDI being hydrophilic and CO-HDI hydrophobic. From modelling the interaction of FN and the substrates, it was concluded that competition for adsorption between the water and FN for the hydrophilic PEG-based surface favours water. The amphiphilic nature of FN means that it features hydrophobic patches, in particular at the N-terminal end, which drives adsorption to surface of varying hydrophobicity (Panos et al. 2012). Nominal differences in the surface energies of FN on the two surfaces lead

Panos and co-workers (2012) to speculate that the surface roughness was also an important component in the interplay of proteins and surfaces (Panos et al. 2012).

A method used to overcome influence of surface characteristics on protein adsorption and conformation is the use of tethers which direct the adsorption and effectively raise the protein off the surface in a controlled manner. An elaborate adhesion system designed for titanium implanted devices involving RGD connected to silk grafted with a newly developed titanium binding peptide showed an increasing attachment of fibroblast cells by 60% (Vidal et al. 2013). Various other systems have been employed to present RGD and other peptides in a directed method, some of which will be discussed in this thesis.

The generation of model substrates which present defined binding motifs from the ECM, such as RGD, can be problematic. This is because the adsorption of a protein in solution to the solid/liquid interface generally involves: i) a change in conformation, ii) relaxation and partial desorption, iii) reorientation and alignment as a function of surface coverage (Kreiner et al. 2009b). The behaviour of the protein at the solid/liquid interface is of importance because changes in conformation and orientation can reduce activity rendering it biological inactive. The ligand conformation may be compromised by immobilised proteins denaturing or adsorbing in the incorrect orientation. In order to have well defined substrates with reproducible results, these adsorption changes should be characterised or controlled.

1.5.4 Multimeric clustered ligands and “nanopatterning”

FN exists in the ECM as a dimer presenting six cell adhesion domains within a small area. In order to simulate this polyvalent display multimeric clustered ligands have been investigated (Watson et al. 2006, Kreiner et al. 2008). Multimeric ligands displaying the RGD motif have been shown to better support cell motility and migration compared to monomeric ligands (Koo et al. 2002). Furthermore, higher ligand density and cluster size have been shown to increase the strength of attachment of fibroblast cells (Maheshwari et al. 2000, Koo et al. 2002). Although simple non-clustered RGD ligands were capable of supporting cell attachment, they were unable to exhibit full spreading of fibroblast cells (Maheshwari et al. 2000).

Research has focused on identifying an “ideal” surface distribution of RGD ligands which support cell adhesion and spreading (Lagunas et al. 2012). By creating a uniform surface with negligible chemical and physical differences (i.e. the same wetting properties and roughness) that presented a controlled gradient of RGD ligands, Lagunas and co-workers (2012) investigated the dependence of cell attachment on spatial distribution of RGD. Their findings indicated that there was a non-linear dependence in which cell attachment and morphology altered significantly within a narrow range of RGD density from 2.5 to 4.4 pmol/cm² (Lagunas et al. 2012). However, their results also suggested that although the density was well controlled, there may have been clustering of RGD ligands which encouraged strong focal adhesion contacts as visualised by fluorescent microscopy. Strong focal adhesion complexes have been shown to foster cell bridging across non-adhesive substrates (Arnold et al. 2009). Surface density and clustering of ligands will therefore have an impact on cell attachment and morphology.

Interaction with cell surface integrins have been shown to be affected by the availability of the ligand on the biomedical surface (Kuhlman et al. 2007). The “height” of a synthetic peptide featuring RGD and PHSRN was varied using increasing lengths of poly(ethylene oxide) (PEO) tethers. Focal adhesion formation of fibroblasts was quicker on substrates presenting a longer PEO tether. It was postulated that this was because the increased length allows for free movement of the peptide to be reorganised by the cell integrins (Kuhlman et al. 2007). Arnold and co-workers (2009) designed a patterned substrate functionalised with equally distributed squares of RGD peptides in controlled densities. Integrin activation was visualised by fluorescence microscopy of actin and paxillin localisation. They demonstrated a clear dependence of cell adhesion on RGD spacing and the subsequent formation of integrin clusters (Arnold et al. 2009). Similar work was performed by Comisar and colleagues (2011), in which they combined data gathered from osteoblast responses to RGD peptide nanopatterning with computational models (Comisar et al. 2011). They found a correlation between nanopatterns able to produce large heterogeneously distributed integrin clusters and increased osteogenic differentiation.

The influence of spacing of the surface integrin binding ligands on adhesion of osteoblasts was measured on surfaces presenting an RGD peptide in an ordered and disordered manner (Huang et al. 2010). Huang and co-workers (2010) designed a surface functionalised with clusters of RGD peptides on the nanolevel scale (10-100 nm) and then backfilled any remaining areas with a cell adhesion resistant PEO-silane. They observed that, on highly ordered substrates increasing the distance between the RGD integrin binding ligand resulted in a lower number of cell adhering

to the substrate. Conversely, a disordered presentation of the RGD peptide, at the same overall surface density, had minimal effect on cell adhesion (Huang et al. 2010). This suggests that although an ordered surface may be useful to gain insight to cell adhesion interactions, it may present a poor imitation of real tissue interactions and hence have limited cell adhesion.

Full length FN has been nanopatterned onto a cell adhesion resistant background to establish the minimal area of integrin-FN clusters required for focal adhesion assembly (Coyer et al. 2012). By using controlled geometric arrangements of FN it was determined that the area required for focal adhesion assembly and therefore cell adhesion and spread morphology could not be constrained and there was a dynamic threshold in equilibrium between the various mechanical parameters (Coyer et al. 2012).

Self-assembling β -sheet peptides forming regular nanofibre structures harbouring RGD have been explored and present an alternative approach to generating a polyvalent RGD display (Zhou et al. 2009). Some related amphiphilic peptide assemblies have involved elaborate work to include both the RGD and PHSRN peptide motifs, generating fibres around 10 nm in diameter and several microns in length (Rexeisen et al. 2010). Such self-assembly approaches challenge the need to coat non-functional polymeric 3-D scaffolds with bioadhesive peptides/proteins, but may be limited with regard to scale-up/cost for clinical application.

1.5.5 Coiled-coil protein systems

A coiled-coil protein sequence involves heptad repeats containing two hydrophobic residues (Harbury et al. 1993). The “leucine zipper” region of yeast transcriptional activator (GCN4) forms a very stable dimer of α -helices in a coiled-coil formation (O'Shea et al. 1989). Harbury and co-workers (1993) found that substitution of key amino acids would promote the formation of di- tri- and tetrameric coiled-coils of GCN4 (Harbury et al. 1993).

The construction of a coiled-coil system involving FN has been achieved by selective mutation of key amino acids in a heptad repeat of the GCN4 leucine zipper helix to allow for direct self-assembly of parallel coiled-coils. A spacer based on an IgG hinge was included to prevent steric clashes between the integrin receptors (i.e. N-FIII9'10 – hinge – coiled-coil – C). In this case, the modified mutant FN fragment FIII9'10 was utilised because of its previously reported enhanced conformational stability (Kreiner et al. 2008). In this way a FIII9'10 dimer, trimer and tetramer were constructed, and the effect of these multimeric systems on baby Hamster kidney (BHK) cells primary endometrial stromal cells and murine embryonic stem (mES) cells was analysed. For both fibroblast and stromal cell lines, increased cell attachment and spreading were observed with increasing multimerisation of FIII9'10 (Kreiner et al. 2008, Li et al. 2011). The morphology of the spread stromal cells on the FIII9'10-tetramer conveyed a spread morphology which suggests that, multimeric constructs have a role to play in endometrial tissue engineering. However, this was not the case for mES cells. Unlike the fibroblast cells the FIII9'10 dimer showed significantly superior support of mES cells compared with monomer

and the other multimers. Furthermore, attachment of cells to the FIII9'10 dimer conferred a change in morphology more characteristic of differentiated cells (Kreiner et al. 2008, Singh et al. 2009).

Coiled-coils may have further use as systems in drug delivery and bioengineering. Fletcher and colleagues (2013) produced a self-assembling “cage-like” particle made from α -helical coiled-coils. The hollow spheres were built from the co-assembly of two new coiled-coils which were soluble when separated but would assemble and precipitate when mixed together. The side chains of the molecules were free to be derivatised and hence the properties of the molecules could be designed adapted to various functions (Fletcher et al. 2013).

1.5.6 Investigating protein adsorption at the solid liquid interface

The interactions of proteins at the solid/liquid interface may be difficult to ascertain with more traditional methods such as NMR, optical microscopy or X-ray diffraction. Neutron reflectivity (NR) is a favourable technology which can yield such measurements at the molecular level (Fragneto-Cusani 2001). Neutrons are subatomic particles with some interesting properties that can be utilised for biological imaging. They are non-charged, have a mass of 1.0087 atomic mass units and possess a magnetic moment. What is of particular use is that neutrons are isotope-sensitive and can distinguish between hydrogen and its isotope deuterium, additionally they interact weakly with samples and so are able to penetrate it without

causing damage in the process. Furthermore they can also adopt two spin states which can be harnessed to give an increased resolution (Harroun et al. 2006).

There are two ways in which to produce neutrons for NR, they can be generated by a nuclear reactor or by spallation source. There are currently several NR facility sites such as Rutherford Appleton Laboratory in Oxfordshire (UK) and the Australian Nuclear Science and Technology Organisation (ANSTO) in Sydney which can be petitioned for time and access. The neutrons at ISIS are created by accelerating protons in a synchrotron and colliding with a tungsten metal target. The impact causes the neutrons to “spall off” the tungsten atoms and these are subsequently channelled through guides to give different beams with different applications. OPAL is a nuclear source, which uses fission of uranium nuclei. Neutrons are released by splitting of the uranium atom which then in turn strike other uranium atoms splitting those and leading to the creation of more neutrons.

At its simplest, the reflection of neutrons from a surface interface can be interpreted in a similar fashion as light. The wavelength of neutrons used for biological work is usually within the range of 2 to 20 Å and the angles of less than 5° (Lakey 2009). Information can be generated regarding the structural composition of the surface from which the neutrons are reflected. The use of a neutron beam at a short wavelength of a few angstroms permits measurements which can go down to a molecular level. Furthermore, different conditions can be explored for the same system by variation of the refractive index of the liquid buffer with isotopic mixtures such as hydrogen and deuterium. This is especially useful for biological systems which tend to be rich in water and hydrogen (Lakey 2009). There is a large

difference in the scattering length of deuterium and hydrogen (they are in the opposite sign) and the contrast between hydrogenous materials containing both can produce a scattering light density which can be matched to different substrates (Harroun et al. 2006). An early study in the use of neutron reflectivity on protein adsorbed to surfaces has been applied to lysozyme adsorbed to silica substrates (Su et al. 1998). They were able to use the calculated layer thickness of the lysozyme on the substrate to propose its orientation and average structural conformation. This has clear application to the study of FN based protein scaffolds adsorbed to solid mediums, however, the conformational results are dependent on the interpretation of the layer thickness which may be influenced by user error and a supplementary technique would be preferable.

Circular dichroism (CD) is a useful tool in ascertaining information regarding the structural aspects of proteins and enzymes. The structural conformation of the secondary and tertiary structure of proteins is elucidated by the differential absorption of left and right polarized light. The level of this absorption is dependent on the chirality of the chromophore. The sample will absorb a quantity of the light from both fields; this is then combined to produce a CD spectrum. It is measured as the difference in absorbance between left and right circularly polarized light ($\Delta A = A_L - A_R$) and given as the ellipticity (θ) in degrees. This differential absorption is measured as a function of the wavelength, from 250-350 nm for near-UV and from 170-250 for far-UV (Kelly and Price 2000, Kelly et al. 2005).

CD has been adapted to investigate protein conformation at the solid/liquid interface. When adsorbed to surfaces, such as silica beads, or gel, which have a particle size of

roughly 40-63 μm (Pereira et al. 2008) the protein remains in solution and forms an adsorbed “film” on the bead surface which can be measured for structural changes. Difficulties arise because of the solid substrate impacting and distorting absorption. Absorption flattening occurs because the adsorbed protein particles are confined and not readily available, leading to light not being fully absorbed. This can be corrected for by the application of a mathematically derived correction factor (Ganesan et al. 2006). Over the time required to take measurements, sedimentation of the protein-coated silica beads can occur, resulting in a non-uniform distribution of sample and reducing the concentration of protein in the light path. This has been overcome by the use of a rotating cell holder which continuously rotates the sample and keeps it constantly moving and therefore mediating the effects of gravity (Ganesan et al. 2006, Pereira et al. 2008). Although this methodology is not yet ideal, it allows for reasonable information regarding the structure of proteins and peptides adsorbed to surfaces to be obtained and will be discussed further.

1.6 Research aims and hypothesis

The initial focus of this project was stimulated by the investigations of Beattie and colleagues (2009), who described the apparent binding of IGFBP-5 to FIII9'10-GGC (Beattie et al. 2009). This prompted thoughts about a novel molecular mechanism by which IGFBP-5 may regulate IGF activity in the pericellular environment. At the beginning of the body of work, it was thought that IGFBP-5 would bind the cell binding domain (CBD) of FN, disrupting cell/ECM interactions. By selective

mutation of the 9th and 10th domains of FN the proposed binding capability for IGFBP-5 was examined.

The second purpose of these studies was to develop a novel FIII9-10 based protein scaffold with increased conformational stability. This would have application in biomedical implants and tissue engineering. To this end, a FIII9'10 based protein fragment designed to specifically target integrin $\alpha 5\beta 1$ was of interest. This integrin is found in many different adhesion structures and involved in control and differentiation of various cell types, including osteogenic differentiation (Martino et al. 2009). Although mouse and human FIII9 show 83% homology, human FIII9-10 is inherently less stable and prone to conformational changes which could be detrimental to function. Total internal reflection fluorescence (TIRF) analysis of FIII9'10 which contains a substitution at Leu 1408 to Pro, (Periera et al. 2008); certainly, in mouse, the sequences contain more proline residues in key area which might contribute to overall conformation stability. A protein engineering approach was used to develop a FIII9'10 based scaffold by substituting individual amino acids in FIII9'10 which is described in the next chapter.

CHAPTER 2. Expression and purification of proteins

2.1 Introduction

In protein engineering, the variation of even a single amino acid can provide the opportunities to alter substrate specificity, stereoselectivity and conformational stability on a variety of supports. For example, the mechanical stability of an immunoglobulin-like domain, human cardiac titin, was altered by substitution of Pro for amino acids at positions 11, 13 or 15, which affected the position of the transition state towards the unfolded state of the molecule (Li et al. 2000). Rotticci and colleagues describe the application of substitution of a single amino acid to engineer a lipase with an enhanced enantioselectivity (the selectivity of a reaction towards one of a pair of enantiomers). The amino acid was selected by generating a computer model of the substrate and identifying the key amino acids in the stereoselectivity pocket of the lipase. By substituting the amino acids Thr42 and Ser47 for either Ala, Val or His they were able to create a variant with doubled enantioselectivity (Rotticci et al. 2001). In addition, the substitution of single amino acids within a protein allows selective alteration of regions to isolate and determine the importance of structural sequences.

The biological activity of the full-length FN molecule has been successfully mimicked by utilising the FN type III 9th and 10th wild type domain pair (FIII9-10) which contains the RGD binding motif (FIII10) and the PHSRN synergy site (FIII9) (Aota et al. 1994). The conformational stability of the FIII9-10 is poor, with the

FIII9 domain being especially unstable (Plaxco et al. 1997). However, mouse FIII9-10 has increased conformational stability compared to human and has an 83 % sequence identity for FIII9. Utilising this, a stable mutated human FIII9-10 domain pair was developed by incorporating substitutions based mouse FIII9-10 (van der Walle et al. 2002). The most successful mutant resulted from the substitution of proline for leucine ¹⁴⁰⁸ (numbering for full FN as in (Leahy et al. 1996)). This mutant, termed FIII9'10 showed enhanced cell adhesive activity and increased protein expression and stability. Figure 2-1 illustrates the amino acid sequence of human FIII9 compared to mouse FIII9 with the substituted Leu¹⁴⁰⁸ underlined. Development of this mutant continued with the extension of the C-terminus with the addition of a GGC tripeptide (termed FIII9'10-GGC) (Kreiner et al. 2008). This variation of the FIII9-10 domain pair was reported to bind to the IGFBP -3 and -5 (Beattie et al. 2009), which formed the basis of the initiation of this research.

```

                1335      1345      1355      1365      1375      1385
                .        .        .        .        .
Hum_Fn GLDSPTGIDFSDITANSFTVHWIAPRATITGYRIRHHPEHFSGRPREDRVPHSRNSITLTN
        .....: .....: .....: .....: .....: .....: .....: .....:
Mus_Fn GLDSPTGFDSSDITANSFTVHWVAPRAPITGYIIRHHAEHVGRPRQDRVPPSRNSITLTN

                1395      1405      1415
                .        .        .
Hum_Fn LTPGTEYVVSIVALNGREESPLLIGQQST
        .....: .....: .....: .....: .....: .....: .....:
Mus_Fn LNPGTEYVVSIIAVNGREESPLLIGQQAT
    
```

Figure 2-1 Sequence alignment of mouse (Mus_Fn) and human (Hum_Fn) FIII9 domains. Every 10th amino acid is noted with an upper dot along with the corresponding sequence number, according to Leahy et al. (1996).

CHAPTER 2. Expression and purification of proteins

As the earlier work using FN generated the stable mutant, FIII9'10-GGC, containing a substitution at Pro¹⁴⁰⁸ for Leu (Altroff et al. 2004) with addition of a GGC tripeptide at the C-terminus (Beattie et al. 2009). This was used as a basis for exploring the effects of site directed mutagenesis of FIII9'10-GGC in IGFBP binding studies to elucidate the part played by FN. The points selected for mutation were Ile¹⁴¹⁰ and Glu¹³⁶⁴ (numbered according to (Leahy et al. 1996), for the entire FN protein).

Further to this the FIII9'10 mutant was used as the basis for the development of a stable protein scaffold by the addition of subsequent mutations. The FIII9'10 domain pair differs from the binding studies as it does not contain the GGC tripeptide. The points selected for mutation were Thr¹³⁵³ and His¹³⁷⁷ (see Figure 2-2). These amino acids were chosen to increase stability by the substitution of proline. In the case of His¹³⁷⁷, this added a Pro-Pro motif exiting a beta-strand, and in the case of Thr¹³⁵³, this included a Pro within a turn between two beta-strands.

```

                1335      1345      1355      1365      1375      1385
                .        .        .        .        .        .
Hum_Fn  GLDSPTGIDFSDITANSFTVHWIAPRATITGYRIRHHPEHFSGRPREDRVPHSRNSITLTN
        : : : : : : : : : : : : : : : : : : : : : : : : : : : : : : : : : : : :
Mus_Fn  GLDSPTGFDSSDITANSFTVHWVAPRAPITGYIIRHHAHESVGRPRQDRVPPSRNSITLTN

                1395      1405      1415
                .        .        .
Hum_Fn  LTPGTEYVVSIVALNGREESPLLIGQQST
        : : : : : : : : : : : : : : : : : : : : : : : :
Mus_Fn  LNPGEYVVSIIAVNGREESPLLIGQQAT
```

Figure 2-2 Sequence alignment of mouse and human FIII9. The amino acids targeted for substitution are underlined.

The production, isolation and purification are described in this chapter. The isolated product was characterised using SDS-PAGE gel, UV spectroscopy and circular dichroism. A total of four variants were produced termed FIII9'10-GGC I2A, FIII9'10-GGC E2A, FIII9''10 T2P and FIII9''10 H2P.

2.2 Materials

Unless otherwise stated all chemicals were purchased from Melford (Suffolk, UK), Fisher Scientific (Leicestershire, UK) or Sigma-Aldrich (Dorset, UK) at analytical standard or equivalent quality. Restriction enzymes were from New England Biolabs (Hertfordshire, UK). *Escherichia coli* strains XL-1 Blue and BL21 (DE3) pLysS were obtained from Promega (Southampton, UK). The FIII9'10 cDNA template used for expression and mutagenesis is described in (van der Walle et al. 2002). Custom primers were purchased from Invitrogen (Paisley, UK). Water was purified to > 14 MΩ.cm with a BioSelect, Purite, UK.

2.3 Buffers and reagents

All buffers and reagents were formulated in distilled water, unless otherwise stated.

LB broth: Low Salt (Lennox L Broth) 1 % (w/v) tryptone, 0.5 % (w/v) NaCl, 0.5 % (w/v) yeast extract.

CHAPTER 2. Expression and purification of proteins

LB agar: 1 % (w/v) tryptone, 0.5 % (w/v) NaCl, 0.5 % (w/v) yeast extract, 15 % (w/v) granulated agar.

Sodium phosphate buffer: 10 mM NaCl, 50 mM NaH₂PO₄, pH 6.0.

Lysis buffer: 50 mM NaH₂PO₄, 300 mM NaCl, 10 mM imidazole; adjust to pH 8.0 with NaOH.

Wash buffer: 50 mM NaH₂PO₄, 300 mM NaCl, 20 mM imidazole; adjust to pH 8.0 with NaOH.

Elution buffer: 50 mM NaH₂PO₄, 300 mM NaCl, 250 mM imidazole; adjust to pH 8.0 with NaOH.

0.5 x TBE buffer: 45 mM tris(hydroxymethyl)aminomethane (Tris) (pH 8.0), 1 mM ethylenediaminetetraacetic acid (EDTA).

SDS-PAGE resolving gel: 15 % (v/v) acrylamide, 375 mM Tris (pH 8.8), 0.1 % (v/v) sodium dodecyl sulphate (SDS), 0.1 % (v/v) ammonium persulphate (APS) and 0.1 mM N,N,N',N'- Tetramethylethylenediamine (TEMED).

SDS-PAGE stacking gel: 5 % (v/v) acrylamide, 125 mM Tris (pH 6.8), 0.1 % (v/v) SDS, 0.1 % (v/v) APS and 0.067 mM TEMED

SDS-PAGE loading buffer (3x): 150 mM Tris HCl pH 6, 300 mM dithiothreitol (DTT), 6 % (w/v) SDS, 0.03 % (w/v) bromophenol blue and 30 % (v/v) glycerol.

10 x SDS-PAGE buffer: 14.4 % (w/v) glycine, 247 mM Tris, 1 % (w/v) SDS.

Coomassie staining mixture: 10 % (v/v) CH₃COOH, 45 % (v/v) CH₃OH and 0.25 % (w/v) Coomassie brilliant blue.

De-staining mixture: 7.5 % (v/v) CH₃COOH and 25 % (v/v) CH₃OH.

2.4 Methods

2.4.1 FIII9'10 mutants and recombinant expression

Individual amino acids were selected for mutation in order to either obtain information regarding IGFBP-5 binding to FIII9'10-GGC or in an attempt to increase conformational stability of FIII9'10. In each case, the methods used to produce the proteins were the same.

Initial work which focused on the binding of FIII9'10-GGC to IGFBP-5 utilised the conformational search program HEX (<http://www.csd.abdn.ac.uk/hex/>) to select amino acids targets for alanine substitution by site directed mutagenesis. This was done to try to knock out binding of FIII9'10-GGC to IGFBP-5.

Following this, the comparison of mouse and human FIII9 was used to select amino acids to introduce Pro-Pro pairs into the FIII9 domain with the aim to decrease the degrees of freedom around the respective β -turn and thereby increase conformational stability of the global fold.

Work done prior to this investigation expressed FIII9'10 in pRSET A, a pUC derived expression vector for high-level protein expression and purification from cloned genes in *E. coli* (see Figure 2-3). There are many advantages of using pRSET

A as a cloning vector, one of which is that it produces proteins containing a polyhistidine tag which acts as a metal binding site for purification using Immobilized Metal Affinity Chromatography (IMAC).

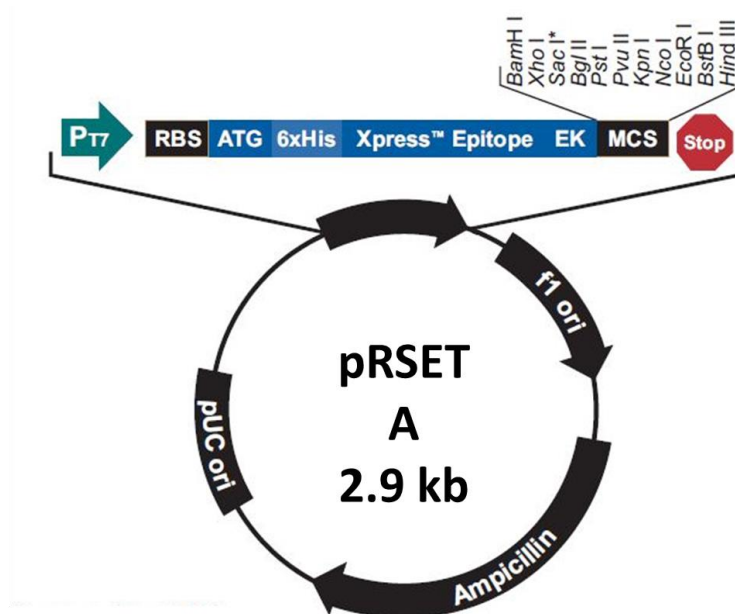


Figure 2-3 Map of pRSET A vector from Invitrogen (Paisley, UK)

2.4.1.1 Primer constructs for mutation of FIII9'10

Primers were designed to effect the desired mutation shown in Table 2-1. Amino acid substitutions intended to probe IGFBP-5/FIII9'10 binding were performed as follows: Ala was substituted for Glu¹³⁶⁴ (E1364A) by changing the GAG codon to GCG, and for Ile¹⁴¹⁰ (I1410A) by changing at ATT codon to GCT. These were used to transform the FIII9'10-GGC mutant.

Amino acid substitutions intended to increase the conformational stability of FIII9'10 involved Pro substitution for Thr¹³⁵³ (T1353P) by changing the ACC codon

to CCA and for His¹³⁷⁷ (H1377P) by changing at CAC codon to CCA. These were used to transform the FIII9'10 mutant.

Table 2-1 Primer design for mutation of FIII9'10-GGC and FIII9'10.

Mutation	Primer designed, with base change underlined (sense strand)
Glu ¹³⁶⁴ to Ala (E1364A)	5'-C CGC CAT CAT CCC <u>G</u> CG CAC TTC AGT GGG AG
Ile ¹⁴¹⁰ to Ala (I1410A)	5'-G GAA AGT CCC CCA TTG <u>G</u> CT GGC CAA CAA TCA ACA G
Thr ¹³⁵³ to Pro (T1353P)	5'-G ATT GCT CCT CGA GCC <u>C</u> CA ATC ACT GGC TAC AGG ATC
His ¹³⁷⁷ to Pro (H1377P)	5'-CGA GAA GAT CGG GTG <u>C</u> CG* <u>C</u> CA TCT CGG AAT TCC ATC AC

*, this base change keeps the wild-type Pro¹³⁷⁶ but was included for optimisation of recombinant expression [CCC has low codon usage in *E.coli*. (Sharp et al. 1988)].

2.4.1.2 Site directed mutagenesis

Polymerase chain reaction (PCR) site-directed mutagenesis was used to modify the FIII9'10 based proteins. The technique used here utilises amplification by PCR coupled with QuikChange[®] protocol (Stratagene, UK), to modify the plasmid to produce the desired mutations (see Figure 2-4). The DNA primers contained the desired mutation and were complementary to the template DNA around the mutation site. The primer was designed so that it would hybridize with the DNA template whilst incorporating the desired mutation. Amplification of the mutated DNA was achieved by PCR.

PCR involves three steps that together can amplify DNA fragments *in vitro* 20 to 40 times. The reaction mixture includes DNA primers containing the desired mutation

along with deoxynucleoside triphosphates (dNTP), a suitable DNA polymerase and DNA template in appropriate buffer. The DNA polymerase is a catalyst for production of new DNA which is synthesised from the dNTPs. The first step of PCR reaction is denaturation, the separation of the two strands of DNA by breaking the hydrogen bonds between them at high temperatures. This is followed by annealing, in which hybridisation between the DNA template and the oligonucleotide primers is initiated by lowering the temperature. The final step is extension of the nucleotides by DNA polymerase (temperature dependant). The DNA polymerase used in this instance was *Pyrococcus furiosus* (*Pfu*); this possesses the useful ability to read the DNA strand both in the 5'-3' direction and the 3'-5' direction, effectively checking itself for errors.

The reaction mixture was composed of 5 µl 10 x *Pfu* buffer, 5 µl 2 mM dNTP mix, 36 µl distilled water, 1 µl double stranded DNA template, 1 µl (125 ng) of each of the primers (both 5'-3' and 3'-5'). This was kept on ice and pipetted gently to mix. Once ready 1 µl *Pfu* polymerase was added to the mixture and the PCR tube was flicked gently, spun briefly (<100 rpm) to mix and then then transferred to a pre-heated PCR (Techne, Techgene) for mutation and amplification.

The PCR cycle started with an initial denaturing step at 95 °C for 30 s, this was then followed by 18 repeated cycles. They involved a denaturing step at 95 °C for 30 s, an annealing step at 55 °C for 1 min and elongation step at 68 °C for 8 min. Once complete, the parental DNA template was digested by the addition of 1 µl of *Dpn I* restriction enzyme. This was mixed thoroughly and incubated at 37 °C for 1 h. The PCR products were stored at -20 °C until required.

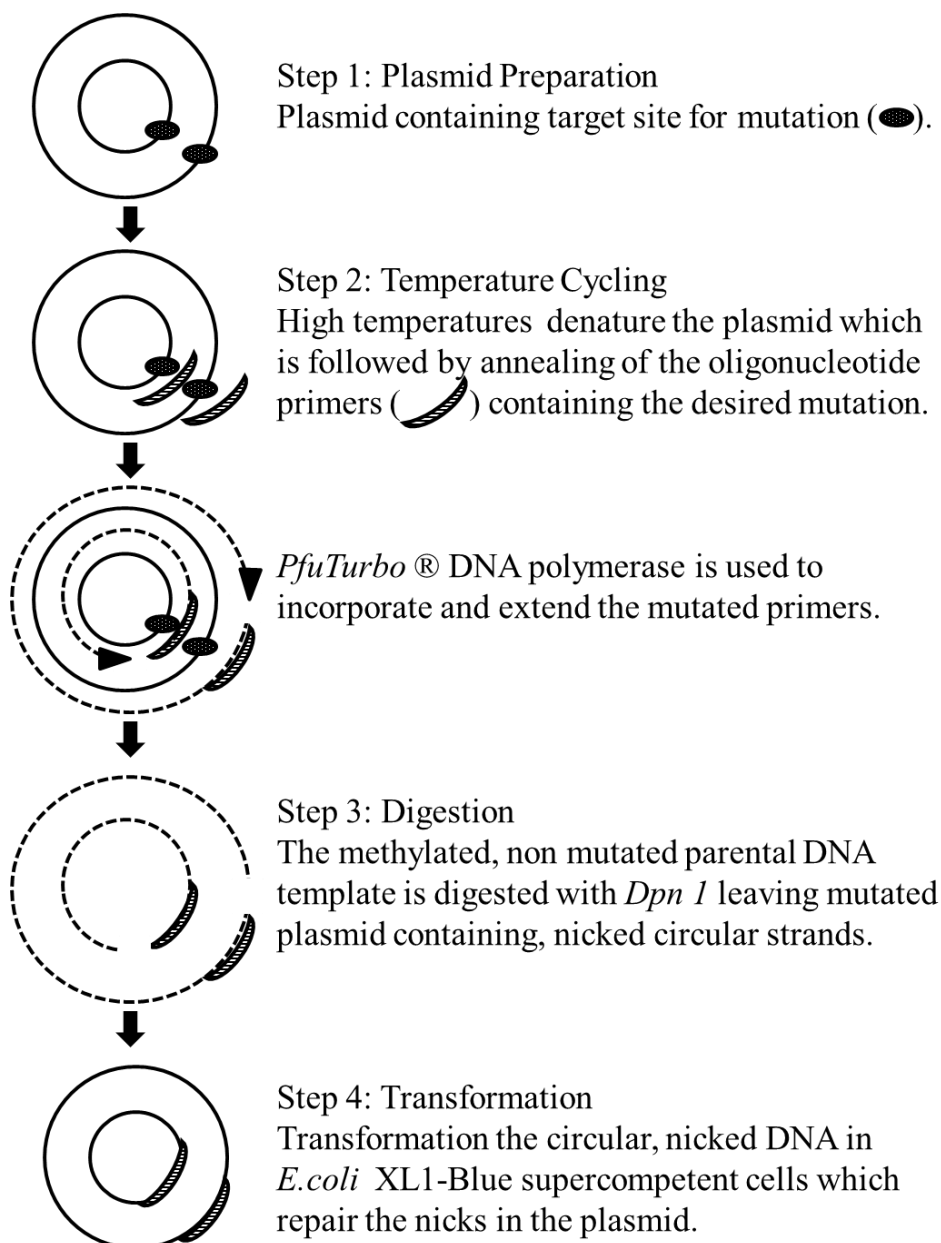


Figure 2-4 Illustration of QuikChange® site-directed mutagenesis protocol.

2.4.1.3 Transformation of mutated plasmid into XL-1 Blue cells

XL-1 Blue *E. coli* cells were used to replicate the mutated DNA plasmid following PCR. The pRSET A vector contains ampicillin resistance therefore when plated onto

ampicillin containing agar, only those cells successfully transfected with the plasmid will grow.

Cells were thawed on ice and kept on ice for the duration of the procedure, unless otherwise stated. The DNA produced by PCR (7.5 μ l) was added to 150 μ l XL-1 Blue cells and incubated on ice for 30 min, this was then heat shocked for no longer than 1 min at 42 °C and returned to ice for a further 5 min. The heat shock stage increases transformation efficiency and therefore required to be timed correctly. The entire ~150 μ l (cells and DNA) was then spread onto a warmed agar plate containing ampicillin (100 μ g/ml) and incubated overnight at 37 °C. Briefly warming (<30 min) the agar at 37 °C prior to use facilitates improved spreading and absorption of the cell mix.

2.4.1.4 Replication and isolation of plasmid DNA from XL-1 Blue colonies

A GenElute™ Plasmid Miniprep kit (Sigma-Aldrich, Dorset, UK), was used to isolate the plasmid DNA from overnight cultures. A single XL-1 Blue colony was picked from the overnight growth using a flamed loop and grown overnight in 5 ml of ampicillin (100 μ g/ml) containing LB broth at 37 °C while shaking (180 rpm). The entire 5 ml growth was centrifuged for 10 min at 3500 rpm (ALC, Multispeed refrigerated centrifuge, PK121R) and the supernatant discarded. The pellet was re-suspended with 200 μ l Resuspension solution and pipetted until homogeneously dispersed. Cells were then lysed with the addition of 200 μ l Lysis solution and gently inverted 6-8 times; the solution then became clear and viscous. The lysis reaction

was stopped after 5 min by the addition of 350 µl Neutralisation/binding solution and mixed gently. Following this, the cells were centrifuged (MIKRO 20, Helmer, Inc.) for 10 min at 130000 rpm, the supernatant was collected and the pellet containing cell debris discarded.

The DNA in the supernatant was collected with the aid of a GenElute™ binding column. This was prepared by the addition of 500 µl of column preparation solution and centrifuged (MIKRO 20, Helmer, Inc.) for 30 sec at 130000 rpm. The flow through was discarded and the lysate (containing the DNA) transferred to the column which was then centrifuged (MIKRO 20, Helmer, Inc.) for 1 min at 130000 rpm. The DNA would adhere to the column enabling it to be separated from the lysate. The column was washed by adding 750 µl Wash solution and centrifuged (MIKRO 20, Helmer, Inc.) for 1 min at 130000 rpm, the column was then dried by further centrifuging (MIKRO 20, Helmer, Inc.) (30 sec to 1 min, 130000 rpm). The column was then transferred to a fresh collection tube and the DNA was eluted with 50-100 µl of Elution solution by centrifuging (MIKRO 20, Helmer, Inc.) for 1 min at 130000 rpm. DNA was quantified using GeneQuantII.

2.4.1.5 Agarose gel electrophoresis

Agarose gel electrophoresis uses an electric current to separate out DNA fragments according to size through a porous agarose gel. The negatively charged DNA migrates through the agarose gel towards the positive cathode; the shorter molecules can move faster causing them to migrate further than longer molecules. The addition

of the fluorescent dye ethidium bromide to the agarose gel allows it to be visualised under UV light as it intercalates between the bases of nucleic acids.

The agarose gel was made by mixing 0.5 g of agarose with 50 ml 0.5 x TBE buffer and microwaving until melted. Ethidium bromide (10 mg/ml) was added (2 µl) and the gel allowed to set in an 8 well mould. The DNA samples were prepared by the addition of 1 µl of 10 x agarose loading buffer to 8.5 µl distilled water and 0.5 µl of DNA sample. Bionline hyperladder I was used as a marker enabling an estimation of the number of base-pairs. The gel was then run in 0.5 x TBE buffer at a setting of 5-15 volts per cm gel. Once completed the gels were viewed under UV light.

2.4.1.6 DNA sequencing

The plasmid DNA was sequenced by The Sequencing Service of the University of Dundee. A 30 µl sample containing approximately 400-600 mg of DNA was prepared. The resultant DNA sequence was then compared to the sequence for the template (FIII9'10) to confirm that the desired mutation had been successful, using nucleotide pairwise sequence alignment tool EMBOSS Needle (http://www.ebi.ac.uk/Tools/psa/emboss_needle/nucleotide.html). Successful minipreps were then expressed in *E. coli*.

2.4.1.7 Protein expression in *Escherichia coli* BL21 (DE3) pLysS

The BL21 (DE3) pLysS strain of *E. coli* is highly efficient at expressing genes under the control of a T7 promoter. This strain carries the DE3 λ lysogen which contains the *lacI* gene, and the T7 RNA polymerase gene under the control of *lacUV5* promoter. The expression is carefully controlled by the T7 lysozyme, carried on pLysS, which lowers the background expression level of genes under the T7 promoter. Induction by isopropyl β -D-thiogalactoside (IPTG) is required to increase synthesis of T7 polymerase, which binds to the promoter to start expressing the target gene.

The mutated double stranded DNA from the Miniprep was thawed on ice along with the BL21 (DE3) pLysS competent cells. DNA (0.5-1 μ l) was added to 100 μ l cells and incubated at room temperature for 20 min. Following this the cells and DNA were heat shocked at 37 °C for 5 min then returned to ice for a minimum of 5 min until required. The entire 100 μ l was spread onto a warmed agar plate containing ampicillin (100 μ g/ml) and chloramphenicol (10 μ g/ml) and incubated overnight at 37 °C.

A single colony was picked from the growth using a flamed loop and transferred into 50 ml LB containing ampicillin (100 μ g/ml) and chloramphenicol (10 μ g/ml). This pre-culture was then incubated overnight at 37 °C while shaking (180-220 rpm).

The pre-culture was then inoculated into 1 litre of warmed LB containing ampicillin (100 μ g/ml) and chloramphenicol (10 μ g/ml). Cells were grown at 37 °C with shaking at 180 rpm until the OD₆₀₀ reached between 0.55 and 0.7. At this point the

cells were induced using IPTG to a final concentration of 0.2 mM, incubation was continued. One hour after induction a further 1 ml ampicillin (100 mg/ml) was added, and the cells were harvested 3 h after induction.

Harvesting involved centrifuging the entire 1 litre culture for 15 min at 5000 rpm at 4 °C (Beckman Coulter Avanti centrifuge, JAL 9.100 rotor, 1L bottles). The supernatant was discarded and the pellets were re-suspended in 15 ml ice-cold lysis buffer for storage at -80 °C at least overnight. Figure 2-5 illustrates some of the stages involved when creating an engineered protein.

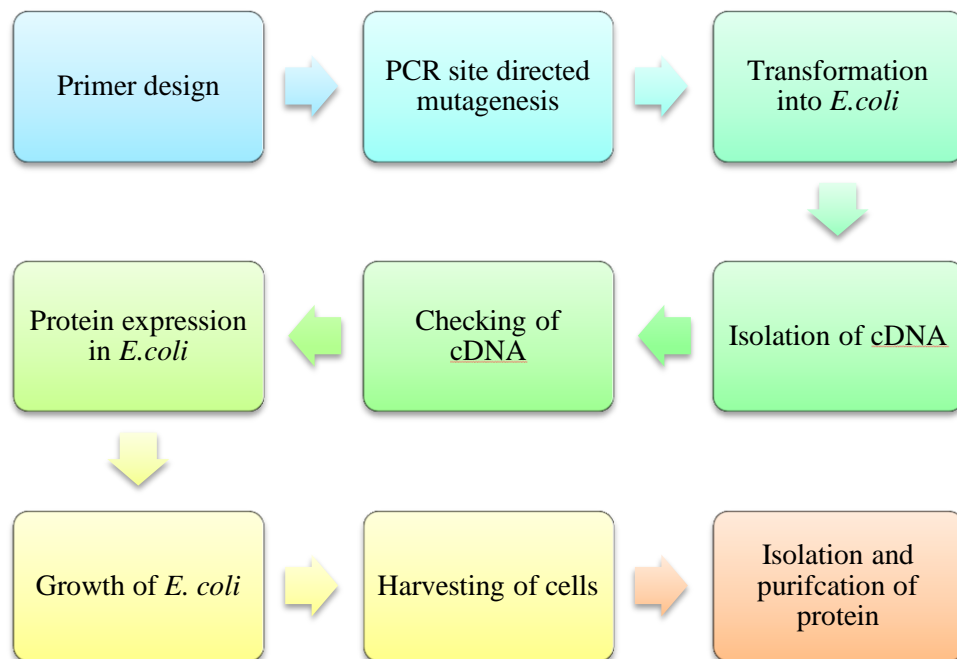


Figure 2-5 Flow diagram illustrating the steps involved in engineering mutated proteins.

2.4.1.8 Cell lysis and protein purification

Immobilised metal affinity chromatography (IMAC) in the form of Ni²⁺-chelation affinity chromatography was utilised to separate contaminants from the protein solution. The protein solution was passed through a column pre-packed with pre-charged Ni Sepharose™ using a fast protein liquid chromatography (FPLC) system. The polyhistidine tag facilitates binding of the protein to the column with high affinity. Proteins that were non-specifically bound will be eluted by a washing step with mild imidazole concentration (20 mM). The target protein can then be eluted by increasing the imidazole concentrations from 20 mM to 250 mM.

The re-suspended cells were thawed in a 37 °C water bath and the cells sheared by 3 x 20 s intervals of sonication (M73 probe, max 30 %) prior to IMAC. During sonication the centrifuge was set to cool to 4 °C and the sheared cells were then centrifuged for 30 min at 20000 rpm, 4 °C (Beckman Coulter Avanti centrifuge, JA-20 rotor with polypropylene tubes), which removed the cell debris.

The bacterial supernatant collected from centrifuging was filtered with a 0.8 µm filter and diluted to 50 ml with lysis buffer. The pH was then adjusted to 8 using NaOH. The sample was then loaded into a 250 ml super loop with lysis buffer. A 5 ml HisTrap™ FF crude column (pre-packed with pre-charged Ni Sepharose™) was prepared by washing with a minimum of 5 volumes of water followed by 5 volumes of lysis buffer which was then pumped continuously until a stable baseline was achieved. The 50 ml sample was injected onto the column at a flow rate of 3 ml/min, a sample from the flow through was collected for future analysis. The column was then washed with 50 ml of wash buffer at a flow rate of 5 ml/min and flow through

sample collected. Following the initial wash a second wash containing 85 % wash buffer and 15 % elution buffer was performed (50 ml at 5 ml/min) and a sample of the flow through collected. Finally the protein was eluted by washing with 100 % elution buffer (30 ml at 5 ml/min) and the appropriate fractions collected that corresponded to the UV absorbance peak.

The resultant solution had a low protein concentration and also a high salt concentration, therefore the next step was to reduce the salts and increase the protein concentration by reducing the volume. One method for concentrating of the protein followed by buffer exchange in a single unit was Amicon Ultrafiltration stirred cell with a 10,000 MWCO regenerated cellulose membrane. The protein solution was reduced to approximately 2-3 ml, giving a concentrated protein solution with high salt buffer. To this up to 50 ml of buffer (10 mM NaH₂PO₄, 50 mM NaCl pH 6.0) was added to facilitate exchange of the salts, this was repeated 3 times and the resultant protein solution stored at -80 °C. An alternative method involved the removal of the salts using a HiPrep 26/10 desalting column prior by concentrating of the protein solution. The column was equilibrated with buffer (10 mM NaH₂PO₄, 50 mM NaCl pH 6.0) and the protein solution injected at a flow rate of 10 ml/min using a 250 ml superloop in batches of 10 ml. The resultant solution was then reduced in volume using a Vivaspin 20 ultrafiltration spin column with a 10000 MWCO or by Ultrafiltration stirred cell. The protein was stored at -80 °C until required. The steps involved in isolating and purifying the mutated protein from the *E. coli* cells are outlined in Figure 2-6.

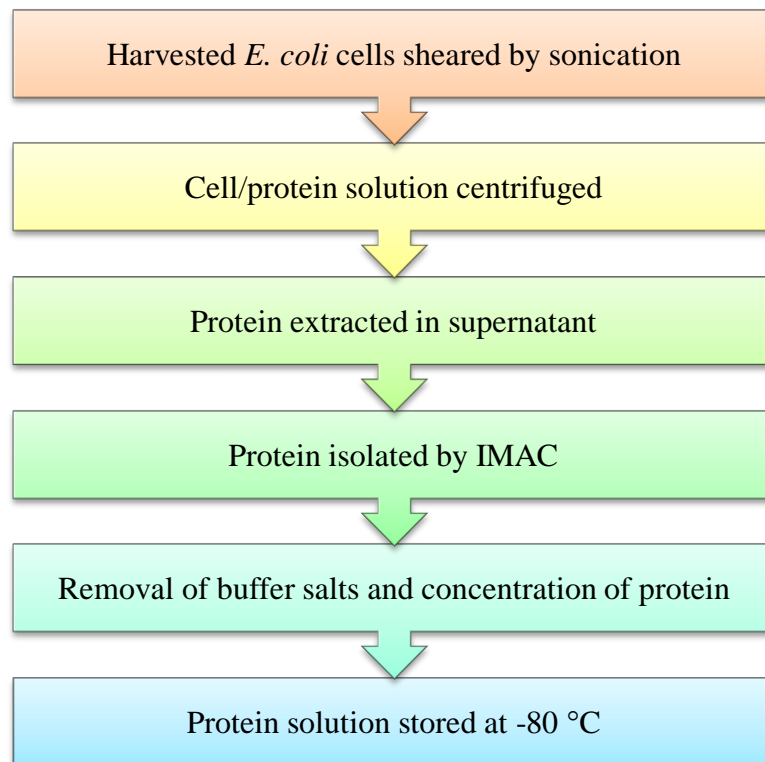


Figure 2-6 Flow diagram outlining steps required for protein purification from *E. coli* cells.

2.4.2 Protein characterisation

Initial characterisation of the purified proteins was performed to confirm the purity, molecular mass and conformation were correct. A loss of native structure can lead to the formation of aggregates in solution and consequently a loss of function, therefore it was important to examine each batch of proteins prior to use.

2.4.2.1 Sodium dodecyl sulphate polyacrylamide gel electrophoresis (SDS-PAGE)

SDS-PAGE was used to assess protein purity and relative molecular mass. The samples taken at various points during the purification were all treated in the same manner and analysed. Gels composed of 15 % resolving and 5 % stacking solutions (Sambrook and Russell 2001) were cast on BioRad plates and casting system. Proteins samples were prepared in 30 μ l volumes consisting of 1/3 distilled water, 1/3 loading buffer (3 x protein loading buffer) and 1/3 protein. The mixture was then heated at 100 °C for 5 min, following this the sample was gently spun in a centrifuge for less than 30 s to prevent reduction in sample due to condensation on the lid. The wells were then loaded with a 10 μ l sample of this mixture. SigmaMarker 6,500-205,000 was also loaded into the gel and used as a reference. Gels were placed in 1 x SDS-buffer and run at continuous amperage of 35 mA per gel, until the dye reached the end of the gel. Proteins were visualised by staining with Coomassie brilliant blue stain for 1 h, followed by de-staining for 1 h in de-stain solution, which was then refreshed and left overnight with constant agitation.

2.4.2.2 Concentration determination by ultraviolet (UV) spectroscopy

Aromatic amino acids present in proteins will absorb ultraviolet light, Tyr and Trp will strongly absorb at 280 nm which allows for protein quantification (Walsh 2002). The concentration of the resultant proteins was calculated by UV spectroscopy. The unknown concentration protein was diluted in buffer (10 mM NaH₂PO₄, 50 mM NaCl pH 6.0) and a UV scan performed using a 1 cm path-length quartz cell. The

concentration was then calculated using the absorbance peak at 280 nm. Beer-Lambert Law states that the absorbance (A) is a linear function of the concentration (c) according the following equation:

$$A = \varepsilon \times l \times c$$

Equation 2-1

Where ε is the molar absorption coefficient and l is the cell path length.

2.4.2.3 Mass determination by size exclusion chromatography (SEC)

Size exclusion chromatography, also known as gel permeation chromatography, utilises a column packed with a chemically inert separation medium to “filter” a solution in order to separate the larger and smaller molecules. This can be used not only to separate mixtures of molecules but also to estimate the molar mass (M_r) by first calibrating the column with a series of known standards.

On entering the column the smaller molecules have further to travel as they can permeate the small gaps in the resin, conversely, larger molecules, due to their size have a limited path and therefore elute faster. M_r determination by SEC can be carried out by comparing the partition coefficient (K_{av}) with the log. of the M_r . The K_{av} is calculated according Equation 2-2.

$$K_{av} = \frac{\left(V_e/V_0\right)}{\left(V_t/V_0\right)}$$

Equation 2-2

Where V_e the elution volume of the sample in ml, V_t is the total volume of the column (ml) and V_0 is the void volume of column. The elution volume of the large molecule blue dextran can be taken as V_0 .

SEC was carried out according to methods described by Watson and co-workers (2006) with some differences (Watson et al. 2006). Superdex™ 75 10/300 GL (17-5274-01) column was prepared by washing with at least 50 ml distilled water at a flow rate of 0.5 ml/min followed by at least 50 ml of phosphate buffer (10 mM NaH_2PO_4 , 50 mM NaCl, pH 7.0) at 0.5 ml/min which was then pumped continuously until a steady baseline was achieved. The column was calibrated with individual protein solutions dissolved in phosphate buffer containing 2.5 mg/ml albumin from chicken egg white (Sigma A7642), 2.5 mg/ml myoglobin (Sigma M0630), 5 mg/ml ribonuclease A (Sigma R5503) and 0.5 mg/ml wild type FIII9-10 (expressed and purified as described for the mutated proteins). A 200 μl sample was injected onto the column at a flow rate of 0.5 ml/min followed by elution with 25ml of phosphate buffer at a flow rate of 0.5 ml/min. The UV absorbance was continuously measured at 280 nm. The mutated proteins were diluted to a concentration of 0.5 mg/ml, injected onto the column and eluted as above.

2.4.2.4 Protein conformation by circular dichroism (CD)

Circular dichroism (CD) is a valuable technique for investigating the structure of a protein in solution. Plane polarised light consisting of two circularly rotating components, left handed (anti-clockwise) and right handed (clockwise) is passed through the sample. The difference in the extent of which the left (A_L) and right (A_R) components are absorbed results in an elliptical polarisation which can be measured. For a CD signal to be observed the chromophore has to be chiral, requiring it to possess an optically active component. The CD spectrometer measures alternately the absorption of left and right polarised light at a frequency of 50 kHz; the CD signal is produced by calculating the difference between them ($\Delta A = A_L - A_R$) (Kelly and Price 2000, Kelly et al. 2005).

The structural information can be gathered by the assignment of spectral bands to distinct structural features. The absorption can be measured in the far UV region from 180-260 nm. Information attaining to the secondary structure can be found below 240 nm as absorption in this region is mainly due to peptide bonds. Regular secondary structural features such as α -helix and β -sheets give rise to characteristic CD spectra thus allowing simple identification (Figure 2-7). However, it should be noted that the spectra is produced by the whole molecule and therefore does not indicate structural type in specific regions of the protein, it eludes to the most prominent conformation. In the near UV CD region, from 260-320 nm, contributions from aromatic amino acid side chains can be identified along with the presence of disulphide bonds. This region gives general information on the overall environment,

such as the degree of hydrogen bonding, polarity, dipole-dipole interactions and their potential to become polarised.

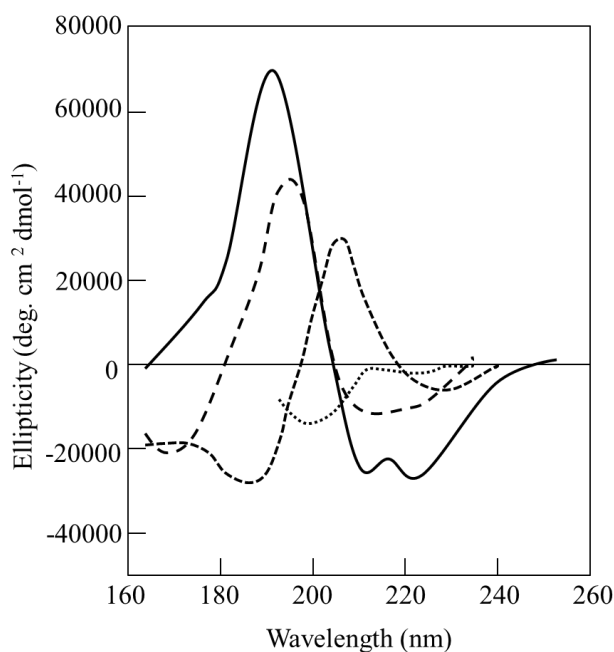


Figure 2-7 Typical far UV spectra displaying various common secondary structures. Including α -helix (solid line), anti-parallel β -sheet (long dashed line), type I β -turn (short dashed line) and random coil (dotted line). [Reproduced from Kelly et al. 2005].

CD spectra were measured with a Chirascan™ spectrometer (Applied Photophysics, Leatherhead, UK). All samples were diluted with distilled water to a concentration of between 0.8-1.2 mg/ml for far UV (180-260 nm). The instrumental parameters comprised of a 0.1 mm path length cell, with a scan speed of 50 nm/min, a 3 sec time constant, a bandwidth of 0.5 nm and 6 repeats. Near UV (260-360 nm) required a higher concentration of protein, therefore measurements were carried out at a concentration of approximately 2 mg/ml, using a 1 mm cell with spacer and only 4 repeats were performed. The mean residual ellipticity ($\text{deg}^\circ\text{cm}^2 \text{dmol}^{-1}$) of the

spectra was calculated from the measured ellipticity (millidegrees) using the following equation:

$$\theta_{MRW} = \frac{MRW \cdot \theta}{10 \cdot l \cdot c}$$

Equation 2-3

Where θ is the measured ellipticity in millidegrees, c is the protein concentration in mg/ml, l is the path length in cm, and MRW is the protein mean residue weight (protein molecular weight / no. of residues – 1).

2.5 Results

2.5.1 Mutation and expression of FIII9'10 proteins

All of the desired mutations (E1364A, I1410A, T1353A and H1377P) were successfully transfected into the plasmid DNA. In order to increase success 2 to 3 repeats of the minipreps were performed and the resultant DNA was first examined using agarose gel electrophoresis. Only satisfactory DNA was taken forward for sequencing to confirm mutation. The first attempt at DNA replication of I1410A and E1364A in XL-1 blue cells had little success and yielded 2 to 4 very small colonies. DNA sequencing showed they did not contain the desired mutation. The quantification of DNA was shown to be quite small with a high salt content and low purity, however this improved with repetition. The expression of protein from successful transfections ranged from 15-30 mg per litre of culture with the more stable T1353P and H1377P being expressed in the highest quantities.

2.5.1.1 Agarose gel electrophoresis

The DNA was shown as an orange line because of the fluorescent properties of ethidium bromide under UV light. As shown in Figure 2-8, it appeared that all the Minipreps for the I1410A, E1365A T1353P and H1377P had been successful, as there was a clear singular band highlighted in red. The weaker bands signify lower concentrations of DNA, as confirmed by absorbance values obtained using GeneQuantII (Table 2-2). An A_{260}/A_{280} ratio of less than 1.8 indicates low purity of DNA in solution and an A_{230}/A_{260} ratio higher than 0.5 signifies high salt contribution. Although the purity was not optimal, the DNA was sent for sequencing.

Table 2-2 DNA values as calculated by GeneQuantII.

DNA sequence	Concentration (ng/ml)	A_{260}/A_{280} ratio	A_{230}/A_{260}
I1410A1	152.7	1.198	0.77
I1410A2	101.5	1.342	0.66
I1410A3	97.2	1.349	0.68
E1364A1	108.6	1.351	0.63
E1364A2	106.6	1.363	0.63
E1364A3	111.2	1.322	0.68
T1353P1	117.3	1.4	0.7
T1353P2	155.1	1.376	0.8
H1377P1	134.4	1.4	0.8
H1377P2	173.0	1.421	0.8

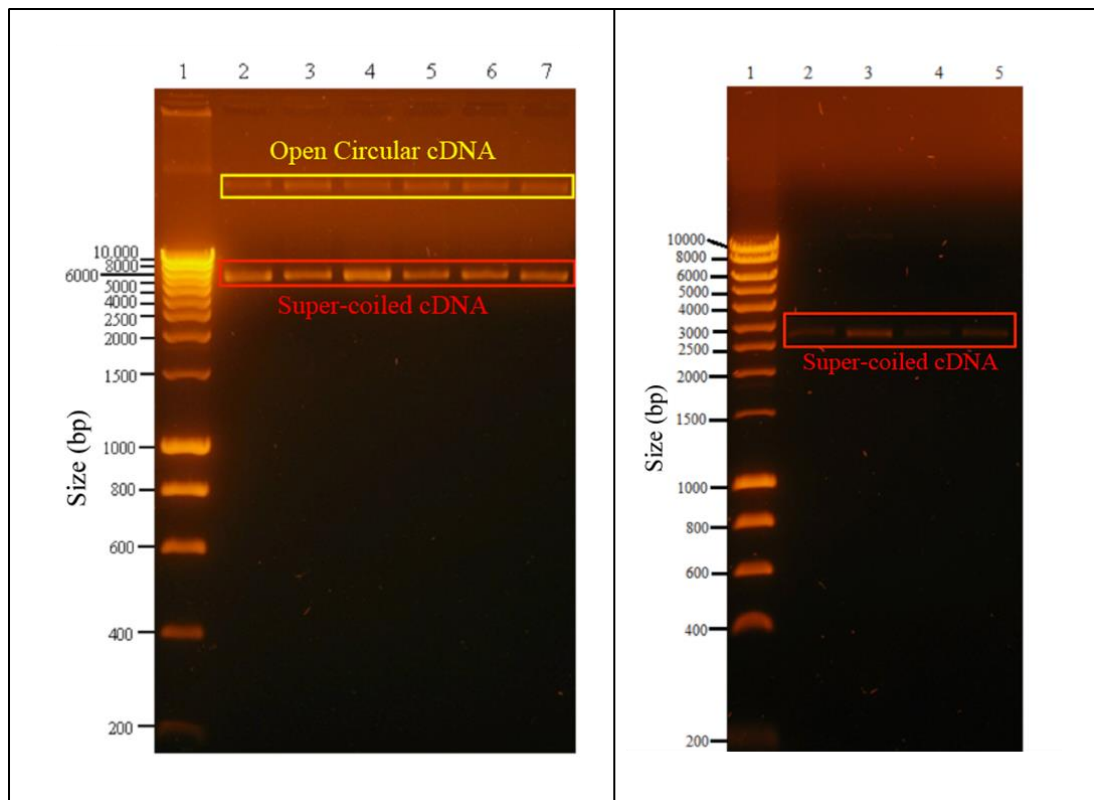


Figure 2-8 Agarose gel electrophoresis of cDNA, Hyperladder I lane 1. Left pane FIII9'10-GGC mutants E1364A lane 2, 3, 4, I1410A lane 5, 6, 7. Right pane FIII9'10 mutants T1353P lane 2 and 3, H1377P lane 4 and 5.

2.5.1.2 DNA sequencing

The DNA sequencing showed that only preparations E1364A-1, I1410A-1, T1353P-2 and H1377P-1 had the desired mutation. Only the successful sequences were carried on to protein expression. The full translated DNA sequence for each of the resultant proteins can be found in Appendix A.

2.5.1.3 Protein purification

The chromatogram for the FPLC purification of the proteins (Figure 2-9) showed the initial loading of the unpurified sample as a large wide peak (A). Once the entire sample had been loaded onto the column and the initial lysis buffer wash began, the peak tailed off (B). A small second peak (C) was caused by the first elution (15%), which only shows a small amount of material being removed from the column. This step was included to increase purity of the protein by removing non-specifically bound protein from the column, a value of 15% was found to give optimum results. The final peak (D) was the protein being eluted, the height and width differed with varying protein concentration produced.

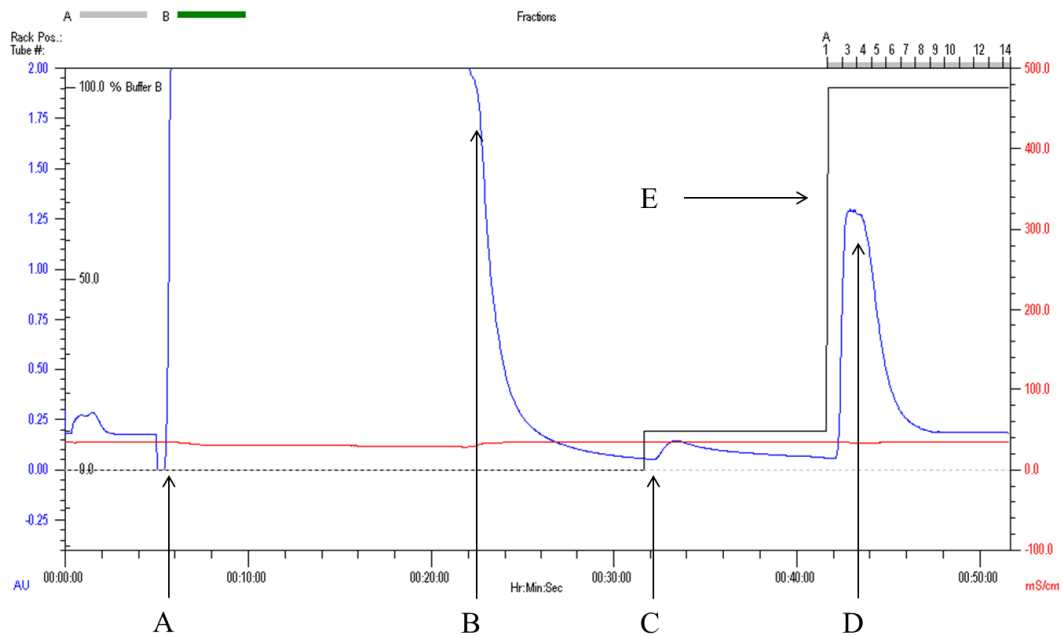


Figure 2-9 Typical chromatogram of FPLC purification of FIII9'10-GGC I2A. Important points indicated including initiation of flow through of cell lysates (A), washing of column with wash buffer (B), washing of column with 15 % elution buffer (C), protein peak (D) and elution buffer % composition (E).

A problem was encountered during the desalting and buffer exchange step by Ultrafiltration, FIII9'10-GGC E2A and FIII9'10-GGC I2A were found to precipitate and block the cellulose membrane. As a result, the filtration took several days and may have resulted in a significant loss of protein. The filtration by VivaSpin columns (FIII9''10 T2P and FIII9''10 H2P) also took a prolonged period of time, but was more successful than using simply Ultrafiltration. The de-salting step using HiPrep 26/10 column produced 35-40 ml of diluted protein in buffer which was above the maximum volume of the Vivaspin columns requiring repeated centrifuging. A combination of HiPrep desalting followed by Ultrafiltration to concentrate the sample was found to give the optimum results.

2.5.2 Protein characterisation

The amino acid sequence of the histidine tagged proteins was used to calculate their relative molecular mass (M_r) and estimate the isoelectric point (pI) and molar extinction coefficient (ϵ) using the online tool Pepstats (<http://www.ebi.ac.uk/Tools/emboss/pepinfo/index.html>) (Table 2-3). The amino acid sequences were then compared using online tool Clustal (<http://www.ebi.ac.uk/Tools/clustalw2/>) (see Figure 2-10 and Figure 2-11).

CHAPTER 2. Expression and purification of proteins

Table 2-3 Computed parameters for His tagged FIII9-10 proteins.

	FIII9'10	FIII9'10- GGC	FIII9'10- GGC E2A	FIII9'10- GGC I2A	FIII9''10 H2P	FIII9''10 T2P
M_r	21469.89	21687.07	21629.10	21645.05	21429.87	21465.90
ε	21620	21620	21620	21620	21620	21620
pI	8.10	7.9011	8.4755	7.9011	8.0326	8.0553
Amino acids	198	201	201	201	198	198
Ala (A)	12	12	13	13	12	12
Cys (C)	0	1	1	1	0	0
Asp (D)	9	9	9	9	9	9
Glu (E)	8	8	7	8	8	8
Phe (F)	4	4	4	4	4	4
Gly (G)	17	19	19	19	17	17
His (H)	11	11	11	11	10	11
Ile (I)	14	14	14	13	14	14
Lys (K)	3	3	3	3	3	3
Leu (L)	9	9	9	9	9	9
Met (M)	2	2	2	2	2	2
Asn (N)	6	6	6	6	6	6
Pro (P)	16	16	16	16	17	17
Gln (Q)	3	3	3	3	3	3
Arg (R)	14	14	14	14	14	14
Ser (S)	22	22	22	22	22	22
Thr (T)	22	22	22	22	22	21
Val (V)	16	16	16	16	16	16
Trp (W)	2	2	2	2	2	2
Tyr (Y)	8	8	8	8	8	8

CHAPTER 2. Expression and purification of proteins

```
FIII9'10-GGC      MRGSHHHHHHGMASGLDSPTGIDFSDITANSFTVHWIAPRATITGYRIRHHPEHFSGRPR 60
FIII9'10-GGC I2A  MRGSHHHHHHGMASGLDSPTGIDFSDITANSFTVHWIAPRATITGYRIRHHPEHFSGRPR 60
FIII9'10-GGC E2A  MRGSHHHHHHGMASGLDSPTGIDFSDITANSFTVHWIAPRATITGYRIRHHPEHFSGRPR 60
*****

FIII9'10-GGC      EDRVPHSRNSITLTNLTGTEYVVSIVALNGREESPLLIGQQSTVSDVPRDLEVVAATPT 120
FIII9'10-GGC I2A  EDRVPHSRNSITLTNLTGTEYVVSIVALNGREESPLLIGQQSTVSDVPRDLEVVAATPT 120
FIII9'10-GGC E2A  EDRVPHSRNSITLTNLTGTEYVVSIVALNGREESPLLIGQQSTVSDVPRDLEVVAATPT 120
*****

FIII9'10-GGC      SLLISWDAPAVTVRYRITYGETGGNSPVQEFTVPGSKSTATISGLKPGVDYTITVYAVT 180
FIII9'10-GGC I2A  SLLISWDAPAVTVRYRITYGETGGNSPVQEFTVPGSKSTATISGLKPGVDYTITVYAVT 180
FIII9'10-GGC E2A  SLLISWDAPAVTVRYRITYGETGGNSPVQEFTVPGSKSTATISGLKPGVDYTITVYAVT 180
*****

FIII9'10-GGC      GRGDPASSKPI SINYRTGGC- 201
FIII9'10-GGC I2A  GRGDPASSKPI SINYRTGGC- 201
FIII9'10-GGC E2A  GRGDPASSKPI SINYRTGGC- 201
*****
```

Figure 2-10 Alignment of amino acid sequences for FIII9'10-GGC proteins, with the difference in the amino acid sequence highlighted.



Figure 2-11 Alignment of amino acid sequences for FIII9-10 proteins, with the difference in the amino acid sequence highlighted.

2.5.2.1 SDS PAGE

The SDS-Page analysis provided information relating to the protein purity and relative molecular weight of the samples. In all cases the M_w appeared to correspond to the computed M_w for the samples. A typical SDS-PAGE gel is shown in Figure

2-12. The desired protein present in the initial un-purified sample (indicated in red) was retained on the column as it was not present in any of the flow through samples. Comparison of the load versus flow indicated that a high amount of the protein was retained on the column as the band was not present in the flow run. A faint band was seen with 15 % elution which corresponds to non-specifically bound proteins. The presence of low M_w protein impurities was shown by the SDS-PAGE gel, however these are minor and would have little influence on the overall sample. All proteins showed a similar M_w and purity when ran on a SDS-PAGE gel (see Figure 2-13).

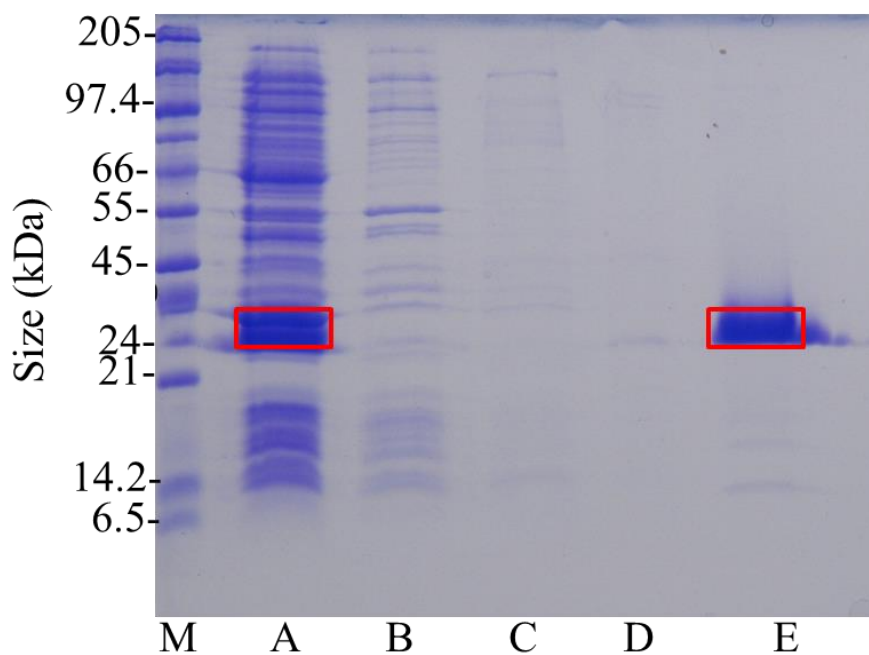


Figure 2-12 SDS-PAGE gel image of FIII9'10-GGC E2A (red rectangles), showing protein Mw marker (M), initial unpurified sample (A), flow through from sample injection (B), initial wash (C), 15 % elutant (D) and final sample (E).

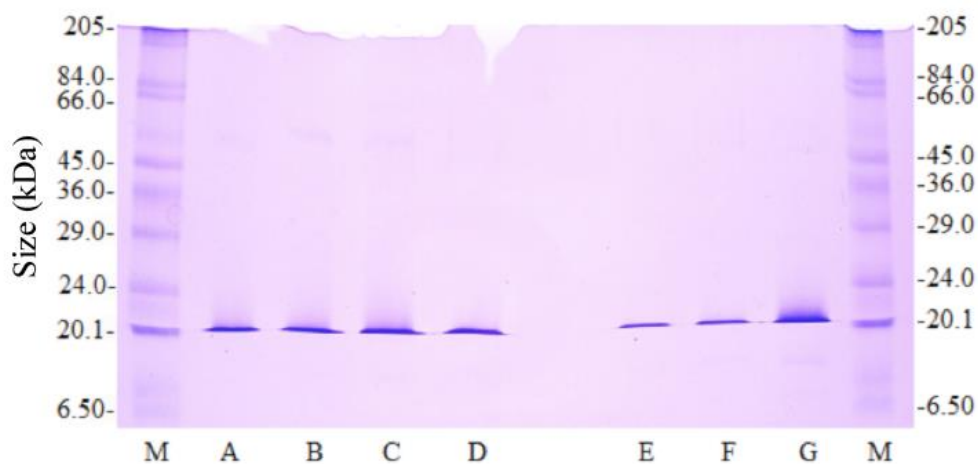


Figure 2-13 SDS-PAGE gel image showing molecular weight marker (kDa) (M) and proteins FIII9-10 (A), FIII9'10 (B), FIII9''10 H2P (C), FIII0''10 T2P (D), FIII9'10-GGC (E), FIII9'10-GGC I2A (F) and FIII9'10-GGC E2A (G).

2.5.2.2 Size exclusion chromatography

The elution peaks obtained from calibration of the SEC column are shown in Figure 2-14 and the corresponding values are displayed Table 2-4, the calculated K_{av} value was then plotted against the M_r which produced a R^2 value of 0.99 for the calibration curve (shown in Figure 2-15). The mutated proteins each eluted as a singular, clear, defined peak indicating the absence of impurities in the sample. For each sample the M_r extrapolated from the calibration was different from the value calculated by interpreting the amino acid sequence, however most were within range (see Table 2-5).

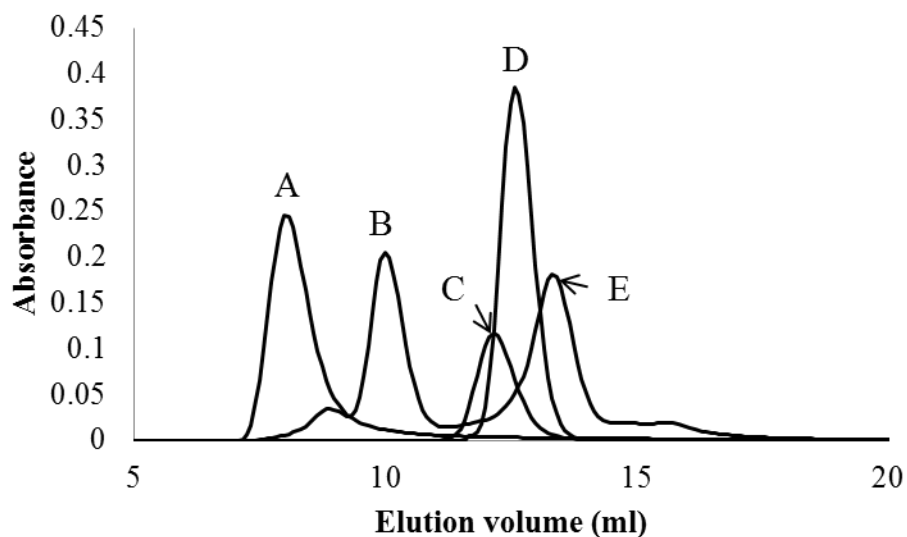


Figure 2-14 Example of chromatogram peaks from calibration of Superdex™ 75 10/300 GL column. Showing blue dextran (A), ovalbumin (B), FIII9-10 (C), myoglobin (D) and ribonuclease A (E).

Table 2-4 Size exclusion chromatography calibration standards.

Protein	Approx. M_r (kDa)	Elution vol. (V_e) ml.	K_{av}
Blue dextran	2000	7.999	1
Ovalbumin	45.0	9.833	0.410
FIII9-10	21.5	12.165	0.507
Myoglobin	17.0	12.582	0.524
Ribonuclease A	13.7	13.165	0.549

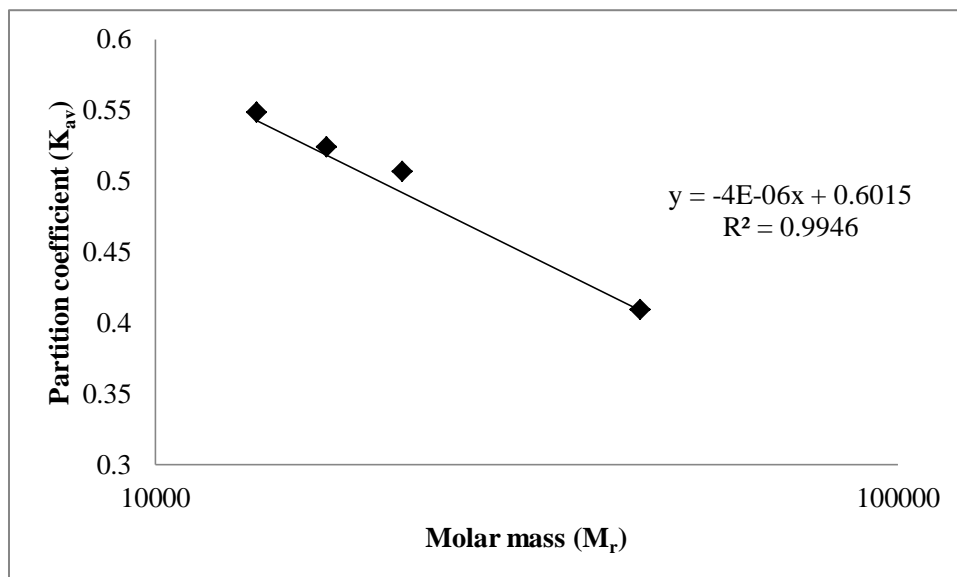


Figure 2-15 Calibration curve for size exclusion chromatography calculations. Equation of line shown on figure.

Table 2-5 Estimation and calculated M_r of the mutated proteins by size exclusion chromatography.

Protein	Pepstats calculated M_r (kDa)	Elution vol. (V_e) ml	K_{av}	Approx. M_r (kDa) (n=3)
FIII9'10-GGC E2A	21.63	12.332	0.514	21.9 ± 1.4
FIII9'10-GGC I2A	21.65	12.276	0.512	22.5 ± 1.1
FIII9''10 H2P	21.43	12.304	0.513	22.2 ± 0.8
FIII9''10 T2P	21.47	12.248	0.510	22.8 ± 0.7

2.5.2.3 Circular dichroism (CD)

The CD spectra in the far UV region was undertaken for all of the proteins and shown together to aid comparison (Figure 2-16). The CD spectrum in the far UV region from 180-260 nm provides information regarding the secondary structure of the proteins. The FIII9-10 proteins all displayed a similar, characteristically β -sheet/turn spectra which is consistent with the known structure and previously

reported spectrum (Pereira et al. 2007). The main spectral features included a strong positive maximum centred around 202 nm, a weak negative maximum centred around 215 nm coupled with the positive CD band centred around 226 nm which indicates aromatic contributions. Therefore the introduction of the mutations did not alter the structure of the protein.

The near UV spectrum (260-320 nm) provides information regarding the aromatic contributions in the proteins (Figure 2-17). As tryptophan, phenylalanine and tyrosine are all present in the FIII9-10 proteins the contributions to the spectra can overlap producing a distinct fingerprint for the proteins similar to previously reported spectra (Pereira et al. 2007). There is an initial peak around 260 nm with a small shoulder around 270 nm followed by a negative band from 276-284 nm. The sharp peak found on FIII9-10 and FIII9''10 H2P at 270 nm due to phenylalanine, although visible the sharpness is reduced in FIII9'10 and FIII9''10 T2P suggesting slight differences. The peak around 288 nm with a negative maximum around 295 nm, followed by a large maxima band from around 302 nm indicates tryptophan contributions. There was an increase in ellipticity with the mutated proteins but an overall reduction in intensity of the mutated spectra compared to the wild type. This suggested that by mutating the proteins it has altered the nature of the environment, possibly with regards to mobility (Kelly and Price 2000, Kelly et al. 2005). However, as near UV has a relatively weak signal further analysis would be required to confirm the specifics.

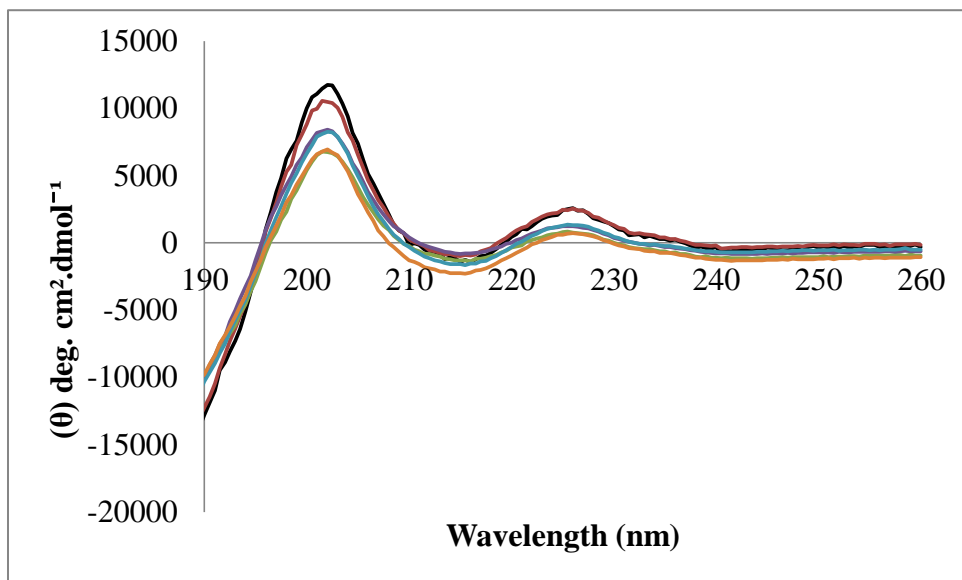


Figure 2-16 Far UV CD spectra of FIII9-10 (black) and mutant variations FIII9'10 (red), FIII9'10-GGC I2A (green), FIII9'10-GGC E2A (purple), FIII9'10 H2P (blue) and FIII9''10 T2P (orange) in sodium phosphate buffer.

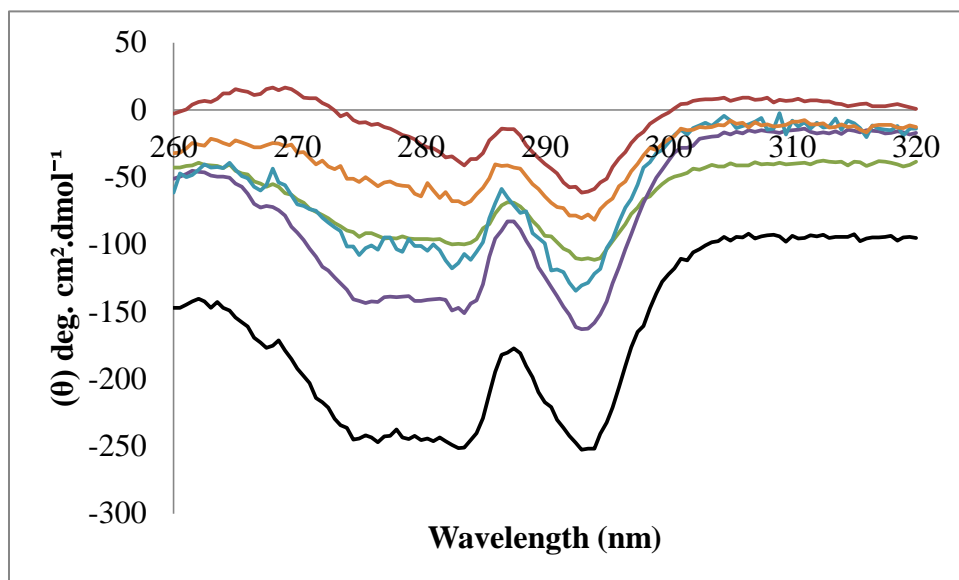


Figure 2-17 Near UV CD spectra of FIII9-10 (black) and mutant variations FIII9'10 (red), FIII9'10-GGC I2A (green), FIII9'10-GGC E2A (purple), FIII9'10 H2P (blue) and FIII9''10 T2P (orange) in sodium phosphate buffer.

2.6 Discussion

2.6.1 Plasmid DNA mutation and replication

The initial low success of the transfection of DNA plasmid into the XL-1 blue strain of *E.coli* is probably due to poor technique as it improved with time. Extraction of DNA with the Miniprep kit yielded low concentrations of DNA which could be due to many reasons, such as poor growth in culture or degradation of the solutions used. The impurities and higher than desired salt content could be due to impurities in the wash solution (this has to be diluted with ethanol prior to use). However, even with this lower than optimum DNA yield, the subsequent protein expression was successful.

The possibility of impurities in the sample is why the screening of the DNA by agarose gel electrophoresis followed with DNA sequencing was vital. Although a limited amount of information was gathered by agarose gel electrophoresis, it allowed for quick assessment of DNA for fragmentation or other undesirable oddities. Coupled with DNA sequencing agarose gel electrophoresis ensures that only suitable DNA gets taken forward to the expression stages. The failed minipreps that did not produce the correctly mutated DNA may have been due to random mutations within the *E.coli* vector.

2.6.2 Protein manufacture

Overall the technique for mutating expressing and purifying proteins was successful as sufficient quantities were produced. The IMAC coupled with FPLC allowed for a fast purification of the protein, which also benefited from graphical output enabling monitoring of purification. Optimisation of the buffer exchange and protein concentration process was necessary to avoid precipitation of protein. The initial technique used ultrafiltration of the protein sample without any prior buffer exchange, which resulted in protein precipitation and so was not continued. Following this, it was decided that removal of the excess salts prior to concentrating would be the best way to proceed. The HiPrep 26/10 column enabled the high salt elution buffer to be exchanged for the preferred sodium phosphate buffer resulting in a low concentration protein solution. The next step, concentrating the proteins, was performed by either vivaspin columns or ultrafiltration. The vivaspin columns had a limited volume capacity and were not ideal for the 30-40 ml produced by the buffer exchange step. Therefore, the best technique was buffer exchange using a HiPrep 26/10 column followed by concentrating by ultrafiltration, this produced concentrated protein solutions with little to no precipitation of protein in the process.

2.6.3 Protein expression

Interestingly, there was greater protein concentrations produced for the FIII9''10 H2P and FIII9''10 T2P mutations than the FIII9'10-GGC I2A and FIII9'10-GGC E2A. This could be due to better stability of the proteins in solution or improved

technique. With the exception of this finding, the protein expression was the same throughout. The CD structure confirmed that the mutated proteins conformed to the previous structures. There was no precipitation of proteins observed over time, as such instability through aggregation was not perceived to be a problem in this work. If there had been anything to indicate precipitation of proteins then further analysis would have been performed such as repeated size exclusion chromatography studies and dynamic light scattering. It should also be noted that batches of proteins were stored at -80 °C in small aliquots to reduce freeze thaw and on average were used within 6 months.

2.6.4 Protein characterisation

Calculation of protein characteristics by Pepstats gave the estimated molecular weight of the protein which was useful for further analysis by SDS-PAGE. The SDS PAGE analysis was an effective and useful tool in evaluating the protein samples. It also acted as a useful tool in checking the efficiency of the columns used for purification. Furthermore the SDS-PAGE results were corroborated by SEC, which showed purified proteins with albeit a slightly higher than estimated M_r but containing minimal impurities. SEC has limitations due to the requirement of manual calibration of the column, the relationship between apparent M_r and V_e relies on a correspondence between the hydrodynamic properties of the protein standards and test protein (Cabre et al. 1989). Multi-angle light scattering (MALS) coupled to SEC avoids the need to calibrate the column and has been shown to be a reliable method for obtaining the absolute molecular weight of even very low molecular weight

polymers (Xie et al. 2002). MALS uses multiple angles for analysis of the scattering of static light (Chaudhuri et al. 2014). The absolute molecular mass calculated by MALS instruments such as the DAWN ® HELEOS ® (Wyatt Technology Corporation, California, USA) employs the detection of the light scattering over a broad range of angles in relation the incident laser beam. This allows for the calculation of sample concentration and the molar mass in the range of 10^3 to 10^9 Daltons. The application of this technique would have been beneficial to this work as an additional “check” of protein quality and purity.

2.6.5 Circular dichroism

The far-UV CD finding of a β -sheet corresponds to work done on FIII9’10 by Pereira and colleagues (2008). Furthermore, the presence of a β -sheet is also in agreement with the known 3-D structure of FN (Leahy et al. 1996). The second peak corresponding to the aromatic residues around 226 nm has also previously been previously reported (Kreiner et al. 2008). This information would suggest that overall the general structure of FIII9-10 proteins is unchanged by the mutations which is favourable as the conformational shape is important for the activity of the protein. The near UV gives limited information as the signals in the range are weaker than in far UV. As a consequence higher concentrations of proteins are required. For this analysis, higher concentration of protein meant that there would also be higher salts from the buffer in the sample. Comparison between the different mutations in this case is limited because the information generated from the difference in observed value for molar ellipticity is unspecific. It is most likely due to a change in

the aromatic environment; however any errors in calculation of the protein concentration would be amplified when converting the signal to mean residue molar ellipticity, therefore the information generated should not be looked at in isolation. Overall the main points which were observed are within the same range for all the protein mutants. The information obtained from CD measurements is limited to low resolution regarding the structure of the proteins; therefore it is required to be used to accompany other complementary techniques. In this instance, CD allowed for a quick and easy assessment of the expressed protein. Had there been any problems during expression of the protein or if the mutations had changed the protein significantly, the structure would have been likely to have been affected; therefore this relatively quick assessment is very useful.

2.7 Summary

The generation of all the FIII9-10 mutants was successful. It can be concluded from the CD, SDS-PAGE and SEC analysis that the engineered protein fragments were of sufficient quantity and quality that they could be used in further experiments. The FIII9'10-GGC mutants I2A and E2A were taken forward to binding analysis to IGFBP-5 and the FIII9''10 mutants H2P and T2P was assessed for their conformational stability. Both of these topics are discussed in the next chapter.

CHAPTER 3. Biophysical and functional characteristics of FIII9-10 mutants

3.1 Introduction

Binding proteins are secreted by diverse cell types and are thought to act as local regulators; for example in bone insulin-like growth factor binding protein 5 (IGFBP-5) plays a role in bone growth by both inhibitory and stimulatory actions (Miyakoshi et al. 2001). Six subtypes of the IGFBP superfamily have been identified by molecular cloning of their cDNAs from rat and human tissues (Clemmons 2001). These are sequentially numbered in the order discovery as IGFBP-1, -2, -3, -4, -5 and -6. IGFBP-5 binds to a number of proteins including FN. It has been suggested that binding of FN-IGFBP-5 is via the C-terminal domain of IGFBP-5 (Beattie et al. 2009). There is some debate if the FN region involved is on a type I repeat (Xu et al. 2004) or type III (Beattie et al. 2009). For the purposes of our investigation we concentrated on the proposed binding between IGFBP-5 and the cell binding domain of FN encompassing the 9th and 10th type III domain.

The integrin binding motif RGD is often conjugated to polymers to form biomimetic scaffolds for tissue engineering and regenerative medicine (Hersel et al. 2003). As described previously, for optimum activity integrin $\alpha 5\beta 1$ requires the 'synergy site' (PHSRN) on the 9th type III FN domain (FIII9) in addition to RGD on FIII10 (Mardon and Grant 1994). The FIII9'10 domain pair is therefore required to fully engage integrin $\alpha 5\beta 1$. The 'spatial relationship' between domain 9 and 10 is critical (Aota et al. 1994, Altroff et al. 2004) therefore any unfolding as a result of the

solution environment or adsorption to surfaces would affect the binding potential of the protein. By improving the conformational stability a more robust functioning FIII9-10 based protein scaffold may be created.

The initial aim of this project was to define the molecular interactions underlying the binding between IGFBP-5 and FIII9-10. To accomplish this, we used the FIII9'10-GGC proteins as described in Chapter 2 for SPR. On the basis of the data acquired for IGFBP-5/FIII9'10-GGC binding, the aim was revised to prepare a FIII9'10 based protein scaffold with increased conformational stability upon surface adsorption. In this study we evaluated the effect of the solution pH, temperature and denaturant concentrations on the conformational stability of the FIII9'10 based proteins.

3.2 Materials

Unless otherwise stated all chemicals were purchased from Melford (Suffolk, UK), Fisher Scientific (Leicestershire, UK) or Sigma-Aldrich (Dorset, UK) at analytical standard or equivalent quality. EZ-Link Maleimide-PEO₂-Biotin (cat. no. 21901), 4'-hydroxyazobenzene-2-carboxylic acid (HABA) avidin and Slid-A-lyser 10 K were purchased from Pierce (UK). HBS-EP buffer was from GE healthcare Bio-Sciences (Uppsala, Sweden). Water was purified to > 14 MΩ.cm with a BioSelect, Purite, UK.

3.3 Buffers and reagents

Sodium phosphate buffer: 50 mM NaCl, 10 mM NaH₂PO₄, pH 6.0

High salt sodium phosphate buffer: 300 mM NaCl, 10 mM NaH₂PO₄, pH 7.0

HABA/Avidin reagent: 24.2 mg HABA dissolved in 9.9 ml of H₂O and 100 µl 1 M NaOH, 10 mg Avidin dissolved in 600 ml of HABA reagent made up to 20 ml with PBS.

3.4 Methods

3.4.1 Binding of FIII9-10 to IGFBP-5

The binding of the IGFBPs and FN has been shown by Beattie and co-workers (2009) who successfully utilised SPR to find that both IGFBP-5 and IGFBP-3 bind to FIII9-10 region of FN. In their investigation it was necessary to add a GGC tripeptide to facilitate the biotinylation of the proteins for SPR, this resulted in the FIII9'10-GGC mutant. For our studies we have developed two single point mutations of FIII9'10-GGC called FIII9'10-GGC E2A and FIII9'10-GGC I2A.

3.4.1.1 *Surface plasmon resonance (SPR)*

SPR analysis of binding of the FIII9'10-GGC mutants with IGFBP-5 has been used previously to analyse the IGF polypeptides and the IGFBPs, both intact and fragmented (Headey et al. 2004, Allan et al. 2006, Beattie et al. 2009). SPR

CHAPTER 3. Biophysical and functional characteristics of FIII9-10 mutants

measured by a Biacore biosensor is a useful tool in investigating the kinetics and affinity of protein-protein interactions. A solution containing one member of a binding complex is passed across a biosensor chip coated with their corresponding binding partner. The protein in solution is referred to as the analyte and the protein immobilised on the sensor chip is referred to as the ligand. Any interaction between the ligand and the analyte results in a measurable output directly proportional to the surface concentration of bound analyte.

Figure 3-1 illustrates the general principle for the Biacore biosensor which works based on the measurement of changes in refractive index. SPR occurs in thin conducting films at an interface between media of different refractive index such as metal films and buffer. Biacore systems use a biosensor chip surface consisting of glass coated in a thin film of gold. Wedged polarised light is focused onto the glass:gold interface of the sensor chip surface through a glass prism and the subsequent reflection is detected. This generates an 'evanescent wave' which propagates beyond the glass:gold surface into the flow channel. Any changes such as binding of the analyte to the ligand will interact with the evanescent wave and alter the angle of incidence, this can be detected and displayed on a sensogram. An increase or decrease in response unit (R.U.) can be directly equated to changes in localised mass and subsequently a value for bound analyte can be obtained. The sensogram produced represents change in mass at the surface over time with an approximate value of one change in R.U. corresponding to a concentration of 1 pg/mm^2 .

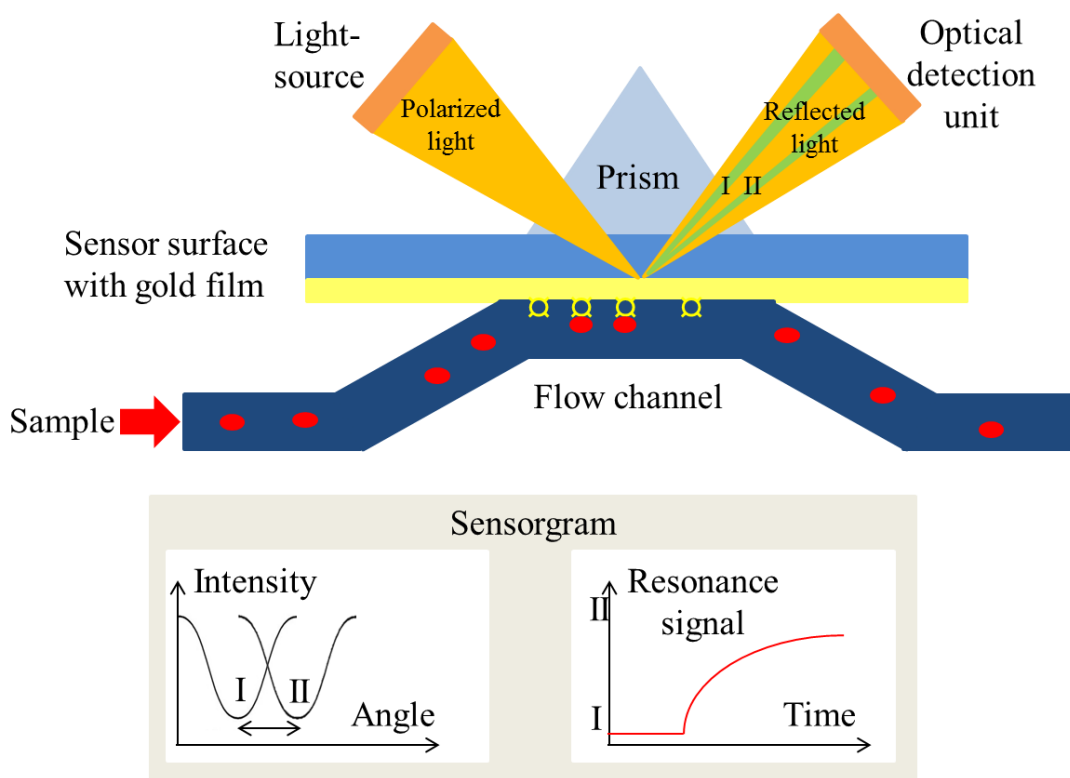


Figure 3-1 Illustration of surface plasmon sensor light path and schematic of intensity and resonance signal. Analyte shown as red oval and ligand as yellow \square [Reproduced from Butler, Biacore UK].

There is a range of commercially available sensor chips for the Biacore SPR system. Generally they consist of a glass surface coated in a uniform layer of gold around 50 nm thick coupled with a secondary coating to enable attachment of the ligand. An SA sensor chip was used for this investigation. The SA chip has a secondary coating of carboxymethylated dextran with immobilised streptavidin for ‘capture’ of biotinylated ligands. Dextran facilitates ligand immobilisation as it provides hydrophilic environment which is preferred for bimolecular interaction. The dextran matrix also allows for covalent attachment of streptavidin. Biotinylated ligands captured on an SA chip surface are extremely stable, almost to equivalent of

covalently immobilised ligands. A single chip can therefore be used repeatedly by regeneration of the surface by removal the analyte, with minimal effect to the ligand surface. The SA sensor chip further benefits from the incorporation of four flow cells with serial flow direction, allowing for the analysis of four different, independent ligands at the same time (Biacore 2008).

For biosensor analysis a fully automated BIAcore 3000 instrument was used with streptavidin-conjugated Sensor Chip SA (BIAcore Ltd, UK). Prior to biotinylation the sodium phosphate buffer (10 mM NaH₂PO₄, 50 mM NaCl pH 6.0) was exchanged for high salt sodium phosphate buffer (10 mM NaH₂PO₄, 300 mM NaCl pH 7.0), to optimise reaction. Protein samples were biotinylated as described in Kreiner and co-workers (2008). A solution of 20 mM PEO₂-maleimide activated biotin was incubated for 2 h at room temperature at a 30-fold molar excess with protein in a buffer of 10 mM NaH₂PO₄, 300 mM NaCl pH 7.0, 5.0 mM Tris[2-carboxyethyl] phosphine (TCEP). The terminal cysteine of the GGC tripeptide provides a sulfhydryl group which reacts with the maleimide group of the biotin and forms a stable thioether bond. Excess, non-reacted maleimide-PEO₂-biotin was removed by extensive dialysis into 2 l high salt sodium phosphate buffer over 24 h with 3 changes using a Slid-A-lyser 10K (Perice, UK).

The biotin incorporation was estimated using the HABA (4'-hydroxyazobenzene-2-carboxylic acid) method. The concentration of the biotinylated proteins in solution was calculated using UV spectroscopy at 280 nm. The absorbance at 500 nm (OD₅₀₀) of 900 µl HABA/Avidin solution was measured and then to this 100 µl of biotinylated protein was added and the OD₅₀₀ measured. The difference in OD₅₀₀ was

CHAPTER 3. Biophysical and functional characteristics of FIII9-10 mutants

then used to determine the ratio of biotinylation of the proteins using the following equations:

$$\Delta A_{500} = (0.9 OD_{500 H/A}) - OD_{500 P}$$

Equation 3-1

Where $OD_{500 H/A}$ is the absorbance measured at 500 nm of the HABA/Avidin reagent, $OD_{500 P}$ is that of sample reaction mixture after adding the biotinylated protein to HABA/Avidin solution and 0.9 is the dilution factor of HABA/Avidin upon addition of sample.

The μmol biotin per ml reaction mixture (C) can be calculated using the mM extinction coefficient at 500 nm (34):

$$C = \frac{\Delta A_{500}}{34}$$

Equation 3-2

The mmol biotin per ml reaction mixture (B) can be found using C and the dilution factor of biotynalted sample (d).

$$B = C \times 10 \times d$$

Equation 3-3

Finally the ratio of biotin to protein can be found by dividing B by the molar concentration of the biotinylated sample (mM).

CHAPTER 3. Biophysical and functional characteristics of FIII9-10 mutants

Biotinylated proteins were diluted to a concentration of 10 µg/ml with HBS-EP buffer (10 mM HEPES pH 7.4, 150 mM NaCl, 3 mM EDTA, 0.005% v/v polysorbate 20). Biotinylated BSA was used as a negative control and biotinylated FIII9'10-GGC as a positive control. Prior to immobilisation of the proteins FIII9'10-GGC I2A and FIII9'10-GGC E2A onto the SA chip the flow cells were cleaned with a pulse of 5 µl of 100 mM HCl, 0.5 M NaCl. Following this HBS-EP buffer was ran at a flow rate of 5 µl/min until a stable baseline was achieved. Each biotinylated protein (5 µl) was then injected over a single flow cell for 60 s, followed by washing with either 100 mM HCl, 0.5 M NaCl for 60 s (5 µl) or ethanolamine (10 µl) for 120 s. The sensogram response was measured, using the baseline as the starting point and the reading following the wash as the addition of immobilised protein. Binding of the analytes IGFBP-5, IGF-1 and $\alpha 2\beta 1$ to the immobilised proteins was performed by injecting over the SA-chip at a flow rate of 30 µl/min for 5 min and the response was measured in the same manner as previously described. Following analyte binding, the SA chip was cleaned with 2 pulses of regeneration buffer (2 mM EDTA, 1 M NaCl) for 30 s at 30 µl/min. The regeneration buffer removes the bound analyte from the immobilised protein without affecting the ligand, allowing for subsequent binding analysis on the same protein.

3.4.2 Physical stability of FIII9-10 based proteins

3.4.2.1 *Equilibrium chemical denaturation measured by fluorescence*

The conformational stabilities of FIII9-10, FIII9'10, FIII9''10 H2P and FIII9''10 T2P were determined by guanidine hydrochloride (GdmCl) denaturation, measured by intrinsic fluorescence of the environment of the tryptophan residues. Fluorescence measures the energy emitted when an electron returns to the ground state following excitation. In proteins the fluorescence is derived from the aromatic residues Phe, Tyr and Trp. The Trp residue tends to dominate fluorescence measurements as both its absorbance and emission are greater than that of Phe and Tyr. Changes in protein conformation caused by unfolding will cause an increase or decrease the fluorescence as the aromatic residues become more/less exposed. In this case, we excited the solution at 290 nm, which selects only for Trp fluorescence. The FIII9-10 proteins only contain two Trp residues, one on each domain. This allows for specific local information to be gained by selectively exciting the Trp residues.

Proteins were incubated in 3 ml 0 to ~8 M GdmCl in 10 mM NaH₂PO₄, 50 mM NaCl pH 6.0. Protein samples were diluted in GdmCl to a concentration of 0.01 mg/ml and allowed to equilibrate for at least 2 h, the thermodynamic nature of the unfolding requires equilibrium to be reached for consistent measurements. Fluorescence spectra were recorded with a Varian Cary Eclipse™ spectrofluorometer using a 1 cm path length, 3.5 ml quartz cuvette. An excitation wavelength of 290 nm was used with an emission scan ranging from 300 to 450 nm, a scanning speed of 600 nm/min, and a slit width of 5 nm. The fluorescence emitted at 350 nm \pm 2 was recorded and the Gibbs free energy (ΔG) between the folded and unfolded states extrapolated to 0

CHAPTER 3. Biophysical and functional characteristics of FIII9-10 mutants

M GdmCl to obtain conformational stability of the protein, ΔG_{H_2O} . At any point of measurement both folded and unfolded conformations will be present (Creighton 1997). At lower concentrations of denaturant there will be more folded than unfolded and hence as denaturant increases the fraction of unfolded (f_U) to folded (f_F) will increase. For any point in a two-state folding mechanism $f_F + f_U = 1$. Subsequently, the observed value of y at any point will be $y = y_F f_F + y_U f_U$, where y_F and y_U represent the values of y characteristic of the folded and unfolded states, respectively. Combining these equations gives:

$$f_U = (y_U - y)(y_F - y_U)$$

Equation 3-4

The following equation can be used to calculate ΔG which requires the equilibrium constant (K) which is equal to $(y_F - y)/(y - y_U)$,

$$\Delta G = -RT \ln K$$

Equation 3-5

Where R is the gas constant ($1.987 \text{ cal mol}^{-1} \text{ K}^{-1}$) and T is the absolute temperature.

Assuming a linear dependence of ΔG on denaturant concentration the data can be fitted to the following equation to extrapolate the value of ΔG_{H_2O} :

$$\Delta G = \Delta G_{H_2O} - m (\text{denaturant})$$

Equation 3-6

Following calculation of the Gibbs free energy, the most stable protein was selected for further analysis.

3.4.2.2 Automated circular dichroism

Extended CD analysis of the three proteins FIII9-10, FIII9'10 and FIII9''10 H2P was performed at Applied Photophysics Ltd. (Leatherhead, UK) using the recently developed Chirascan™ -Plus Automated CD (ACD) spectrometer. This allowed for many samples to be analysed over a prolonged period of time with minimum supervision in a variety of conditions. The modified sample housing (Figure 3-2) consisted of an automated injection needle, temperature controlled sample platform and reagent stock platform connected to a Chirascan plus instrument. A custom adapted 0.2 mm path-length flow cell with temperature control was used for all ACD scans. A 96-well reaction plate at 4 °C was used to house samples prior to injection into the system.

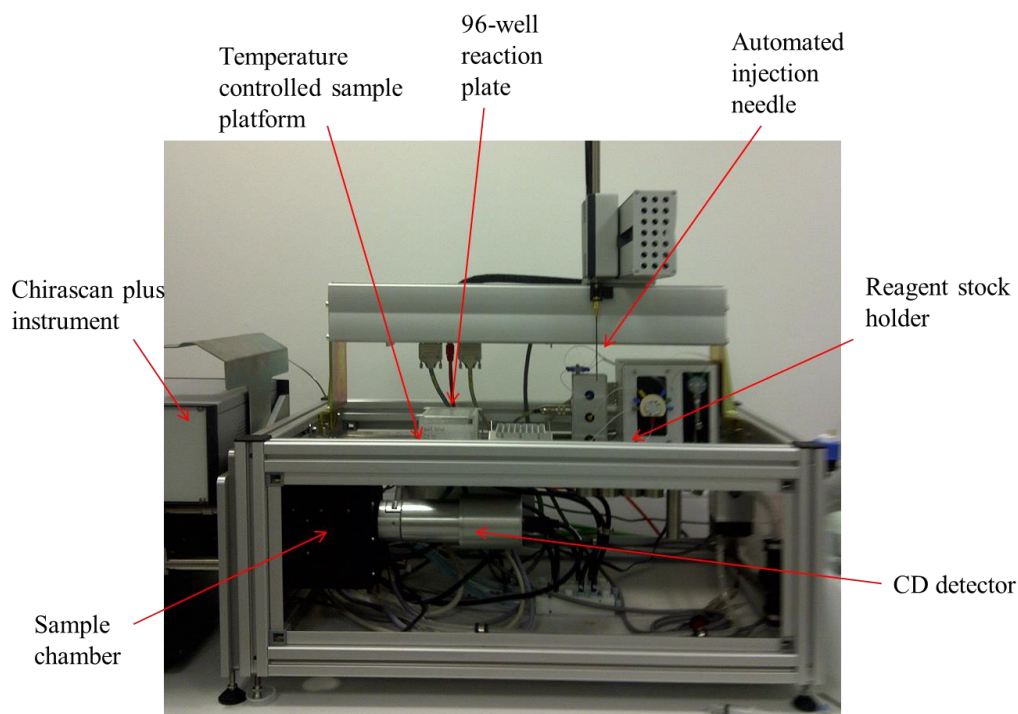


Figure 3-2 Photograph of modified Automated CD sample housing, important features are annotated.

Following sample injection and ACD scan, the sample cell was automatically cleaned by flushing with 20 % (v/v) DECON in H₂O then 100 % acetone and dried thoroughly. A typical sample plate is shown in Figure 3-3 allowing for a range of 15 different condition data points for each protein sample. Buffer was run in between each protein condition to obtain a suitable baseline and check that the sample cell was cleaned sufficiently.

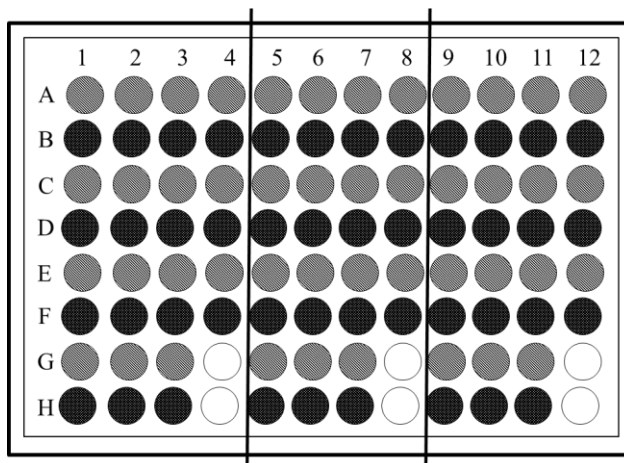


Figure 3-3 Illustration of typical 96 well plate auto sampler set up with buffer (grey) and protein incubated in specified conditions (black). Protein mutations were grouped together, separation indicated here by black line (Read A1 to H1 then A2 to H2 and so on).

Stability over a pH range of ~2-8 for the three proteins was investigated. The pH range was generated using a function of the auto-sampler, a ‘master plate’ was created by mixing and diluting different volumes of 100 mM citric acid and 200 mM Na_2HPO_4 . Solution was withdrawn from the ‘master plate’ and used to dilute protein samples (concentration 1 mg/ml) which were then incubated for at least 1 h at 10 °C prior to ACD scan.

Unfolding of the protein by GdmCl was also measured by ACD at a concentration range of ~0-6 M. The maximum GdmCl concentration was limited by the flow cell because at high concentrations, salt build up can block the flow cell. Protein samples were incubated in GdmCl solution for over 2 h at 4 °C and ACD scan was performed from 210-260 nm at 20 °C. The strong absorbance of GdmCl in the far UV region restricted the range of the scan to above 210 nm.

CHAPTER 3. Biophysical and functional characteristics of FIII9-10 mutants

Finally, thermal unfolding was investigated using ACD to track the structural changes in the far UV for FIII9-10, FIII9'10 and FIII9''10 H2P. The samples were prepared as a 1 mg/ml concentration in 10 mM NaH₂PO₄, 50 mM NaCl pH 6.0 buffer. Spectra were collected while the sample was heated at 1 °C a minute from 20 to 95 °C with scanning from 150 to 250 nm in 1 nm steps and with 0.7 second per point sampling time. Between each denaturation experiment, a sample of buffer was loaded and spectrum taken that could be used as a baseline for the subsequent sample spectra. All thermal data analysis was carried out by the Applied Photophysics' Global 3 analysis package.

3.5 Results

3.5.1 Interactions between IGFBP-5 and FIII9'10-GGC mutants

The 4 serial flow cells of the SA-chips allowed for biotinylated BSA to be used as a direct comparison to FIII9'10-GGC, FIII9'10-GGC I2A and FIII9'10-GGC E2A for analyte binding. Any non-specific binding that may occur at the sensor chip surface could be compensated for by subtracting the response unit (R.U.) of the BSA. The immobilisation of the biotinylated proteins on the SA chips had a density of 859-5534 R.U.s for chip 1 and 728-1087 R.U.s for chip 2.

The SPR sensogram data shown in Figure 3-4 is the product of the response for the FIII9'10-GGC ligands minus the response for the BSA control. The FIII9'10-GGC E2A (blue line) mutant had a higher immobilisation onto the SA-chip 1 surface (5534 R.U.) giving an increased baseline compared to FIII9'10-GGC (red line) and

FIII9'10-GGC I2A (yellow line) (Figure 3-4). The spikes between 500-600 s corresponded to the start and end of injection of IGFBP-5 over the surface area of the SA-chip. Following injection of the IGFBP-5 the sensogram returns to the baseline, indicating no binding. The BSA negative control showed higher non-specific binding with IGFBP-5 than FIII9'10-GGC and its derivatives. Therefore the resultant response was negative for FIII9'10-GGC and FIII9'10-GGC I2A, the higher immobilisation of FIII9'10-GGC E2A gave an increased baseline, consequently, after subtraction of BSA the sensogram for this had a positive value.

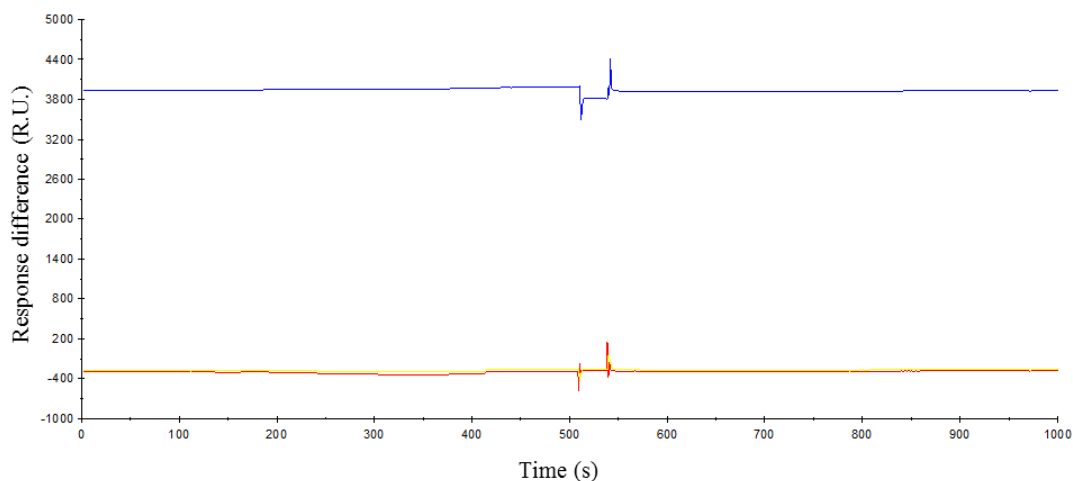


Figure 3-4 Binding of IGFBP-5 to immobilised FIII9'10-GGC (red line), FIII9'10-GGC I2A (yellow line) and FIII9'10-GGC E2A (blue line).

Following the initial attempt, a fresh protein immobilised SA chip was formulated. This also showed no interaction between FIII9'10-GGC and IGFBP-5 (Figure 3-5). The SA chip was regenerated and IGF-1 was injected into the system to see if it would elicit a response. The results were similar to the previous run and indicated that there was no interaction. The binding ability of the FIII9'10-GGC proteins was

tested using integrin $\alpha 2\beta 1$, which showed binding (Figure 3-6 and Table 3-1) indicated by the steady increase in R.U. value for the duration of the injection. The integrin bound to the proteins; however, it could not be readily removed by regeneration buffer.

The binding of FIII9'10-GGC to IGFBP-5, as seen by Beattie and colleagues (2009) could not be replicated. Due to the inability to replicate IGFBP-5/FIII9'10-GGC binding, this work was aborted.

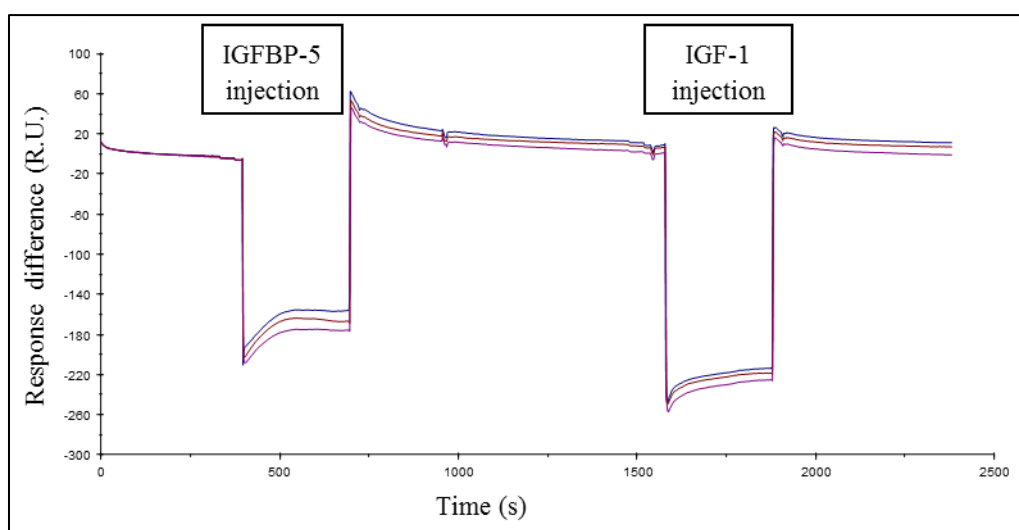


Figure 3-5 SPR binding spectra of IGFBP-5 and IGF-1 to immobilised FIII9'10-GGC (blue), FIII9'10-GGC I2A (purple) and FIII9'10-GGC E2A (red).

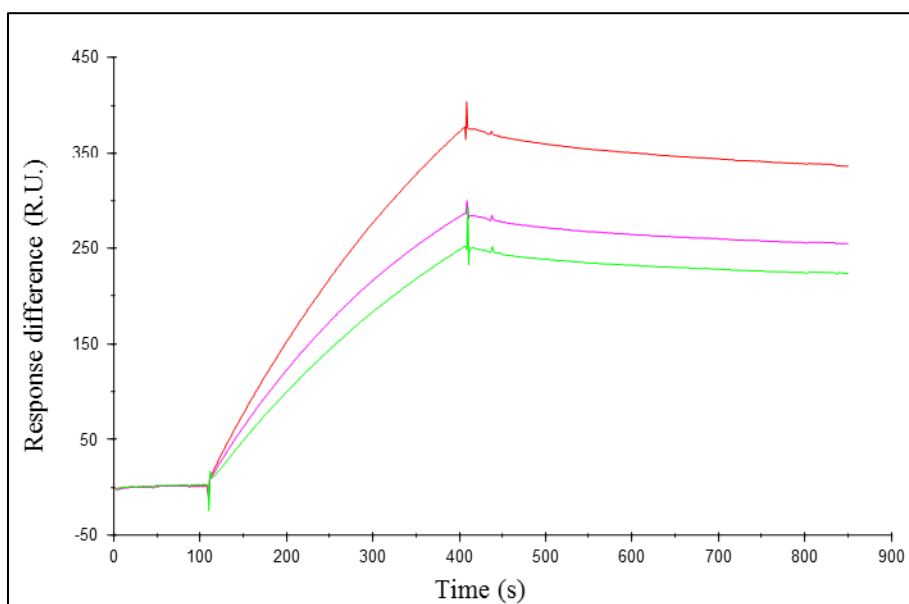


Figure 3-6 SPR binding spectra of integrin $\alpha 2\beta 1$ to immobilised FIII9'10-GGC (orange), FIII9'10-GGC I2A (green) and FIII9'10-GGC E2A (pink).

Table 3-1 SPR response for binding of integrin $\alpha 2\beta 1$ to FIII9'10-GGC mutants.

Protein	Baseline (R.U.)	Response (R.U.)	Total (R.U.)
FIII9'10-GGC	253	628	357
FIII9'10-GGC E2A	-176	107	283
FIII9'10-GGC I2A	-260	-11	249

3.5.2 Equilibrium chemical denaturation measured by fluorescence

The fluorescence was measured at 350 nm ± 2 nm and the average taken, the data was normalised and the percentage maximum fluorescence plotted against GdmCl concentration (Figure 3-7). For each of the FIII9-10 proteins a two-step unfolding curve was observed with the initial step representing unfolding of the 9th domain and the second step corresponding to the 10th domain. These results were consistent with

CHAPTER 3. Biophysical and functional characteristics of FIII9-10 mutants

previous findings (Spitzfaden et al. 1997) (Figure 3-7). From 0 M to around 4 M the increase in fluorescence was caused by unfolding of domain FIII9 and the exposure of the Typ residue within. Increasing the GdmCl concentration above 4 M initiates the further unfolding of domain 10.

The FIII9-10 protein unfolded rapidly under lower denaturant conditions than the mutated proteins, conversely FIII9''10 H2P did not begin to unfold until GdmCl reached around 2 M. The unfolding of FIII9''10 T2P followed the FIII9'10 very closely but began unfolding at slightly lower GdmCl concentrations than FIII9'10. From 5 M to 8 M GdmCl all of the proteins exhibited a similar increase in fluorescence representing the unfolding of domain FIII10. The values obtained from linear regression analysis of the slope and y-axis intercept of the corresponding unfolding domain are shown in Table 3-2. The FIII9''10 H2P mutant displayed an increased Gibbs free energy for domain FIII9, nearly double that of FIII9-10, and a substantial increase compared to the FIII9'10. The FIII9''10 T2P mutant showed a decrease in Gibbs free energy compared to FIII9'10 in domain FIII9 but a slight increase in domain FIII10. All of the mutants were found to have an increased Gibbs free energy in the 10th FIII domain compared to the wild type. Due to the findings of decreased conformational stability of the FIII9''10 T2P mutant work with FIII9''10 T2P was discontinued. For all other stability testing, the FIII9''10 H2P mutant was compared to its predecessor FIII9'10 and the wild type FIII9-10.

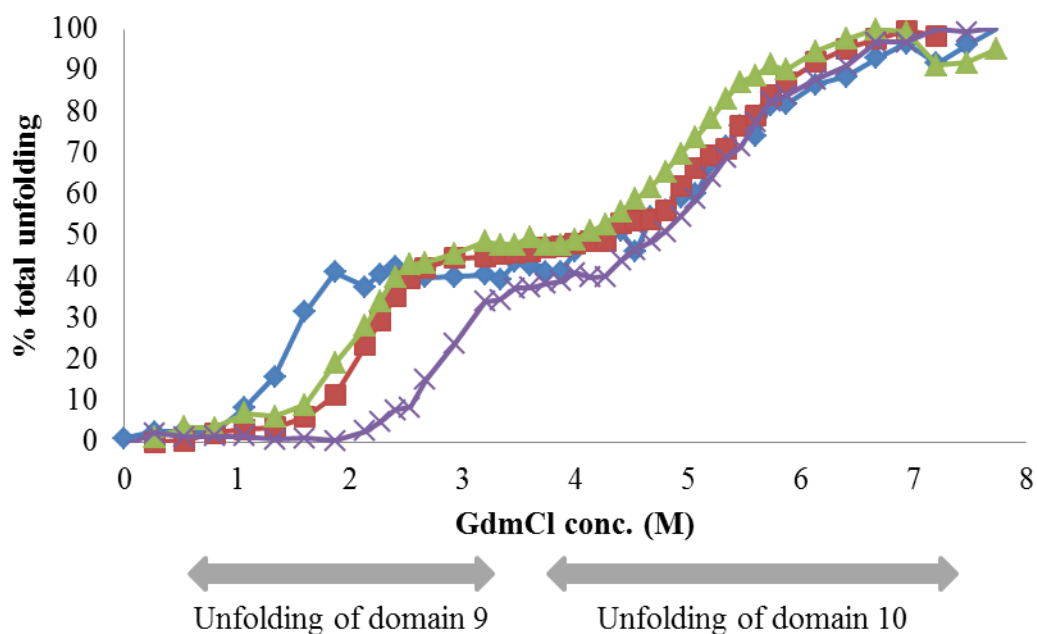


Figure 3-7 Chemical equilibrium denaturation using GdmCl of FIII9-10 (blue) and mutants FIII9'10 (red), FIII9''10 T2P (green) and FIII9''10 H2P (purple). The step-wise unfolding of each domain is indicated.

Table 3-2 Equilibrium chemical denaturation of FIII9-10 and mutants.

FIII domain	[GdmCl]_{1/2} (M)	<i>m</i> (kcal/mol/M)	ΔG_{H_2O} (kcal/mol)
FIII9'	2.15	3.41	7.33
H2P FIII9''	2.85	3.23	9.20
T2P FIII9''	2.01	2.99	6.03
Wild type FIII9	1.46	3.77	5.51
FIII10	5.36	1.86	10.00
H2P FIII10	5.41	2.04	11.03
T2P FIII10	5.06	2.07	10.45
Wild type FIII10	5.42	1.79	9.71

3.5.3 Automated circular dichroism data

3.5.3.1 *Thermally induced unfolding of FIII9-10 proteins*

Scans were obtained in 1 °C increments for each temperature from 20-95 °C, however only a representative selection are shown on the figure ranging from 35-85 °C in 10 °C increments with 5 °C either side of the calculated T_m (Figure 3-8). As the temperature increased, the CD spectra showed a gradual loss of structure with the loss of the positive bands around 202 and 222 nm and an increase in the negative maxima. The thermal denaturation of the mutated proteins showed that they were able to retain their structure at a greater temperature (up until around 60 °C) compared to the FIII9-10 which started losing structure at around 50 °C. The T_m for the proteins calculated as an average from three scans was found to be 47.8 °C (± 0.12) for FIII9-10, 56.9 °C (± 0.29) for FIII9'10 and 59.5 °C (± 0.26) for FIII9''10 H2P. The mutated proteins showed a marked increase in T_m compared to the wild type, a 9.1°C increase for the FIII9'10 mutant and 11.7 °C for the FIII9''10 H2P mutant. The data fitted a single transition model with high reproducibility.

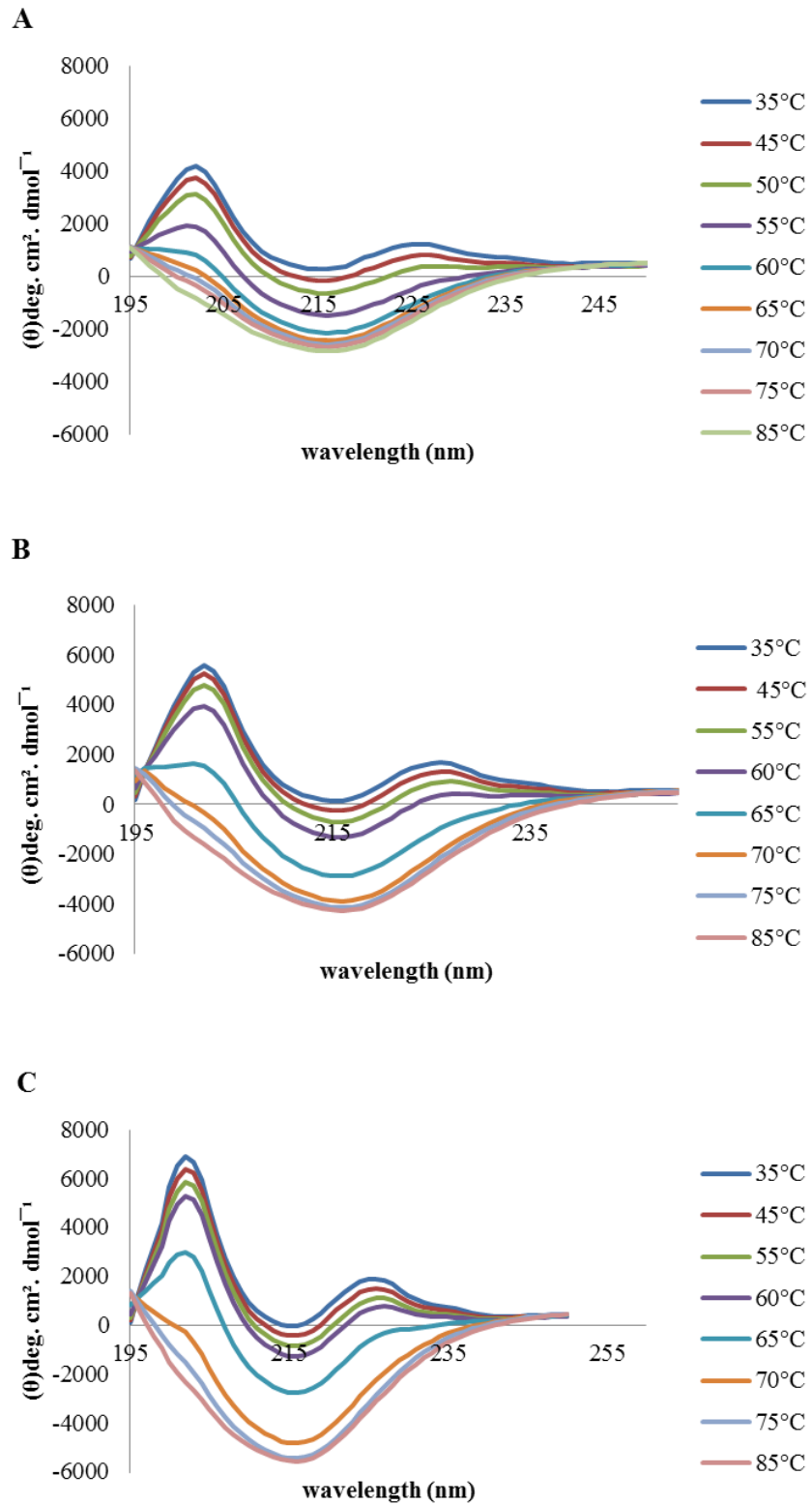


Figure 3-8 Far UV CD spectra of thermal denaturation for FIII9-10 protein fragments, FIII9-10 (A), FIII9'10 (B) and FIII9''10 H2P (C). Change in spectra indicates unfolding occurs at a temperature of above 55-60 °C.

CHAPTER 3. Biophysical and functional characteristics of FIII9-10 mutants

The increased T_m of the mutant FIII9-10 variants was clearly shown by comparing the percentage of folded and unfolded protein in solution over the temperature range (Figure 3-9, right pane). The folded and unfolded CD spectrum of the three proteins and the repeats (Figure 3-9, left pane) showed a loss of β -sheet structure as the temperature increased.

Table 3-3 Calculated transition values from temperature unfolding of FIII9-10 domain pairs.

Domain pair	van't Hoff enthalpy (kJ/mol) (average)	T_m (average)
FIII9-10	298.067	47.833
FIII9'10	418.4	56.967
FIII9''10 H2P	444.433	59.5

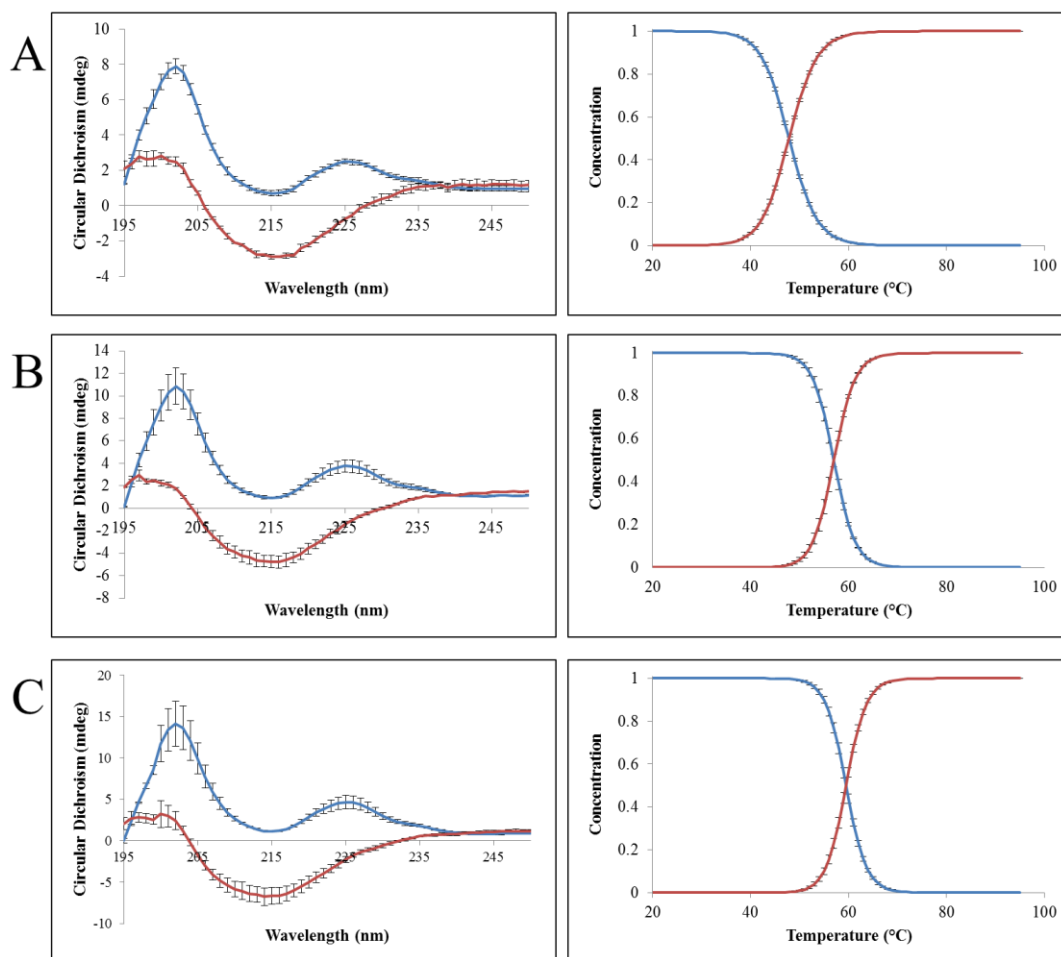


Figure 3-9 Global analysis of CD spectra data for thermal denaturing of proteins FIII9-10 (A) FIII9'10 (B) and FIII9''10 H2P (C) showing average folded species (blue) and unfolded species (red). Left pane shows comparison of the different spectral shapes. Right pane shows concentration profile comparing the different species at 20 to 100 °C. Error bars represent the standard deviation of the mean of three runs.

3.5.3.2 FIII9-10 protein conformation as a function of pH

Changes in protein conformation of FIII9-10, FIII9'10 and FIII9''10 H2P were tracked using CD for a range of pH values from pH 2.2 - 7.8. There was a slight change observed when altering the pH, however this was minimal over all three proteins (Figure 3-10). The main observed difference in spectra was found to be that

as the pH increased the positive maxima (202 nm) decreased by around 2000 $^{\circ}\text{cm}^2.\text{dmol}^{-1}$.

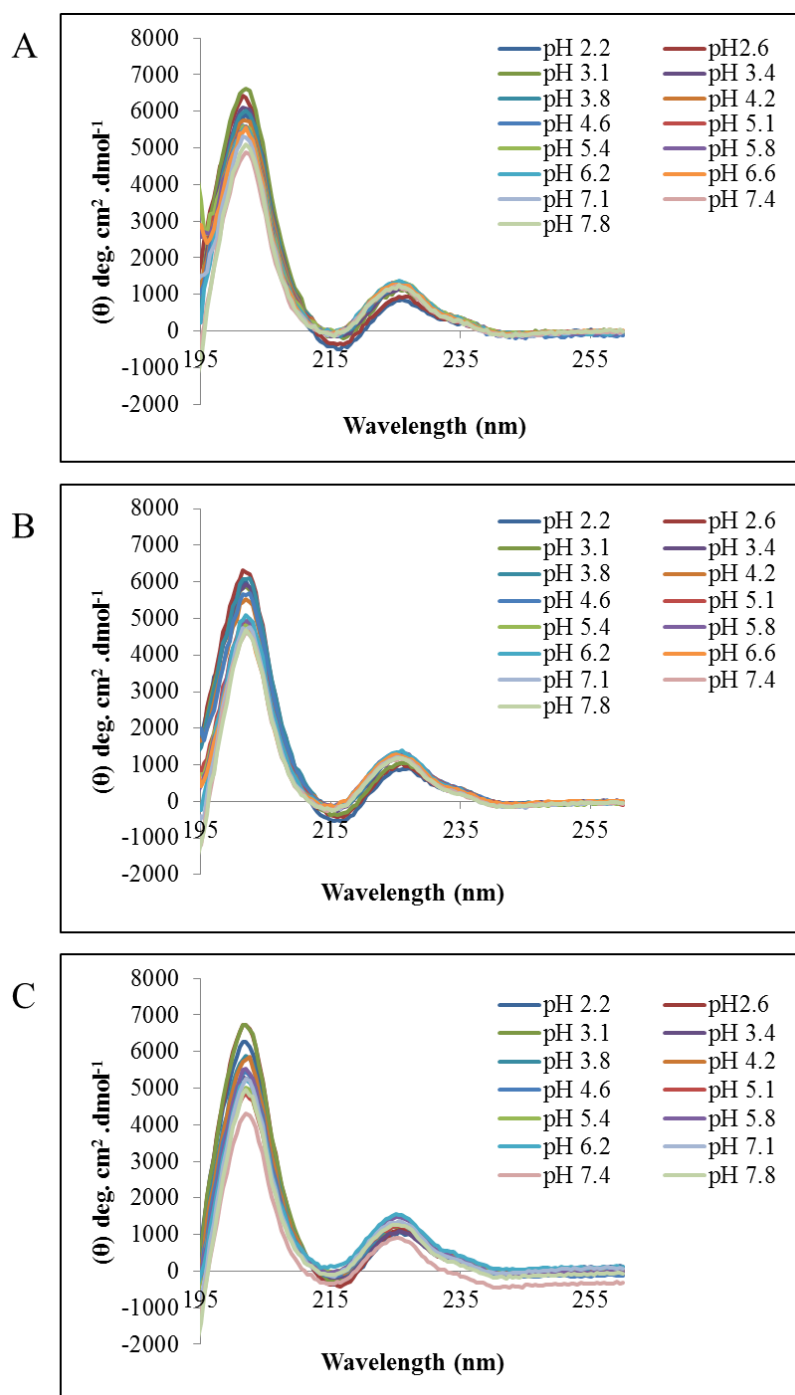


Figure 3-10 Far UV CD spectrum of FIII9-10 (A), FIII9'10 (B) and FIII9''10 H2P (C) following incubation in buffer with varying pH.

3.5.3.3 *Equilibrium chemical denaturation measured by circular dichroism*

Changes in protein conformation of FIII9-10, FIII9'10 and FIII9''10 H2P were tracked using CD for a range of GdmCl concentrations from 0 M to around 6M. The FIII9''10 H2P mutant retained its structure at a higher GdmCl concentration than both the FIII9-10 and FIII9'10, shown in Figure 3-11. For each of the proteins there were three species present in the unfolding, species 1, corresponding to the folded domain pair, species 2 corresponding to one domain unfolding and species 3 corresponding to the second domain unfolding (Figure 3-11).

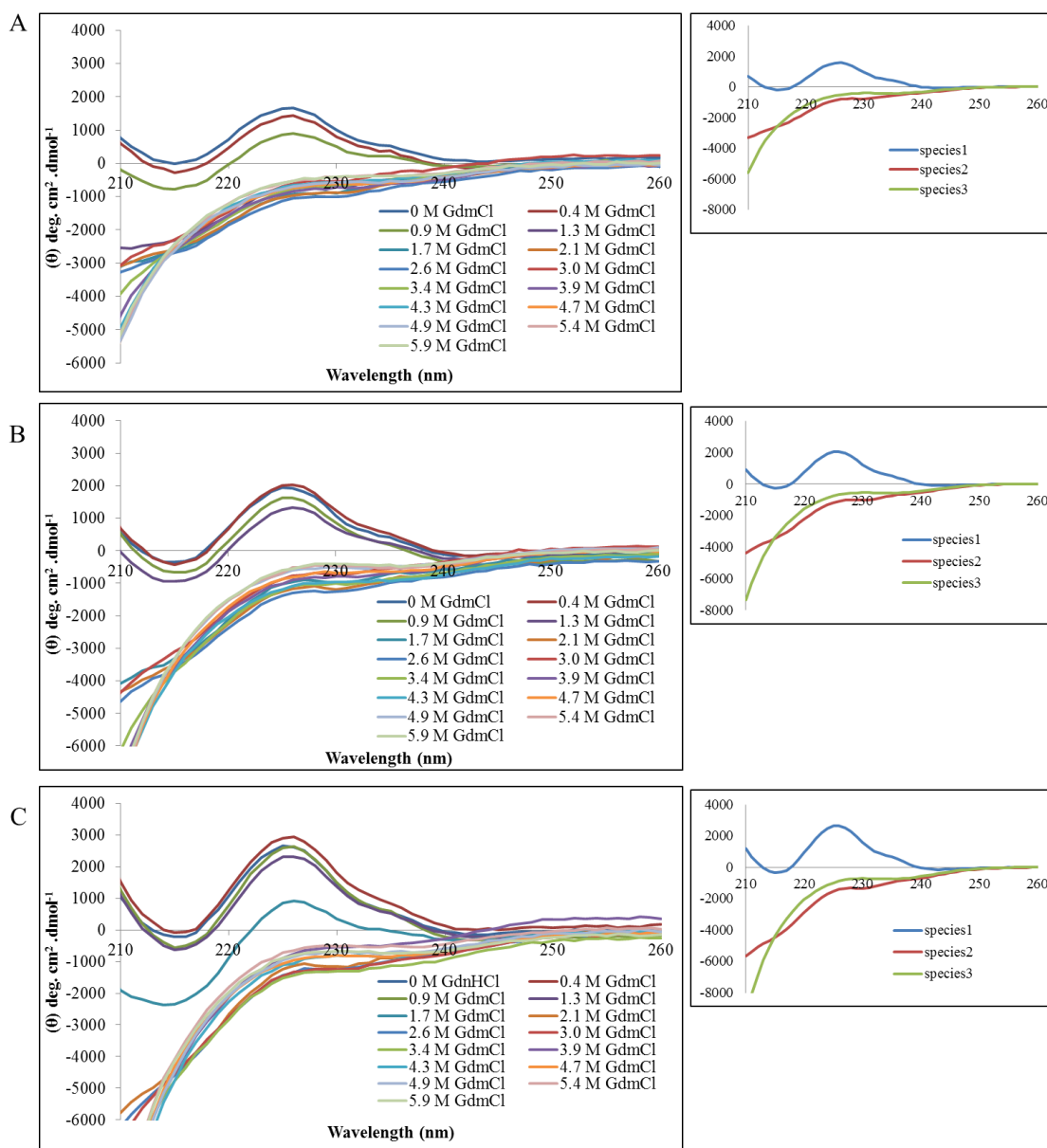


Figure 3-11 Far UV CD of FIII9-10 (A), FIII9'10 (B) and FIII9''10 H2P (C) following incubation with varying concentrations of GdmCl in 10 mM NaH_2PO_4 , 50 mM NaCl, pH 6.0 buffer. Inset shows unfolding of protein indicating different species 1 (blue), 2 (red) and species 3 (green).

3.6 Discussion

3.6.1 Surface Plasmon resonance

The lack of success with SPR analysis was disappointing as the cause could not be determined, each of the different components were checked further in order to ascertain the source of the error. A new batch of IGFBP-5 was tried but produced the same result. Insulin, FIII9'10-GGC and IGF-1 were coated onto a fresh chip and subjected to a flow of IGFBP-5 to test the SA-chip and the IGFBP-5 further, which confirmed they were both satisfactory. It was deduced that the problem must lie with the biotinylated samples. Therefore fresh samples were prepared and immobilised on a new SA-chip, however, the results were the same. The positive control FIII9'10-GGC was from a stock supply and may therefore have degraded over time, however, the positive result for binding of integrin $\alpha 2\beta 1$ indicated that it still retained some functionality. The lack of binding in FIII9'10-GGC I2A and FIII9'10-GGC E2A may have been a result of the point mutations, but as there was no positive control to compare the findings with the results are inconsequential.

The successful binding to the integrin $\alpha 2\beta 1$ demonstrates that the FIII9'10-GGC domain pairs show some activity. The inability to detach the $\alpha 2\beta 1$ from the immobilised proteins may be a cause for concern. This would not normally be a problem, as one of the advantages of SPR analysis is the ability to re-use protein immobilised SA chips for a range of binding molecules.

There is a possibility that the findings of Beattie and co-workers (2009) are not reproducible, at least under the current conditions. There still could be a fundamental problem with the FIII9'10-GGC proteins, possibly occurring during biotinylation or

transport and storage. The findings are therefore inconclusive and this work was discontinued.

3.6.2 Unfolding by GdmCl denaturant

In order to investigate the effects on stability of the point mutations FIII9''10 T2P and FIII9''10 H2P the denaturant unfolding was compared to the FIII9'10 template and to the native wild type FIII9-10. The results were consistent with previous work (Spitzfaden et al. 1997) which demonstrated a two stage unfolding mechanism in which the initial step represents the unfolding of domain FIII9 and the second step the unfolding of domain FIII10. Analysis with GdmCl unfolding showed the mutation of His¹³⁷⁷ to Pro yielded a protein with significantly increased conformational stability compared to wild type and FIII9'10 variants.

The mutation of Thu¹³⁵³ to Pro did show improved stability compared to the wild type, but the increase in stability was not as great as that for mutation of FIII9 to FIII9'. Domain FIII10 is known to be relatively stable (Plaxco et al. 1997), the increase in free energy for FIII10 of the T2P mutant was small compared to FIII10 from FIII9'10. There was also a loss in stability for domain FIII9 in FIII9''10 T2P compared to the template protein FIII9'10. The clear increase in stability of both FIII9 and FIII10 in the FIII9''10 H2P made a viable candidate for further testing.

Overall the FIII10 was considerably more stable than the FIII9 in all FIII9-10 mutants, which agreed with work done previously (Plaxco et al. 1997). The values obtained by linear extrapolation differed from those obtained by van der Walle and

co-workers (2002) for the same FIII9'10 construct. The values obtained for m and $[GdmCl]_{1/2}$ (M) were comparable but ΔG_{H_2O} was found to be lower for FIII9', 7.33 kcal/mol compared to 9.20 kcal/mol. Furthermore the values corresponding to the FIII10 were very different, with a decreased ΔG_{H_2O} and m indicating that although the conformational stability had decreased, the effect of denaturant had also decreased. There are many possible explanations as to why there was such disparity between the results. First, the experimental method differed slightly in that the GdmCl solution was constituted in 20mM NaOAc, pH 4.8, compared to 10mM NaH_2PO_4 , 50mM NaCl pH 6.0 used here. Secondly, this could be from error associated with the linear extrapolation of ΔG_{H_2O} back to zero concentration of GdmCl. The error associated with linear extrapolation of values is a disadvantage of this method, as it may not allow for direct comparison between different groups data.

3.6.3 Extended circular dichroism analysis

The use of the auto sampler allowed for a great number of samples to be analysed in a short time, producing a significant volume of data. By assessing the structure at various pH points it was shown that the protein appears to be stable over a wide range. This would be beneficial as it may be able to be used at the various pHs. The mutation of His¹³⁷⁷ to Pro showed spectra which were more overlapping and closer together, suggesting less change in shape than for the other two proteins.

The temperature unfolding analysis confirmed that the addition of the mutation of His¹³⁷⁷ Pro increased stability, shown by the increased T_m . The application of CD to

determine T_m may be a useful alternative to differential scanning calorimetry (DSC) as the structural changes can be followed by the CD spectra. The findings here are similar to that of Pereira and co-workers (2007). However their use of DSC found the T_m of FIII9'10 to be around 59.7 °C, which is higher than our findings. The thermal unfolding supports the increased conformational stability from the chemical unfolding data. Using the CD spectra we were able to map the changes in secondary structure of the proteins. There was a rapid loss of secondary structure as the temperature reached the T_m values for all of the proteins. Unlike the chemical unfolding, there was a single transition for the thermal unfolding. The diminished contributions from aromatic contributions at the peak around 226 nm suggests that the environment is less rigid (Pereira et al. 2007). The CD spectrophotometer also measures absorbance from which protein aggregation data can be deduced, this confirmed that all of the proteins aggregated to a similar extent after unfolding. The unfolding by GdmCl measured by CD supports our prior findings that the mutation of His¹³⁷⁷ to Pro increased conformational stability. The ability to visualise the change in structure using the CD spectrum is a great advantage. The structural forms that the proteins take suggest the unfolding of the different domains, further supporting the findings that FIII10 unfolds in a distinct step subsequent to FIII9 unfolding.

3.7 Summary

The FIII9'10-GGC mutants FIII9'10-GGC I2A and FIII9'10-GGC E2A were analysed by SPR and the results of Beattie and co-workers (2009) could not be repeated. We could not show binding of FIII9'10-GGC to IGFBP-5 and therefore

CHAPTER 3. Biophysical and functional characteristics of FIII9-10 mutants

this work was halted. Extensive analysis of FIII9''10 H2P and FIII9''10 T2P showed that the FIII9''10 H2P variant had increased stability in a number of conditions including GdmCl chemical induced unfolding and thermal induced unfolding. Therefore work with this protein was continued to assess its usefulness as a support scaffold for cells. The next chapter concentrates on protein surface interactions with solid substrates.

CHAPTER 4. Surface adsorption and biological activity of FIII9-10 mutants

4.1 Introduction

The extracellular matrix presents a complex mixture of ligands, some of which will be responsible for adhesion whereas others are important for signalling, although these may not be mutually exclusive phenomena. In the previous chapter, we described the substitution of histidine to proline in the PHSRN region of the FN fragment (FIII9''10 H2P) which resulted in an increased stability in solution. As described by van der Walle and colleagues (2002), substitution by proline at point Leu 1408 produced FIII9'10 variant which displayed improved cell adhesion and spreading by around ~25 % and ~50 %, compared to wild type (van der Walle et al. 2002). The adsorption of both full length and FN fragments onto solid supports as a means of improving cell attachment is an area of substantial interest. In the studies described in this chapter, the available fibronectin-based variants, specifically the wild type and the two mutants FIII9'10 and FIII9''10 H2P, described in Chapter 3, provide an opportunity to examine the impact of enhanced structural stability on surface attachment.

Eisenberg and colleagues have studied the role of RGD and PHSRN in cell adhesion by the use of Au/Ti treated glass coverslips coated with phosphonate ligands, to covalently immobilise variants of FIII 9th and 10th domain fragments which appear to cooperatively enhance cell adhesion and spreading (Eisenberg et al. 2009). Thus

supporting the concept that the adsorption of a ligand onto a suitable surface can provide a scaffold for cell adhesion onto a solid support.

The surface properties of the support may have an influence on the behaviour of the proteins adsorbed to them. Toworfe and colleagues determined that surface hydrophobicity of the synthetic support altered the density of adsorbed whole-length fluorescent-labelled fibronectin (Toworfe et al. 2004). The change in density was estimated from surface roughness revealed in the AFM images. This could effectively alter the orientations of the protein which could reduce the area available to interact with the cell ligands. Surface wettability of the support influences the organisation of both soluble and adsorbed fibronectin (Tzoneva et al. 2002). Furthermore, interacting with hydrophobic surfaces may result in completely irreversible conformational changes within the protein (MacDonald et al. 2002).

Garcia and colleagues reviewed the adsorption of full length fibronectin onto various treated polystyrene surfaces and the subsequent effect on integrin binding of myoblast C2C12 cells (Garcia et al. 1999). The production of variants containing differences surrounding the RGD motif allowed an aspect of the structural component on surface association to be examined.

This chapter concentrates on the ‘successful’ protein mutant FIII9’10 H2P (as described in previous chapters) and investigates the difference in surface stability compared to FIII9’10 and FIII9-10. The remainder of the chapter concerns the assessment of the biological activity of FIII9’10 H2P including ELISA with $\alpha 5\beta 1$ adhesion assay on plastic and fluorescent microscopy images of BHK cells on protein coated titania surfaces.

4.2 Materials

Unless otherwise stated, all general chemical reagents were sourced from Sigma-Aldrich (Dorset, UK), or Fisher Scientific (Leicestershire, UK) or Melford Laboratories (Ipswich, UK), at analytical grade or equivalent quality. Integrin $\alpha 5\beta 1$ was purchased from Sino Biological Inc. (cat. no. CT014-H2508H; Beijing, China). Silica beads (227196) pore size 60 Å, particle size 230-400 mesh, 43-60 µm, and silanes: trichlorooctylsilane (TCOS), (3-aminopropyl)trimethoxysilane (APTMS), 1H, 1H, 2H, 2H-perfluorooctyltriethoxysilane (PFTOS), were purchased from Sigma-Aldrich. Methoxy-polyethylene glycol-silane (mPEG-silane; 1000 MW PEG group) was purchased from Creative PEGWorks (Winston Salem, USA). IPG buffer pH 6-11 (71-5005-82), Immobiline DryStrip pH 6-9 (17-6001-88), High range pI (pH 5-10.5) calibration kit (17-0473-01) and Immobiline DryStrip cover fluid (17-1335-01) were purchased from GE-Healthcare UK Ltd (Buckinghamshire, UK). Anti-HisG-HRP antibody and cell culture medium Dulbecco's Modified Eagle Medium (DMEM, high glucose, GlutaMAX, 61965026) was purchased from Invitrogen (Paisley, UK). Baby hamster kidney (BHK) cell line BHK-21 (C-13) was purchased from American Type Culture Collection (Virginia, USA). Texas Red conjugated anti mouse antibody (ab6726) was obtained from Abcam (Cambridge, UK), anti-vinculin antibody (V9131) and fluorescein-phalloidin (P5282) were both purchased from Sigma-Aldrich. TiO₂ plated borosilicate glass coverslips were produced by Helia Photonics (Livingston, UK). Bradford Reagent (B6916) was purchased from Sigma-Aldrich. Water was purified to > 14 MΩ.cm with a BioSelect, Purite, UK.

4.3 Buffers and reagents

Phosphate buffered saline (PBS) 0.01 M was prepared from tablets (Sigma, P4417): one tablet dissolved in 200 ml deionized water then autoclaved at 120 °C, contains 0.0027 M KCl and 0.137 M NaCl, pH 7.4.

Phosphate buffer was prepared from 10 mM NaH₂PO₄, 50 mM NaCl, adjusted to pH 6.0 with 1 M NaOH/HCl.

Piranha solution was prepared by mixing a 3:1 ratio of sulphuric acid to hydrogen peroxide.

Quenching solution: 3 % (v/v) acetic acid, 47 % (v/v) methanol and 50 % (v/v) H₂O

Isoelectric focusing (IEF) Rehydration solution: 2 % (v/v) Triton x-100, 0.5 % IPG buffer pH 6-11, 30 % (w/v) DTT and 0.0002% (w/v) of bromophenol blue.

IEF Sample solution: 0.5 % (v/v) Triton x-100, 0.5 % (v/v) IPG buffer (6-9) 0.2 % (w/v) DTT and 0.0002% (w/v) bromophenol blue.

IEF Fixing solution: 10 % (w/v) trichloroacetic acid in H₂O.

IEF Equilibration solution: 25 % (v/v) methanol, 5 % (v/v) acetic acid, 70 % (v/v) H₂O.

IEF Gel stain: 1 % (w/v) coomassie blue G-250 dissolved in 25 % (v/v) methanol, 5 % (v/v) acetic acid and 70 % (v/v) H₂O.

IEF Preservation solution: 5 % glycerol, 25 % methanol, 70 % H₂O.

ELISA buffer (EB): 25 mM Tris-HCl, pH 7.4, 150 mM NaCl, 1 mM MgCl₂, 0.1 mM CaCl₂.

CHAPTER 4. Surface adsorption and biological activity of FIII9-10 mutants

ELISA Blocking solution: 5 % BSA, 25 mM Tris-HCl, pH 7.4, 150 mM NaCl, 1 mM MgCl₂, 0.1 mM CaCl₂.

Anti-HisG-HRP antibody prepared in: 1:2000 dilution in 25 mM Tris-HCl, pH 7.4, 150 mM NaCl, 1 mM MgCl₂, 0.1 mM CaCl₂.

Cell culture medium: DMEM plus glutamax and 10 % (v/v) foetal bovine serum (FBS).

Cell culture blocking solution: 5 % (w/v) BSA in PBS.

Cell culture fixing solution for plasticware: 4 % (v/v) glutaraldehyde, 4 % (v/v) formaldehyde and 92 % (v/v) PBS.

Cell culture fixing solution for TiO₂ substrates: 3 % (v/v) paraformaldehyde (PFA) and 97 % (v/v) PBS.

Cell culture permeabilization solution: 10 mM Hepes, pH 7.4, 200 mM sucrose, 3 mM MgCl₂, 50 mM NaCl, 0.5 % Triton X-100.

Anti-vinculin antibody prepared as: 1:400 dilution in PBS containing 0.1 % (w/v) BSA.

Texas red prepared as: 1:100 (0.02 mg/ml) dilution in PBS containing 0.1 % (w/v) BSA.

Fluorescein-phalloidin prepared as: 1:20 (25 µg/ml) dilution in PBS containing 0.1 % (w/v) BSA.

4.4 Methods

4.4.1 Probing protein adsorption onto surfaces

The properties of a protein adsorbed to a surface can be radically affected by single site mutations resulting in a change in conformation; relaxation and partial desorption; reorientation and alignment (Kreiner et al. 2009b). Our strategy was to create surfaces with a range of hydrophobicities by using different organosilane molecules with varying chemical compositions to determine if the surface free energy and thus wettability will have an influence on the conformation of our protein fragments.

4.4.1.1 *Creating surfaces of varying wettability*

To create surfaces of varying hydrophobic properties, bare borosilicate glass coverslips were functionalised by silanization (generating a covalent -Si-O-Si- bond) with trichlorooctylsilane (TCOS), (3-aminopropyl)trimethoxysilane (APTMS), 1H,1H,2H,2H-perfluorooctyltriethoxysilane (PFTOS), and methoxy-polyethylene glycol-silane (mPEG-silane). Bare glass cover slips were cleaned using “piranha solution” (3:1 concentrated sulphuric acid: hydrogen peroxide) and rinsed with deionized water before being dried under nitrogen. The cover slips were then immersed in 1 mM solutions of each of the silanes in anhydrous toluene overnight at room temperature. Following incubation they were rinsed three times in toluene then *N, N*-dimethylformamide (DMF) and finally deionised water. To aid washing, the

slides were sonicated gently for 20 min at each step (Lamprou et al. 2010). Finally they were dried under nitrogen and stored in sealed vials until required.

4.4.1.2 Measurement of surface wettability

Measuring the contact angle of a liquid droplet of known properties on a solid surface can give useful information relating to the surface energy, tension and hydrophobic/hydrophilic nature (Giovambattista et al. 2007). The point of measurement of interest is where the three phase boundary in which a liquid, gas and solid intersect (Figure 4-1), this represents the balancing of the adhesive forces between the liquid and solid and the cohesive forces within the liquid (Amirfazli and Neumann 2004). To measure this angle, drop shape analysis can be used, assuming that the drop is symmetrical about the vertical axis and the drop is not in motion. The instrumentation consists of a video camera connected to a computer with image analysis software that allows for an accurate determination of contact angle θ . A sessile drop method is commonly used in which a small droplet of liquid is deposited onto the horizontal substrate surface using a very fine, vertically orientated syringe. A high resolution image is then captured of the droplet on the surface and the contact angle calculated from this.

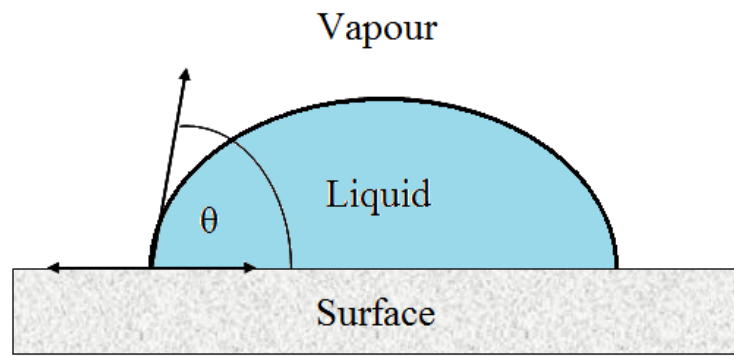


Figure 4-1 Contact angle (θ) of energies and forces at the interface of a solid surface, a liquid and a vapour.

The surface hydrophobicity of the silanized substrates was assessed by contact angle measurements of water-on-solid. The angle of a tangent drawn at the boundary between the liquid droplet in contact with the solid surface is known as contact angle goniometry (CAG). Examples of typical droplet formation are shown in Figure 4-2, a flattened more spread out drop is typical of water on a hydrophilic surface and a more spherical drop is characteristic of a hydrophobic surface.

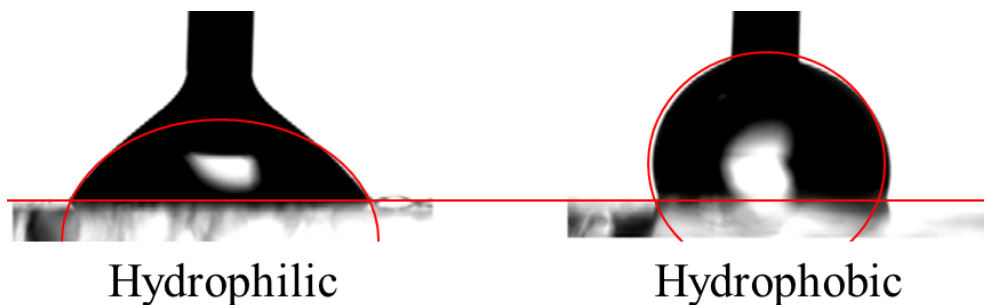


Figure 4-2 Photograph of filtered water being deposited on to hydrophilic and hydrophobic surface. Different contact angles are created and highlighted in red

The static contact angles were measured using a Krüss DSA30B contact angle goniometer (Hamburg, Germany). Small drops of deionized water were placed on horizontal glass substrates (microscope slides either bare or silanized as above) and a high resolution image captured. The 'left' and 'right' contact angles were taken after placement of the drop, five drops per substrate were measured and two individual substrates prepared for each surface. Contact angle measurements were also taken for tissue culture plasticware, surface samples were carefully cut from a 6-well culture plate of the same specifications as that used for tissue culture and the water contact angle measured as before.

4.4.1.3 Conformation of proteins on surfaces measured by CD

As discussed in the previous two chapters, CD can be utilised to ascertain structural information relating to proteins in solution. Ganesan and colleagues (2006) developed a system which could capture the changes in spectra shape and magnitude of a Carlsberg protease immobilised onto silica particles (40-63 μm) (Ganesan et al. 2006). Particle sedimentation, differential light scattering and absorption flattening are the three major areas which can be problematic for the application of CD to proteins adsorbed on to solid supports (Ganesan et al. 2006).

Any solid in the sample would sediment at a rate faster than the measurement time (20-50 min), meaning that over time the light path would be reduced, resulting in a distorted spectrum. To minimise the effects of particle sedimentation a custom-built rotating cylindrical cell holder (Figure 4-3) was developed at the University of Strathclyde, based on the system first introduced by Ganesan and co-workers (2006).

The rotating device consisted of a circular cell holder which contained the sample cell and motor which controlled rotating by a regulator with a variable input voltage.



Figure 4-3 Photograph of the motorised rotating cell holder (left), developed at the University of Strathclyde and standard circular cell holder (right). Both are shown containing circular cells, the stoppers used for the rotating cell were modified to allow for free movement.

Differential light scattering occurs when the left and right circularly polarised light is scattered with different efficiency upon interaction with the chiral particles. This can distort the spectra and reduce the apparent ellipticity. The effects of differential light scattering can be minimised by maximising the photon collection efficiency (Ganesan et al. 2006). In these experiments this was accomplished by placing the sample as close to the detector as possible and thus increasing the solid angle of detection (Ganesan et al. 2012).

Finally, spectra had to be corrected for absorption flattening. A heterogeneous distribution of the chromophores in the light path is caused by the protein being held

onto the surface of the particles, the light beam therefore would pass through areas of the sample unabsorbed. Because of this, the spectra are flattened in the region where the chromophore absorbs relative to a homogeneous distribution of protein in solution. To compensate, a semi-empirical correction was developed by Ganesan and colleagues (Ganesan et al. 2006).

The extent of absorption flattening is proportional to the absorbance (A) at a given wavelength. The spectrum of the suspension was adjusted by using the absorbance and mean residual molar ellipticity of the protein solution spectra for a specified point (between 195-197 nm for far UV and at 275 nm for near UV). The observed ellipticity (θ_{obs}) of the CD spectra in suspension was multiplied by Q which was calculated based upon the difference between the spectra for the protein in solution and adsorbed to a solid surface. This was based on the principle that it is proportional to the absorbance of θ_{obs} multiplied by a factor of $1/(1-Q)$ (Ganesan et al. 2006). The value of Q at a given wavelength is derived from the factor (x) required to multiply the uncorrected suspension data so the ellipticity at this wavelength is equal to the solution data at the same wavelength.

Where Q_{λ} is the absorption flattening at a given wavelength which can be calculated as follows:

$$Q_{\lambda} = x \left(\frac{A_{\lambda}}{A_{nm}} \right)$$

Equation 4-1

The value for x was calculated for each individual spectrum by dividing the ellipticity of the solution spectra at an optimised wavelength (A_{nm}) by the corresponding θ_{obs} of the suspension spectra.

The corrected ellipticity (θ_{corr}) was calculated using the following equation based on the observed ellipticity (θ_{obs}):

$$\theta_{corr} = \theta_{obs} \left(\frac{1}{1 - Q_{\lambda}} \right)$$

Equation 4-2

4.4.1.4 Sample preparation

Silica beads of varying hydrophobicity were prepared by the method used to coat the glass slides as described in section 4.4.1.1. To adsorb the protein to the bare and surface functionalised silica beads, a solution of protein, concentration of 1 mg/ml for far UV and 2 mg/ml for near UV, was added to 0.1 g of dried silica beads (bare or silane coated). The bead suspension was mixed by vortexing briefly and then rotated gently overnight at room temperature to ensure a complete protein adsorption. The suspensions were then centrifuged at $\sim 10,000$ g for 5 min and the beads then washed with 1 ml distilled water to remove any unadsorbed protein, this was repeated at least 3 times. UV absorbance of the supernatant washings showed complete absorbance of the protein to the 0.1 g of silica.

4.4.1.5 Measuring CD

CD spectra were recorded in the far (180-260 nm) and near (260-320 nm) UV, as described in Chapter 2, with the only difference being that a 0.02 cm path length cell was used for far UV and an 0.05 cm cell was used for near UV. As described previously a longer path length is required for near UV due to the weaker signal. A 0.02 cm path length cell was used for the far UV to aid application of the silica slurry and the 0.05 cm cell was the longest circular cell path length that was available at the time. All experiments were performed on a ChirascanTM spectrometer (Applied Photophysics Ltd, UK) at room temperature. The circular cell was constantly rotated at 45 rpm for the duration of each scan. The cell was placed as close to the detector as possible (~2 mm distance) to reduce the contributions of light scattering. The suspensions were allowed to rotate for 5 min prior to spectra measurements to ensure a homogenous distribution of the slurry. Following measurement, the CD spectra were corrected for absorption flattening as described previously. The reference absorption was derived from 195-197 nm for far UV readings since this wavelength corresponds to positive ellipticities in the spectra, and 274 nm was used for far UV as this value correlated best for all the spectra.

4.4.2 Surface mapping using neutron reflectometry

The first descriptions of the use of neutron reflectivity to measure the dimensions within organic multilayers was described by Hayter and colleagues in a key paper published in 1981 (Hayter et al. 1981). Although previous methods had been described for the measurement of reflection of neutrons from multilayer surfaces,

Hayter's work showed that using a deuterated substrate, the air/film and film/glass reflectivity profiles enabled the measurement of a stearic acid bilayer thickness. By additional vapour phase measurements, the associated water in the organic film could also be calculated (Hayter et al. 1981). For protein measurements, the compound of interest is adsorbed onto a highly polished surface, usually silicon, which is relatively transparent to the neutron beam.

Neutron reflectivity follows the general rules of reflection as discussed in Chapter 1. When the neutron beam at incident angle θ is projected onto a substrate surface the neutrons are reflected at the same reflective angle as shown in Figure 4-4 (Lu 1999). If the substrate were to have a thin adsorbed film on the surface, such as a protein layer, this will alter the path of the reflected neutrons and by comparing the change in reflectivity the depth of this layer can be calculated.

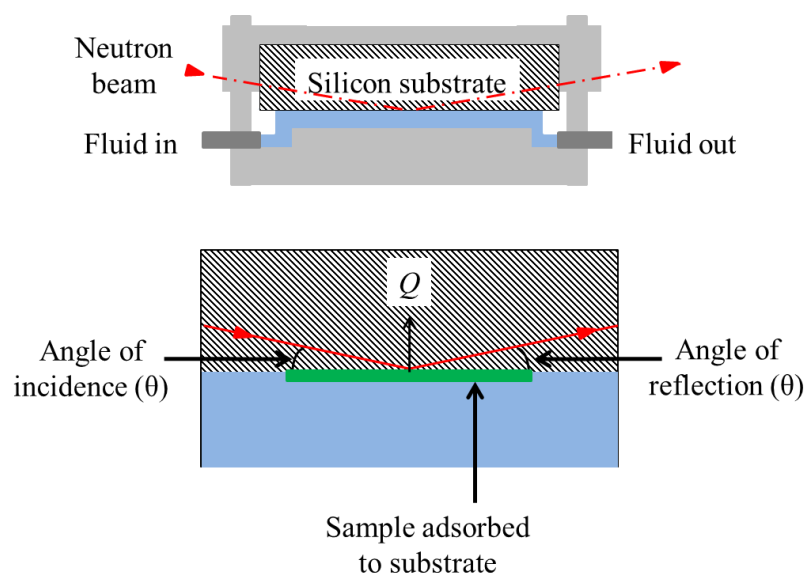


Figure 4-4 Schematic representation of the basic set up for neutron reflectometry. Top image shows silicon substrate clamped in place with sample solution in blue. Lower image shows expanded point of contact of sample in solution and silicon substrate.

Reflectivity, R , is the ratio between the intensities of both the incoming incident beam and outgoing reflected beam. This is normally plotted as a function of moment transfer (Q) perpendicular to the interface defined by:

$$Q = \frac{4 \pi \sin \theta}{\lambda}$$

Equation 4-3

This represents the change in the neutron wave vector on reflection at the boundary where λ is the wavelength of the incident beam and θ is the angle of the beam with the interface. The measured reflectivity is related to the scattering length density (SLD) of the sample which is calculated from the sum of the scattering lengths of its components divided by its molecular volume (Lakey 2009). Neutron reflectivity utilises isotopic substitution to distinguish between the aqueous solution and the adsorbed layer by replacing the buffer with a deuterated form which has an opposite SLD than that of the hydrogenated.

Structural information from the reflectivity profile can be obtained by fitting the data to a given model using a trial and error approach. An optical matrix method is the most commonly used, which assumes that the layers are homogeneous and parallel to the interface with a uniform scattering length density (Fragneto-Cusani 2001).

The National deuteration facility located within the Australian Nuclear Science and Technology Organisation (ANSTO) has previously produced high quality deuterated forms of proteins (Chen et al. 2012). The fermentation process involved expression of the recombinant protein using bacterial cells, in this case *E. coli*, in a minimal

medium containing glycerol in D₂O. Chen and colleagues (2012) were able to produce a deuterated human protein galectin-2 mutant at a bioreactor scale. The purification process combined affinity chromatography and ion exchange chromatography.

NR measurements in this chapter were made at the Platypus neutron reflectometer (ANSTO) and all experiments were performed by the Platypus instrument scientist Dr Stephen Holt assisted by Dr Christopher van der Walle. In addition to the FIII9'10 and FIII9''10 H2P expressed at Strathclyde, the experiments described in this chapter employed deuterated proteins constructed from the same cDNA at the National Deuteration facility (proteins referred to as d-FIII9'10 and d-FIII9''10 H2P, with the d to denote deuteration). The cDNA was transported to the facility on filter paper and following expression the generated deuterated proteins were purified and lyophilised prior to NR analysis. The methodology followed by the facility is described below.

Silicon substrates coated with a TiO₂ layer were washed with Decon 90, thoroughly rinsed with deionised water and dried under a nitrogen stream. The cleaned silicon substrate was then clamped in a custom made Teflon trough with a void volume of around 3ml. The experiments were performed by incubating the surfaces with a range of protein concentrations, 10, 30, 100 and 200 mg/L in phosphate buffer. The samples were analysed at fixed incident angles and the data reduced to yield a single reflectivity profile. A flat background, determined by extrapolation to high values of moment transfer Q ($Q = 4\pi\sin\theta/\lambda$, where θ is the glancing angle of incident and λ the wavelength) was subtracted. All experiments were conducted at ambient temperature (~25 °C). Blank substrate/buffer measurements were performed for substrate

characterisation. Following adsorption of protein samples to the TiO₂ surface for 30 min, surfaces were rinsed by flushing the trough through with 5 volumes of phosphate buffer, D₂O/H₂O as appropriate to investigate changes at the surface. NR data were fitted using a Global MOTOFIT analysis following a trial and error approach (Nelson 2006). First, a structural model was assumed and the reflectivity calculated using the optical matrix method (Fragneto-Cusani 2001). This method assumes that the interface is composed of a series of parallel layers characterised by their thickness, and scattering length density, ρ , and the reflectivity profile calculated by matrices multiplication. The fit that is produced is then assessed for quality (goodness) by comparison with the measured data and the parameters modified by the least-square iteration method (Su et al. 1998) until an acceptable χ^2 value was obtained. Data fitting and interpretation was performed by myself with assistance from Dr Stephen Holt and Dr Christopher van der Walle.

Protein samples were used at 10, 30, 100 and 200 mg/L concentrations in phosphate buffer made with D₂O for FIII9'10 and FIII9''10 H2P but made with H₂O for the deuterated forms d-FIII9'10 and d-FIII9''10 H2P. Following adsorption, surfaces were rinsed with phosphate buffer (D₂O or H₂O, where appropriate) to investigate the extent of protein desorption. Blank silicon/TiO₂ surfaces measurements were performed for surface characterisation using either D₂O or H₂O based buffers.

4.4.2.1 Preparing samples by lyophilisation

Protein samples were prepared for lyophilisation by first exchanging the storage phosphate buffer for 50 mM ammonium acetate solution using a PD-10 (Amersham

Bioscience, Buckinghamshire, England) desalting column. A protein sample containing approximately 5 mg protein was diluted to 2.5 ml and passed through a PD-10 column that had previously been equilibrated with 50 mM ammonium acetate buffer as per the instructions. The initial 3.5 ml of solution eluted from the column was then distributed evenly between 4 small collection tubes and incubated in a -80 °C freezer for at least 4 hours. The frozen protein samples were then transferred to a MicroModulyo (Thermo Scientific) freeze-dry system and dried under vacuum conditions maintained at -50 °C for over 24 h.

4.4.2.2 Mass spectrometry measured hydrogen/deuterium (H/D) exchange

Complete exchange of all of the hydrogen atom to deuterium is unlikely, the literature suggests that around 70-90 % exchange can be expected (Kreiner et al. 2009b). The process of H/D exchange involves the liable side chain hydrogen's being exchanged for deuterium in solution and only partial exchange of the amide backbone (Efimova et al. 2007). The rate of exchange can be dependent on the stability of the protein, with more stable proteins having been shown to have a reduced exchange rate due to their reduced flexibility (Larsericdotter et al. 2004).

The H/D exchange experiments used here were adapted from a method described by Larsericdotter and co-workers (2004) (Larsericdotter et al. 2004). Approximately 1 mg of the lyophilised protein sample was dissolved in 100 µl distilled water. H/D exchange was initiated by the addition of 900 µl deuterium oxide to the hydrated sample, resulting in a solution with 90 % of the protons in solution being deuterium atoms. Over a range of time points from 5s to 48 h, 80 µl samples were withdrawn

and the H/D exchange quenched by mixing with 1 ml of an ice cold solution of 3 % acetic acid, 47 % methanol and 50 % H₂O (quenching solution). Following quenching, the samples were kept on ice until mass spectrometry analysis which was performed at the University of Strathclyde by Mr Tong Zhang. Each mass spectrum consisted of an accumulation of 100 scans and the mass was calculated as the average of three mass-to-charge (m/z) ratios.

4.4.2.3 Isoelectric focusing

Deuteration might result in changes in protein conformation or subtle changes in physicochemical properties. Concertpharma, a small niche drug development company in the US, has suggested that deuterated compounds differ perceptibly in physicochemical and metabolic reactions (Tung 2010) and so it was of interest to determine whether deuteration changed the isoelectric point of the deuterologue. The isoelectric point of a protein is defined as the measured pH at which positive and negative charges on the molecule are equal and is measured by isoelectric focusing.

Approximately 1 mg of lyophilised protein sample was dissolved in 500 µl of distilled water and the concentration calculated using Bradford Reagent method. A 96-well plate assay protocol was used here because of the ability to use a small sample volume and perform multiple samples at once. A calibration curve was created using known standards of BSA dissolved in water ranging from 0.1-1.4 mg/ml. Each of concentration standards (5µl) and unknown concentration protein samples (5 µl d-FIII9'10, d-FIII9''10 H2P, FIII9'10 and FIII9''10 H2P) were added to separate wells of a 96-well plate. In addition, 5 µl of water was added to blank

wells. To each well, 250 μ l of Bradford Reagent was added and the plate was shaken at 480 rpm for 30 s in a Multiskan Ascent plate reader (Thermo-Labsystems) and then incubated at room temperature for 5 minutes. Following this, the absorbance was read at 570 nm and the concentration of the unknown proteins calculated from the calibration curve. Due to the time dependant nature of the colour change with Bradford Reagent, a fresh calibration was performed for each occurrence.

The IEF Immobiline™ DryStrips required to be rehydrated overnight with a rehydration solution containing 2 % (v/v) Triton x-100, 0.5 % IPG buffer pH 6-11 (GE Healthcare, cat. No. 71-5005-82), 30 % (w/v), dithiothreitol (DTT) and 0.0002% (w/v) bromophenol blue. For the 18 cm Immobiline™ DryStrips (pH 6-9) used in this instance, 340 μ l rehydration solution was transferred to each required lane of an Immobiline® DryStrip Reswelling tray. The strips were carefully placed gel side down in the rehydration solution, following this each lane was overlaid with 2 ml Immobiline DryStrip cover fluid and incubated at room temperature for over 17 hours.

Protein samples were diluted to a concentration of 0.2 mg/ml with sample solution (0.5 % (v/v) Triton x-100, 0.5 % (v/v) IPG buffer (6-9) 0.2 % DTT and 0.0002% (w/v) bromophenol blue). Focusing of the gel was performed on an Ettan IPGphor IEF system (Amersham Biosciences) connected to a Multi Temp TM III thermostatic circulator set at 20 °C. Prior to application of the gel strips 3 ml of DryStrip cover fluid was added to each strip channel. The rehydrated gel strips were placed gel side up into the strip channel of the electrode plate with the acidic end toward the anode. IEF electrode wicks (Amersham, 18-1004-40) were prepared by soaking in distilled

water and blotting dry. These were then placed over each end of the gel strips and the electrodes carefully lowered on top at each end to provide electrical contact. Samples were loaded using the sample cup method, in which sample cups were placed on top of the gel strips near the anodic end with the cup touching the gel surface ensuring good contact to prevent leakage. DryStrip cover fluid (~110 ml) was then poured over the system and 100 µl of protein sample loaded into the cup. Electrophoresis was carried out according to Table 4-1.

Table 4-1 Running conditions for 18 cm Immobiline DryStrip on Ettan IPGphor Isoelectric focusing unit.

Phase	Voltage hold	Voltage (V)	Time (h:min)	Volt hours (KVh)
1	Step and hold	500	8:00	0.5
2	Gradient	1000	1:00	0.8
3	Gradient	8000	3:00	13.5
4	Step and hold	8000	4:30	35.2

Visualisation of the proteins following focusing involved several steps. Firstly the proteins in the gels were fixed by immersing in an aqueous solution of 10 % (w/v) trichloroacetic acid for 1 h. The gel strips were then equilibrated for 30 min by immersing in an aqueous solution of 25 % (v/v) methanol and 5 % (v/v) acetic acid (equilibration solution) to remove carrier ampholytes. The gel stain consisted of 0.1 % Coomassie blue G-250 dissolved in equilibration solution, the gels were submerged in this for 10 min with constant agitation. Following staining, the gels were returned to equilibration solution until the background became clear and the protein bands were visible. Gels were preserved by immersing in an aqueous solution of 5 % glycerol, 25 % methanol for 1 h and then dried at room temperature.

The distance the protein had travelled in relation to the cathode was measured and given as a percentage of the total gel length.

4.4.3 Functional analysis of mutated proteins

It was important to ensure that the biological activity of the FIII9''10 H2P protein was intact following mutation. Ideally this would follow the same principle as the FIII9'10 mutant which had improved activity following mutation to increase conformational stability (van der Walle et al. 2002). The His to Pro mutation in the FIII9''10 H2P mutant was within the important synergistic PHSRN region of the FN fragment therefore binding to integrin $\alpha 5\beta 1$ may have been affected. To this end first binding to this integrin was tested to ensure activity, following this, cell culture adhesion assays were performed.

4.4.3.1 Binding to integrin $\alpha 5\beta 1$ measured by ELISA

Enzyme linked immunosorbent assay (ELISA) is a commonly used approach to investigate protein-protein interactions. The basic principle involves an antigen immobilised onto a surface in a way in which when exposed to a solution containing the corresponding binding partner will allow the two to interact. The interaction can be followed by the further addition of an antibody enzyme conjugate which bonds to the binding partner and then subsequently reacts to provide some form of colorimetric change (see Figure 4-5).

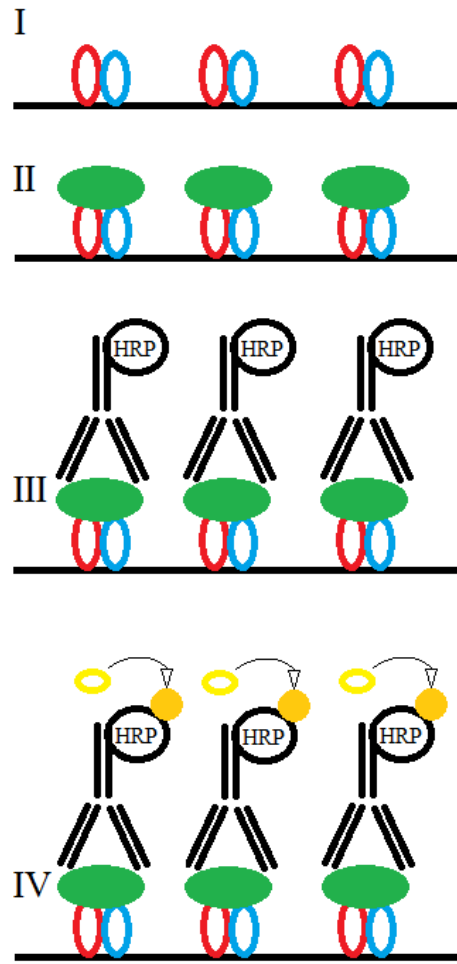


Figure 4-5 Schematic depicting (I) integrin on surface, (II) protein binding to integrin, (III) antibody conjugate binding to protein and (IV) colorimetric change initiated by binding to horseradish peroxidase (HRP).

In this instance, the interaction between integrin $\alpha 5 \beta 1$ and the developed proteins was investigated to determine the binding activity of the mutated proteins compared to the wild-type and to ensure that by substituting amino acids we did not disrupt binding. Measurement of bound FIII9-10 based proteins was facilitated by the use of Anti-HisG-HRP antibody, which recognises the polyhistidine tag present on the proteins, as mentioned previously. The antibody is cross-linked with horseradish

peroxidase (HRP) which is in turn detected using SigmaFast™ OPD (*o*-Phenylenediamine dihydrochloride) tablets.

ELISA was performed based on the method as described in (Altroff et al. 2001) with some changes. 96-well flat bottomed plates (Thermo Scientific, UK) were coated with 50 µl of a 2.5 µg/ml integrin $\alpha 5\beta 1$ (Sino Biological Inc. (cat. no. CT014-H2508H; Beijing, China)) solution in ELISA buffer (EB) composed of 25 mM Tris-HCl, pH 7.4, 150 mM NaCl, 1 mM MgCl₂, 0.1 mM CaCl₂ and incubated overnight at 4 °C. The plates were then washed three times with 200 µl EB and blocked with 200 µl of a solution containing 5 % bovine serum albumin (BSA) in EB for 1 h at 37 °C. The wells were then washed as above, and the plates were incubated for 2 h at 37 °C with doubling dilutions of FIII9-10, FIII9'10 or FIII9''10 H2P diluted in EB containing 1% BSA. The wells were washed as above and incubated for 1 h at room temperature with 50 µl anti-HisG-HRP antibody (1:2000 dilution in EB containing 1% BSA) (Life Technologies Ltd, Paisley, UK). The wells were then washed 4 times as above, following this they were incubated with 200 µl SigmaFast™ OPD tablet prepared according to the manufacturer's instructions. The reaction was stopped after 30 min with 3 M HCl and absorbance read at 500 nm. Assays were performed in triplicate and the background antibody binding in the absence of ligand was subtracted from the readings. Dose-response data from the assays were analysed by non-linear regression using a sigmoidal curve fit (Prism, GraphPad Software).

4.4.3.2 BHK-cell culture adhesion assay

The adhesion of BHK 21 cells to cell culture surfaces has been previously shown to be improved using FIII9'10 as an intermediate (van der Walle et al. 2002). For this reason this fibroblast cell line was selected for adhesion testing.

All cell culture experiments were performed with the assistance of Mrs Christine Whitelaw at University of Strathclyde. Baby hamster kidney (BHK) cells were maintained in DMEM plus GlutaMax (61965026, Gibco®, life technologies™) containing 10 % foetal bovine serum, at 37 °C in 5 % CO₂ incubator. Cell attachment assays were carried out according to methods previously described in (Mardon and Grant 1994), with some variations. The surface of the wells of a flat-bottomed 96-well plate (Nuclon®) was coated with doubling dilutions of 100 µg/ml protein in buffer and incubated overnight at 4 °C. Excess protein was gently washed off with phosphate buffered saline, pH 7.4 (PBS) and uncoated plastic blocked with 5 % bovine serum albumin (BSA) in PBS for 1 h at 37 °C. A total of 10⁴ BHK cells were inoculated into each well and incubated for 1 h at 37 °C, 5 % CO₂. Adherent cells were washed gently with PBS and fixed with 100 µl of 4 % glutaraldehyde/ 4 % formaldehyde in PBS. Adhesion was determined by staining with 0.1 % crystal violet for 30 min and solubilised with 200 µl methanol. Absorbance was read at a wavelength of 570 nm and the data normalised by the largest reading value. The data presented are expressed as the means ± the standard error of 8 replicates performed in three independent experiments.

4.4.3.3 Immunofluorescence of BHK cell adhesion to TiO₂ coated surfaces

TiO₂ plated borosilicate glass coverslips were prepared by rinsing with absolute ethanol (200 proof) and then air dried. Coating with proteins was achieved by incubating with either FIII9-10, FIII9'10 or FIII9''10 H2P at 100 µg/ml at room temperature for 60 min and carefully washing with PBS to remove any unabsorbed protein. Following this, BHK cells were seeded onto TiO₂-plated glass coverslips coated with desired protein, and incubated for one hour at 37 °C, 5 % CO₂. A negative control was prepared by incubating a coverslip with buffer and proceeding as above. The coverslips cultures of BHK cells were then washed in PBS and fixed with 3 % paraformaldehyde (PFA) in PBS for 10 min. Permeabilization of the cells was achieved by incubating with 10 mM Hepes, pH 7.4, 200 mM sucrose, 3 mM MgCl₂, 50 mM NaCl, 0.5 % Triton X-100 for 5 min at room temperature and washed with PBS containing 3 % w/v BSA. They were then incubated overnight at 4 °C with anti-vinculin antibody, diluted 1:400 in PBS containing 0.1 % BSA. This was followed by incubation with Texas Red conjugated anti mouse antibody diluted 1:100 in PBS containing 0.1% BSA for 60 min in the dark, at room temperature. Actin was visualised with the use of fluorescein-phalloidin (dilution 1:20) for 90 min at RT. The coverslips were then washed in PBS containing 3 % BSA and cells post fixed with 3% PFA (10min), following this they were washed in PBS 3 % BSA before mounting with Vectashield medium containing DAPI.

The images were recorded with the assistance of David Blatchford on a Leica SP5 Laser scanning confocal microscope which is based on a Leica DM600B upright microscope. The images were captured with a 63x NA 1.4 oil immersion objective at

an 8bit depth and 1024 x 1024 pixels. The pinhole was set to its default of 94.6 μ m. Zoom is as shown and ranged from 1x to 5 according to the desired field of view. Eight frames were averaged for each scan which was acquired sequentially. The SP5 is equipped with tuneable acousto-optical filters thus emission can be tailored precisely for the characteristics of each fluorophore. DAPI was excited with a 405 LED and emission was detected between 423 and 504nm, green fluorescence was excited with a 488 Argon laser line and emission recorded between 501-573 and the red fluorophores was excited with a 543 HeNe laser line and detected fluorescence was captured from 588-675nm.

4.5 Results

4.5.1 Conformation of proteins on surfaces of varying wettability

4.5.1.1 *Surface hydrophobicity*

The surface wettability was probed using contact angle measurements with water. Silanized glass substrates were prepared relatively simply. From the water contact angles the hydrophobicity for the surfaces can be classed in the order TCOS \approx PFTOS \gg APTMS \gg mPEG-silane $>$ bare glass. The measurement of the contact angle suggested that the plasticware was slightly more hydrophobic than glass. The average value of the contact angle for the surfaces is shown in Table 4-2, the readings reported are the average of 10 drops from two independently created surfaces. It was noted at the time of measurement the silanization may not be homogenous over the surfaces as indicated by the high standard deviation of some of the angles. Although the contact angles for mPEG-silane and APTMS correspond

well to the values previously reported in the literature the other surfaces tended to differ from the reported values.

Table 4-2 Advancing contact angles of water on surfaces.

Surface	Contact angle θ	Value of θ for water from literature
Bare glass	41.5 ± 4	29 ± 1 ^a
mPEG-silane	42.8 ± 2	48 ± 2 ^b
APTMS	51.0 ± 3	54.5 ^c
PFTOS	93.5 ± 11	117 ± 2 ^d
TCOS	97.3 ± 5	107 ± 1 ^e
Culture plate	68.6 ± 4	-

^a (Lamprou et al. 2010), ^b (Kang et al. 2007), ^c (Song et al. 2006), ^d (Noel et al. 2004), ^e (Kulkarni and Vijayamohan 2007).

Production of the silanized silica beads was similar to coating the glass slides, however, because of the small size they were unsuitable for contact angle measurements. The slides were used as a representative to indicate the wettability of the silanized silica beads. Following silanization, a visual inspection of the dried, coated silica beads indicated no obvious difference between coated and uncoated. However, attempts to mix the more hydrophobic beads (PFTOS and TCOS) with water proved to be difficult and uniform slurry similar to that of bare silica could not be obtained. This indicated that silanization of the surface was successful shown by the altered wettability.

4.5.1.2 Protein adsorption to silica beads

The UV measurements suggested that the protein had completely adsorbed to the silica beads. The absorbance of the water washings was found to be negligible, suggesting that adsorption of the complete sample to the beads had occurred and the concentration on the beads was the maximum 1 mg/ml. Interestingly, the PFTOS and TCOS coated beads had a visually increased wettability following rotation with protein solution, implying that the former hydrophobic surface was now coated allowing it to be more hydrophilic or that the hydrophobic coating had been removed. However, as a precaution, samples of each of the beads were also rotated with deionised water to be used as a “blank” for CD measurements. These samples retained their hydrophobic properties indicating that the silane coatings remained.

4.5.1.3 Protein conformation on silica beads of varying wettability

The coated and bare silica beads had been maintained in deionised water following adsorption of protein samples. The loading of the “slurry” into the 0.2 mm path length CD cell proved to be somewhat troublesome. This was because the water that the beads were suspended in would transfer to the cell via capillary action leaving the beads behind. A delicate system had to be adopted to allow sufficient transfer of beads into the cell. An exact mass of beads which were loaded could not be determined. Instead, a visual examination of the cell was performed following rotation and before the CD scan to confirm that each sample contained a similarly homogenous distribution of slurry.

Correction of the data was assisted by an Excel spread sheet method in which the observed ellipticity of the protein on the surface and the absorbance values were set against the solution values for the same protein and the values for $1/(1-Q)$ calculated. This method had the advantage of including all of the absorbance values for solution and a systematic based approach was used to find the optimum absorbance value to correct the data to whilst still maintaining a true representation of conformation upon a solid support.

Far UV CD spectra for FIII9-10 adsorbed to silica beads and silanized silica are shown in Figure 4-6, CD spectrum of FIII9-10 in solution is shown in inset for comparison. Even after correcting of the adsorbed spectra there was still a large reduction in the ellipticity compared to solution. For all of the surfaces there was a large reduction in the positive maxima around 200 nm, however, the overall shape was similar to the solution spectra.

In general the adsorbed FIII9-10 did not retain its conformation when adsorbed to any of the surfaces with no dependency on the surface wettability. The loss of the positive minima around 225 nm was indicative of changes in the aromatic environment, suggesting that the protein adopts a non-native conformation at the silica surface.

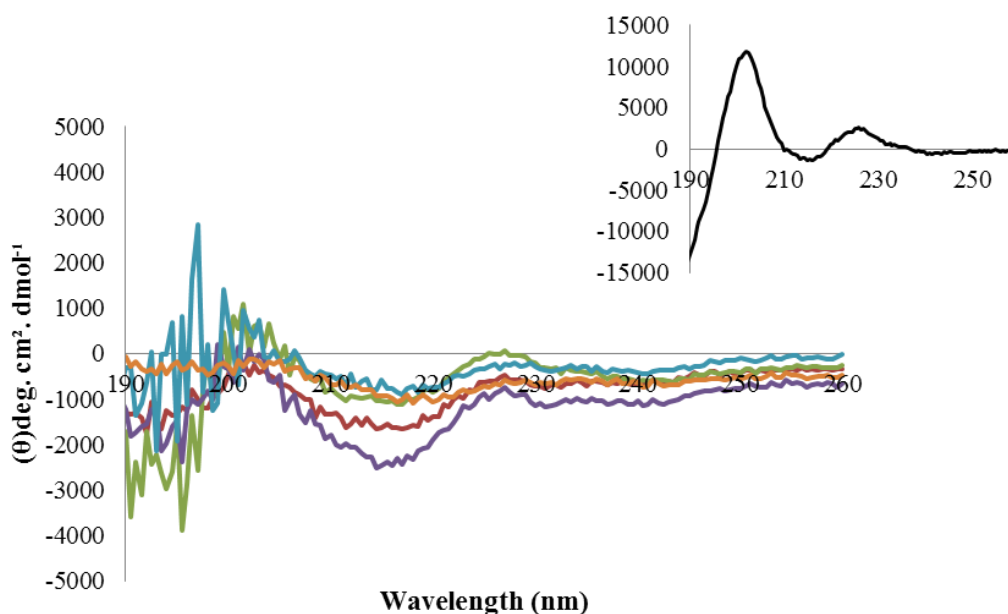


Figure 4-6 Far UV CD spectra for FIII9-10 adsorbed to beads with surfaces of increasing hydrophobicity: silica (red), mPEG-silane (purple), APTMS (green), PFTOS (orange) and TCOS (blue). Inset shows far UV CD spectrum for FIII9-10 in aqueous solution.

Far UV CD spectra for FIII9'10 adsorbed to silica beads and silanized silica are shown in Figure 4-7, to aid comparison, CD spectrum for the protein in solution is shown in inset. There was a noticeable improvement in the shape of the spectra for the FIII9'10 protein, compared to FIII9-10, as it appeared to retain most of the features of the protein in solution. The most obvious loss of shape was for FIII9'10 on PFTOS surfaces as the spectra here featured the positive maxima shifting to the left and the positive minima shifting to the right with a reduction to nearly zero ellipticity, indicating a near total loss of native structure.

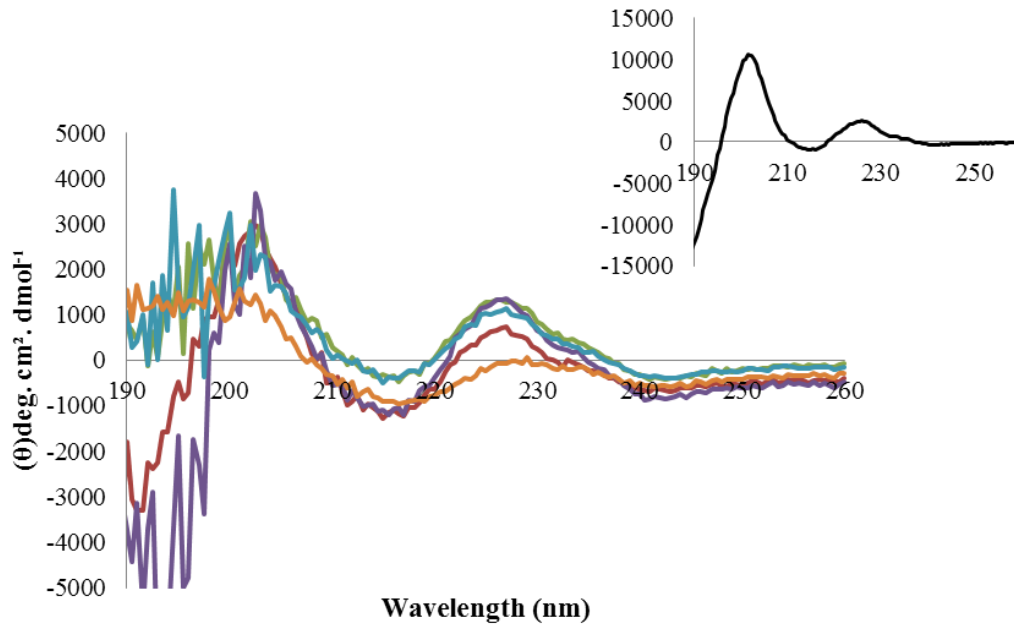


Figure 4-7 Far UV CD spectra for FIII9'10 adsorbed to beads with surfaces of increasing hydrophobicity: silica (red), mPEG-silane (purple), APTMS (green), PFTOS (orange) and TCOS (blue). Inset shows far UV CD spectrum for FIII9'10 in aqueous solution.

There was a large variation in the recorded spectra for the FIII9''10 H2P protein adsorbed to the different surfaces (Figure 4-8). Interestingly these spectra had a higher signal than the other two proteins for most of the surfaces, the notable exception being mPEG-silane. Even on the highly hydrophobic surfaces the FIII9''10 H2P appeared to retain its native conformation.

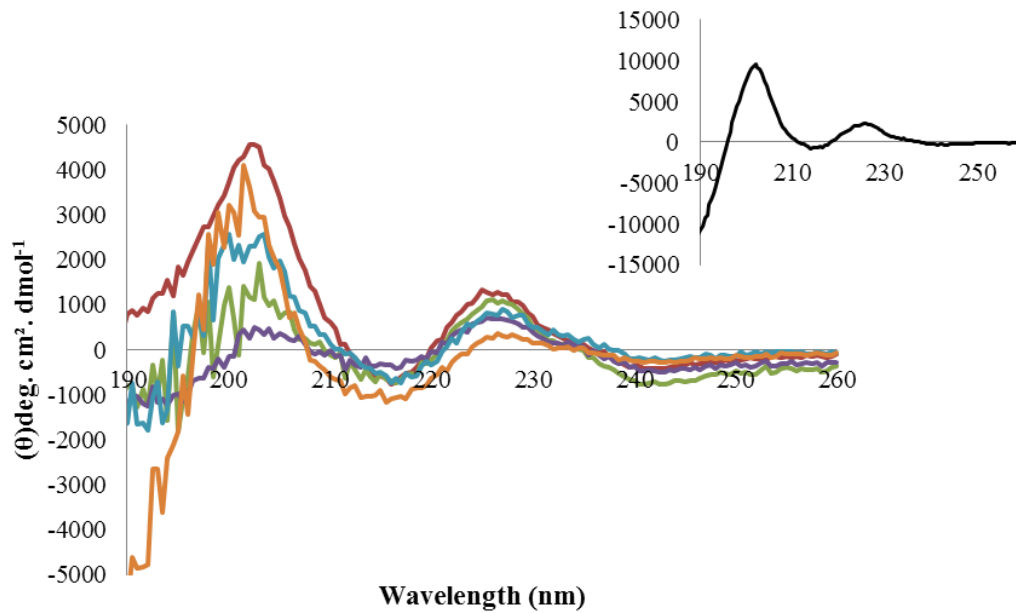


Figure 4-8 Far UV CD spectra for FIII9''10 H2P adsorbed to beads with surfaces of increasing hydrophobicity: silica (red), mPEG-silane (purple), APTMS (green), PFTOS (orange) and TCOS (blue). Inset shows far UV CD spectrum for FIII9''10 H2P in aqueous solution.

Interestingly, the near UV scans for adsorbed proteins (Figure 4-9) were very similar to the solution spectra, but featured a noisier signal. On its own this indicated that there was not a large amount change in the aromatic environment of the proteins, however as mentioned earlier the far UV data suggested differently. The noise in the signal was inversely proportional to the thermodynamic stability of the proteins. Noise decreased in the order FIII9-10 > FIII9'10 > FIII9''10 H2P.

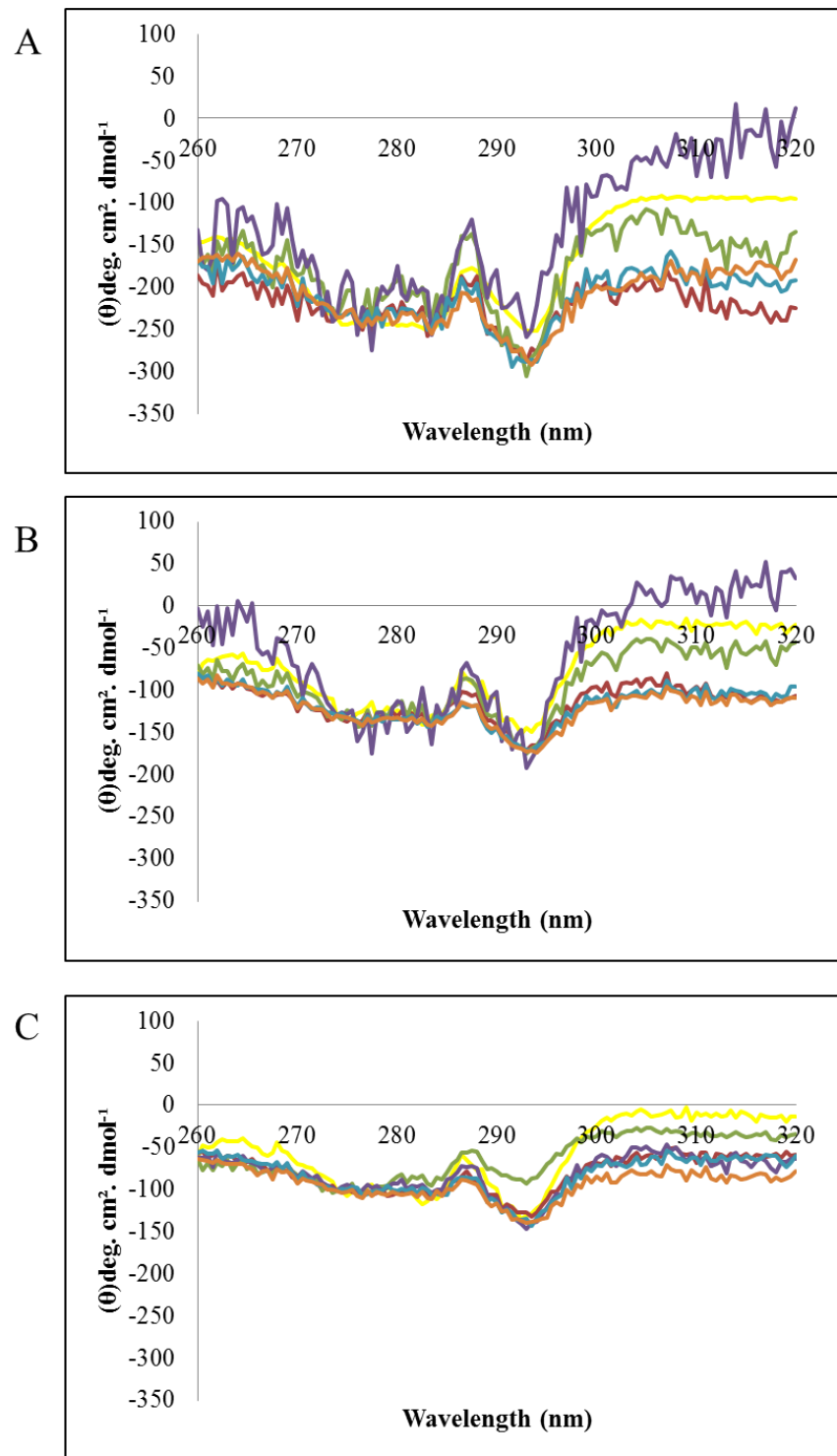


Figure 4-9 Near UV CD spectra for FIII9-10 (A), FIII9'10 (B) and FIII9''10 H2P (C) in solution (yellow) and adsorbed to beads with surfaces of increasing hydrophobicity: silica (red), mPEG-silane (purple), APTMS (green), PFTOS (orange) and TCOS (blue).

4.5.2 Protein adsorption studies by neutron reflectivity

4.5.2.1 Isoelectric focusing

Focussing of the proteins proved to be more difficult than expected. Typically, IEF strips are used as the first step in two dimensional polyacrylamide gel electrophoresis (2D-PAGE) of protein mixtures from cell lysates (Celis and Gromov 1999). That system would employ the use of a large sized SDS-PAGE gel (up to 26 cm x 20 cm) to further separate out the protein by mass (M_r) following separation by isoelectric point (pI). As our samples were single proteins of relatively high purity the second step was not required.

The resolution of the proteins on the IEF gel strips was poor and featured streaking. In an attempt to optimise conditions, sample solution was initially prepared containing 8 M urea to prevent precipitation of the proteins. However, it was found that this affected the pI calibration kit and so samples and gels were prepared without urea. Consequently, the resolution of the sample protein band improved, but unfortunately not the quality of the calibration kit. The lack of appropriate calibration meant that an accurate pI could not be calculated for the proteins however, the positioning of them on the gels could be compared. From this it was concluded that there was very little change in the pI of the deuterated proteins compared to the hydrogenated version. The actual measurements of the bands are shown in Table 4-3. The percentage distance travelled was calculated by measuring the entire strip from the point of introduction of the protein to the end of the gel. The breadth of the bands varied from 0.2 cm to 0.4 cm which reduced the accuracy of the percentage calculation and hence a range has been shown.

Table 4-3 Measurement of protein bands following isoelectric focusing.

Protein sample	Actual distance travelled from starting point (cm)	% distance travelled from cathode
FIII9'10	10.5-10.8	59-61
d-FIII9'10	10.4-10.7	58-60
FIII9''10 H2P	10.4-10.8	58-61
d-FIII9''10 H2P	10.3-10.5	58-59

4.5.2.2 H/D exchange

The buffer of the protein samples was changed prior to H/D exchange to facilitate better exchange and to reduce salts which could affect the mass spectrometry scan. The protein samples were then lyophilised to remove the hydrogenated buffer. The mass spectrometry scan was analysed using Xcalibur™ software. Three of the most abundant consecutive peaks were chosen and the mass to charge ratio converted into a calculated mass.

The increase in mass of the protein exposed to D₂O compared to the mass of non deuterated protein as a function of the exchange time is plotted in Figure 4-10. Overall the increase in mass was found to be relatively small, up to around 50 Da. This would suggest that only a small number of liable hydrogen atoms undergo exchange which is contrary to previous estimations of around 70- 90% (Kreiner et al. 2009b).

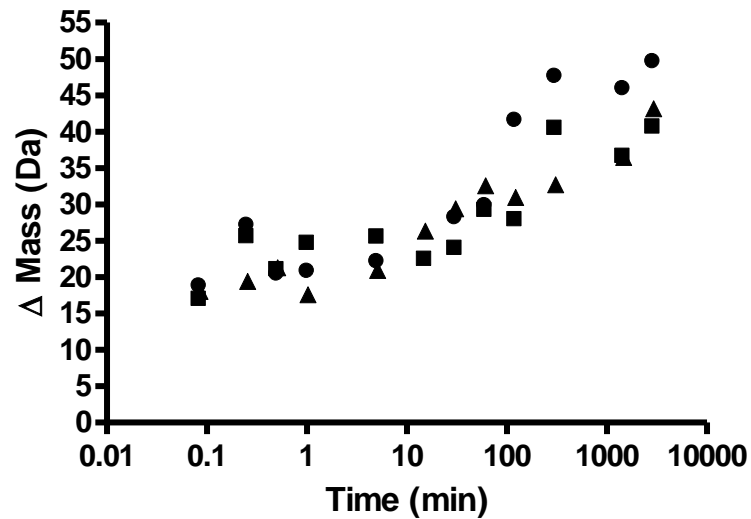


Figure 4-10 Mass increase as a function of the H/D exchange time (on a logarithmic scale) for FIII9-10 (■), FIII9'10 (▲) and FIII9''10 H2P (●).

4.5.2.3 Protein adsorption studies by neutron reflectivity

Analysis of the NR data allowed for information to be generated relating to the molecular nature of the proteins at the solid liquid interface. This is of use because it will help to give information on the arrangement of the proteins at the surface in terms of how thick the layer is and also percentage coverage. A simplified representation of the pathway of the beam as it is refracted and altered by the subsequent layers formed at the substrate surface is shown in Figure 4-11.

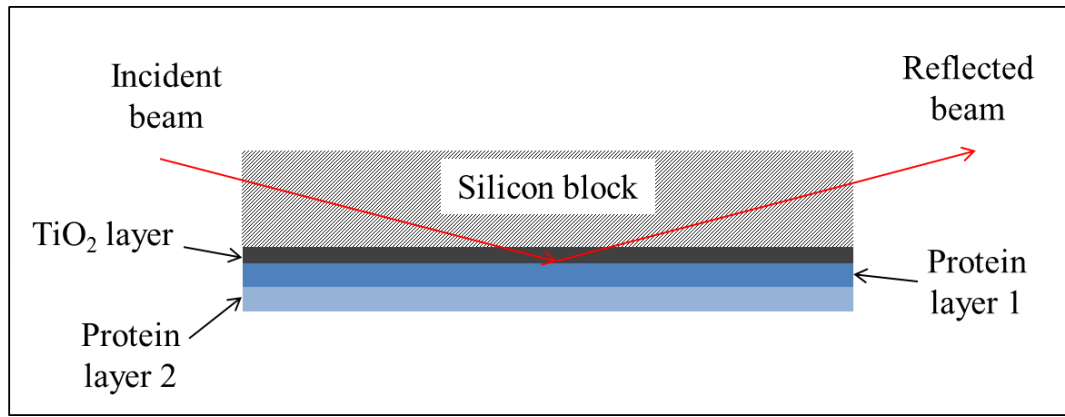


Figure 4-11 Schematic of neutron beam reflection pathway as it interacts with a protein bilayer formed at solid liquid interface between protein sample and TiO_2 substrate surface.

The blank substrates were hydrated with either D_2O or H_2O and characterised prior to adsorption of proteins. This analysis included the silicon block, the SiO_2 layer (omitted from Figure 4-11) and the TiO_2 surface. The modelled results are shown in Table 4-4; the SLD for the silicon block was kept constant at $2.078 \times 10^{-6} \text{ \AA}^{-2}$. To provide a contrast, the NR scans for the hydrogenated proteins were carried out in deuterated phosphate buffer and the deuterated proteins were examined in hydrogenated phosphate buffer, for simplicity this is indicated as either D_2O or H_2O phosphate buffer. Solutions of increasing protein concentration were sequentially injected followed by a washing step of phosphate buffer prepared in D_2O or H_2O as appropriate.

Table 4-4 Calculated neutron reflectivity parameters for bare substrate surfaces.

Substrate	SLD D ₂ O/H ₂ O x10 ⁻⁶ (Å ⁻²)	SLD SiO ₂ x10 ⁻⁶ Å ⁻²	Thickness SiO ₂ (Å)	Roughness of SiO ₂ (Å)	SLD TiO ₂ x10 ⁻⁶ Å ⁻²	Thickness of TiO ₂ (Å)	Roughness of TiO ₂ (Å)	χ^2
A (H₂O)	-0.55	3.47	42.63	3	2.38	252.15	3.62	7.01
B (D₂O)	6.10	3.47	35.05	3	2.25	253.18	5.83	7.01
C (H₂O)	-0.56	3.94	26.92	1.06	2.30	251.37	1.69	7.57
D (D₂O)	6.02	3.47	24.95	2.19	2.13	253.62	5.43	7.57

The scattering length density for water is the opposite sign as to D₂O which is why it is a negative value, the calculated values as shown in Table 4-4 are similar to those found in the literature (Brouette et al. 2013). Differences in the SLD, thickness and roughness of the TiO₂ layer for the different substrates were a consequence of manufacturing variability. When fitting the data for substrates C and D the Q value was restricted due to an unusual effect at the first incident angle. This may be due to the SiO₂ layer being significantly thinner than in substrates A and B.

In order to calculate the scattering length density for the proteins the inter and intra-molecular hydrogen bonds had to first be calculated. This was achieved by using the Volume/Area/Dihedral Angle Reporter (VADAR programme, version 1.8, <http://redpoll.pharmacy.ualberta.ca/vadar/>) (Willard et al. 2003), using the Protein Data Bank (PDB) coordinates for the wild type FIII9-10 as a guide (Annan et al. 2006, Kreiner et al. 2009b). An H/D exchange of ~80 % was assumed as this value provided data with the best fit for the data. Although this value was higher than the value calculated from the mass spectrometry analysis performed earlier in this

chapter, it is more consistent with levels found in the literature (Larsericdotter et al. 2004). The SLD (ρ_{prot}) for each protein were then calculated using Equation 4-4 (Holt et al. 2002), where SL_{prot} is the scattering length of the protein and V_{prot} is the volume occupied.

$$\rho_{prot} = \frac{SL_{prot}}{V_{prot}}$$

Equation 4-4

These are valid assuming that the protein had not denatured at the surface, which was reasonable to assume based on the solid state CD data for FIII9'10 and FIII9''10 H2P adsorbed to silica.

Calculation of the surface coverage (α) of the protein layer was achieved using Equation 4-5 (Kreiner et al. 2009b).

$$\rho_{fitted} = (1 - \alpha)\rho_{D_2O/H_2O} + \alpha \cdot \rho_{calculated}$$

Equation 4-5

Where ρ_{fitted} is the SLD made up from contributions of the protein and subphase in D₂O or H₂O as appropriate. The parameters used are displayed in Table 4-5, the calculated SLD ($\rho_{calculated}$) was kept constant for the hydrogenated and deuterated forms of the proteins at $3.014 \times 10^{-6} \text{ \AA}^{-2}$ and $5.121 \times 10^{-6} \text{ \AA}^{-2}$, respectively.

Table 4-5 Neutron reflectivity parameters used for calculation of the surface coverage of protein at a range of bulk concentrations from 10 to 200 mg/L.

Protein	Bulk conc. (mg/L)	Subphase SLD (ρ_{D_2O/H_2O}) $\times 10^{-6}/\text{\AA}^{-2}$	Protein SLD (layer 1) (ρ_{fitted}) $\times 10^{-6}/\text{\AA}^{-2}$	Protein SLD (layer 2) (ρ_{fitted}) $\times 10^{-6}/\text{\AA}^{-2}$
FIII9'10	10	6.103	5.702	N/A
	30	6.225	5.218	N/A
	100	6.097	4.925	4.929
	200	6.069	4.991	5.094
	wash	6.18	5.077	5.177
d-FIII9'10	10	-0.55	2.006	N/A
	30	-0.55	1.772	N/A
	100	-0.55	2.197	0.459
	200	-0.55	2.636	2.134
	wash	-0.55	2.094	0.213
FIII9''10 H2P	10	6.0189	5.2715	N/A
	30	6.0025	5.2234	N/A
	100	6.0521	4.2225	4.7156
	200	6.0588	4.3574	4.6067
	wash	6.0115	4.7104	4.9932
d-FIII9''10 H2P	10	-0.56	1.4495	N/A
	30	-0.56	1.5258	N/A
	100	-0.56	1.8167	-0.12198
	200	-0.56	1.8728	0.44225
	wash	-0.56	1.8898	0.22314

For the experiments performed at low incubation concentrations of 10 to 30 mg/L a model assuming a monolayer was sufficient however, at higher bulk concentrations, from 100-200 mg/L, a bilayer model best fitted the data. Similar results have been obtained for the adsorption of FIII9'10 to SiO₂ surfaces which showed there was a clear transition to a bilayer at higher concentrations (Kreiner et al. 2009b). It was assumed that the layer thickness of the deuterated and hydrogenated forms of the protein would be the same. By constraining these values the different surface coverage between the two forms of the proteins was evaluated.

The experimental and modelled data for FIII9'10 adsorption at incubation concentrations of 10, 30, 100 and 200 mg/L onto titania (TiO_2) substrate B, and subsequent washing are shown in Figure 4-12 and summarised in Table 4-6.

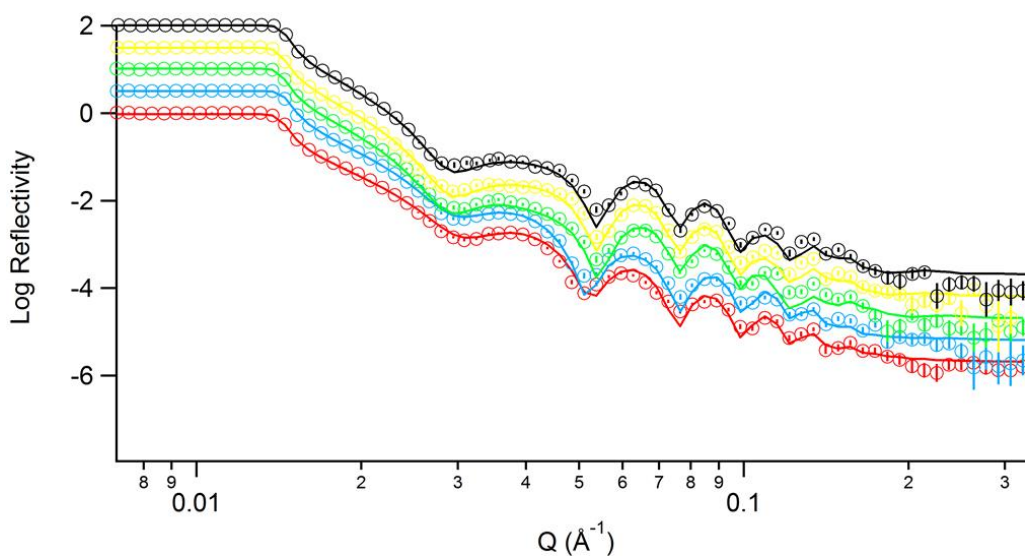


Figure 4-12 Reflectivity profile for FIII9'10 adsorbed to TiO_2 coated silicon substrate surface at bulk concentrations of 10 (red), 30 (blue), 100 (green) and 200 (yellow) mg/L in D_2O phosphate buffer. Data points shown as empty circles with the fitted reflectivity profiles shown as solid lines of the same colour. For clarity, reflectivity profiles for increasing bulk concentrations are sequentially offset in the ordinate by a factor of $\log_{10}0.5$. Surface following washing (black) displayed with highest offset.

Table 4-6 Calculated neutron reflectivity parameters for FIII9'10 adsorbed to TiO_2 obtained from measurements in D_2O phosphate buffer.

Bulk conc. of FIII9'10 mg/L	Layer 1 thickness (Å)	Layer 2 thickness (Å)	Layer 1 protein fraction	Layer 2 protein fraction
10	36.82	N/A	0.130	N/A
30	48.77	N/A	0.314	N/A
100	53.76	23.94	0.380	0.379
200	46.48	38.63	0.353	0.319
Wash	52.82	32.25	0.348	0.317

Increasing the bulk concentration of FIII9'10 from 10 to 30 mg/L showed an increase in both the monolayer thickness and the surface coverage implying a slight increase in the amount of protein at the surface (see Table 4-6). Washing with the D₂O phosphate buffer caused relatively little of the FIII9'10 to desorb from the surface. This was similar to the findings of the solid state CD experiments in which little to no protein was found to desorb from the silica surface and others upon washing.

The axial dimensions of wild type FIII9-10 have been previously determined by NMR and X-ray crystallography to be a length of ~70 Å and a diameter of 24-34 Å (Leahy et al. 1996, Copie et al. 1998). The relative position of the protein was elucidated from a correlation of the calculated layer thickness with the dimensions of the individual protein molecules. For the purpose of this investigation it was reasonable to assume that there would not be a large variation in the overall length and diameter of the mutants FIII9'10 and FIII9''10 H2P compared to the wild type.

Comparison of the calculated layer thickness with the proposed axial diameter of FIII9'10 indicated that at low bulk concentrations the proteins were aligned in the horizontal with the substrate. An increasing layer thickness suggested that with increasing bulk concentration the protein began to orientate vertically with the substrate. As the bulk concentration increased from 30 to 100 mg/L, these proteins formed a bilayer with an initial layer of vertically orientated FIII9'10 complete with a more relaxed, thinner layer of FIII9'10 on top. Increasing from 100 to 200 mg/L saw a reduction in vertical alignment coupled with an increase in layer 2 thicknesses and a decrease in surface coverage. There was very little decrease after washing but it showed a shift in layer thickness with layer 1 increasing and layer 2 decreasing.

The optimum bulk concentration for highest surface coverage was 100 mg/L. A visual interpretation of these results is depicted in Figure 4-13 in which two joined grey ovals represent domain 9 and 10. For simplicity these have been constrained in the same position throughout the pictorial representation. However, in reality, they have a degree of freedom to move at a tilt angle of 12-30° (Leahy et al. 1996).

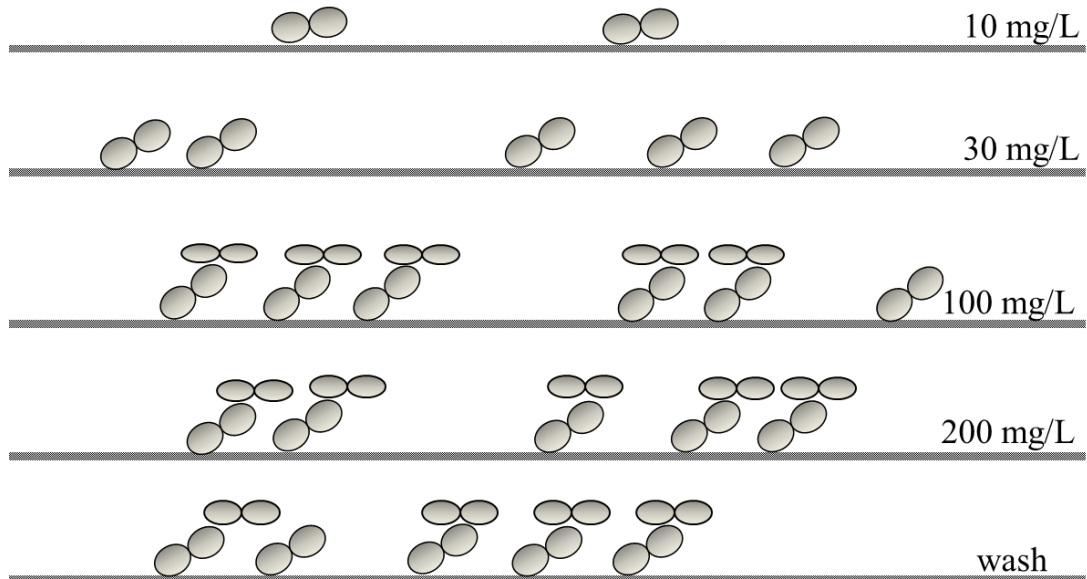


Figure 4-13 Schematic depicting the possible arrangement of FIII9'10 (grey ovals) adsorption following incubation with concentrations of 10 mg/L, 30 mg/L, 100 mg/L, 200 mg/L and following washing at the TiO₂ surface (shown as grey line).

The deuterated d-FIII9'10 was adsorbed to substrate A and showed a similar reflectivity profile (Figure 4-14) to the hydrogenated form (Figure 4-12). Interestingly, even with an offset, the profile for the wash overlapped with that of the 200 mg/L bulk concentration, suggesting that the surface was washed off. Analysis of the fitted data, shown in Table 4-7, confirmed that the surface coverage of layer 2 was reduced following washing. This is in contrast to the results for FIII9'10, which maintained the surface coverage on washing. The layer thickness was constrained to

be the same for d-FIII9'10 as FIII9'10, it was assumed when fitting that it would adopt the same thickness.

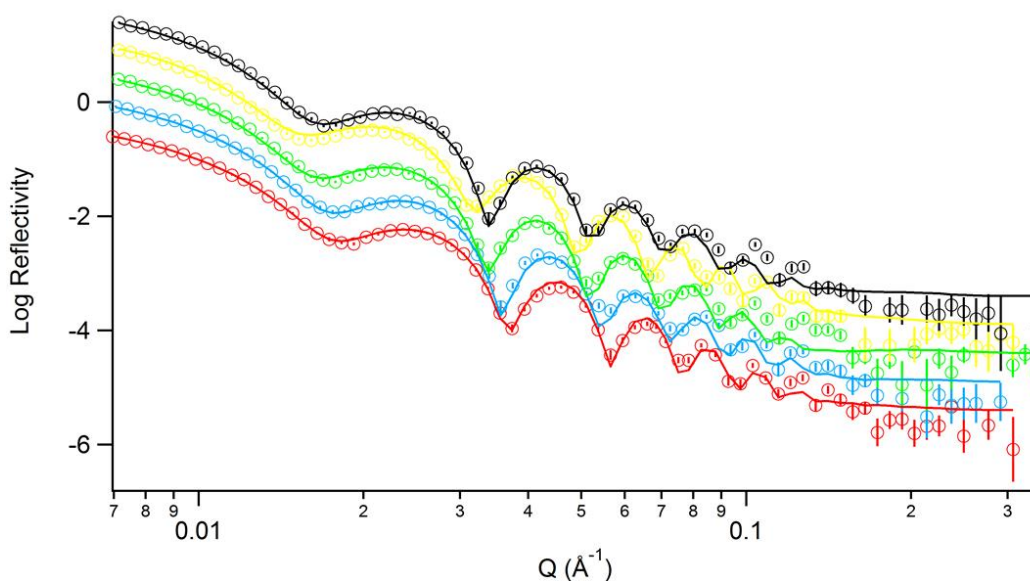


Figure 4-14 Reflectivity profile for d-FIII9'10 adsorbed to TiO₂ coated silicon substrate surface at bulk concentrations of 10 (red), 30 (blue), 100 (green) and 200 (yellow) mg/L in H₂O phosphate buffer. Data points shown as empty circles with the fitted reflectivity profiles shown as solid lines in the same colour. For clarity, reflectivity profiles for increasing bulk concentrations are sequentially offset in the ordinate by a factor of log₁₀0.5. Surface following washing (black) displayed with highest offset.

Table 4-7 Calculated neutron reflectivity parameters for d-FIII9'10 adsorbed to TiO₂ obtained from measurements in H₂O phosphate buffer.

Bulk conc. of d-FIII9'10 mg/L	Layer 1 thickness (Å)	Layer 2 thickness (Å)	Layer 1 protein fraction	Layer 2 protein fraction
10	36.82	N/A	0.451	N/A
30	48.77	N/A	0.409	N/A
100	53.76	23.94	0.484	0.178
200	46.48	38.63	0.562	0.473
Wash	52.82	32.25	0.466	0.135

The layer fraction (surface coverage) of d-FIII9'10 ranged from around 40 to 56 % for layer 1, peaking at 56 % when 200 mg/L bulk concentration was used. The

reduction in surface coverage when 10 to 30 mg/L bulk concentrations were used could have been caused by an increase in the angle relative to the TiO₂ surface causing an increased thickness but decrease in surface fraction. The second layer formed when incubated at a bulk concentration of 100 mg/L only accounted for around 18% of the surface coverage. Although, this increased to around 47% when bulk concentration was increased to 200 mg/L it was easily washed off and the overall protein adsorption appeared to return to a state similar to that at 100 mg/L. This is a strong indication that 100 mg/L was the optimum bulk concentration at which the d-FIII9'10 was adsorbed. The images relating to the possible protein arrangement on the surface are shown in Figure 4-15.

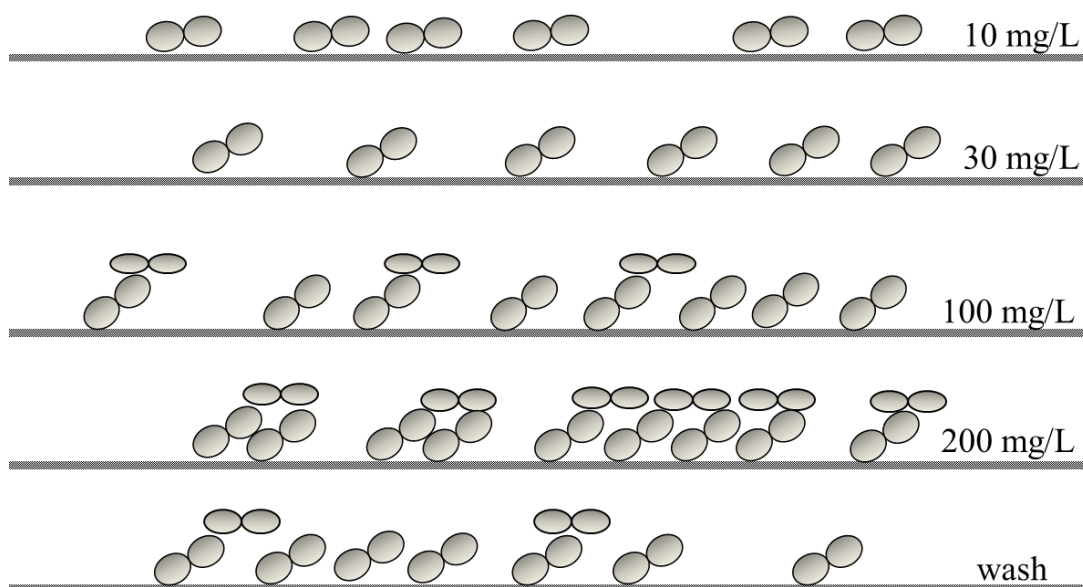


Figure 4-15 Schematic depicting the possible arrangement of d-FIII9'10 adsorption following incubation with concentrations of 10 mg/L, 30 mg/L, 100 mg/L, 200 mg/L and following washing (top to bottom) at the TiO₂ surface (shown as grey line).

The experimental and modelled data for FIII9'10 H2P adsorption at bulk concentrations of 10, 30, 100 and 200 mg/L onto TiO₂ substrate D, and subsequent

washing are shown in Figure 4-16 and summarised in Table 4-8. Due to the unusual artefact at the first incident angle the fitting was restricted to a Q value starting at 0.02. As with all the proteins a bilayer formed when incubated with protein concentrations of 100 mg/L and 200 mg/L. The high layer thickness of 59 and 60 Å at bulk concentration of 100 mg/L and 200 mg/L respectively suggested that the protein was almost at a right angle to the surface as it was nearly the maximum length of the protein (~70 Å). The surface coverage for layer 1 was over 50 % for both 100 mg/L and 200 mg/L bulk concentration and over 40% for layer 2. After washing this was only reduced by around over 10-17%.

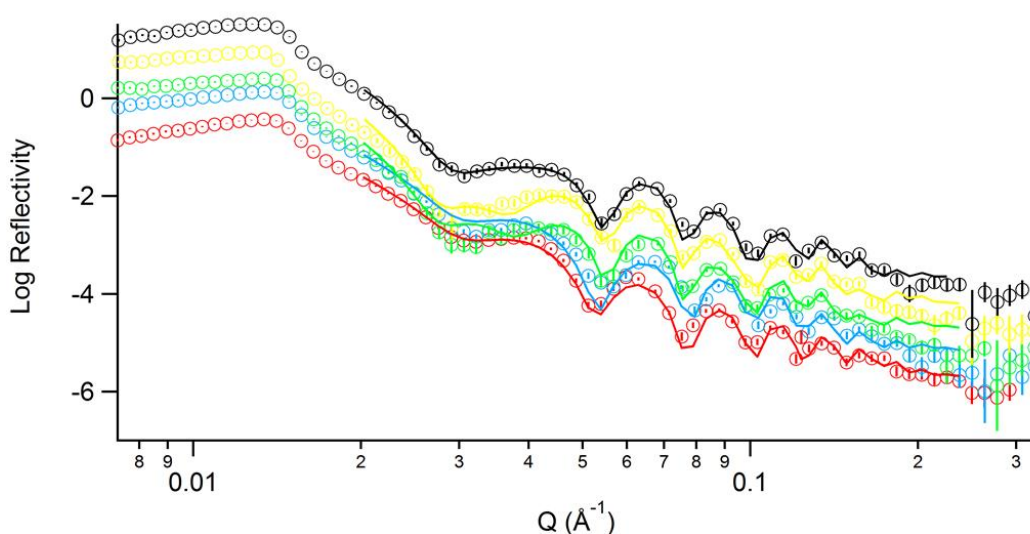


Figure 4-16 Reflectivity profile for FIII9-10 H2P adsorbed to TiO_2 coated silicon substrate surface at bulk concentrations of 10 (red), 30 (blue), 100 (green) and 200 (yellow) mg/L in D_2O phosphate buffer. Data points shown as empty circles with the fitted reflectivity profiles shown as solid lines in the same colour. For clarity, reflectivity profiles for increasing bulk concentrations are sequentially offset in the ordinate by a factor of $\log_{10}0.5$. Surface following washing (black) displayed with highest offset.

Table 4-8 Calculated neutron reflectivity parameters for FIII9^{''}10 H2P adsorbed to TiO₂ obtained from measurements in D₂O phosphate buffer.

Bulk conc. of FIII9^{''}10 H2P mg/L	Layer 1 thickness (Å)	Layer 2 thickness (Å)	Layer 1 protein fraction	Layer 2 protein fraction
10	40.699	N/A	0.249	N/A
30	57.225	N/A	0.261	N/A
100	59.455	37.859	0.602	0.440
200	60.601	36.424	0.559	0.477
Wash	49.038	42.547	0.434	0.340

Analysis of the NR data for FIII9^{''}10 H2P showed it to have an increased layer thickness over the range of bulk concentrations compared to FIII9'10. Even at a bulk concentration of 10 mg/L the thickness was greater than the largest point in the diameter of the molecule. This could indicate that the protein is in fact larger than the wild type FIII9-10, which could be because the mutation is in the exposed loop of the 9th domain. It could also be that the increased conformational stability of FIII9^{''}10 H2P allowed for it to adsorb to the surface in a more rigid fashion causing it to have an increased angle at the surface. The images proposed in Figure 4-17 are for a scenario in which the angle is increased. The layer fraction for a bulk concentration of 10 mg/L was nearly twice as high for FIII9^{''}10 H2P compared to FIII9'10. This was only slightly increased when bulk concentration was increased to 30 mg/L. The image shows a relatively even spread of protein molecules over the surface however, the NR data does not differentiate between an evenly spaced surface and a surface with several small tightly packed clusters of protein spread over the 26% of the substrate.

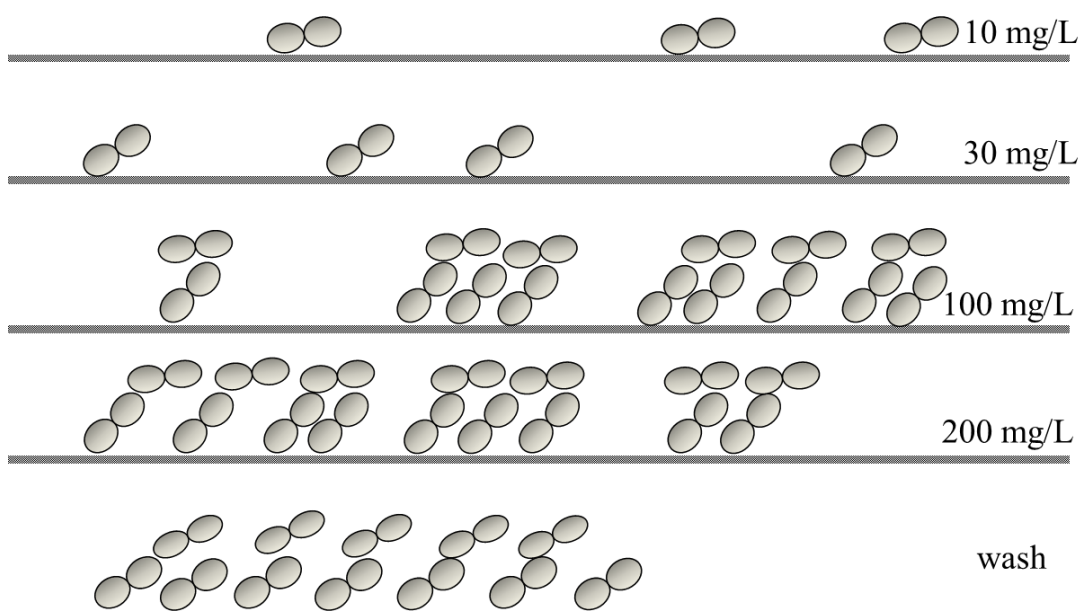


Figure 4-17 Schematic depicting the possible arrangement of FIII9'10 H2P adsorption following incubation with concentrations of 10 mg/L, 30 mg/L, 100 mg/L, 200 mg/L and following washing (top to bottom) at the TiO₂ surface (shown as grey line).

Similarly to the d-FIII9'10, d-FIII9''10 H2P had an increase in surface coverage at low bulk concentrations compared to the hydrogenated form. The reflectivity profile, Figure 4-18, of d-FIII9''10 H2P on substrate C has many overlapping fringes and an interestingly high surface coverage at a bulk concentration of 10 mg/L. As with substrate D, the fitting was restricted and started at a Q value of 0.02. The summarised results, shown in Table 4-9, indicated the maximum layer fraction at the higher bulk concentrations of d-FIII9''10 H2P, 100 mg/L and 200 mg/L was significantly less than for FIII9''10 H2P. The layer 2 was less than 10 % for 100 mg/L rising to around 18 % for 200 mg/L then reduced to roughly 14 % after washing. This is distinctly different than the results for FIII9''10 H2P which maintained a high surface coverage for the second layer.

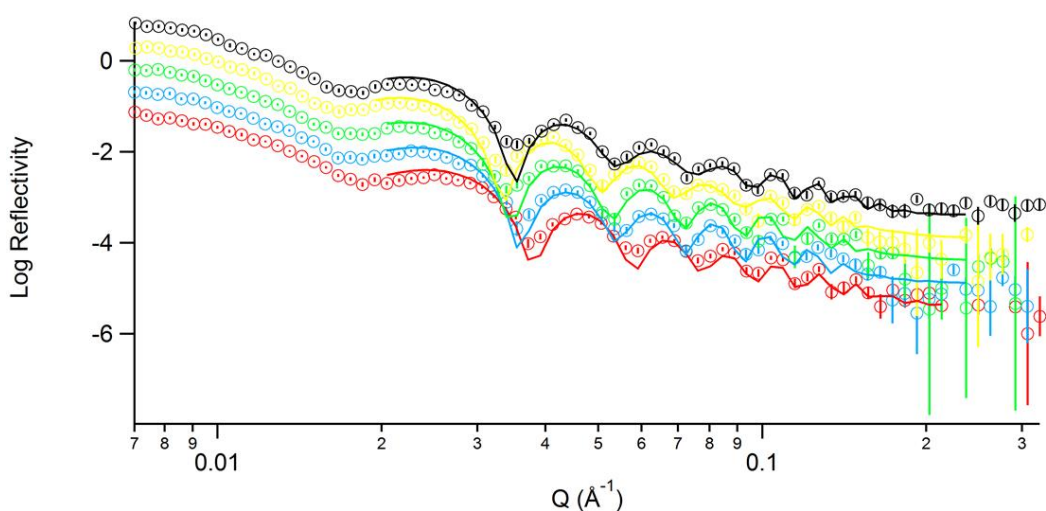


Figure 4-18 Reflectivity profile for d-FIII9''10 H2P adsorbed to TiO₂ coated silicon substrate surface at bulk concentrations of 10 (red), 30 (blue), 100 (green) and 200 (yellow) mg/L in H₂O phosphate buffer. Data points shown as empty circles with the fitted reflectivity profiles shown as solid lines in the same colour. For clarity, reflectivity profiles for increasing bulk concentrations are sequentially offset in the ordinate by a factor of log₁₀0.5. Surface following washing (black) displayed with highest offset.

Table 4-9 Calculated neutron reflectivity parameters for d-FIII9''10 H2P adsorbed to TiO₂ obtained from measurements in H₂O phosphate buffer.

Bulk conc. of d-FIII9''10 H2P mg/L	Layer 1 thickness (Å)	Layer 2 thickness (Å)	Layer 1 protein fraction	Layer 2 protein fraction
10	40.699	N/A	0.354	N/A
30	57.225	N/A	0.367	N/A
100	59.455	37.859	0.418	0.077
200	60.601	36.424	0.428	0.176
Wash	49.038	42.547	0.431	0.138

The schematic representation of the possible protein arrangement of d-FIII9''10 H2P at the TiO₂ surface is shown in Figure 4-19. Their layer thicknesses were the same as that for FIII9''10 H2P but the surface coverage ranged from around 35 % to about 43% for layer 1. The low variation in surface coverage over the varying concentrations was unusual compared to the other proteins studied.

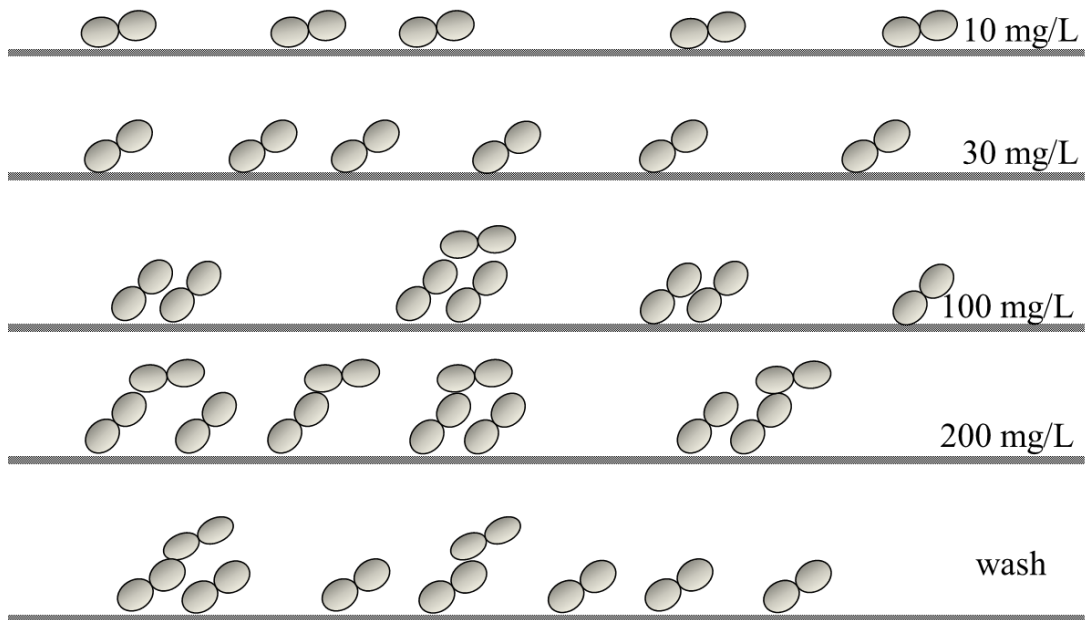


Figure 4-19 Schematic depicting the possible arrangement of d-FIII9'10 H2P adsorption following incubation with concentrations of 10 mg/L, 30 mg/L, 100 mg/L, 200 mg/L and following washing (top to bottom) at the TiO₂ surface (shown as grey line).

The surface coverage of FIII9'10 and FIII9''10 H2P on TiO₂ substrates generally had greater coverage when incubated with a bulk concentration of 100 mg/L, hence this was the value used for cell culture experiments on TiO₂ coated glass coverslips.

4.5.3 Functional analysis of the FIII9-10 mutants

The structural stability, conformation and surface coverage of FIII9'10 and FIII9''10 have been confirmed by the above results included in this chapter. Therefore the next step was to confirm that the proteins still functioned as ligands to integrin $\alpha 5\beta 1$ and as a useful substrate for cell attachment.

4.5.3.1 ELISA assay with $\alpha 5\beta 1$

Initial functionality of the FIII9-10 mutants was determined by the binding of FIII9-10 ligands to integrin $\alpha 5\beta 1$ as measured by ELISA. One site specific binding dose response curves for FIII9-10, FIII9'10 and FIII9''10 H2P were fitted using nonlinear regression (Figure 4-20). Analysis showed that the binding of FIII9'10 and FIII9''10 H2P was not impinged by the addition of the mutations however; it also displayed no improvements on FIII9-10.

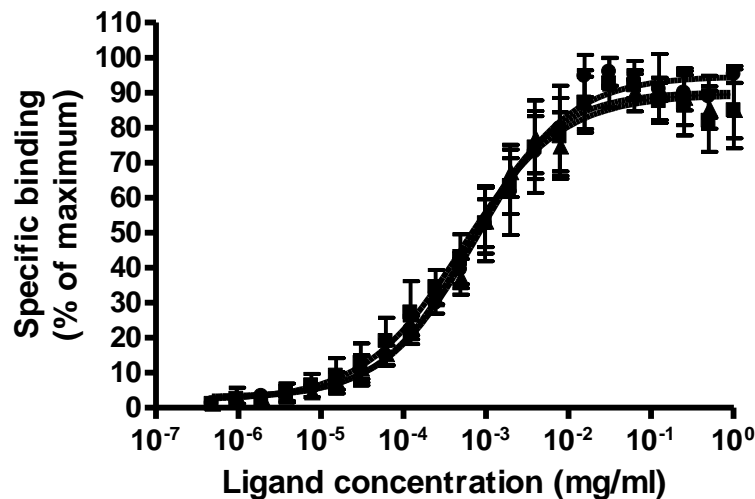


Figure 4-20 Binding of FIII9-10 (■), FIII9'10 (▲) and FIII9''10 H2P (●) to integrin $\alpha 5\beta 1$ as measured by ELISA. Results are normalised and expressed as percentages of maximum binding activity.

The dissociation constant (K_d) calculated from one site specific binding analysis, were found to be 4.2×10^{-4} ($\pm 6 \times 10^{-5}$) for FIII9-10, 5.2×10^{-4} ($\pm 6 \times 10^{-5}$) for FIII9'10 and 6.3×10^{-4} ($\pm 8 \times 10^{-5}$) for FIII9''10 H2P. Comparison of the binding for the three ligands by Friedman's test concluded that the data was not significantly different ($P= 0.83$). The ELISA results were for binding of a solution containing either FIII9-10, FIII9'10 or FIII9''10 H2P to the immobilised ligand, $\alpha 5\beta 1$, therefore

increased conformational stability of the mutated protein fragments may not be expected to lead to an increase in binding affinity.

4.5.3.2 BHK adhesion assay

As binding to integrin $\alpha 5\beta 1$ was found to be functioning, the next logical step was to test the protein fragments using BHK fibroblast cells. Cells were found to adhere to the surfaces coated with all of the FIII9-10 proteins in a similar range, showing adhesion from concentrations starting from as low as 1 $\mu\text{g/ml}$ (Figure 4-21). Binding to uncoated surfaces was limited, the absorbance value obtained for this was consequently subtracted from the overall absorbance to compensate for any unspecific binding of the cells.

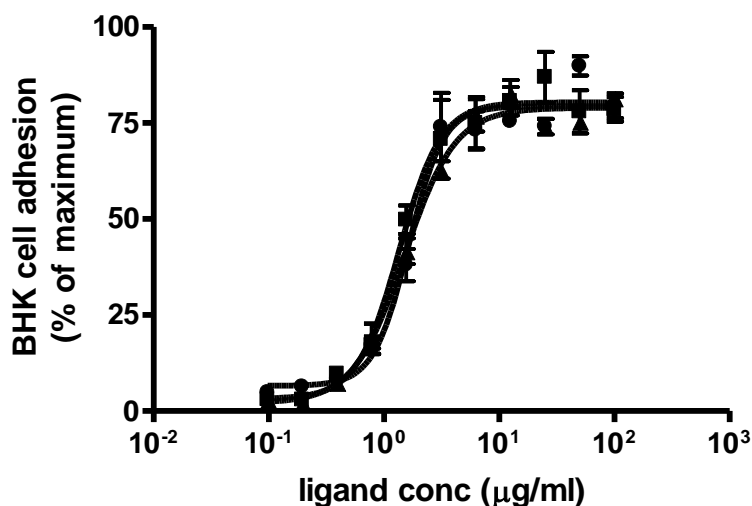


Figure 4-21 BHK cell adhesion data for surfaces coated with FIII9-10 (■), FIII9'10 (▲) and FIII9''10 H2P (●). Error bars represent the sample standard deviation.

Similarly to the ELISA analysis this cell culture assay displayed data that was not significantly different, confirmed by Friedman's test ($P=0.7321$). Each of the proteins had a similar K_d : 1.5 (± 0.4) for FIII9-10, 1.7 (± 0.4) for FIII9'10 and 1.7 for FIII9''10 H2P (± 0.4) for FIII9''10 H2P. The standard error was such that any apparent difference in value was negated. This was contrary to previous work which had found cell attachment to improve for FIII9'10 compared to the wild type FIII9-10 (van der Walle et al. 2002).

4.5.3.3 Non-specific protein adsorption to titania surfaces as measured by immunofluorescence

As determined by the NR studies the FIII9'10 and FIII9''10 H2P were known to form a bilayer at the TiO_2 surface at concentrations of 100 mg/L after an incubation of 30 min. It was therefore assumed that the FIII9-10, FIII9'10 and FIII9''10 H2P would form a similar adsorption pattern after incubation for 60 min on the TiO_2 coated glass substrates. The water contact angle for the TiO_2 surfaces was measured to be $68.7^\circ (\pm 4)$ which suggested that the surfaces were relatively hydrophilic.

BHK cell attachment to TiO_2 coated glass coverslips was visualised by immunofluorescence, the colour of the original images was inverted to aid contrast the original images can be found in Appendix B. The staining of the vinculin focal adhesions (blue) was obscured by the brightness of the fluorescein-phalloidin staining for the actin stress fibres (pink). Due to this affect an attempt was made to optimise fluorescein-phalloidin dilution and a range was used from 10-25 $\mu\text{g/ml}$ however, image clarity was lost at the lower concentrations hence the higher

concentration of 25 $\mu\text{g/ml}$ was used. The image software allowed for zoom-in on interesting features which gave a variation in the scale for the images at 63x magnification.

Cells incubated with surfaces lacking any protein coating showed marginal cell attachment after 60 minutes. The image shown in Figure 4-22 was typical of the entire surface. Only a few individual small cells were found in which only the nucleus could clearly be visualised. At lower magnification the majority of the cells lacked clear focal adhesions and organised actin stress fibres however some focal adhesions could be seen in blue on the image at 63x magnification.

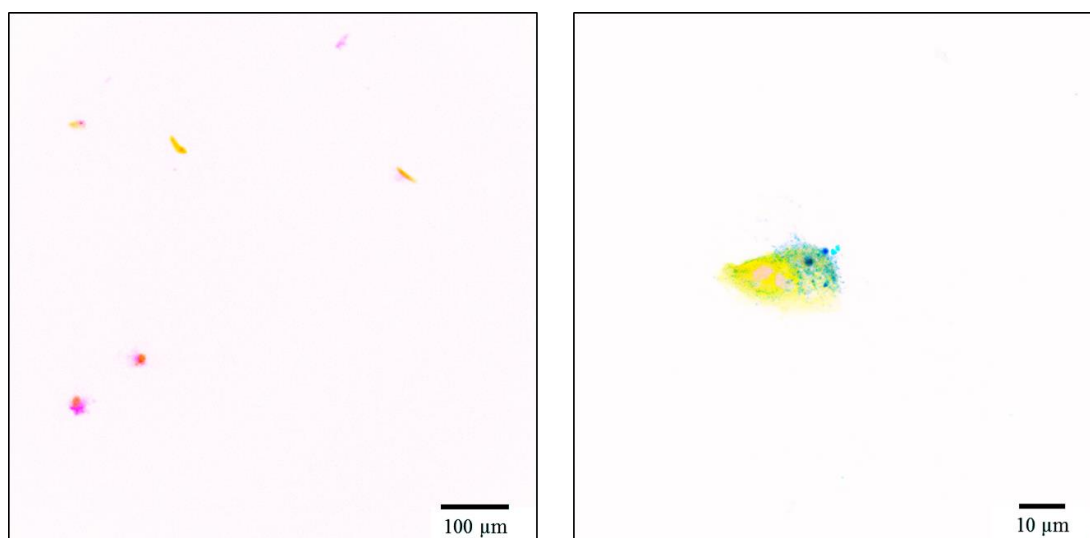


Figure 4-22 Immunofluorescence image showing BHK cell attachment onto untreated TiO_2 substrate stained for vinculin (blue), actin (pink), and the nuclei (yellow). Images are shown with colour inverted to aid contrast and were photographed at 20x magnification (left) and 63x magnification (right).

Comparison of the untreated surfaces cell growth with the treated showed significantly more cell attachment for FIII9-10, FIII9'10 and FIII9''10 H2P coated surfaces. Cells were seen in various states of attachment and spreading in Figure

4-23, as before the images chosen each represented a typical example of the entire surface. The zoomed-in images were each selected as they portrayed a slight variation of the features that were present on all three of the surfaces.

The cells attached to the FIII9-10 coated surfaces (section A of Figure 4-23) featured several groupings of 5 to 8 cells together that were large and well spread. The focal adhesions and actin stress fibres were clearly visible. The close up of the cell indicated that they featured mostly small focal adhesions which were seen throughout the area of the cell and along the perimeter of the spread cell. Several small rounded individual cells and areas of no cell adhesion were also captured in the image.

The BHK cell adhesion to FIII9'10 coated substrate were similarly spread in different directions with actin stress fibres spanning the length of the cell. At higher magnification very pronounced stress fibres were seen to be curving round the right side of the cell in a crescent shape. FIII9''10 H2P coated surfaces featured large cells with some large focal adhesions. The small cell in the top right corner of the 63x magnification image displayed a large gathering of vinculin at the edge of an apex of the cell. Generally the cells were spread in unevenly several directions but there were also some circular type cells. The images featured in Figure 4-23 C contained shortened stress fibres compared to the other cells.

The immunofluorescence images only suggested slight differences which could be seen between the differently coated surfaces. For example, in the FIII9-10 coated surfaces there appeared to be more areas without cell coverage and the cells were generally found more in clusters. The FIII9'10 and FIII9''10 H2P substrates,

however, tended to have a relatively even distribution of attached cells. It must be noted that without accurate quantification these results cannot be confirmed statistically and only give a suggestion as to the behaviour of the cells on the different surfaces.

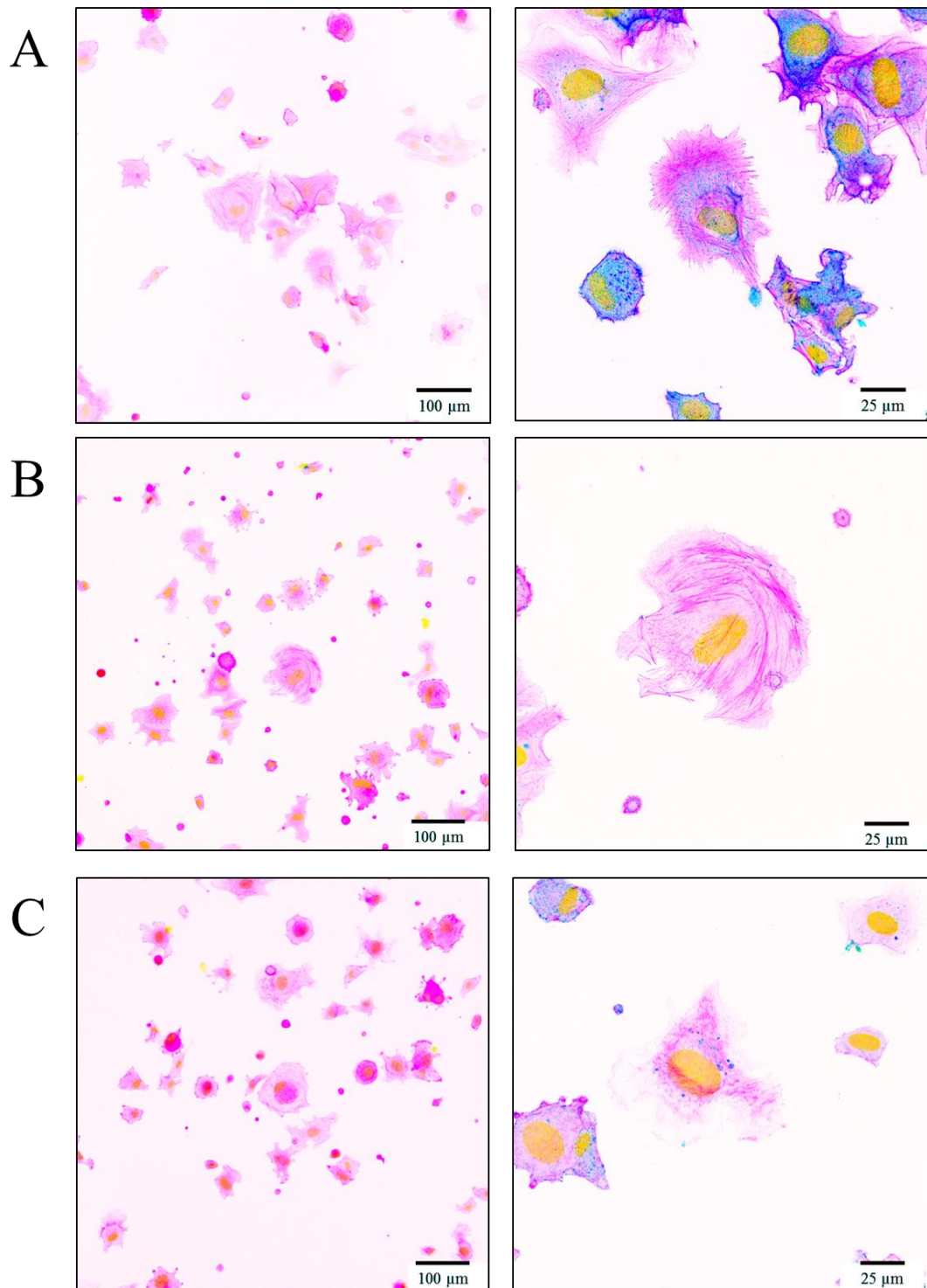


Figure 4-23 Immunofluorescence image showing BHK cell attachment onto TiO_2 substrate coated with either 100 $\mu\text{g/ml}$ FIII9-10 (A), FIII9'10 (B) or FIII9''10 H2P (C). Cells were stained for vinculin (blue), actin (pink), and the nuclei (yellow). Images are shown with colour inverted to aid contrast and were photographed at 20x magnification (left) and 63x magnification (right).

4.6 Discussion

The complex process of adsorption of a protein in solution to a solid surface is driven by a combination of surface protein interactions including van der Waals forces, electrostatic and hydrophobic interactions (Norde et al. 1986). There are many factors to consider such as the surface hydrophobicity, chemical composition and surface roughness, in addition to these the protein structure and stability which will have an effect on the overall adsorption characteristics. Adsorption of proteins to TiO₂ surfaces has been shown to be mostly irreversible and can occur spontaneously from solution (Pegueroles et al. 2012).

4.6.1 Surface wettability effects on protein conformation

Surface hydrophobicity was the main focus of the initial work. A water contact angle of greater than 90° was considered to be characteristic of a hydrophobic surface (Giovambattista et al. 2007). Surfaces were synthesised to give a range of water contact angles from 40 to nearly 100° to represent the range of possible surfaces that a protein may come into contact with. Cell culture plasticware is hydrophilic (contact angle of ~ 69°) however, it has relatively poor wettability. Therefore the selection of silanized surfaces used here were a poor representation for culture plasticware. However, useful information can still be gained from studying the conformation over such a range of surfaces. The bare glass coverslip surface may not have been sufficiently rinsed, leaving traces of piranha solution on the surface, which could explain why the values for the water contact angle was around 7-15° larger than the

literature value of $\sim 29^\circ$ for similar glass coverslips (Lamprou et al. 2010). It is unlikely that the functionalised PFTOS surfaces were homogenous as the calculated standard deviation was high (± 11). It would be useful to have a topographical study of the surfaces to understand the functionalization better.

Circular dichroism analysis of the conformation of the proteins provided some interesting results, mainly that there was no clear correlation between the degree of hydrophobicity of a surface and the retention of conformation of the protein fragments. It must be stressed that even a slight variation in the spacing and relative angle or even sequence separating the 9th and 10th type III FN domains will result in a decrease of bioactivity compared to full length FN (Grant et al. 1997, Altroff et al. 2004).

As expected, the wild type FIII9-10 displayed a large loss of secondary structure upon adsorption to all of the surfaces which is supported by previous findings (Pereira et al. 2008). FIII9'10 and FIII9''10 H2P spectra intensity varied and was lowest for the more hydrophobic surfaces but the conformation, although altered, generally retained the characteristic β -sheet. For some of the surfaces for both the FIII9'10 and FIII9''10 H2P proteins there was an increase in the peak around 226 nm, this region is associated with aromatic contributions suggesting that the unfolding or rearrangement of the proteins on the surface could make them more exposed and hence contribute to the increase in peak height.

It was clear from the denaturing data in section 3.5.2 that the FIII9''10 H2P mutant was more resistant to unfolding, it would then be expected that when adsorbed to surfaces it will be able to retain its native structure to a greater extent than the other

forms. However, this was not always the case. Conformational changes were greatest on the mPEG functionalised surface which was relatively hydrophilic. Antifouling surfaces coated in mPEG have shown minimal non-specific protein adsorption (Prime and Whitesides 1993), it is thought that tightly bound water molecules on hydrophilic antifouling surfaces form a “water barrier” which the protein cannot remove (Li et al. 2005). The mutation of His1377 to Pro in FIII9’10 H2P changed a positively charged His residue on the exposed loop of the 9th domain to a non-polar Pro which is unlikely to participate in hydrophilic interactions. PEG-functionalised surfaces are known to promote non-fouling behaviour dependent on the chain length and packing density (Li et al. 2005). The mPEG used in this investigation was relatively low molecular weight and had a shorter chain length which may be responsible for the surface adsorption of FIII9-10, FIII9’10 and FIII9’’10 H2P. Small proteins (~16 kDa) have been shown to penetrate between PEG chains and adsorb to surfaces presenting a low PEG packing density (Michel et al. 2005). FIII9-10 and the mutants had a molecular weight of around 21 kDa and so may be able to operate in the same manner. FIII9’10, which maintains the His amino acid may find it easier to interact with the water barrier on the mPEG surface and hence retain the conformation on the mPEG surfaces.

The hydrophobic nature of the surface is a key factor in protein adsorption, however it is one of many driving forces that influence the unfolding of a protein on a surface. Any interactions between the silane terminal functional group and the surface of the protein will also be an influencing factor. The hydrophobic properties of the surfaces were determined by the silane terminal groups which face the air/surface interface and interact with water for contact angle measurements. The two hydrophobic

surfaces each presented different chemical end groups, an octyl and a perfluorooctyl for TCOS and PFTOS respectively. The more hydrophilic groups presented and amine terminal group (APTMS) and a methoxy terminal group (mPEG). It has been previously reported for a FN protein fragment consisting of domains FIII7 to FIII10 (FIII7-10) that change in conformation was greatest on surfaces presenting the end group CH₃ which in that study had the highest hydrophobicity. They also reported that the surface conformation did not correlate to hydrophobicity for amine terminal group (Michael et al. 2003).

Although intended as a substitute to represent substrates of different hydrophobicity the resultant surfaces are poor representatives because they are only focusing on the wetting ability and not taking the impact of the different functional groups into consideration. The silanized surfaces provide useful information however there are more variables to consider than simply wetting ability of the substrate. Due to the absorption effects of high salt content on CD spectra all scans were performed with protein adsorbed beads suspended in water. One important factor that was not investigated using CD was protein concentration. This can have a direct effect on protein organisation by influencing orientation, conformation and packing arrangement, however this was explored by neutron reflectometry.

4.6.2 Protein adsorption to titania surfaces

Biomedical devices are commonly constructed from titanium and titanium alloys because they have good fatigue strength, corrosion resistance and biocompatibility

(MacDonald et al. 2002, Liu et al. 2004). The layer of the titanium biomedical device which will be in contact with tissue consists of TiO_2 which will influence the biocompatibility of the implant. Several studies have explored the effects of pre-treating the implant surface with integrin binding peptides to enhance biocompatibility, RGD grafted on to titanium rods have displayed increase bone thickness in *in vivo* testing in rats (Ferris et al. 1999). *In vivo* osteoblastic differentiation was further improved by utilising FIII7-10, which showed a 3-fold enhancement compared to RGD grafted implants in rats, this was attributed to the preferential binding of FIII7-10 to integrin $\alpha 5\beta 1$ (Petrie et al. 2008). In both these studies, a degree of control on the protein or peptide adsorption was exerted by using gold-thiol chemistry or a polymer coating. For our work the non-specific adsorption of protein onto TiO_2 surfaces was examined.

Full length FN has been shown to reach its maximum concentration for adsorption onto TiO_2 following only 30 min incubation time (i.e. the concentration of adsorbed FN does not increase significantly after 30 min incubation), irrespective of surface hydrophobicity (MacDonald et al. 2002). In the NR experiments the protein solution was incubated with the surface for 30 min and so it was assumed that the maximum adsorption would have occurred. On surfaces with poor wettability that have a water contact angle of $\geq 60^\circ$ surface protein interaction tends to be driven by a two-step process. The initial stage is rapid and occurs within a time range of seconds to minutes in which the protein interacts with the substrate surface. This is followed by a second slower stage in which the hydrophobic core of the protein becomes exposed to the surface, this point can involve conformational changes within the protein (Xu and Siedlecki 2007).

The NR experiments gave an insight into the thickness and the volume fraction of the adsorbed protein layers allowing for structural assumptions to be made for the proteins (i.e. if native structure or denatured state). This was very useful for the TiO₂ surface as we did not have access to TiO₂ coated silica beads and could not analysis the structure by solid state CD (it should be noted that the slightly opaque nature of the TiO₂ plated slides used for immunofluorescence suggested that silica beads would not be suitable for measurement). Although the water contact angle for the NR substrates was not known it was assumed that they were slightly hydrophilic and in turn the proteins would retain their structural conformation. The surface coverage of all of the proteins studied (FIII9'10, d-FIII9'10, FIII9''10 H2P and d-FIII9''10 H2P) was found to be concentration dependant and a bilayer was only formed at higher protein concentrations (≥ 100 mg/L), similarly, a concentration dependence was displayed for BSA on TiO₂ as measured by spectroscopic ellipsometry (Wehmeyer et al. 2010). Interestingly the second layer formed from the FIII9'10 proteins, both hydrogenated and deuterated forms, was slightly “flattened” compared to the native dimensions for the protein. Proteins adsorbing from high concentrations have been known to become compressed and molecules with different degrees of unfolding coexisting (Pegueroles et al. 2012). The average surface value obtained from the NR therefore may not be a sufficient representation of the different forms which will be coexisting. FIII9''10 H2P protein layers exhibited less “flattening” in the bilayer; this could be attributed to the increased conformational stability, making it more resistant to exposure of the hydrophobic core. It is understood that the addition of proline substitutions to give β -turns decreases the entropy of the denatured state and hence increase stability (Fu et al. 2009).

UV illumination of TiO₂ surfaces has been shown to increase the surface wettability to the point that water contact angle as low as 0° have been achieved on single crystal surfaces of TiO₂ (Wang et al. 1999). Although, this process has been found to be reversible in some cases by storing the substrates in the dark overnight (Wang et al. 1999). Ozone treatment is commonly used to clean surfaces prior to NR measurements but it can also induce super-hydrophilicity on TiO₂ surfaces (Mills and Crow 2008). The handling and cleaning process of the TiO₂ surface may affect the wettability and hence the protein adsorption. Protein adsorption to a hydrophobic surface can be stronger than for a hydrophilic (Arima and Iwata 2007) and therefore washing may displace the protein more effectively on a super-hydrophilic surface created by the cleaning process for the TiO₂ substrates. Further to this, higher adhesion has been found on surfaces of a slightly hydrophobic nature with a water contact angle of $\geq 60^\circ$ that display poor wetting ability (Xu and Siedlecki 2007).

IEF was employed to investigate the difference between deuterated and hydrogenated proteins which could possibly explain the difference in surface coverage. However, the poor resolution of the IEF strips meant that any differences between the proteins could not be accurately distinguished. An accurate value for the pI of the proteins would have been very useful to these studies because proteins have been shown to have the highest and most rapid adsorption from buffers which are close to their pI (Wehmeyer et al. 2010). From the Pepstats information calculated in section 2.5.2 it was assumed that the pI of FIII9'10 was around 8.1 and the pI of FIII9''10 H2P was 8.0.

Data mining has been used to ascertain any structural effects due to deuteration of 26 small molecule structures and it concluded that there were only small differences in a select few (Fisher and Helliwell 2008). However, exchange to a deuterated solvent may lead to slight changes in mechanical properties of the protein. Ribonuclease A, for example, displays a shift in transition temperature when measured by DSC by 4 °C from hydrogenated solvent to deuterated solvent, it displayed a stronger and more compact hydration in D₂O plus increase in protein compactness (Sasisanker et al. 2004). Slight differences in the protein properties in D₂O compared to H₂O may be the reason for the variation in surface coverage.

4.6.3 Functional analysis of proteins

As confirmed by the ELISA assay the proteins all retained their ability to bind to integrin $\alpha 5\beta 1$. The binding of integrin $\alpha 5\beta 1$ is a key factor in the adhesion (Cutler and Garcia 2003) and so by investigating integrin binding it gave an indication of the efficiency of the protein performance when in contact with cells. The substitution of Pro for His occurs in the PHSRN synergy region of domain 9 and so it was especially important that the integrin binding studies were successful. It has been shown that the key amino acid in the PHSRN sequence is the R¹³⁷⁹, however for optimum efficiency all 5 are required (Aota et al. 1994). Overall the integrin binding studies were successful but it was unexpected that there was no observed improvement in the cell attachment studies for the BHK cells as seen previously (van der Walle et al. 2002). However, our studies did not ascertain the number of spread

cells compared to “round” cells as a means of differentiating the attachment and so we cannot confidently say there was or was not a difference in attachment.

The attachment of a cell to a substrate can occur when a surface integrin, in our case $\alpha 5\beta 1$, interacts with a binding partner (RGD and PHSRN components of FIII9-10, FIII9’10, FIII9’’10 H2P). FN is of particular interest because it is very important in determining the shape of a cell as the actin cytoskeleton will become aligned with exogenous FN (Becker et al. 2006). In the case of fibroblast cells, movement occurs in three main steps: (i) initial projection of the leading edge of the cell; (ii) adhesion to the substrate at the “front end” with simultaneous detachment at the “rear end”; (iii) forward-pull of the cell by cytoskeletal contractions (Ananthakrishnan and Ehrlicher 2007). The different steps will present as different morphologies of the cells.

Cell attachment to the TiO_2 substrates coated with either FIII9-10, FIII9’10 or FIII9’’10 H2P was demonstrated morphologically by the spreading of the cells and confirmed by the production of focal adhesions where the cytoplasm is in close contact with the substrate. The degree of focal contact was visualised by staining for vinculin which was shown by a red colour under immunofluorescence (shown in blue in Figure 4-22 and Figure 4-23). The three substrates had a similar distribution of vinculin both on the periphery of the cells and throughout. The formation of actin cytoskeleton suggested organisation of the cell as they extended across the length of the spread cells. In all cases the coated substrates had increased cell attachment compared to a “blank” uncoated control. These results demonstrated that prominent formation of focal adhesions and cytoskeletal organisation were possible by seeding

cells onto TiO₂ substrates coated with FIII9-10, FIII9'10 and FIII9''10 H2P. From the NR experiments we can suggest that the surface coating of the substrates by the proteins may be around 38-60% and a bilayer will be formed. Unfortunately from these initial experiments it could not be determined if the different proteins gave an improved attachment of cells because the numbers were not verified. This is something that would have been done had time permitted.

Lin and co-workers (2011) developed a glutathione S-transferase-tagged (GST-tagged) FIII8-11 protein for the study of fibroblast cell survival on plasticware. The presence of an amino-terminal GST-tag has been shown to significantly improve protein surface adsorption to plasticware (Wang et al. 2005). They found that although initial cell attachment of FN-null cells over the first 24 hours was positive and comparable to full length FN, FIII1-11 and FIII8-v15 after 24 hours cells began to autophagy followed by apoptosis at 72 h (Lin et al. 2011). Suggesting that the protein could not maintain the cell attachment properties.

It was important that serum-free media was used for the incubation onto TiO₂ surfaces because previous studies have demonstrated that for full length FN there can be a significant displacement of the protein by the components of the serum (Middleton et al. 2007). Another important consideration was the change in pH of the buffers, for initial adsorption the proteins were in phosphate buffer (pH 6). The TiO₂ surface will be negatively charged at pH of above ~6.2 (Topoglidis et al. 2001) and hence the surface will undergo a change in charge when the pH 6 buffer is exchanged for pH 7.4 PBS on washing. Although the change in pH should have limited effect on the protein the change in surface charge may influence adsorption.

This may be mitigated by the patches of differently charged areas on the protein itself (Topoglidis et al. 2001).

Surface patterning was an area which was overlooked in the present study. Nanophase ceramics were found to adsorb greater quantities of vitronectin which may have contributed to enhanced adhesion of osteoblasts; this adsorption was dependent on the surface topography and independent of surface chemistry. It was suggested that the difference in surface roughness may affect adsorbed protein conformation and therefore the availability of the active domains (Webster et al. 2000). Although the surface roughness was measured for NR and integrated into the data fitting, it was assumed that the TiO₂ coated glass slides all had a similar topography and it was not investigated as a defining factor in protein adsorption and subsequent cell attachment.

4.7 Summary

Protein adsorption is a complex process and some of the elements involved were investigated in this present study. This included surface wettability, which was found to be a significant factor in conformation of adsorbed proteins, however the effects of surface chemistry should not be overlooked and played a definitive role in the organisation of the conformational stable FIII9''10 H2P protein fragment. Protein adsorption onto titania surfaces is equally complex and has many defining factors. Here we confirmed that surface coverage is concentration dependant with bilayers of protein forming above 100 mg/L concentrations. The functional activity of FIII9'10 and FIII9''10 H2P was retained after mutation, shown by ELISA and cell culture

assays. Overall, we could not differentiate between the different variations of the protein by activity; however, further analysis may be able to shed light on this.

CHAPTER 5. Exploring multimeric integrin ligands

5.1 Introduction

The main focus of this thesis up to this point has been the development of non-specifically adsorbed FIII9-10 based proteins as scaffolds for cell attachment and spreading. The objective was the enhancement of conformational stability of the protein to reduce adsorption induced changes that may occur which can decrease functionality. However, ligand density and orientation should not be ignored, as they too are important for cell adhesion and spreading. Investigations into surfaces which present a controlled number of RGD peptides have shown that cell migration and actin polymerisation were greater on surfaces presenting cluster of ligands (Maheshwari et al. 2000, Koo et al. 2002). A reduction in required ligand density necessary to support cell migration was found for clustered ligands displaying RGD (Maheshwari et al. 2000). Nanoscale clusters of RGD containing peptide immobilised onto a polyethylene oxide presented a range ligand densities with improved adhesion properties on clusters displaying 3.6 and 5.4 RGD motifs (Koo et al. 2002). These studies demonstrated that for optimum cell integration with a surface the integrin ligands require to be presented as grouped together rather than homogeneously dispersed on a surface.

Prior to this work, multimeric clustered integrin $\alpha 5\beta 1$ ligands displaying FIII9'10 were produced (Kreiner et al. 2008). These “multimers” consisted of mutant leucine zipper-derived coiled-coils which promoted self-assembly of FIII9'10 domains on

IgG-derived spacers (Figure 5-1). The function of the spacers was to facilitate ligand motility by minimising steric hindrance. The multimers presented 2, 3 or 4 FIII9'10 ligands and hence were termed dimer, trimer and tetramer. Another useful feature of the multimers which facilitated directed binding to gold (Au) surfaces was the C-terminal cysteine which allowed for covalent bonding via a free thiol bond in the presence of the reducing agent TCEP. These were fully characterised and found to have increased attachment and spreading of fibroblast cells compared to the monomeric unit, FIII9'10-GGC (Kreiner et al. 2008, Kreiner et al. 2009a). More recently the multimers have been shown to give improved spreading of human endometrial stromal cells (EnSCs) when specifically orientated using biotin (Li et al. 2011).

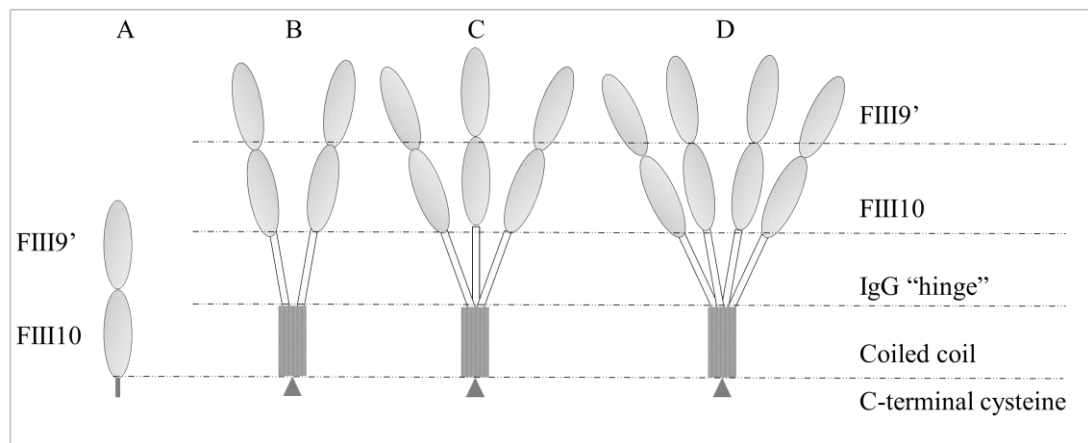


Figure 5-1 Schematic of the ligands FIII9'10-GGC (A), FIII9'10-dimer (B), FIII9'10-trimer (C) and FIII9'10-tetramer (D). Each "portion" of the multimeric ligand is described and dashed lines are a visual aid to help distinguish between sections. For simplicity the coiled-coils are drawn as one block.

The multimeric ligands can be specifically orientated by covalently bonding to Au surfaces, this is of use for areas such as biosensors by mimicking cell surfaces to

measure protein-protein interactions or cell adhesion (Cornell et al. 1997). A surface of Au alone is hydrophobic and has high potential energy which instigates denaturation of proteins. This can be compensated for by pre-treating the surfaces with a short chain thiol such as β -mercaptoethanol which will form a self-assembling monolayer (SAM) on the Au surface (Porter et al. 1987, Terrettaz et al. 2002, Keegan et al. 2005). It has been suggested that the weak thiol bonds allow for interpenetration by larger molecules (Holt et al. 2009). In this way the multimeric ligands can then penetrate the alkyl-thiol layer in an orientated way which presents the FIII9'10 motif free for binding with cell integrins. In this study 11-mercaptoundecanol (11-MUD) was used with a short incubation time in order to produce an incomplete SAM, making it easier for the multimeric ligands to come into contact with the Au surface.

In this chapter we explore the surface orientation of the multimers on Au supports using NR. Following this we tested their capacity to support adhesion of baby hamster kidney (BHK) cells by utilising immunofluorescence to ascertain their organisation of actin cytoskeleton and focal adhesions. As the multimers had been in storage at $-80\text{ }^{\circ}\text{C}$ for some time (>2 years) we initially used CD to confirm their structural integrity.

5.2 Materials

Multimeric ligands were a gift from Dr Michaela Kreiner, University of Strathclyde (Glasgow, UK). Unless otherwise stated, all general chemical reagents were sourced from Sigma-Aldrich (Dorset, UK), or Fisher Scientific (Leicestershire, UK) or

Melford Laboratories (Ipswich, UK), at analytical grade or equivalent quality. Gold coated glass slides and silicon substrates with a buried magnetic layer of pure iron permalloy (80 % nickel, 20 % iron) were purchased from Helia Photonics (Livingston, UK). Cell culture medium Dulbecco's Modified Eagle Medium (DMEM, high glucose, GlutaMAX, 61965026) was purchased from Invitrogen (Paisley, UK). Baby hamster kidney (BHK) cell line BHK-21 (C-13) was purchased from American Type Culture Collection (Virginia, USA). Texas Red conjugated anti mouse antibody (ab6726) was obtained from Abcam (Cambridge, UK), anti-vinculin antibody (V9131) and fluorescein-phalloidin (P5282) were both purchased from Sigma-Aldrich. Water was purified to $> 14 \text{ M}\Omega\cdot\text{cm}$ with a BioSelect, Purite, UK.

5.3 Buffers and reagents

All buffers and reagents were formulated in distilled water or D_2O where appropriate ($\text{pD} = \text{pH} + 0.4$).

Low salt buffer: 10 mM NaH_2PO_4 , 50 mM NaCl , pH 7.0

High salt buffer: 10 mM NaH_2PO_4 , 300 mM NaCl , pH 7.0

Low salt D_2O buffer: 20 mM NaH_2PO_4 , 50 mM NaCl , pH 7.4 prepared in D_2O

High salt D_2O buffer: 20 mM NaH_2PO_4 , 150 mM NaCl , pH 7.4 prepared in D_2O

5.4 Methods

5.4.1 Conformational analysis by circular dichroism

CD was used to establish if any degradation or change had occurred to the multimeric proteins during prolonged storage at $-80\text{ }^{\circ}\text{C}$. The ACD (Automated CD, Applied Photophysics Ltd.) equipment as described in section 3.4.2.2 was utilised for extensive analysis. As before, a 0.2 mm path length cell was used. Spectra were recorded in the far UV and represent an average of six scans, run at 50 nm/min with a 1 s time constant unless otherwise stated.

Stability over a range of salt (NaCl) concentrations for the three proteins, dimer, trimer and tetramer was investigated. The auto sampler function was utilised to create a range of salt concentrations in 10 mM NaH_2PO_4 , pH 7.0 buffer from 110 mM to 500 mM NaCl. Proteins were diluted to 1 mg/ml with the range of buffers and incubated for at least 1 h at $10\text{ }^{\circ}\text{C}$ prior to far UV ACD scan from 200 nm to 260 nm.

Unfolding of the protein by GdmCl was also measured by ACD at a concentration range of $\sim 0\text{-}6\text{ M}$. Protein samples were incubated in GdmCl solution prepared in 10 mM NaH_2PO_4 , 300 mM NaCl, pH 7.0 buffer for over 2 h at $4\text{ }^{\circ}\text{C}$ and ACD scan was performed from 210-250 nm at $20\text{ }^{\circ}\text{C}$. The strong absorbance of GdmCl in the far UV region restricted the range of the scan to above 210 nm.

Thermal unfolding was investigated using ACD to track the structural changes in the far UV for the dimer, trimer and tetramer. The samples were prepared as a 1 mg/ml concentration in high salt buffer. Spectra were collected while the sample was heated at $1\text{ }^{\circ}\text{C}$ a minute from 20 to $95\text{ }^{\circ}\text{C}$ with scanning from 150 to 250 nm in 1 nm steps

and with 0.7 second per point sampling time. Between each denaturation experiment, a sample of buffer was loaded and spectrum taken that could be used as a baseline for the subsequent sample spectra. All thermal data analysis was carried out by the Applied Photophysics' Global 3 analysis package.

5.4.2 Surface mapping of multimers on gold using neutron reflectometry

NR measurements in this chapter were made at ISIS on the CRISP beam at Rutherford Appleton Laboratory (Didcot, UK). The NR in this chapter differs from the previous (section 4.4.2) because polarised (up- or down- spin) neutrons were used. Polarisation of the incoming neutron beam was achieved using a specialised spin filter on the CRISP beam line. This technique utilised a silicon substrate which included a magnetic layer buried under the surface Au layer. Two scattering length density sets were obtained for the substrate by using the polarised neutron beam which, due to the magnetic layer, will produce “up” and “down” spin states (Saerbeck et al. 2012). The increased contrast allowed for high resolution scans to be obtained.

CRISP is a time-of-flight reflectometer on a spallation source supplying a multiwavelength neutron beam. It was operated in polarised beam mode which features a “spin flipper” which sets the direction of the neutron beam polarisation onto the sample. An external magnetic field was used to induce the magnetisation of the buried permalloy layer under the Au surface. The “spin flipper” flips the direction of the neutron polarisation so that it is either parallel (“up” spin) or anti-parallel (“down” spin) to the magnetised layer (Holt et al. 2009).

All experiments were performed by the CRISP instrument scientist Dr Stephen Holt assisted by Dr Christopher van der Walle. The substrates were cleaned prior to use using piranha solution and thoroughly rinsed with deionised water. A “rough” 11-MUD layer was created by incubation of the substrate for 10 min with a 1 mM solution of 11-MUD in ethanol. Following incubation the substrates (termed Au/11-MUD) were cleaned by rinsing with distilled water and dried under a nitrogen stream. The cleaned substrate was then clamped in a custom made Teflon trough with a void volume of around 3 ml, as described in 4.4.2. The substrates were analysed at fixed incident angles of 0.35, 0.8 and 1.8 and the data reduced to yield a single reflectivity profile. All experiments were conducted at ambient temperature (~25 °C). The surfaces were initially characterised with D₂O followed by gold matched water (GMW, 75 % D₂O: 25 % H₂O). GMW was used as it has the same scattering length density as Au and therefore would be “invisible” against the Au sub-layer alluding to the 11-MUD surface layer only.

Protein samples (FIII9’10-GGC, trimer and tetramer) were incubated in buffer containing 5 mM TCEP for a minimum of 2 h prior to use. TCEP was added to the protein solutions to reduce the C-terminal cysteine residue and allow it to form a thiol-bond with the Au surface. A low salt D₂O buffer was used for FIII9’10-GGC and a high salt D₂O buffer was used for trimer and dimer. The proteins were incubated on the Au/11-MUD surface at a bulk concentration of 100 mg/L, for 30 min. Following incubation the surfaces were washed by flushing the trough through with 5 volumes of D₂O buffer and then GMW, characterisation was performed following each wash.

The free thiol bond of the protein should be able to interpenetrate the 11-MUD to form a layer system as depicted in Figure 5-2. A SiO_2 layer would be present at the surface of the silicon block followed by a magnetic permalloy layer then Au and the “rough” 11-MUD layer interpenetrated by the protein at the outermost layer. The extent of the spontaneous replacement by the protein could be interpreted from the NR spectral data.

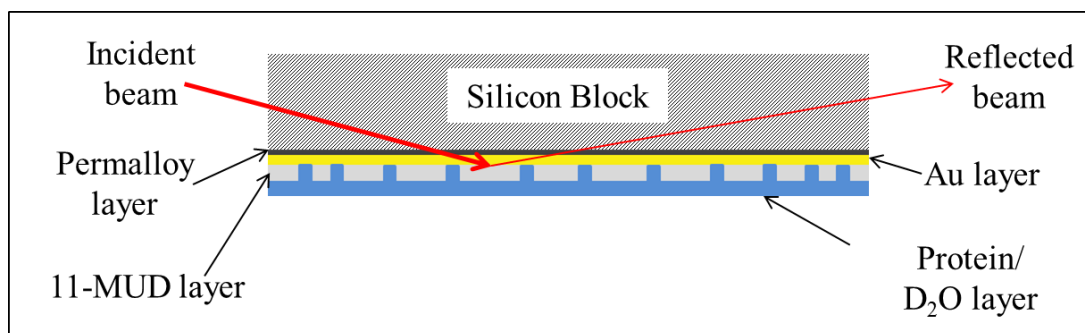


Figure 5-2 Schematic of surface layers of Au magnetic contrast NR substrate, including 11-MUD passivation layer interpenetrated with protein in D_2O buffer.

NR data were fitted using a Global MOTOFIT analysis following a trial and error approach as described in Chapter 4 in which all parameters were set to refine to the same value except the SLD of the magnetic layer (Nelson 2006). Additional statistical analysis was required because the nature of the 11-MUD layer did not allow for an average of several experiments to be obtained. It would be very difficult to create a layer of 11-MUD which is exactly the same each time. Therefore, Monte Carlo resampling procedure was used to evaluate the data by generating fits cloned from the real data. Gaussian deviations from the data, based on the weighted counting statistics of each data point, were applied to generate a minimum of 1000 synthetic data sets. Analysis of the synthetic data sets was performed in the same

way as for the actual data, with variations and analysis at each parameter. A plot of fitted values was generated by the fit to the synthetic data. Statistical analysis was performed with the value reported as the midpoint of the 95% confidence interval. Errors were reported as twice the standard deviation of the distribution (Holt et al. 2009, Kreiner et al. 2009b).

5.4.3 Cell adhesion study of multimeric ligands on gold surfaces

Previous reports had analysed cell adhesion to the multimeric ligands by specifically orientating the multimers by utilising a biotin-avidin bond (Kreiner et al. 2008, Li et al. 2011), which required the additional step of biotinylation of the protein. To visualise cell adhesion to the multimeric ligands we investigated directed thiol bonding onto Au plated glass coverslips treated in a similar way as the NR substrates. As in the NR experiments, here we utilised a 11-MUD layer on top of the Au surface to reduce protein denaturation and non-specific binding for directed thiol-Au bonding of the protein.

The surfaces were prepared by rinsing with absolute ethanol (200 proof) and then air dried. Following this they were incubated for 10 min with a 1 mM 11-MUD in ethanol solution, a monolayer will start to form in the first few minutes however this will not be sufficient time to form a densely packed monolayer and hence is described as a “rough” SAM. After the incubation the substrates (Au/11-MUD) were rinsed with ethanol and air dried. Protein solutions were prepared at a concentration of 100 µg/ml and incubated for a minimum of 2 h in a solution containing 5 mM TCEP with a low salt buffer used for FIII9’10-GGC and high salt

buffer used for the multimers. Coating with proteins was achieved by incubating the substrate with the desired protein at room temperature for 30 min and carefully washing with PBS to remove any unbound protein. Following this, BHK cells were seeded onto protein coated Au/11-MUD coverslips and incubated at 37 °C, 5 % CO₂ for 1 h, as described in section 4.4.3.3. A negative control was prepared by incubating an 11-MUD treated Au coverslip with buffer and proceeding as above. Actin, vinculin and the cell nucleus were stained using immunofluorescence procedure as outlined in section 4.4.3.3. Images were also recorded in the same manner.

5.5 Results

5.5.1 Conformation analysis of multimeric ligands following storage

CD spectra of the dimer, trimer and tetramer, shown in Figure 5-3, was similar to published results displaying a prominent α -helical structure due to the presence of the coiled-coils (Kreiner et al. 2008). Due to the high salt content the spectra was cut off below 200 nm, thus obscuring the expected positive maximum at 192 nm present in α -helix spectra. Two minima's were clearly evident at one at 208 nm and a second at 222 nm which confirm the predominant α -helical structure of the coiled-coils. The ellipticity of minima around 222 nm was reduced because of contributions from the FIII9'10 domains present on the multimer (Kreiner et al. 2008). As shown in previous chapters FIII9'10 had a positive ellipticity around 226 nm, the increased number of FIII9'10 on the trimer and tetramer may explain the slight difference in

the spectra. From the initial inspection of the multimers there appeared to be no negative effects caused by storage.

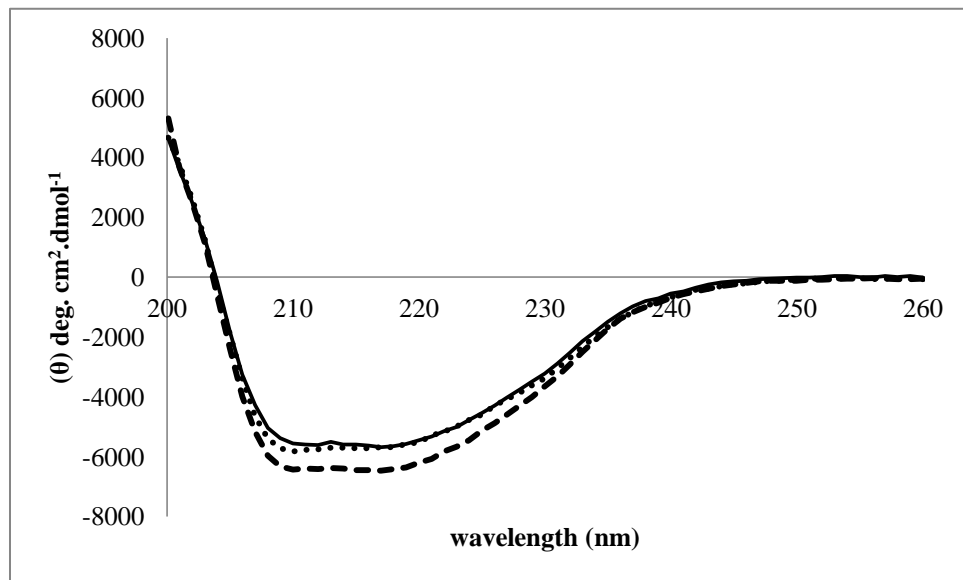


Figure 5-3 Far UV CD spectra of the dimer (dashed line), trimer (solid line) and tetramer (dotted line) in 10 mM NaH_2PO_4 , 300 mM NaCl, pH 7.0.

5.5.1.1 Multimer conformation as a function of salt content

The multimers had previously been found to be unstable at salt concentrations below 150 mM (Kreiner et al. 2008). The structural changes at different NaCl concentrations were mapped using CD, a range from 110 mM to 500 mM was investigated which generally showed no distinct change in spectra shape (Figure 5-4). The negative minima at 208 nm and 222 nm indicating an α -helical conformation were visible, although there was a slight variation in ellipticity. The notable exceptions were for the dimer at 440 mM and the tetramer at 320 mM. There was a large reduction in ellipticity at 440 mM NaCl concentration in the dimer. A shift in the spectra was present at 320 mM NaCl in the tetramer, in which there was a

large reduction at 208 nm and a slight reduction at 222 nm. The positive maximum also shifted to around 200 nm. This suggested a change in conformation, although this was not continued for the other lower NaCl concentrations.

It should be noted that the spectra were corrected for loss in concentration due to aggregation of protein. In an attempt to force a change, proteins were incubated in buffer containing 50 mM NaCl. This showed a distinct change in spectra shape in all of the proteins with a large reduction in ellipticity and the suggestion of a shift in the positive maximum.

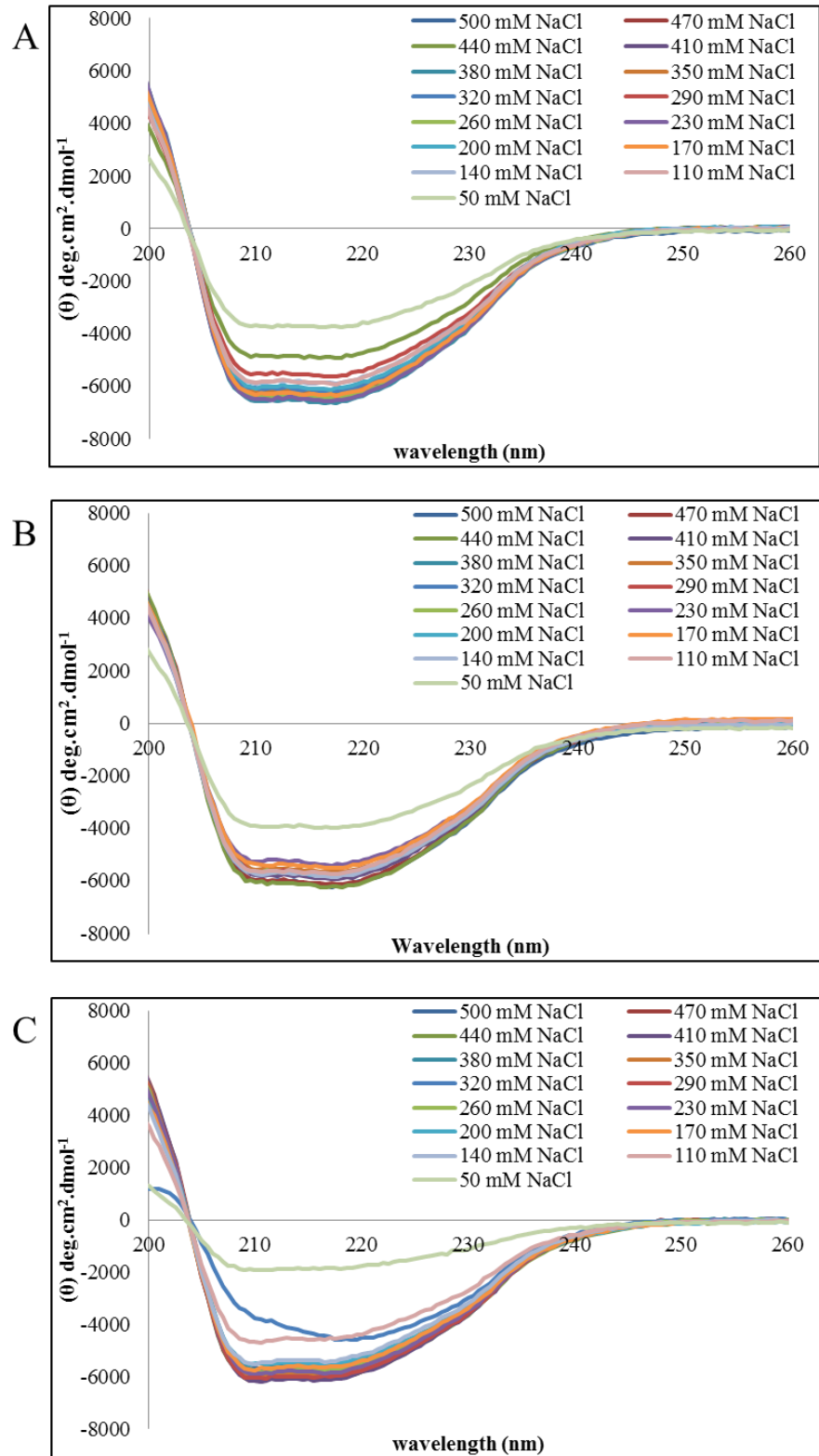


Figure 5-4 Far UV CD spectra for multimeric ligands dimer (A), trimer (B) and tetramer (C) in 10 mM NaH_2PO_4 , pH 7 buffer following incubation with varying salt concentrations from 50 to 500 mM.

5.5.1.2 *Thermally induced unfolding of multimeric ligands*

Scans were obtained in 1 °C increments for each temperature from 20-95 °C, however only a representative selection are shown on Figure 5-5 ranging from 40-90 °C in 10 °C increments with 5 °C either side of the calculated T_m. Previous work had performed a CD thermal study of the multimers using buffer containing 6 M GdmCl to denature the FIII9'10 component of the multimer as to focus on the thermal denaturation of the coiled-coil (Kreiner et al. 2009a). By unfolding FIII9'10 the positive contributions at 226 nm would be removed and hence would not impact the spectra. In the present study using ACD we attempted both with and without GdmCl denaturant. The spectral contributions from 6 M GdmCl were incompatible with the sensitivity of the Global 3 analysis software and so these results were not analysed.

The only results analysed and shown were from the “normal” high salt buffer run, Figure 5-5. The spectra showed that the multimers were relatively stable with little change in structural conformation from 20 to 40 °C. At around 50 °C the dimer displayed an increase in negative maxima around 222 nm, this continued until around 80 °C. Above which, the spectra started to show some disorder and a decrease in ellipticity. Similar results were obtained for the trimer but there was also a slight decrease in negative maxima from 20 to 50 °C from then it increased significantly up to around 80 °C. By 90 °C contributions suggested complete unfolding. For the tetramer there was no large change in ellipticity or spectral shift from 20 to 50 °C. The negative maxima started to increase significantly from 65 °C onwards up until it reached 80 °C after which the spectra lost its shape.

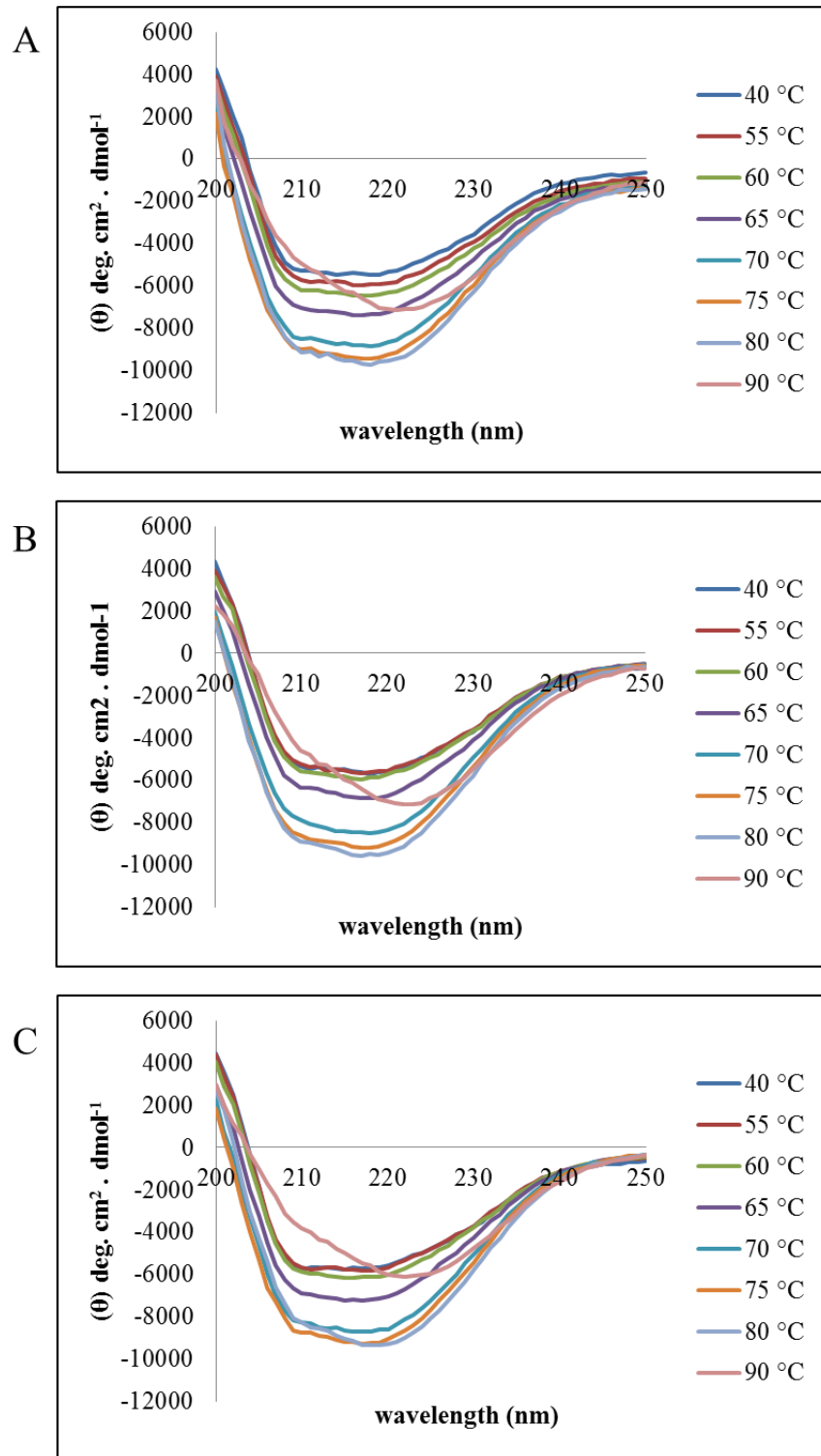


Figure 5-5 Far UV CD spectra of thermal denaturation of multimeric ligands dimer (A), trimer (B) and tetramer (C) in 10 mM NaH_2PO_4 , 300 mM NaCl, pH 7 buffer.

Analysis of the spectra found that all three multimers best fit a 2 stage unfolding model, with similar T_m values calculated for each step. The calculated results for the T_m are shown in Table 5-1. The T_m for step one of the trimer was similar to previous results in the original study by Kreiner and co-workers (2009), which found it to be around 63 °C, although they had a single unfolding of just the coiled-coil. The results for the T_m of the dimer were higher than the prior work which estimated the first step to be at around 25-45 °C and the second step to be from 45-75 °C. Previously, T_m for the tetramer could not be calculated because the ellipticity changes around 222 nm did not reach a plateau suggesting that the T_m was above 80 °C (Kreiner et al. 2009a).

The analysis software was ran repeated times and the same results were found each time. Differences between these results and those from Kreiner and co-workers may be due to the contributions from the FIII9'10 “disguising” the CD measured unfolding. However the previous work focused on the coiled-coil where as we were looking at the whole multimeric structure. Interestingly, the van't Hoff enthalpy for the multimers decreases in the order tetramer > trimer > dimer, indicating that although the T_m may be similar, the amount of energy required has increased.

Table 5-1 Temperature unfolding of FIII9'10 GCC multimeric ligand calculated transition values.

Protein	van't Hoff enthalpy (kJ/mol)	T_m
Dimer – step 1	165.6 ± 2.3	59.3
Dimer – step 2	502.1 ± 9.7	74.3
Trimer – step 1	287.6 ± 3.5	60.2
Trimer – step 2	544.9 ± 9.4	76.3
Tetramer– step 1	283.5 ± 4.2	59.0
Tetramer– step 2	708.0 ± 13.5	73.3

Similar profiles were obtained for each of the multimers for the change in spectra shape and concentration of each species. Figure 5-6 showed the initial folded multimer then an intermediate step in which the spectral intensity of the species had increased significantly followed by the unfolded multimer with a significant loss of the negative maxima around 208 nm.

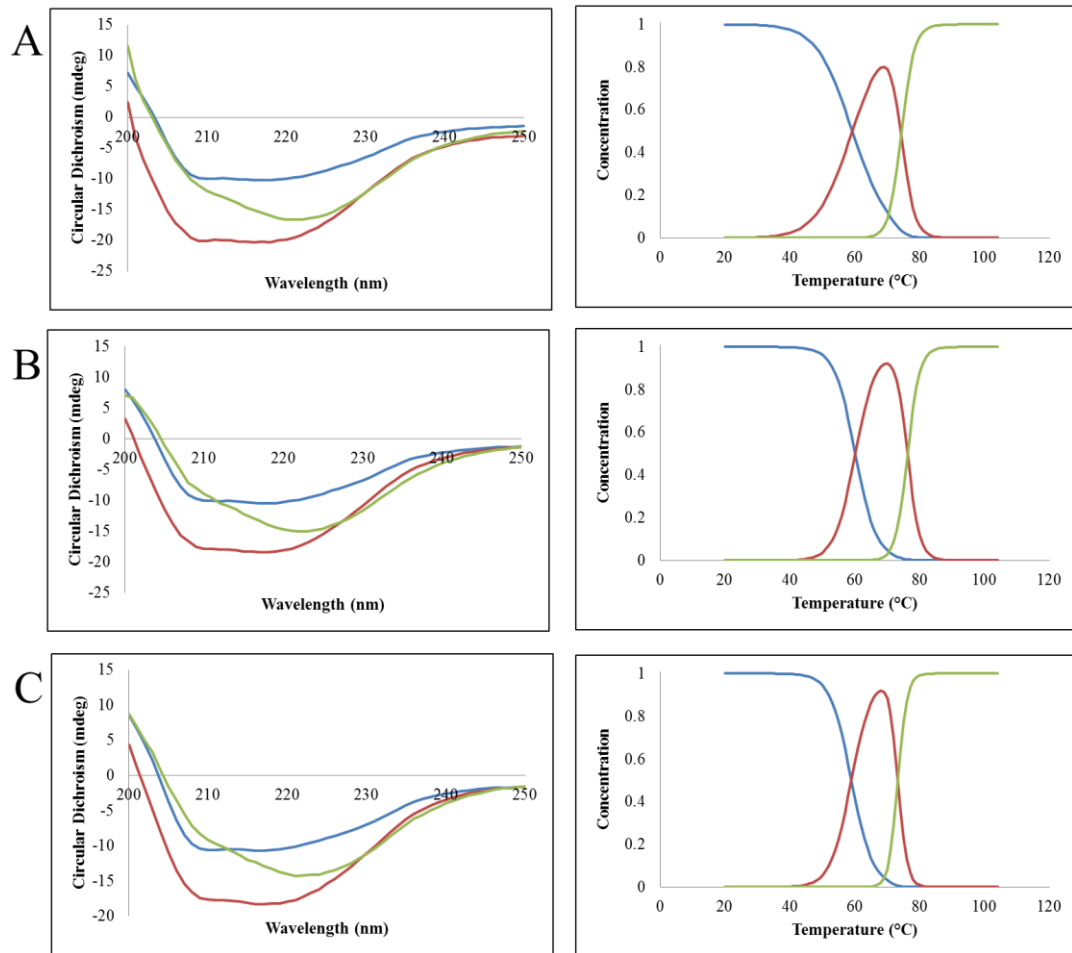


Figure 5-6 Global analysis of CD spectra data for thermal denaturing of multimers dimer (A) trimer (B) and tetramer (C) showing folded species (blue), intermittent step (red) and unfolded species (green). Left pane shows comparison of the different spectral shapes. Right pane shows concentration profile comparing the different species at 20 to 100 °C.

5.5.1.3 Equilibrium chemical denaturation

The spectra for denaturing of the multimers with GdmCl followed similar pattern for each of the multimers (Figure 5-7). There was a slight variation in ellipticity intensity up to 2.8 M, after which the negative maxima around 208 nm became more prominent and doubled in intensity. Below this we could not ascertain any useful information because of the contributions from the GdmCl. The increase in ellipticity will be due to FIII9'10 unfolding and a reduction in the aromatic contributions at 226 nm.

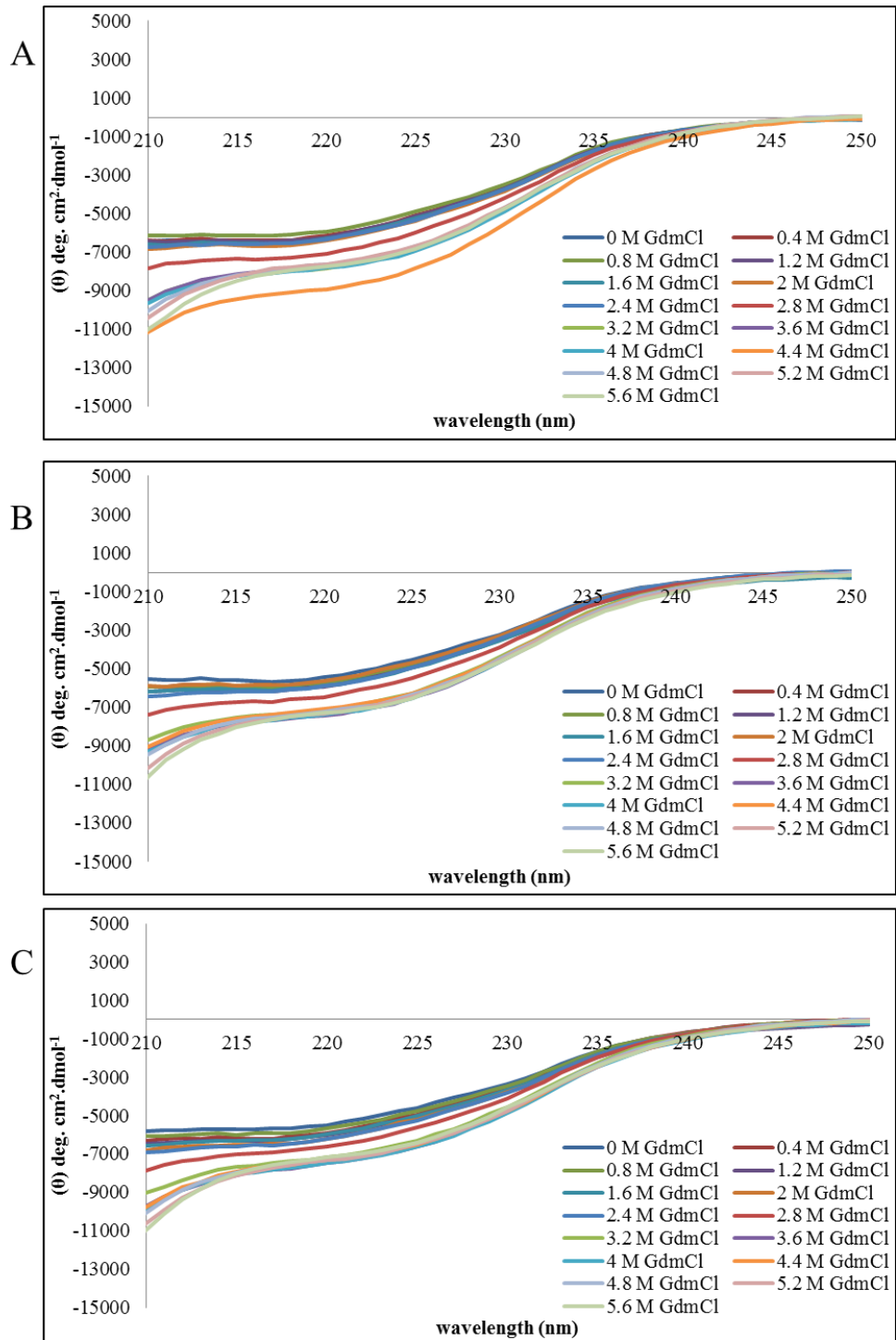


Figure 5-7 Far UV CD spectrum of multimeric ligands, dimer (A), trimer (B) and tetramer (C) following incubation with varying concentrations of GdmCl in 10 mM NaH_2PO_4 , 300 mM NaCl, pH 7 buffer.

5.5.2 Protein adsorption studies by neutron reflectivity

We utilised polarised magnetic contrast NR to help to distinguish between multiple layers a few Ångströms thick. This technique was very useful to resolve the thin 11-MUD layer added to the Au substrate to reduce protein denaturation at the surface. Due to time constraints NR studies were only completed on the “monomeric” unit FIII9’10-GGC and the multimeric ligands trimer and tetramer. A repetition of the NR capture for the FIII9’10-GGC was performed. Interestingly this showed that the surface had increased coverage and thickness of the protein. Data was only captured once for the trimer and tetramer. A new substrate was used for each protein sampled.

The NR profiles (Figure 5-8) showed slight changes in the “up” and “down” spin following incubation with the proteins to the Au/11-MUD surface. Initial inspection of the reflectivity profile suggested that there were only small differences between the 11-MUD layer alone and after incubation with the proteins. This was to be expected because the 11-MUD layer would have been displaced by the protein during binding to the Au sub-layer. For the monomeric unit (FIII9’10-GGC) the change was most obvious from a Q value of around 3 \AA^{-1} . A reduction in reflectivity was present around a Q value of below 2 \AA^{-1} following incubation of the substrate with the trimer. Overall the spectra were very similar. A similar pattern was seen for the tetramer in which a shift was present around 3 \AA^{-1} .

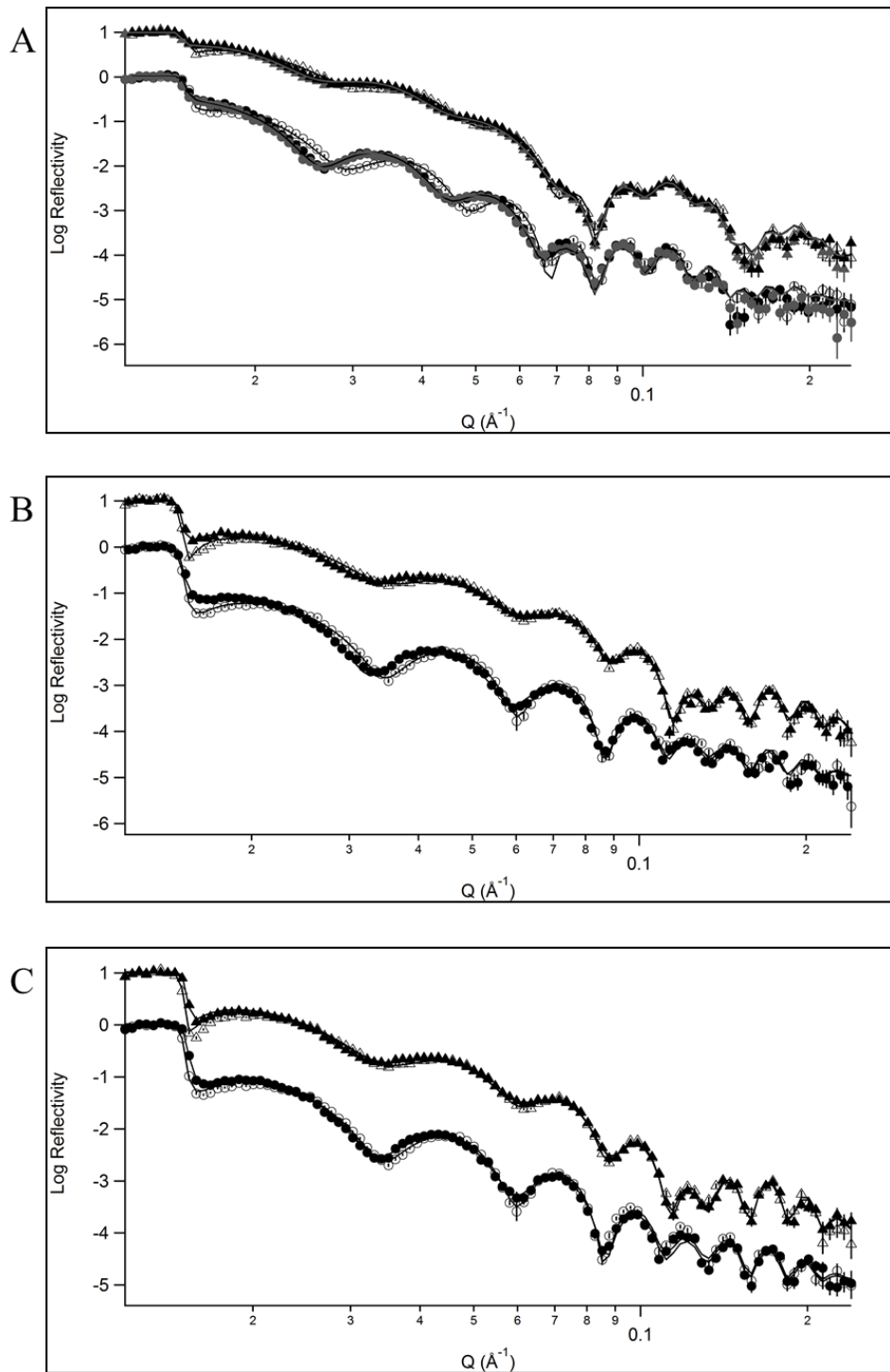


Figure 5-8 Reflectivity profile showing up-spin (triangles) and down-spin (circles) for magnetic Au surface coated with self-assembling monolayer of 11-MUD (empty shapes) and proteins (filled shapes) layer one (black) layer two (grey): FIII9'10-GGC (A), trimer (B) and tetramer (C). Data points shown as empty/filled circles/triangles with the fitted reflectivity profiles shown as solid lines of the same colour. For clarity, reflectivity profiles for up-spin have been offset in the ordinate by a factor of \log_{10} .

Analysis of the data provided values for the thickness of each layer, shown in Table 5-2. The layer thickness for 11-MUD varied for each of the Au/11-MUD surfaces from 8 and 13 Å. Protein layer thickness on the outermost surface ranged from 48.5 to 57.5, suggesting that the FIII9'10 moieties are lying horizontal at a slight angle on the substrate surface. The axial dimensions of wild type FIII9-10 have been previously determined by NMR and X-ray crystallography to be a length of ~70 Å and a diameter of 24-34 Å (Leahy et al. 1996, Copie et al. 1998). The best fit for thickness of the proteins was found by including the 11-MUD layer in the Monte Carlo fits.

Table 5-2 Layer thickness and component volume fractions from constrained fits to multiple data sets using Monte Carlo analysis.

	FIII9'10-GGC	Trimer	Tetramer
SiO₂ thickness (Å)	5.42 ± 1.28	9.523 ± 1.58	7.904 ± 1.16
PermAlloy thickness (Å)	81.24 ± 0.32	47.958 ± 0.268	50.535 ± 0.28
Au thickness (Å)	239.54 ± 1.1	188.94 ± 0.5	189.67 ± 0.44
11-MUD thickness (Å)	8.72 ± 0.52	12.79 ± 0.68	13 ± 0.39
Protein layer thickness sample 1 (Å)	48.5 ± 3	57.54 ± 2.43	51.022 ± 3.01
Protein layer thickness sample 2 (Å)	54.81 ± 3.1	-	-
Protein volume fraction Sample 1	0.563	0.271	0.149
Protein volume fraction Sample 2	0.604	-	-

Incubation with the thiolated proteins lead to replacement of the 11-MUD on the surface of the Au substrate this was most obviously seen from the SLD profiles, Figure 5-9. These profiles display the change in SLD as a result of each different layer on the substrate. The SLD was constrained for each of the parameters with the

exception being the permalloy layer, hence this caused an overlap in each of the SLD profiles until the point where the protein layer was added. SLD was allowed to vary for the permalloy which is why it is very different for the “up” and “down” spin states.

There was a large reduction in SLD corresponding to 11-MUD on non-protein coated surfaces, as distance from interface increased this value returned to that for D₂O indicating the termination of the 11-MUD layer. At the same point, after incubation with proteins, the SLD increased but not to the same extent as that for D₂O. It reached a value corresponding to the protein and then continued until the end of the protein layer, after which it returned to that of D₂O. The difference decreased in the order FIII9'10-GGC > trimer > tetramer, which corresponded to the decreasing surface coverage of the proteins. The displacement of 11-MUD was clear for monomer and tetramer as there was a distinct change in the trough related to the 11-MUD layer. The difference in thickness on second scanning of the monomer was represented by the two lines.

It was clearly evident from the NR data that the proteins were able to penetrate the 11-MUD surface to form a specifically orientated tethered ligand. As their integrin binding had already been confirmed by Kreiner and colleagues (2008) we proceeded to cell culture immunofluorescence to detail the cell characteristics on the surfaces.

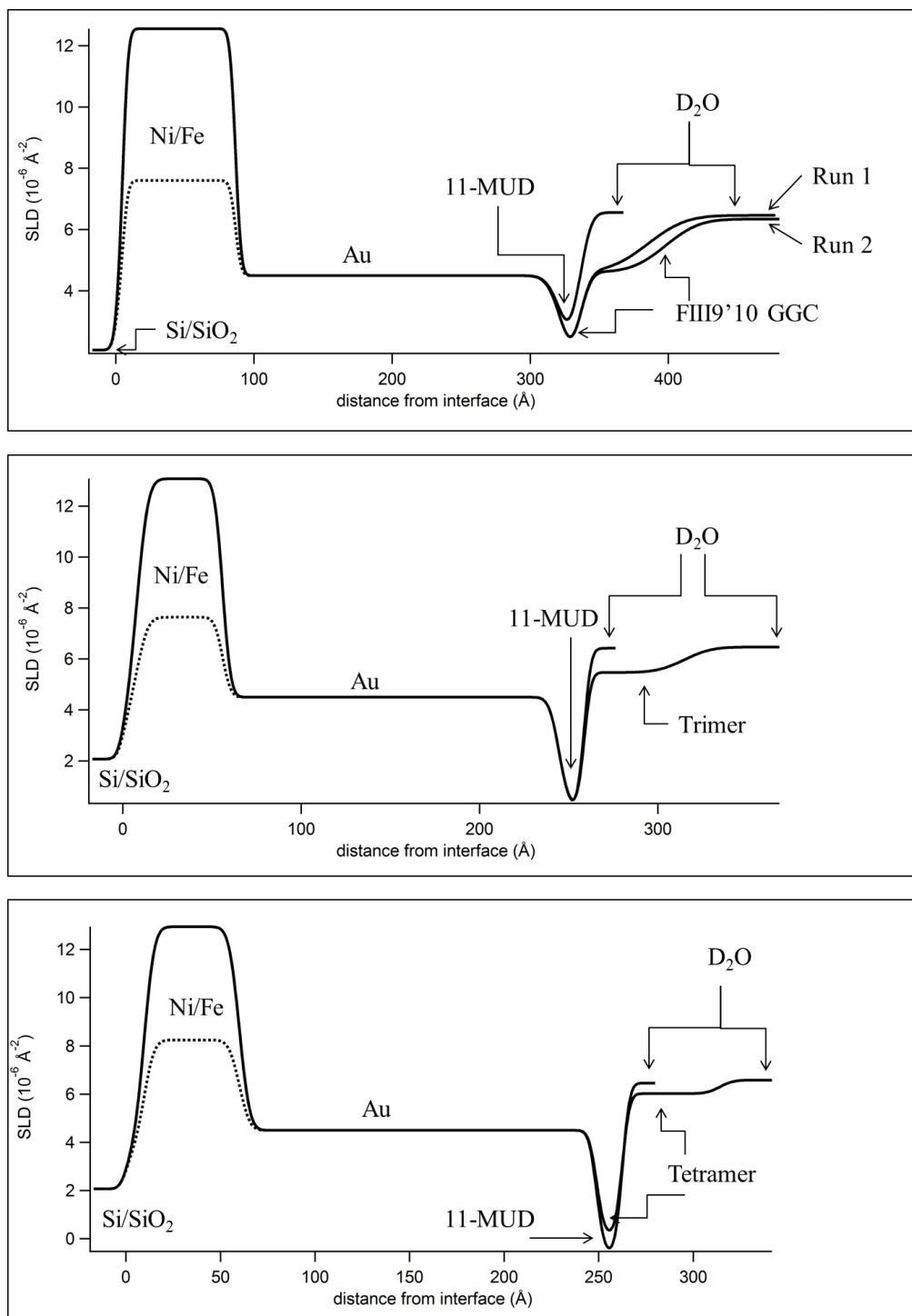


Figure 5-9 Fitted SLD for reflectivity data corresponding to the fits of all polarisation data for FIII9'10 GGC, trimer and tetramer adsorbed to Au/11-MUD substrate from solution in 10 mM NaH₂PO₄, 50 mM NaCl, pH 7.4 for FIII9'10-GGC and 10 mM NaH₂PO₄, 300 mM NaCl, pH 7.4 for trimer and tetramer prepared with D₂O. Profiles are shown as the distance from the Silicon/SiO₂ substrate interface and labels are used as a guide for the SLD of each layer. Solid line shows "up" spin and dotted line corresponds to "down" spin.

5.5.3 Cell adhesion to multimeric proteins on gold surfaces

Immunofluorescence images following 60 min incubation of BHK cells with an Au/11-MUD surface displayed minimal cell attachment. As in the previous chapter the original images can be found in Appendix B, the images shown here have had the colour inverted to aid contrast. The image shown in Figure 5-10 was typical of the entire surface. There were a few small rounded, non-spread cells which featured no organisation of actin fibres and the indication of very small focal adhesion-like artefacts throughout the cell.

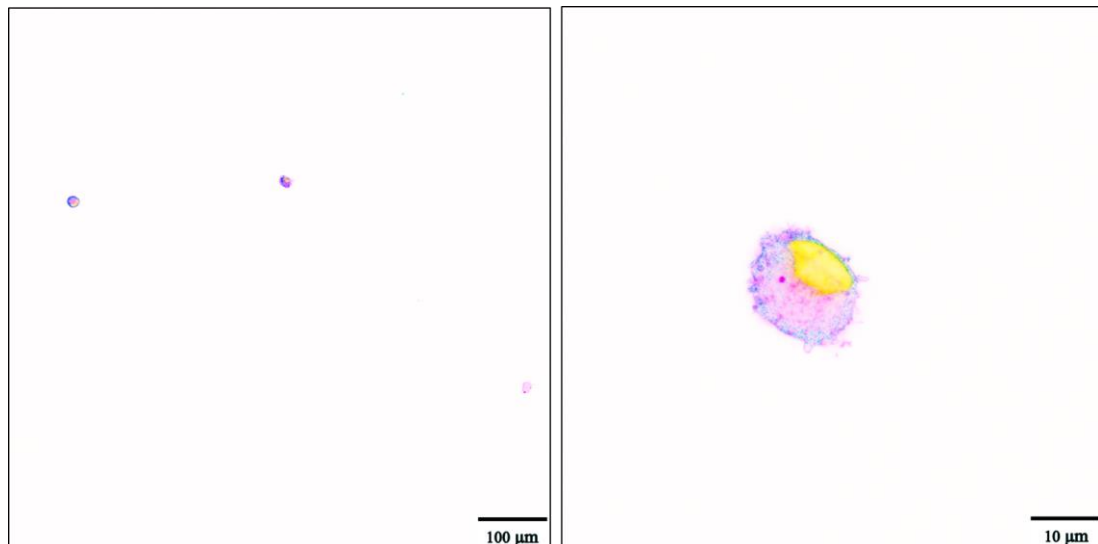


Figure 5-10 Immunofluorescence image showing BHK cell attachment onto Au/11-MUD substrate stained for vinculin (blue), actin (pink), and the nuclei (yellow). Images are shown with colour inverted to aid contrast and were photographed at 20x magnification (left) and 63x magnification (right).

The surfaces coated with FIII9'10-GGC featured large clusters of elongated cells in a diverse meshwork which also included well spread cells, Figure 5-11. The cells featured in Figure 5-11A conveyed a typical fibroblast-like morphology at a high density. Also present on the surface were smaller, rounder cells with several spindle-

like protrusions with focal adhesions at their tip (B). The focal adhesions were clearer to see on closer magnification (C&D).

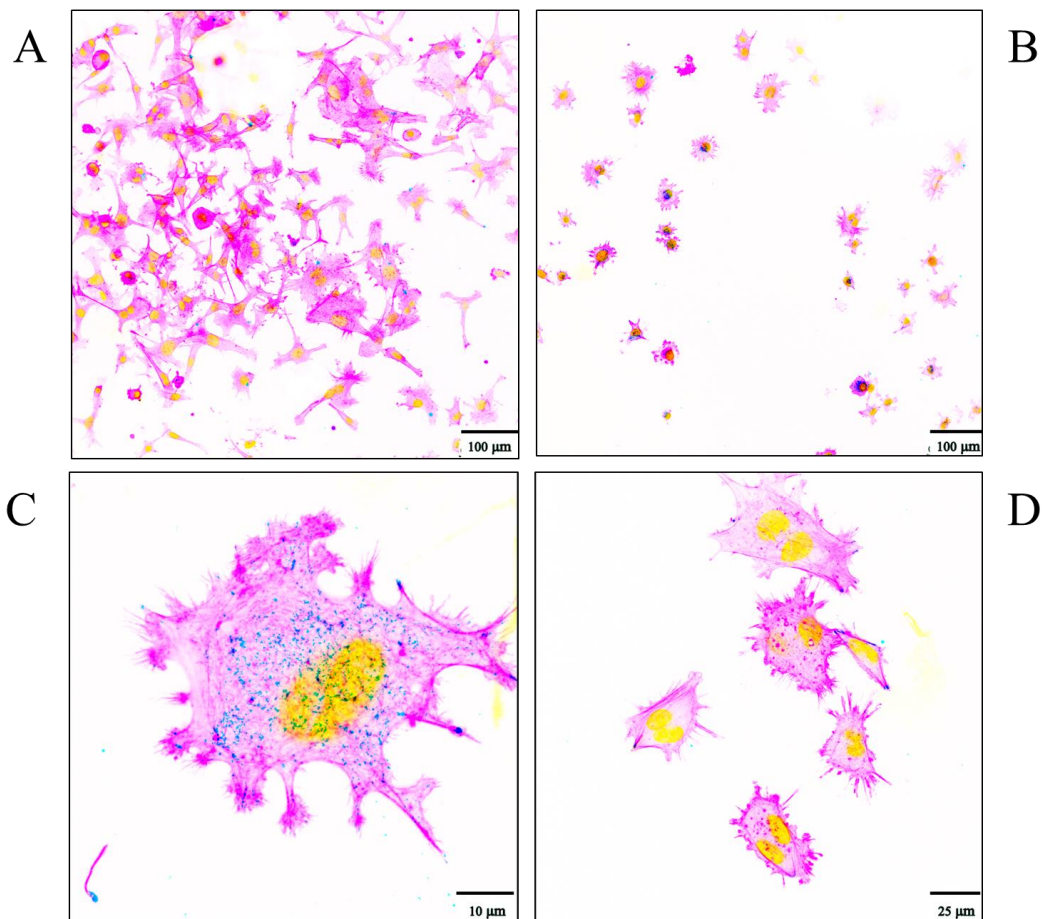


Figure 5-11 Immunofluorescence image showing BHK cell attachment onto Au/11-MUD substrate coated with FIII9'10-GGC, stained for vinculin (blue), actin (pink), and the nuclei (yellow). Images are shown with colour inverted to aid contrast and were photographed at 20x magnification (A and B) and 63x magnification (C and D).

Cell attachment to the trimer coated Au/11-MUD surface was similar to that of FIII9'10-GGC. As seen in Figure 5-12, there were two main types of spread morphology which may correspond to different densities of the trimer. In addition to the traditional fibroblast-like cell morphology, the surface featured cells which had several projections around the circumference of the cell. These projections could

represent the cell attaching to the FIII9'10 presented on the substrate surface. At increased magnification in Figure 5-12C, an organised actin cytoskeleton stretching from end to end in the cell was seen. Figure 5-12D featured cells with irregular membranes and numerous short actin fibres at varying densities.

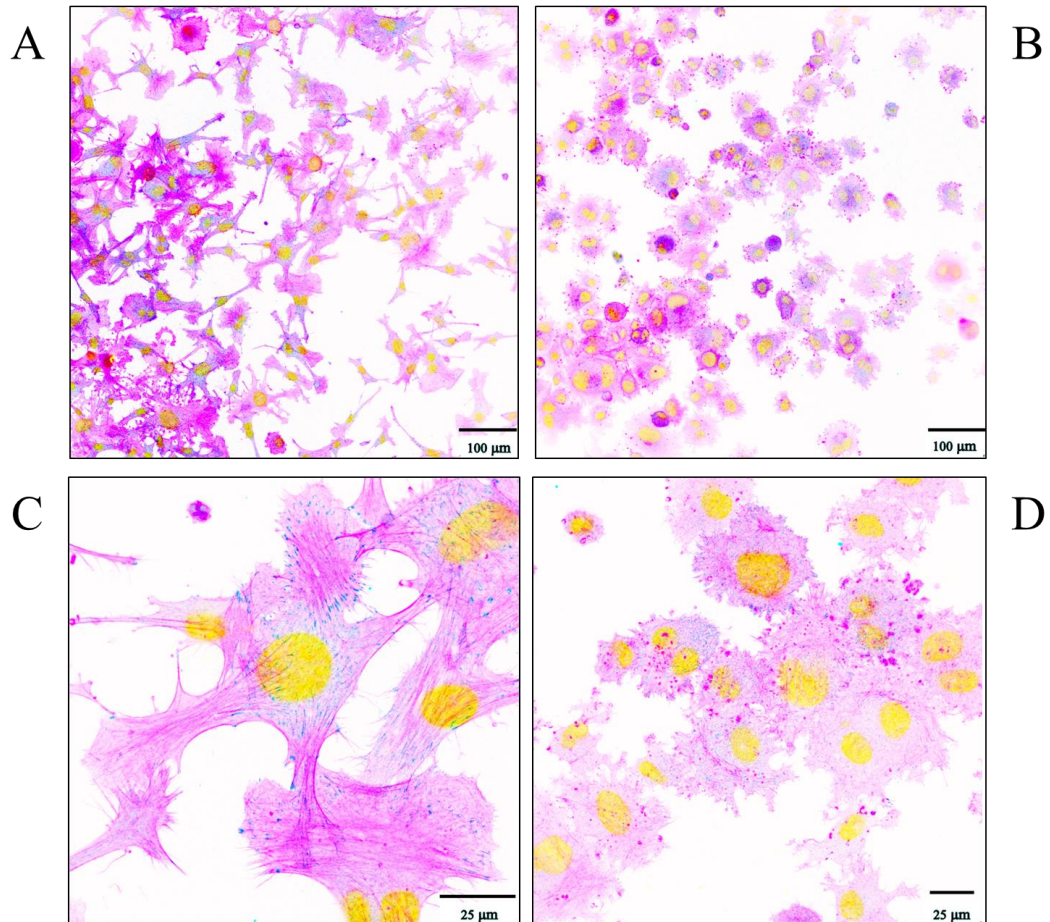


Figure 5-12 Immunofluorescence image showing BHK cell attachment onto Au/11-MUD substrate coated with trimer, stained for vinculin (blue), actin (pink), and the nuclei (yellow). Images are shown with colour inverted to aid contrast and were photographed at 20x magnification (A and B) and 63x magnification (C and D).

There were fewer elongated cells present on the tetramer coated surfaces, Figure 5-13. These images showed mostly groupings of several cells which were spread in several directions. An example of a typical lamellipodium was seen in Figure 5-13B

and close up in Figure 5-13D, this showed the cell front of a motile cell reaching into an area which was not yet populated. The image in Figure 5-13C is an example of the localisation of focal adhesions at the tips of the spindle-like protrusions, filopodia. Each of the images here represented a typical area of the substrate surface, quantification of surface characterises was not performed.

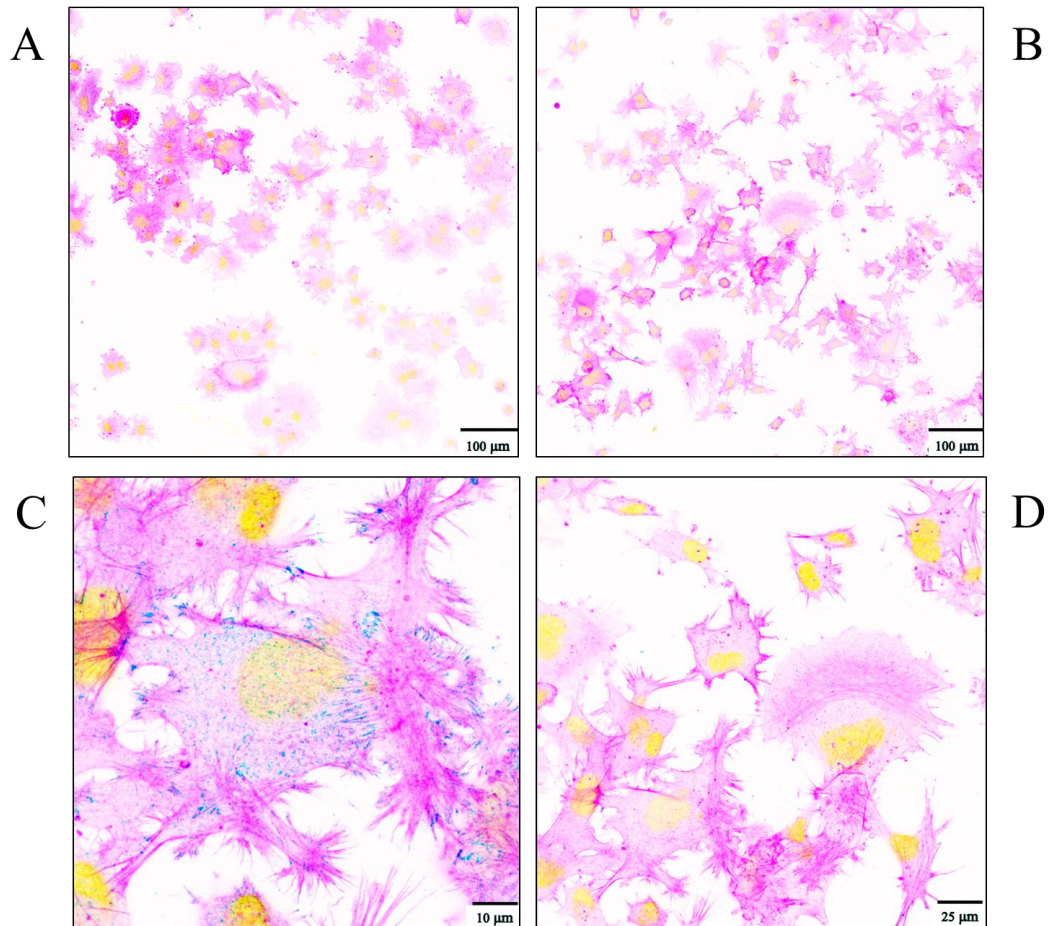


Figure 5-13 Immunofluorescence image showing BHK cell attachment onto Au/11-MUD substrate coated with tetramer, stained for vinculin (blue), actin (pink), and the nuclei (yellow). Images are shown with colour inverted to aid contrast and were photographed at 20x magnification (A and B) and 63x magnification (C and D).

5.6 Discussion

5.6.1 Conformational analysis

CD spectra for the multimers corresponded to previous reports (Kreiner et al. 2008). In this study we concentrated on far UV but it may have been useful to also have studied near UV. The near UV would allow us to track changes in the aromatic environment for the FIII9'10 part of the multimer. The contributions from FIII9'10 distort the spectra in the far UV and may have disguised any changes in the conformation as it has a β -sheet like secondary structure which gives a different spectral shape from α -helix. In addition FIII9'10 features an unusual positive maxima around 226 nm which may have reduced the contributions from the negative maxima around 222 nm for α -helical coiled-coils. After storing at $-80\text{ }^{\circ}\text{C}$ for ~ 2 years there was no secondary structure conformational changes measured by CD.

Varying the salt content only slightly altered the spectra of the multimers. Previous work had found that some dimeric species will present as a mixture of both dimer and trimer, switching between each depending on the environmental contributions (Burkhard et al. 2000). Differences between dimer and trimer could not be distinguished by CD as the secondary structures are similar. The stabilising effects of salts are complex and can be affected by the nonpolar areas on the exposed surface of the protein (Tadeo et al. 2009). The multimers consist of two main distinct parts separated by an IgG hinge. The coiled-coil has been the subject of continued studies since it was determined to be very stable (O'Shea et al. 1989), it is thought that the hydrophobic interactions occurring along the coiled-coil interface may be key driving force of this stability (Burkhard et al. 2000). Increasing NaCl concentrations shield protein electrostatic charges at smaller distances from the surface, such that

ionic forces are effectively ‘screened out’. Where the net ionic forces induce protein-protein repulsion, this screening effect would lead to protein aggregation. Thus, in the case of the multimers, a net attractive ionic force (between localised surface patches) must be screened out since aggregation is attenuated in high salt conditions. From our own work in Chapter 3 FIII9’10 was also found to be stable under a variety of conditions. That being said, the effect of changes the NaCl concentration was not investigated for FIII9’10 alone. This data may have been useful to track what, if any, changes happen to the individual FIII9’10 which may affect the spectra of the multimeric form. Precipitation of a protein occurs when the chemical potential of the molecule in solution becomes greater than its chemical potential in solid phase (Trevino et al. 2008). At lower NaCl concentrations the spectra had to be corrected for loss in concentration, which indicates that precipitation had occurred. Although the requirement for a high NaCl concentration for the multimers limited the wavelength span of our CD experiments the proteins were shown to be stable under physiological conditions (150 mM NaCl) indicating that they are suitable to use for cell experiments.

We used CD to assess the thermal stability of the entire multimer secondary structure. Thermal unfolding all three multimers appeared to undergo a 2 step process with similar T_m values. Here we were looking at the entire multimer as a whole structure in the far UV. From our previous experiments described in section 3.5.3.1 we found that FIII9’10 unfolds around 57 °C. The initial unfolding step of the multimers at 59 °C may therefore correspond to FIII9’10 domains and the second step at ~ 75 °C may be due to the coiled-coil. Nonetheless, without the addition of near UV to observe the aromatic contributions we are limited to what we can

confirm. Monomeric coiled-coil in physiological conditions have been shown to have a T_m of around 57 °C (O'Shea et al. 1989) however, oligomerisation of coiled-coils to form di- tri- and tetrameric coils showed an increase in T_m of up to 94 °C for the tetrameric species (measured in 3M GdmCl) (Harbury et al. 1993). Therefore it would be expected that the multimeric coiled-coils would show a similar increase in T_m . It may be that the interactions between the FIII9'10 and coiled-coils are stabilising/destabilising the overall thermostability of the protein. This is something that may warrant further investigation. Conversely it may simply be contributions from the FIII9'10 distorting the spectra. It would have been useful to map the changes in the aromatic environment of FIII9'10 for the different multimers by near UV. It may also have been apt to see if the unfolding of the multimers was reversible and to ascertain if on cooling the multimers not only regain their shape but their original conformations as either di-, tri- or tetramer. SEC could have been used to determine if the oligomerisation state of the multimers was the same following thermal treatment. For the purpose of our study, there should be no structural effects on the multimers when used at a temperature range from 20 to 37 °C.

There were minimal changes in the secondary structure recorded by CD for increasing concentrations of GdmCl up to ~6 M. A noticeable shift in spectra was observed at around 2.8 M GdmCl, after which there was a gradual change in the intensity of the spectra. The coiled-coil of the multimers is stable even at high concentrations of GdmCl (Kreiner et al. 2009a), thus from our CD measurements we will be measuring changes in the FIII9'10 secondary structure. From our previous results in section 3.5.3.3, FIII9'10 displayed changes in the secondary structure that would suggest unfolding at 1.4 M and 3.4 M. Domain FIII9' unfolds at a lower

concentration and is followed by FIII10 unfolding. These values were lower than those for the unfolding measured by fluorescence in section 3.5.2 which found FIII9' unfolds at 2.2 M and FIII10 at 5.4 M. Fluorescence measured unfolding of FIII9'10 is preferable to far UV CD due to the measurement of the tryptophan residues as indicators of the unfolding. A lower initial unfolding calculated by CD can be explained by shift in the conformation before exposure of the tryptophan residues which can be monitored by CD but would not be visible by fluorescence.

5.6.2 Multimeric $\alpha 5\beta 1$ ligands on gold support

NR data suggested that the monomer FIII9'10-GGC, trimer and tetramer are all able to penetrate the imperfect 11-MUD brush border. Due to the Au-thiol bonding they will be orientated with the FIII9'10 portion projecting from the surface. The layer thickness for each of the proteins was around 50 Å, which is less than the length of FIII9'10 (~70 Å) but more than the diameter (24-34 Å), implying they are arranged horizontal with the surface in a slightly tilted orientation. Similar results have previously been reported for bulk concentrations of the dimer on an Au surface (Singh et al. 2009). Singh and colleagues (2009) found that a bilayer was formed with a thickness of 41-47 Å (Singh et al. 2009). The absence of a bilayer in our experiments may be due to the 11-MUD treatment of the Au surface preventing any non-specific interactions. The surface coverage (volume fraction) was different for each of the proteins and decreased as cluster size increased.

Au/11-MUD surfaces not presenting FIII9'10 domains were unable to support cell attachment within the 60 min incubation time used in this chapter. The result allows

for an indirect comparison of cell attachment on substrates presenting orientated FIII9'10-GGC and the non-specifically adsorbed FIII9'10 as described in section 4.5.3.3. The morphology of the cells on FIII9'10-GGC substrates was visibly different from that on FIII9'10 coated surfaces. The BHK cells were elongated and more densely packed on the orientated surfaces. This suggests that the non-specifically adsorption of the FIII9'10 may not present the integrin binding domains in a way in which can interact with the cell surface integrins; therefore there is less surface coverage of the cells.

There were two main cell morphologies observed for the BHK cells in this chapter, the first was an elongated spread cell with an organised actin cytoskeleton with well-formed stress fibres, typical of a fibroblast cell. The other common morphology was more prevalent on the multimeric coated surfaces and featured a somewhat round shaped cell with several projections and short bunched actin fibres. The variations suggest different types of cell/substrate interaction. The question arises as to what was causing the different morphologies? It could be that the variation in surface density of the different ligands leads to different morphologies or “patterns” of cell growth.

The specific capture of BHK cells using a fibroblast growth factor on an Au surface found that cells would readily attach to areas with bound growth factor (Peelen et al. 2006). However, Peelen and co-workers observed that after incubation over 2 days the “captured” cells did not grow and retained a rounded morphology. Interestingly the cells did grow and were well spread on the alkanethiol Au surface surrounding the “capture area”, growth was found to improve as incubation duration increased (Peelen et al. 2006). The two contrasting cell morphologies are similar to those we

found, however our experiments only had a short incubation time of 60 min to reduce the laying down of the cells own FN. We can therefore not determine from our current results if the different cell morphologies were caused by the cells adhering to the exposed Au/11-MUD patches of the substrate surface. If this was the case, it could be that the multimers are acting as an anchor which initially encourages cell attachment and this then stimulated attachment of the rest of the surface.

Additionally and probably more likely, the different morphologies could be caused by differences in the multimer density (i.e. areas with numerous multimers versus areas with very few). From inspection of the immunofluorescence images the round morphology was more common on the multimeric surfaces and also appeared to increase with FIII9'10 cluster number increased. Roy and Hocking (2013) postulated that by presenting a surface with a high density of specific integrin ligands there is a preferential selection which then disrupts the cells own attachment and spreading process (Roy and Hocking 2013). It could be in this same manner that the multimers are essentially occupying most of the cell surface $\alpha 5\beta 1$ and thus preventing further spreading of the cells. This is something that may warrant further investigation, as we currently have not defined which parts of the substrate present high density highly clustered ligands and which do not.

5.7 Summary

The use of multimeric ligands is a very interesting area of research which was only briefly examined in this chapter. CD analysis of the multimers confirmed them to be

stable for a prolonged time period when stored at the optimum conditions. We have also demonstrated that multimeric $\alpha 5\beta 1$ ligands presented in a specific orientation and cluster size support adhesion of fibroblast cells.

CHAPTER 6. Conclusions and future work

The work described in this thesis focused on the development and characterisation of a robust protein based on the 9th and 10th repeat of the type III domain of fibronectin. This was achieved by utilising site directed mutagenesis of the previously developed FIII9'10 mutant and characterised through various methods both in solution and at the solid liquid interface. Finally, the functionality of the protein was verified using integrin $\alpha 5\beta 1$ and baby hamster kidney cells (BHK). We successfully developed FIII9''10 H2P with the aim of using it as a functional coating for biomedical implants to improve the healing process.

Our initial studies centred on exploring the possible binding of IGFBP-5 and FIII9'10 GGC and the subsequent consequences this may have on breast tumour metastasis. Surface plasmon resonance could not determine an interaction between the two proteins and so this work was halted and the focus turned to using FIII9'10 as a protein scaffold for the promotion of cell adhesion. If there had been sufficient time, work on IGFBP-5 would have been restarted again and cell culture methods utilised, such as inhibition assays to further explore the possible interaction between IGFBP-5 and FIII9'10.

In the first instance a simple validation of the proteins was performed using circular dichroism, size exclusion chromatography, and UV spectroscopy. Following this, a more comprehensive characterisation of the proteins was implemented. Fluorescence measured GdmCl unfolding of two FIII9'10 mutants termed FIII9''10 T2P and FIII9''10 H2P determined that the later had enhanced conformational stability.

Furthermore the FIII9''10 H2P mutant proved to have improved conformational stability in solution compared to FIII9'10 and the wild type FIII9-10. This was shown in part by automated circular dichroism studies of the protein over a range of pH's, temperatures and with increasing concentrations of denaturant, GdmCl.

Protein interactions at the solid/liquid interface were explored by implementing an innovative method involving a rotating sample holder. From this we gained useful insight to the conformational effects of varying the wettability of the surface has on the protein conformation. The FIII9''10 H2P mutant was found to retain its secondary structure on increasingly hydrophobic surfaces, implying that when adsorbed to various substrates the binding activity and function would not be impaired by hydrophobic induced conformational changes. The surface interactions of the proteins were further examined using neutron reflectometry (NR). NR revealed that the proteins FIII9'10 and FIII9''10 H2P at bulk concentrations formed a stable bilayer on TiO₂ which was retained on washing. The surface packing arrangements differed between the two proteins with FIII9''10 H2P forming a thicker layer, indicating that the protein units were more orientated in a tilted manor with respect to the surface.

FIII9''10 H2P includes the common binding peptide RGD and also the synergy site PHSRN which make it preferential to integrin $\alpha 5\beta 1$. Therefore as a preliminary test of the function of the protein ELISA was used with integrin $\alpha 5\beta 1$, this proved successful. The next step was to confirm the activity of the protein using cell culture adhesion assay, interestingly there was no statistical difference observed between the different proteins (FIII9-10, FIII9'10 and FIII9''10 H2P). Finally immunofluorescence microscopy was employed to visualise cell adhesion to TiO₂

surfaces coated with FIII9-10, FIII9'10 and FIII9''10 H2P. Similar cell morphologies were present for all of the proteins, confirming that they can all successfully support cell adhesion.

To conclude this investigation we restarted previous work using multimeric clusters of FIII9'10. The surface interaction between the multimeric proteins and gold was first characterised using NR. We passivated the gold surface using 11-MUD to form an incomplete self-assembling monolayer, thus allowing the thiol-gold interaction of the multimers to orientate in a way which would present the FIII9'10 constructs on the surface of the substrate. BHK cell adhesion was notably different from the non-specifically adsorbed FIII9'10 on TiO₂ supports. This could have been a feature of the different surfaces and so a direct comparison was not obtained; however it highlighted the different spread morphologies of the BHK cells.

Due to time limitations, cell culture assays were not explored fully. Ideally it would have been preferable to have better optimised the fluorescent labelling procedure so that the vinculin (blue) formation was easier to see. Incubation with BHK cell lines was only performed for one hour to reduce the laying down of the cells own fibronectin. However to gain better insight, it would have been useful to have a longer assay and sample at different time points in order to determine if the quicker adhesion of cells to the coated substrates allowed for an improved cell/substrate interaction. Quantification of the immunofluorescence images was not performed due to time constraints. By classifying the attached cells spread morphology it may have been possible to see a difference between the different proteins used to coat the substrates. Simple visual inspection suggested subtle differences in the cell

morphologies presented on the different substrates; however, this was not confirmed statistically and so no definitive conclusions were drawn from it.

An important area that was not exploited in this current work was the effects of surface topography on the protein adsorption and subsequent cell morphology. Recent work has demonstrated that etching a parylene-C and silicon dioxide surface with piranha solution has a significant effect on the cell morphology thought to be due to differential serum protein adsorption (Hughes et al. 2013). Furthermore, titanium surfaces displaying differing micro- and nano-topographies have been shown to exhibit improved differentiation behaviours in preosteoblast cells which can subsequently form bone (Zuo et al. 2013). Subtle differences in the topography of three titanium based substrates were observed by atomic force microscopy and scanning electron microscopy which distinguished that the substrate featuring randomly distributed cavities with sharp peaks and pattern ridges was optimum (Zuo et al. 2013). Had we also employed these techniques we would have gained a better understanding of our substrates and the effects that the topography may have on our protein adsorption and cell adhesion.

Defining and controlling cell patterns and morphology onto substrates has application not just in biomedical implants but also in the developing field of lab-on-chip technology. Hughes and co-workers (2013) studied human embryonic kidney cells as a precursor to eventually making controlled neuronal networks. The techniques described in this thesis could be applied to the generation and evaluation of protein complexes that could be designed for use in creating cellular patterns for future technologies.

References

- Abdelghani-Jacquín, C., Abdelghani, A., Chmel, G., Kantlehner, M. and Sackmann, E. (2002) 'Decorated surfaces by biofunctionalized gold beads: application to cell adhesion studies', *European Biophysics Journal with Biophysics Letters*, 31(2), 102-110.
- Adair, B. D., Xiong, J. P., Maddock, C., Goodman, S. L., Arnaout, M. A. and Yeager, M. (2005) 'Three-dimensional EM structure of the ectodomain of integrin alpha V beta 3 in a complex with fibronectin', *Journal of Cell Biology*, 168(7), 1109-1118.
- Adams, J. C. E. (2002) *Methods in cell-matrix adhesion*, San Diego: San Diego : Academic Press.
- Ahn, E. H. and Schroeder, J. J. (2010) 'Induction of Apoptosis by Sphingosine, Sphinganine, and C-2-Ceramide in Human Colon Cancer Cells, but not by C-2-Dihydroceramide', *Anticancer Research*, 30(7), 2881-2884.
- Akkiprik, M., Feng, Y. M., Wang, H. M., Chen, K. X., Hu, L. M., Sahin, A., Krishnamurthy, S., Ozer, A., Hao, X. S. and Zhang, W. (2008) 'Multifunctional roles of insulin-like growth factor binding protein 5 in breast cancer', *Breast Cancer Research*, 10(4).
- Albers, B. B., D. Lewis, J. Raff, M. Roberts, K. Watson, JD. (1994) *Molecular biology of the cell 3rd edition*, Garland Publishing, Inc.
- Allan, G. J., Tonner, E., Szymanowska, M., Shand, J. H., Kelly, S. M., Phillips, K., Clegg, R. A., Gow, I. F., Beattie, J. and Flint, D. J. (2006) 'Cumulative mutagenesis of the basic residues in the 201-218 region of insulin-like growth factor (IGF) binding protein-5 results in progressive loss of both IGF-I binding and inhibition of IGF-I biological action', *Endocrinology*, 147(1), 338-349.
- Altroff, H., Schlinkert, R., van der Walle, C. F., Bernini, A., Campbell, I. D., Werner, J. M. and Mardon, H. J. (2004) 'Interdomain tilt angle determines integrin-dependent function of the ninth and tenth FIII domains of human fibronectin', *Journal of Biological Chemistry*, 279(53), 55995-56003.

- Altroff, H., van der Walle, C. F., Asselin, J., Fairless, R., Campbell, I. D. and Mardon, H. J. (2001) 'The eighth FIII domain of human fibronectin promotes integrin alpha(5)beta(1) binding via stabilization of the ninth FIII domain', *Journal of Biological Chemistry*, 276(42), 38885-38892.
- Amirfazli, A. and Neumann, A. W. (2004) 'Status of the three-phase line tension', *Advances in Colloid and Interface Science*, 110(3), 121-141.
- Ananthakrishnan, R. and Ehrlicher, A. (2007) 'The forces behind cell movement', *International Journal of Biological Sciences*, 3(5), 303-317.
- Annan, W. S., Fairhead, M., Pereira, P. and van der Walle, C. F. (2006) 'Emulsifying performance of modular beta-sandwich proteins: the hydrophobic moment and conformational stability', *Protein Engineering Design & Selection*, 19(12), 537-545.
- Aota, S., Nomizu, M. and Yamada, K. M. (1994) 'The short amino-acid-sequence Pro-His-Ser-Arg-Asn in human fibronectin enhances cell-adhesive function', *Journal of Biological Chemistry*, 269(40), 24756-24761.
- Arai, T., Parker, A., Busby, W., Jr. and Clemmons, D. R. (1994) 'Heparin, Heparan Sulfate, and Dermatan Sulfate Regulate Formation of the Insulin-like Growth Factor-I and Insulin-like Growth Factor-binding protein Complexes', *Journal of Biological Chemistry*, 269(32), 20388-20393.
- Arima, Y. and Iwata, H. (2007) 'Effect of wettability and surface functional groups on protein adsorption and cell adhesion using well-defined mixed self-assembled monolayers', *Biomaterials*, 28(20), 3074-3082.
- Arnold, M., Schwieder, M., Bluemmel, J., Cavalcanti-Adam, E. A., Lopez-Garcia, M., Kessler, H., Geiger, B. and Spatz, J. P. (2009) 'Cell interactions with hierarchically structured nano-patterned adhesive surfaces', *Soft Matter*, 5(1), 72-77.
- Bach, L. A., Headey, S. J. and Norton, R. S. (2005) 'IGF-binding proteins - the pieces are falling into place', *Trends in Endocrinology and Metabolism*, 16(5), 228-234.
- Balian, G., Click, E. M. and Bornstein, P. (1980) 'Location of a collagen-binding domain in fibronectin', *Journal of Biological Chemistry*, 255(8), 3234-3236.

- Barczyk, M., Carracedo, S. and Gullberg, D. (2010) 'Integrins', *Cell and Tissue Research*, 339(1), 269-280.
- Barker, T. H. (2011) 'The role of ECM proteins and protein fragments in guiding cell behavior in regenerative medicine', *Biomaterials*, 32(18), 4211-4.
- Beattie, J., Allan, G. J., Lochrie, J. D. and Flint, D. J. (2006) 'Insulin-like growth factor-binding protein-5 (IGFBP-5): a critical member of the IGF axis', *Biochemical Journal*, 395, 1-19.
- Beattie, J., Kreiner, M., Allan, G. J., Flint, D. J., Domingues, D. and van der Walle, C. F. (2009) 'IGFBP-3 and IGFBP-5 associate with the cell binding domain (CBD) of fibronectin', *Biochemical and Biophysical Research Communications*, 381(4), 572-576.
- Beattie, J., Phillips, K., Shand, J. H., Szymanowska, M., Flint, D. J. and Allan, G. J. (2005) 'Molecular recognition characteristics in the insulin-like growth factor (IGF)-insulin-like growth factor binding protein-3/5 (IGFBP-3/5) heparin axis', *Journal of Molecular Endocrinology*, 34(1), 163-175.
- Becker, W. M., Kleinsmith, L. J. and Hardin, J. (2006) *The world of the cell*, 6th ed., San Francisco: Pearson Benjamin Cummings.
- Beckerle, M. C. (2001) *Cell Adhesion*, Oxford University Press.
- Berrier, A. L. and Yamada, K. M. (2007) 'Cell-matrix adhesion', *Journal of Cellular Physiology*, 213(3), 565-573.
- Biacore (2008) 'Biacore Sensor Surface Handbook',
- Boutinaud, M., Shand, J. H., Park, M. A., Phillips, K., Beattie, J., Flint, D. J. and Allan, G. J. (2004) 'A quantitative RT-PCR study of the mRNA expression profile of the IGF axis during mammary gland development', *Journal of Molecular Endocrinology*, 33(1), 195-207.
- Brouette, N., Fragneto, G., Cousin, F., Moulin, M., Haertlein, M. and Sferrazza, M. (2013) 'A neutron reflection study of adsorbed deuterated myoglobin layers on hydrophobic surfaces', *Journal of Colloid and Interface Science*, 390, 114-120.

- Bunn, R. C. and Fowlkes, J. L. (2003) 'Insulin-like growth factor binding protein proteolysis', *Trends in Endocrinology and Metabolism*, 14(4), 176-181.
- Burkhard, P., Meier, M. and Lustig, A. (2000) 'Design of a minimal protein oligomerization domain by a structural approach', *Protein Science*, 9(12), 2294-2301.
- Butt, A. J., Dickson, K. A., Jambazov, S. and Baxter, R. C. (2005) 'Enhancement of tumor necrosis factor-alpha-induced growth inhibition by insulin-like growth factor-binding protein-5 (IGFBP-5), but not IGFBP-3 in human breast cancer cells', *Endocrinology*, 146(7), 3113-3122.
- Butt, A. J., Dickson, K. A., McDougall, F. and Baxter, R. C. (2003) 'Insulin-like growth factor-binding protein-5 inhibits the growth of human breast cancer cells in vitro and in vivo', *Journal of Biological Chemistry*, 278(32), 29676-29685.
- Cabre, F., Canela, E. I. and Canela, M. A. (1989) 'Accuracy and precision in the determination of Stokes radii and molecular masses of proteins by gel-filtration chromatography', *Journal of Chromatography*, 472(2), 347-356.
- Calderwood, D. A., Shattil, S. J. and Ginsberg, M. H. (2000) 'Integrins and actin filaments: Reciprocal regulation of cell adhesion and signaling', *Journal of Biological Chemistry*, 275(30), 22607-22610.
- Celis, J. E. and Gromov, P. (1999) '2D protein electrophoresis: can it be perfected?', *Current Opinion in Biotechnology*, 10(1), 16-21.
- Chaudhuri, R., Cheng, Y., Middaugh, C. R. and Volkin, D. B. (2014) 'High-Throughput Biophysical Analysis of Protein Therapeutics to Examine Interrelationships Between Aggregate Formation and Conformational Stability', *Aaps Journal*, 16(1), 48-64.
- Chen, X., Wilde, K. L., Wang, H., Lake, V., Holden, P. J., Middelberg, A. P. J., He, L. and Duff, A. P. (2012) 'High yield expression and efficient purification of deuterated human protein galectin-2', *Food and Bioprocess Processing*, 90(C3), 563-572.
- Chillakuri, C. R., Jones, C. and Mardon, H. J. (2010) 'Heparin binding domain in vitronectin is required for oligomerization and thus enhances integrin mediated cell adhesion and spreading.', *Febs Letters*, 584(15), 3287-3291.

- Clemmons, D. R. (2001) 'Use of mutagenesis to probe IGF-binding protein structure/function relationships', *Endocrine Reviews*, 22(6), 800-817.
- Comisar, W. A., Mooney, D. J. and Linderman, J. J. (2011) 'Integrin organization: Linking adhesion ligand nanopatterns with altered cell responses', *Journal of Theoretical Biology*, 274(1), 120-130.
- Copie, V., Tomita, Y., Akiyama, S. K., Aota, S., Yamada, K. M., Venable, R. M., Pastor, R. W., Krueger, S. and Torchia, D. A. (1998) 'Solution structure and dynamics of linked cell attachment modules of mouse fibronectin containing the RGD and synergy regions: Comparison with the human fibronectin crystal structure', *Journal of Molecular Biology*, 277(3), 663-682.
- Cornell, B. A., BraachMaksvytis, V. L. B., King, L. G., Osman, P. D. J., Raguse, B., Wieczorek, L. and Pace, R. J. (1997) 'A biosensor that uses ion-channel switches', *Nature*, 387(6633), 580-583.
- Coyer, S. R., Singh, A., Dumbauld, D. W., Calderwood, D. A., Craig, S. W., Delamarche, E. and Garcia, A. J. (2012) 'Nanopatterning reveals an ECM area threshold for focal adhesion assembly and force transmission that is regulated by integrin activation and cytoskeleton tension', *Journal of Cell Science*, 125(21), 5110-5123.
- Creighton, T. E., ed. (1997) *Protein Structure: A Practical Approach*, U.S.A.: Oxford University Press.
- Cutler, S. M. and Garcia, A. J. (2003) 'Engineering cell adhesive surfaces that direct integrin alpha(5)beta(1) binding using a recombinant fragment of fibronectin', *Biomaterials*, 24(10), 1759-1770.
- Dillow, A. K., Lowman, A.M. (Eds.) (2002) *Biomimetic materials and design : biointerfacial strategies, tissue engineering, and targeted drug delivery*, New York: New York : Marcel Dekker.
- Efimova, Y. M., Haemers, S., Wierczinski, B., Norde, W. and van Well, A. A. (2007) 'Stability of globular proteins in H₂O and D₂O', *Biopolymers*, 85(3), 264-273.
- Eisenberg, J. L., Piper, J. L. and Mrksich, M. (2009) 'Using Self-Assembled Monolayers to Model Cell Adhesion to the 9th and 10th Type III Domains of Fibronectin', *Langmuir*, 25(24), 13942-13951.

- Faull, R. J. and Ginsberg, M. H. (1996) 'Inside-out signaling through integrins', *Journal of the American Society of Nephrology*, 7(8), 1091-1097.
- Ferris, D. M., Moodie, G. D., Dimond, P. M., Gioranni, C. W. D., Ehrlich, M. G. and Valentini, R. F. (1999) 'RGD-coated titanium implants stimulate increased bone formation in vivo', *Biomaterials*, 20(23-24), 2323-2331.
- Firth, S. M. and Baxter, R. C. (2002) 'Cellular actions of the insulin-like growth factor binding proteins', *Endocrine Reviews*, 23(6), 824-854.
- Fisher, S. J. and Helliwell, J. R. (2008) 'An investigation into structural changes due to deuteration', *Acta Crystallographica Section A*, 64, 359-367.
- Fletcher, J. M., Harniman, R. L., Barnes, F. R. H., Boyle, A. L., Collins, A., Mantell, J., Sharp, T. H., Antognozzi, M., Booth, P. J., Linden, N., Miles, M. J., Sessions, R. B., Verkade, P. and Woolfson, D. N. (2013) 'Self-Assembling Cages from Coiled-Coil Peptide Modules', *Science*, 340(6132), 595-599.
- Flint, D. J., Boutinaud, M., Tonner, E., Wilde, C. J., Hurley, W., Accorsi, P. A., Kolb, A. F., Whitelaw, C. B. A., Beattie, J. and Allan, G. J. (2005) 'Insulin-like growth factor binding proteins initiate cell death and extracellular matrix remodeling in the mammary gland', *Domestic Animal Endocrinology*, 29(2), 274-282.
- Fragneto-Cusani, G. (2001) 'Neutron reflectivity at the solid/liquid interface: examples of applications in biophysics', *Journal of Physics-Condensed Matter*, 13(21), 4973-4989.
- Frantz, C., Stewart, K. M. and Weaver, V. M. (2010) 'The extracellular matrix at a glance', *Journal of Cell Science*, 123(24), 4195-4200.
- Friess, W. (1998) 'Collagen - biomaterial for drug delivery', *European Journal of Pharmaceutics and Biopharmaceutics*, 45(2), 113-136.
- Fu, H. L., Grimsley, G. R., Razvi, A., Scholtz, J. M. and Pace, C. N. (2009) 'Increasing protein stability by improving Beta-turns', *Proteins-Structure Function and Bioinformatics*, 77(3), 491-498.
- Ganesan, A., Price, N. C., Kelly, S. M., Petry, I., Moore, B. D. and Halling, P. J. (2006) 'Circular dichroism studies of subtilisin Carlsberg immobilised on

- micron sized silica particles', *Biochimica Et Biophysica Acta-Proteins and Proteomics*, 1764(6), 1119-1125.
- Ganesan, A., Watkinson, A. and Moore, B. D. (2012) 'Biophysical characterisation of thermal-induced precipitates of recombinant anthrax protective antigen: Evidence for kinetically trapped unfolding domains in solid-state', *European Journal of Pharmaceutics and Biopharmaceutics*, 82(3), 475-484.
- Garcia, A. J., Vega, M. D. and Boettiger, D. (1999) 'Modulation of cell proliferation and differentiation through substrate-dependent changes in fibronectin conformation', *Molecular Biology of the Cell*, 10(3), 785-798.
- Geiger, B. and Bershadsky, A. (2001) 'Assembly and mechanosensory function of focal contacts', *Current Opinion in Cell Biology*, 13(5), 584-592.
- Geiger, B. and Yamada, K. M. (2011) 'Molecular Architecture and Function of Matrix Adhesions', *Cold Spring Harbor Perspectives in Biology*, 3(5).
- Giamblanco, N., Zhavnerko, G., Tuccitto, N., Licciardello, A. and Marletta, G. (2012) 'Coadsorption-dependent orientation of fibronectin epitopes at hydrophilic gold surfaces', *Soft Matter*, 8(32), 8370-8378.
- Giovambattista, N., Debenedetti, P. G. and Rosky, P. J. (2007) 'Effect of surface polarity on water contact angle and interfacial hydration structure', *Journal of Physical Chemistry B*, 111(32), 9581-9587.
- Grant, R. P., Spitzfaden, C., Altroff, H., Campbell, I. D. and Mardon, H. J. (1997) 'Structural requirements for biological activity of the ninth and tenth FIII domains of human fibronectin', *Journal of Biological Chemistry*, 272(10), 6159-6166.
- Grimberg, A. and Cohen, P. (2000) 'Role of insulin-like growth factors and their binding proteins in growth control and carcinogenesis', *Journal of Cellular Physiology*, 183(1), 1-9.
- Gui, Y. T. and Murphy, L. J. (2001) 'Insulin-like growth factor (IGF)-binding protein-3 (IGFBP-3) binds to fibronectin (FN): Demonstration of IGF-I/IGFBP-3/FN ternary complexes in human plasma', *Journal of Clinical Endocrinology & Metabolism*, 86(5), 2104-2110.

- Guo, W. J. and Giancotti, F. G. (2004) 'Integrin signalling during tumour progression', *Nature Reviews Molecular Cell Biology*, 5(10), 816-826.
- Harbury, P. B., Zhang, T., Kim, P. S. and Alber, T. (1993) 'A switch between 2-stranded, 3-stranded and 4-stranded coiled coils in GCN4 leucine-zipper mutants', *Science*, 262(5138), 1401-1407.
- Harley, B. A. C. and Gibson, L. J. (2008) 'In vivo and in vitro applications of collagen-GAG scaffolds', *Chemical Engineering Journal*, 137(1), 102-121.
- Harroun, T. A., Wignall, G. D. and Katsaras, J. (2006) 'Neutron Scattering for Biology', *Neutron Scattering in Biology: Techniques and Applications*, (1).
- Hayashi, M., Schlesinger, D. H., Kennedy, D. W. and Yamada, K. M. (1980) 'Isolation and characterization of a heparin-binding domain of cellular fibronectin', *Journal of Biological Chemistry*, 255(21), 17-20.
- Hayter, J. B., Highfield, R. R., Pullman, B. J., Thomas, R. K., McMullen, A. I. and Penfold, J. (1981) 'Critical reflection of neutrons - A new technique for investigating interfacial phenomena', *Journal of the Chemical Society-Faraday Transactions I*, 77, 1437-1448.
- Headey, S. J., Leeding, K. S., Norton, R. S. and Bach, L. A. (2004) 'Contributions of the N- and C-terminal domains of IGF binding protein-6 to IGF binding', *Journal of Molecular Endocrinology*, 33(2), 377-386.
- Helle, S. I. (2004) 'The insulin-like growth factor system in advanced breast cancer', *Best Practice & Research Clinical Endocrinology & Metabolism*, 18(1), 67-79.
- Hersel, U., Dahmen, C. and Kessler, H. (2003) 'RGD modified polymers: biomaterials for stimulated cell adhesion and beyond', *Biomaterials*, 24(24), 4385-4415.
- Hirsh, S. L., McKenzie, D. R., Nosworthy, N. J., Denman, J. A., Sezerman, O. U. and Bilek, M. M. M. (2013) 'The Vroman effect: Competitive protein exchange with dynamic multilayer protein aggregates', *Colloids and Surfaces B-Biointerfaces*, 103, 395-404.
- Holt, S. A., Henderson, M. J. and White, J. W. (2002) 'Thermal denaturation of interfacial protein layers', *Australian Journal of Chemistry*, 55(6-7), 449-459.

- Holt, S. A., Le Brun, A. P., Majkrzak, C. F., McGillivray, D. J., Heinrich, F., Loesche, M. and Lakey, J. H. (2009) 'An ion-channel-containing model membrane: structural determination by magnetic contrast neutron reflectometry', *Soft Matter*, 5(13), 2576-2586.
- Huang, X., Zauscher, S., Klitzman, B., Truskey, G. A., Reichert, W. M., Kenan, D. J. and Grinstaff, M. W. (2010) 'Peptide Interfacial Biomaterials Improve Endothelial Cell Adhesion and Spreading on Synthetic Polyglycolic Acid Materials', *Annals of Biomedical Engineering*, 38(6), 1965-1976.
- Hughes, M. A., Bunting, A. S., Cameron, K., Murray, A. F. and Shipston, M. J. (2013) 'Modulating patterned adhesion and repulsion of HEK 293 cells on microengineered parylene-C/SiO₂ substrates', *Journal of Biomedical Materials Research Part A*, 101A(2), 349-357.
- Humphries, J. D., Byron, A. and Humphries, M. J. (2006) 'Integrin ligands at a glance', *Journal of Cell Science*, 119(19), 3901-3903.
- Humphries, M. J. (2000) 'Integrin structure', *Biochemical Society Transactions*, 28, 311-340.
- Huxley-Jones, J., Foord, S. M. and Barnes, M. R. (2008) 'Drug discovery in the extracellular matrix', *Drug Discovery Today*, 13(15-16), 685-694.
- Hynes, R. O. (2002) 'Integrins: Bidirectional, allosteric signaling machines', *Cell*, 110(6), 673-687.
- Hynes, R. O. and Yamada, K. M. (1982) 'Fibronectins - Multifunctional modular glycoproteins', *Journal of Cell Biology*, 95(2), 369-377.
- Jones, J. I., Gockerman, A., Busby, W. H., Wright, G. and Clemmons, D. R. (1993) 'Insulin-like growth-factor binding protein-1 stimulates cell-migration and binds to the alpha-5-beta-1 integrin by means of its Arg-Gly-Asp sequence', *Proceedings of the National Academy of Sciences of the United States of America*, 90(22), 10553-10557.
- Kang, E., Park, J.-W., McClellan, S. J., Kim, J.-M., Holland, D. P., Lee, G. U., Franses, E. I., Park, K. and Thompson, D. H. (2007) 'Specific adsorption of histidine-tagged proteins on silica surfaces modified with Ni²⁺/NTA-derivatized poly(ethylene glycol)', *Langmuir*, 23(11), 6281-6288.

- Keegan, N., Wright, N. G. and Lakey, J. H. (2005) 'Circular dichroism spectroscopy of folding in a protein monolayer', *Angewandte Chemie-International Edition*, 44(30), 4801-4804.
- Kelly, S. M., Jess, T. J. and Price, N. C. (2005) 'How to study proteins by circular dichroism', *Biochimica Et Biophysica Acta-Proteins and Proteomics*, 1751(2), 119-139.
- Kelly, S. M. and Price, N. C. (2000) 'The Use of Circular Dichroism in the Investigation of Protein Structure and Function', *Current Protein & Peptide Science*, 1(4), 349-384.
- Koo, L. Y., Irvine, D. J., Mayes, A. M., Lauffenburger, D. A. and Griffith, L. G. (2002) 'Co-regulation of cell adhesion by nanoscale RGD organization and mechanical stimulus', *Journal of Cell Science*, 115(7), 1423-1433.
- Kreiner, M., Byron, O., Domingues, D. and van der Walle, C. F. (2009a) 'Oligomerisation and thermal stability of polyvalent integrin alpha 5 beta 1 ligands', *Biophysical Chemistry*, 142(1-3), 34-39.
- Kreiner, M., Chillakuri, C. R., Pereira, P., Fairhead, M., Li, Z. H., Mardon, H. J., Holt, S. A. and van der Walle, C. F. (2009b) 'Orientation and surface coverage of adsorbed fibronectin cell binding domains and bound integrin alpha 5 beta 1 receptors', *Soft Matter*, 5(20), 3954-3962.
- Kreiner, M., Li, Z., Beattie, J., Kelly, S. M., Mardon, H. J. and van der Walle, C. F. (2008) 'Self-assembling multimeric integrin alpha 5 beta 1 ligands for cell attachment and spreading', *Protein Engineering Design & Selection*, 21(9), 553-560.
- Kuhlman, W., Taniguchi, I., Griffith, L. G. and Mayes, A. M. (2007) 'Interplay between PEO tether length and ligand spacing governs cell spreading on RGD-modified PMMA-g-PEO comb copolymers', *Biomacromolecules*, 8(10), 3206-3213.
- Kulkarni, S. A. and Vijayamohan, K. P. (2007) 'Interfacial behavior of alkyltrichlorosilane monolayers on silicon: Control of flat-band potential and surface state distribution using chain length variation', *Surface Science*, 601(14), 2983-2993.

- Lagunas, A., Comelles, J., Martinez, E., Prats-Alfonso, E., Acosta, G. A., Albericio, F. and Samitier, J. (2012) 'Cell adhesion and focal contact formation on linear RGD molecular gradients: study of non-linear concentration dependence effects', *Nanomedicine-Nanotechnology Biology and Medicine*, 8(4), 432-439.
- Lakey, J. H. (2009) 'Neutrons for biologists: a beginner's guide, or why you should consider using neutrons', *Journal of the Royal Society Interface*, 6, S567-S573.
- Lamprou, D. A., Smith, J. R., Nevell, T. G., Barbu, E., Willis, C. R. and Tsibouklis, J. (2010) 'Towards the Determination of Surface Energy at the Nanoscale: A Further Assessment of the AFM-Based Approach', *Journal of Advanced Microscopy Research*, 5(2), 137-142.
- Larsericdotter, H., Oscarsson, S. and Buijs, J. (2004) 'Thermodynamic analysis of lysozyme adsorbed to silica', *Journal of Colloid and Interface Science*, 276(2), 261-268.
- Laukaitis, C. M., Webb, D. J., Donais, K. and Horwitz, A. F. (2001) 'Differential dynamics of alpha 5 integrin, paxillin, and alpha-actinin during formation and disassembly of adhesions in migrating cells', *Journal of Cell Biology*, 153(7), 1427-1440.
- Leahy, D. J., Aukhil, I. and Erickson, H. P. (1996) '2.0 angstrom crystal structure of a four-domain segment of human fibronectin encompassing the RGD loop and synergy region', *Cell*, 84(1), 155-164.
- Li, H. B., Carrion-Vazquez, M., Oberhauser, A. F., Marszalek, P. E. and Fernandez, J. M. (2000) 'Point mutations alter the mechanical stability of immunoglobulin modules', *Nature Structural Biology*, 7(12).
- Li, J., Chen, J. and Kirsner, R. (2007) 'Pathophysiology of acute wound healing', *Clinics in Dermatology*, 25(1), 9-18.
- Li, L. Y., Chen, S. F., Zheng, J., Ratner, B. D. and Jiang, S. Y. (2005) 'Protein adsorption on oligo(ethylene glycol)-terminated alkanethiolate self-assembled monolayers: The molecular basis for nonfouling behavior', *Journal of Physical Chemistry B*, 109(7), 2934-2941.

- Li, X. Q., Cao, X. C., Li, X., Zhang, W. and Feng, Y. M. (2007) 'Expression level of insulin-like growth factor binding protein 5 mRNA is a prognostic factor for breast cancer', *Cancer Science*, 98, 1592-1596.
- Li, Z., Kreiner, M., van der Walle, C. F. and Mardon, H. J. (2011) 'Clustered integrin alpha 5 beta 1 ligand displays model fibronectin-mediated adhesion of human endometrial stromal cells', *Biochemical and Biophysical Research Communications*, 407(4), 777-782.
- Lin, F., Ren, X.-D., Pan, Z., Macri, L., Zong, W.-X., Tonnesen, M. G., Rafailovich, M., Bar-Sagi, D. and Clark, R. A. F. (2011) 'Fibronectin Growth Factor-Binding Domains Are Required for Fibroblast Survival', *Journal of Investigative Dermatology*, 131(1), 84-98.
- Ling, Y., Maile, L. A. and Clemmons, D. R. (2003) 'Tyrosine phosphorylation of the beta 3-subunit of the alpha V beta 3 integrin is required for membrane association of the tyrosine phosphatase SHP-2 and its further recruitment to the insulin-like growth factor I receptor', *Molecular Endocrinology*, 17(9), 1824-1833.
- Liu, X. Y., Chu, P. K. and Ding, C. X. (2004) 'Surface modification of titanium, titanium alloys, and related materials for biomedical applications', *Materials Science & Engineering R-Reports*, 47(3-4), 49-121.
- Lochrie, J. D., Phillips, K., Tonner, E., Flint, D. J., Allan, G. J., Price, N. C. and Beattie, J. (2006) 'Insulin-like growth factor binding protein (IGFBP)-5 is upRegulated during both differentiation and apoptosis in primary cultures of mouse mammary epithelial cells', *Journal of Cellular Physiology*, 207(2), 471-479.
- Lu, J. R. (1999) 'Neutron reflection study of globular protein adsorption at planar interfaces', *Annual Report on the Progress of Chemistry, Vol 95, Section C: Physical Chemistry*, 95, 3-45.
- Luo, B.-H., Carman, C. V. and Springer, T. A. (2007) 'Structural basis of integrin regulation and signaling', *Annual Review of Immunology*, 25, 619-647.
- MacDonald, D. E., Deo, N., Markovic, B., Stranick, M. and Somasundaran, P. (2002) 'Adsorption and dissolution behavior of human plasma fibronectin on thermally and chemically modified titanium dioxide particles', *Biomaterials*, 23(4), 1269-1279.

- Maheshwari, G., Brown, G., Lauffenburger, D. A., Wells, A. and Griffith, L. G. (2000) 'Cell adhesion and motility depend on nanoscale RGD clustering', *Journal of Cell Science*, 113(10), 1677-1686.
- Mao, Y. and Schwarzbauer, J. E. (2005) 'Fibronectin fibrillogenesis, a cell-mediated matrix assembly process', *Matrix Biology*, 24(6), 389-399.
- Mardon, H. J. and Grant, K. E. (1994) 'The role of the 9th and 10th type-III domains of human fibronectin in cell-adhesion', *Febs Letters*, 340(3), 197-201.
- Marshman, E., Green, K. A., Flint, D. J., White, A., Streuli, C. H. and Westwood, M. (2003) 'Insulin-like growth factor binding protein 5 and apoptosis in mammary epithelial cells', *Journal of Cell Science*, 116(4), 675-682.
- Martino, M. M., Mochizuki, M., Rothenfluh, D. A., Rempel, S. A., Hubbell, J. A. and Barker, T. H. (2009) 'Controlling integrin specificity and stem cell differentiation in 2D and 3D environments through regulation of fibronectin domain stability', *Biomaterials*, 30(6), 1089-1097.
- McCaig, C., Perks, C. M. and Holly, J. M. P. (2002) 'Intrinsic actions of IGFBP-3 and IGFBP-5 on Hs578T breast cancer epithelial cells: inhibition or accentuation of attachment and survival is dependent upon the presence of fibronectin', *Journal of Cell Science*, 115(22), 4293-4303.
- Memmo, L. M. and McKeown-Longo, P. (1998) 'The alpha v beta 5 integrin functions as an endocytic receptor for vitronectin', *Journal of Cell Science*, 111, 425-433.
- Michael, K. E., Vernekar, V. N., Keselowsky, B. G., Meredith, J. C., Latour, R. A. and Garcia, A. J. (2003) 'Adsorption-induced conformational changes in fibronectin due to interactions with well-defined surface chemistries', *Langmuir*, 19(19), 8033-8040.
- Michel, R., Pasche, S., Textor, M. and Castner, D. G. (2005) 'Influence of PEG architecture on protein adsorption and conformation', *Langmuir*, 21(26), 12327-12332.
- Middleton, C. A., Pendegrass, C. J., Gordon, D., Jacobs, J. and Blunn, G. W. (2007) 'Fibronectin silanized titanium alloy: A bioinductive and durable coating to enhance fibroblast attachment in vitro', *Journal of Biomedical Materials Research Part A*, 83A(4), 1032-1038.

- Mills, A. and Crow, M. (2008) 'A study of factors that change the wettability of titania films', *International Journal of Photoenergy*.
- Miyakoshi, N., Richman, C., Kasukawa, Y., Linkhart, T. A., Baylink, D. J. and Mohan, S. (2001) 'Evidence that IGF-binding protein-5 functions as a growth factor', *Journal of Clinical Investigation*, 107(1), 73-81.
- Mohan, S. and Baylink, D. J. (2002) 'IGF-binding proteins are multifunctional and act via IGF-dependent and -independent mechanisms', *Journal of Endocrinology*, 175(1), 19-31.
- Nam, T., Moralez, A. and Clemmons, D. (2002) 'Vitronectin binding to IGF binding protein-5 (IGFBP-5) alters IGFBP-5 modulation of IGF-I actions', *Endocrinology*, 143(1), 30-36.
- Nam, T. J., Busby, W. H., Rees, C. and Clemmons, D. R. (2000) 'Thrombospondin and osteopontin bind to insulin-like growth factor (IGF)-binding protein-5 leading to an alteration in IGF-I-stimulated cell growth', *Endocrinology*, 141(3), 1100-1106.
- Nelson, A. (2006) 'Co-refinement of multiple-contrast neutron/X-ray reflectivity data using MOTOFIT', *Journal of Applied Crystallography*, 39, 273-276.
- Nishida, N., Xie, C., Shimaoka, M., Cheng, Y., Walz, T. and Springer, T. A. (2006) 'Activation of leukocyte beta2 integrins by conversion from bent to extended conformations', *Immunity*, 25(4), 583-94.
- Nishiuchi, R., Takagi, J., Hayashi, M., Ido, H., Yagi, Y., Sanzen, N., Tsuji, T., Yamada, M. and Sekiguchi, K. (2006) 'Ligand-binding specificities of laminin-binding integrins: A comprehensive survey of laminin-integrin interactions using recombinant alpha 3 beta 1, alpha 6 beta 1, alpha 7 beta 1 and alpha 6 beta 4 integrins', *Matrix Biology*, 25(3), 189-197.
- Noel, O., Brogly, M., Castelein, G. and Schultz, J. (2004) 'In situ determination of the thermodynamic surface properties of chemically modified surfaces on a local scale: An attempt with the atomic force microscope', *Langmuir*, 20(7), 2707-2712.
- Noh, H. and Vogler, E. A. (2007) 'Volumetric interpretation of protein adsorption: Competition from mixtures and the Vroman effect', *Biomaterials*, 28(3), 405-422.

- Norde, W., Macritchie, F., Nowicka, G. and Lyklema, J. (1986) 'Protein adsorption at solid liquid interfaces - reversibility and conformation aspects', *Journal of Colloid and Interface Science*, 112(2), 447-456.
- O'Shea, E. K., Rutkowski, R. and Kim, P. S. (1989) 'Evidence that the leucine zipper is a coiled coil', *Science*, 243(4890), 538-542.
- Ohashi, T., Kiehart, D. P. and Erickson, H. P. (1999) 'Dynamics and elasticity of the fibronectin matrix in living cell culture visualized by fibronectin-green fluorescent protein', *Proceedings of the National Academy of Sciences of the United States of America*, 96(5), 2153-2158.
- Pankov, R. and Yamada, K. M. (2002) 'Fibronectin at a glance', *Journal of Cell Science*, 115(20), 3861-3863.
- Panos, M., Sen, T. Z. and Ahunbay, M. G. (2012) 'Molecular Simulation of Fibronectin Adsorption onto Polyurethane Surfaces', *Langmuir*, 28(34), 12619-12628.
- Peelen, D., Kodoyianni, V., Lee, J., Zheng, T., Shortreed, M. R. and Smith, L. M. (2006) 'Specific capture of mammalian cells by cell surface receptor binding to ligand immobilized on gold thin films', *Journal of Proteome Research*, 5(7), 1580-1585.
- Pegueroles, M., Tonda-Turo, C., Planell, J. A., Gil, F.-J. and Aparicio, C. (2012) 'Adsorption of Fibronectin, Fibrinogen, and Albumin on TiO₂: Time-Resolved Kinetics, Structural Changes, and Competition Study', *Biointerphases*, 7(1-4).
- Pelham, R. J., Jr. and Wang, Y. (1997) 'Cell locomotion and focal adhesions are regulated by substrate flexibility', *Proc Natl Acad Sci U S A*, 94(25), 13661-5.
- Pereira, P., Kelly, S. M., Cooper, A., Mardon, H. J., Gellert, P. R. and van der Walle, C. F. (2007) 'Solution formulation and lyophilisation of a recombinant fibronectin fragment', *European Journal of Pharmaceutics and Biopharmaceutics*, 67(2), 309-319.
- Pereira, P., Kelly, S. M., Gellert, P. R. and van der Walle, C. F. (2008) 'Interdomain mobility and conformational stability of type III fibronectin domain pairs

- control surface adsorption, desorption and unfolding', *Colloids and Surfaces B-Biointerfaces*, 64(1), 1-9.
- Perks, C. M., McCaig, C., Clarke, J. B., Clemmons, D. R. and Holly, J. M. P. (2002) 'Effects of a non-IGF binding mutant of IGFBP-5 on cell death in human breast cancer cells', *Biochemical and Biophysical Research Communications*, 294(5), 995-1000.
- Perks, C. M., Newcomb, P. V., Norman, M. R. and Holly, J. M. P. (1999) 'Effect of insulin-like growth factor binding protein-1 on integrin signalling and the induction of apoptosis in human breast cancer cells', *Journal of Molecular Endocrinology*, 22(2), 141-150.
- Petrie, T. A., Raynor, J. E., Reyes, C. D., Burns, K. L., Collard, D. M. and Garcia, A. J. (2008) 'The effect of integrin-specific bioactive coatings on tissue healing and implant osseointegration', *Biomaterials*, 29(19), 2849-2857.
- Pierschbacher, M. D. and Ruoslahti, E. (1984) 'Cell attachment activity of fibronectin can be duplicated by small synthetic fragments of the molecule', *Nature*, 309(5963), 30-3.
- Plaxco, K. W., Spitzfaden, C., Campbell, I. D. and Dobson, C. M. (1997) 'A comparison of the folding kinetics and thermodynamics of two homologous fibronectin type III modules', *Journal of Molecular Biology*, 270(5), 763-770.
- Plow, E. F., Haas, T. K., Zhang, L., Loftus, J. and Smith, J. W. (2000) 'Ligand binding to integrins', *Journal of Biological Chemistry*, 275(29), 21785-21788.
- Porter, M. D., Bright, T. B., Allara, D. L. and Chidsey, C. E. D. (1987) 'Spontaneously organized molecular assemblies .4. Structural characterization of normal-alkyl thiol monolayers on gold by optical ellipsometry, infrared-spectroscopy, and electrochemistry', *Journal of the American Chemical Society*, 109(12), 3559-3568.
- Prime, K. L. and Whitesides, G. M. (1993) 'Adsorption of proteins onto surfaces containing end-attached oligo(ethylene oxide) - A model system using self-assembled monolayers', *Journal of the American Chemical Society*, 115(23), 10714-10721.

- Randlett, O., Poggi, L., Zolessi, F. R. and Harris, W. A. (2011) 'The oriented emergence of axons from retinal ganglion cells is directed by laminin contact in vivo', *Neuron*, 70(2), 266-80.
- Rexeisen, E. L., Fan, W., Pangburn, T. O., Taribagil, R. R., Bates, F. S., Lodge, T. P., Tsapatsis, M. and Kokkoli, E. (2010) 'Self-assembly of fibronectin mimetic peptide-amphiphile nanofibers', *Langmuir*, 26(3), 1953-9.
- Rotticci, D., Rotticci-Mulder, J. C., Denman, S., Norin, T. and Hult, K. (2001) 'Improved enantioselectivity of a lipase by rational protein engineering', *Chembiochem*, 2(10).
- Roy, D. C. and Hocking, D. C. (2013) 'Recombinant Fibronectin Matrix Mimetics Specify Integrin Adhesion and Extracellular Matrix Assembly', *Tissue Engineering Part A*, 19(3-4), 558-570.
- Sachdev, D. and Yee, D. (2001) 'The IGF system and breast cancer', *Endocrine-Related Cancer*, 8(3), 197-209.
- Saerbeck, T., Klose, F., Le Brun, A. P., Fuezi, J., Brule, A., Nelson, A., Holt, S. A. and James, M. (2012) 'Invited Article: Polarization "Down Under": The polarized time-of-flight neutron reflectometer PLATYPUS', *Review of Scientific Instruments*, 83(8).
- Samanen, J., Jonak, Z., Rieman, D. and Yue, T. L. (1997) 'Vascular indications for integrin alpha v antagonists', *Current Pharmaceutical Design*, 3(6), 545-584.
- Sambrook, J. and Russell, D. W. (2001) *Molecular cloning: a laboratory manual*, 3rd ed., Cold Spring Harbor, N.Y.: Cold Spring Harbor Laboratory Press.
- Sasisanker, P., Oleinikova, A., Weingartner, H., Ravindra, R. and Winter, R. (2004) 'Solvation properties and stability of ribonuclease A in normal and deuterated water studied by dielectric relaxation and differential scanning/pressure perturbation calorimetry', *Physical Chemistry Chemical Physics*, 6(8), 1899-1905.
- Sharp, P. M., Cowe, E., Higgins, D. G., Shields, D. C., Wolfe, K. H. and Wright, F. (1988) 'Codon usage patterns in Escherichia-coli, bacillus-subtilis, saccharomyces-cerevisiae, schizosaccharomyces-pombe, drosophila-melanogaster and homo-sapiens - A review of the considerable within-species diversity', *Nucleic Acids Research*, 16(17), 8207-8211.

- Shattil, S. J. (1999) 'Signaling through platelet integrin alpha IIb beta 3: inside-out, outside-in, and sideways', *Thromb Haemost*, 82(2), 318-25.
- Shin, H., Jo, S. and Mikos, A. G. (2003) 'Biomimetic materials for tissue engineering', *Biomaterials*, 24(24), 4353-4364.
- Singh, M. D., Kreiner, M., McKimmie, C. S., Holt, S., van der Walle, C. F. and Graham, G. J. (2009) 'Dimeric integrin alpha 5 beta 1 ligands confer morphological and differentiation responses to murine embryonic stem cells', *Biochemical and Biophysical Research Communications*, 390(3), 716-721.
- Sitar, T., Popowicz, G. M., Siwanowicz, I., Huber, R. and Holak, T. A. (2006) 'Structural basis for the inhibition of insulin-like growth factors by insulin-like growth factor-binding proteins', *Proceedings of the National Academy of Sciences of the United States of America*, 103(35), 13028-13033.
- Song, D.-P., Chen, M.-J., Liang, Y.-C., Bai, Q.-S., Chen, J.-X. and Zheng, X.-F. (2010) 'Adsorption of tripeptide RGD on rutile TiO₂ nanotopography surface in aqueous solution', *Acta Biomaterialia*, 6(2), 684-694.
- Song, X. Y., Zhai, J., Wang, Y. L. and Jiang, L. (2006) 'Self-assembly of amino-functionalized monolayers on silicon surfaces and preparation of superhydrophobic surfaces based on alkanolic acid dual layers and surface roughening', *Journal of Colloid and Interface Science*, 298(1), 267-273.
- Spitzfaden, C., Grant, R. P., Mardon, H. J. and Campbell, I. D. (1997) 'Module-module interactions in the cell binding region of fibronectin: Stability, flexibility and specificity', *Journal of Molecular Biology*, 265(5), 565-579.
- Stockmann, A., Hess, S., Declerck, P., Timpl, R. and Preissner, K. T. (1993) 'Multimeric vitronectin. Identification and characterization of conformation-dependent self-association of the adhesive protein', *J Biol Chem*, 268(30), 22874-82.
- Su, T. J., Lu, J. R., Thomas, R. K., Cui, Z. F. and Penfold, J. (1998) 'The adsorption of lysozyme at the silica-water interface: A neutron reflection study', *Journal of Colloid and Interface Science*, 203(2), 419-429.
- Tadeo, X., Lopez-Mendez, B., Castano, D., Trigueros, T. and Millet, O. (2009) 'Protein Stabilization and the Hofmeister Effect: The Role of Hydrophobic Solvation', *Biophysical Journal*, 97(9), 2595-2603.

- Takagi, J., Petre, B. M., Walz, T. and Springer, T. A. (2002) 'Global conformational rearrangements in integrin extracellular domains in outside-in and inside-out signaling', *Cell*, 110(5), 599-11.
- Tapley, P., Horwitz, A., Buck, C., Duggan, K. and Rohrschneider, L. (1989) 'Integrins isolated from Rous sarcoma virus-transformed chicken embryo fibroblasts', *Oncogene*, 4(3), 325-33.
- Terrettaz, S., Ulrich, W. P., Vogel, H., Hong, Q., Dover, L. G. and Lakey, J. H. (2002) 'Stable self-assembly of a protein engineering scaffold on gold surfaces', *Protein Science*, 11(8), 1917-1925.
- Thomas, G. J., Nystrom, M. L. and Marshall, J. F. (2006) 'alphavbeta6 integrin in wound healing and cancer of the oral cavity', *J Oral Pathol Med*, 35(1), 1-10.
- Topoglidis, E., Campbell, C. J., Cass, A. E. G. and Durrant, J. R. (2001) 'Factors that affect protein adsorption on nanostructured titania films. A novel spectroelectrochemical application to sensing', *Langmuir*, 17(25), 7899-7906.
- Toworfe, G. K., Composto, R. J., Adams, C. S., Shapiro, I. M. and Ducheyne, P. (2004) 'Fibronectin adsorption on surface-activated poly(dimethylsiloxane) and its effect on cellular function', *Journal of Biomedical Materials Research Part A*, 71A(3), 449-461.
- Trevino, S. R., Scholtz, J. M. and Pace, C. N. (2008) 'Measuring and increasing protein solubility', *Journal of Pharmaceutical Sciences*, 97(10), 4155-4166.
- Tung, R. (2010) 'The Development of Deuterium-Containing Drugs', *Innovations in Pharmaceutical Technology*,
- Tzoneva, R., Groth, T., Altankov, G. and Paul, D. (2002) 'Remodeling of fibrinogen by endothelial cells in dependence on fibronectin matrix assembly. Effect of substratum wettability', *Journal of Materials Science-Materials in Medicine*, 13(12), 1235-1244.
- van der Walle, C. F., Altroff, H. and Mardon, H. J. (2002) 'Novel mutant human fibronectin FIII9-10 domain pair with increased conformational stability and biological activity', *Protein Engineering*, 15(12), 1021-1024.

- Vidal, G., Blanchi, T., Mieszawska, A. J., Calabrese, R., Rossi, C., Vigneron, P., Duval, J.-L., Kaplan, D. L. and Egles, C. (2013) 'Enhanced cellular adhesion on titanium by silk functionalized with titanium binding and RGD peptides', *Acta Biomaterialia*, 9(1), 4935-4943.
- von Wichert, G., Haimovich, B., Feng, G. S. and Sheetz, M. P. (2003) 'Force-dependent integrin-cytoskeleton linkage formation requires downregulation of focal complex dynamics by Shp2', *Embo Journal*, 22(19), 5023-5035.
- Walsh, G. (2002) *Proteins : biochemistry and biotechnology*, Chichester ; New York: J. Wiley.
- Wang, R., Sakai, N., Fujishima, A., Watanabe, T. and Hashimoto, K. (1999) 'Studies of surface wettability conversion on TiO₂ single-crystal surfaces', *Journal of Physical Chemistry B*, 103(12), 2188-2194.
- Wang, R. X., Clark, R. A. F., Mosher, D. F. and Ren, X. D. (2005) 'Fibronectin's central cell-binding domain supports focal adhesion formation and rho signal transduction', *Journal of Biological Chemistry*, 280(31), 28803-28810.
- Watson, N., Duncan, G., Annan, W. S. and Van Der Walle, C. F. (2006) 'A tetravalent RGD ligand for integrin-mediated cell adhesion', *Journal of Pharmacy and Pharmacology*, 58(7), 959-966.
- Wayner, E. A., Orlando, R. A. and Cheresch, D. A. (1991) 'Integrin alpha-V-beta-3 and integrin alpha-V-beta-5 contribute to cell attachment to vitronectin but differentially distribute on the cell-surface', *Journal of Cell Biology*, 113(4), 919-929.
- Webster, T. J., Ergun, C., Doremus, R. H., Siegel, R. W. and Bizios, R. (2000) 'Specific proteins mediate enhanced osteoblast adhesion on nanophase ceramics', *Journal of Biomedical Materials Research*, 51(3), 475-483.
- Wehmeyer, J. L., Synowicki, R., Bizios, R. and Garcia, C. D. (2010) 'Dynamic adsorption of albumin on nanostructured TiO₂ thin films', *Materials Science & Engineering C-Materials for Biological Applications*, 30(2), 277-282.
- White, E. S., Baralle, F. E. and Muro, A. F. (2008) 'New insights into form and function of fibronectin splice variants', *Journal of Pathology*, 216(1), 1-14.

- Willard, L., Ranjan, A., Zhang, H. Y., Monzavi, H., Boyko, R. F., Sykes, B. D. and Wishart, D. S. (2003) 'VADAR: a web server for quantitative evaluation of protein structure quality', *Nucleic Acids Research*, 31(13), 3316-3319.
- Wozniak, M. A., Modzelewska, K., Kwong, L. and Keely, P. J. (2004) 'Focal adhesion regulation of cell behavior', *Biochimica Et Biophysica Acta-Molecular Cell Research*, 1692(2-3), 103-119.
- Xie, T., Penelle, J. and Verraver, M. (2002) 'Experimental investigation on the reliability of routine SEC-MALLS for the determination of absolute molecular weights in the oligomeric range', *Polymer*, 43(14), 3973-3977.
- Xiong, J. P., Stehle, T., Diefenbach, B., Zhang, R. G., Dunker, R., Scott, D. L., Joachimiak, A., Goodman, S. L. and Arnaout, M. A. (2001) 'Crystal structure of the extracellular segment of integrin alpha V beta 3', *Science*, 294(5541), 339-345.
- Xiong, J. P., Stehle, T., Zhang, R. G., Joachimiak, A., Frech, M., Goodman, S. L. and Arnaout, M. A. (2002) 'Crystal structure of the extracellular segment of integrin alpha V beta 3 in complex with an Arg-Gly-Asp ligand', *Science*, 296(5565), 151-155.
- Xu, L.-C. and Siedlecki, C. A. (2007) 'Effects of surface wettability and contact time on protein adhesion to biomaterial surfaces', *Biomaterials*, 28(22), 3273-3283.
- Xu, Q. J., Yan, B., Li, S. H. and Duan, C. M. (2004) 'Fibronectin binds insulin-like growth factor-binding protein 5 and abolishes its ligand-dependent action on cell migration', *Journal of Biological Chemistry*, 279(6), 4269-4277.
- Yu, H. and Rohan, T. (2000) 'Role of the insulin-like growth factor family in cancer development and progression', *Journal of the National Cancer Institute*, 92(18), 1472-1489.
- Zhang, S. G., Marini, D. M., Hwang, W. and Santoso, S. (2002) 'Design of nanostructured biological materials through self-assembly of peptides and proteins', *Current Opinion in Chemical Biology*, 6(6), 865-871.
- Zhou, M., Smith, A. M., Das, A. K., Hodson, N. W., Collins, R. F., Ulijn, R. V. and Gough, J. E. (2009) 'Self-assembled peptide-based hydrogels as scaffolds for anchorage-dependent cells', *Biomaterials*, 30(13), 2523-30.

- Zhu, J., Luo, B.-H., Xiao, T., Zhang, C., Nishida, N. and Springer, T. A. (2008) 'Structure of a Complete Integrin Ectodomain in a Physiologic Resting State and Activation and Deactivation by Applied Forces', *Molecular Cell*, 32(6), 849-861.
- Zhu, J., Luo, B. H., Xiao, T., Zhang, C., Nishida, N. and Springer, T. A. (2008) 'Structure of a complete integrin ectodomain in a physiologic resting state and activation and deactivation by applied forces', *Mol Cell*, 32(6), 849-61.
- Zuo, J., Huang, X., Zhong, X., Zhu, B., Sun, Q., Jin, C., Quan, H., Tang, Z. and Chen, W. (2013) 'A comparative study of the influence of three pure titanium plates with different micro- and nanotopographic surfaces on preosteoblast behaviors', *Journal of biomedical materials research. Part A*, 101(11), 3278-84.

Appendix A

Translated DNA sequence of mutated proteins

FIII9'10-GGC E2A

```

1 M R G S H H H H H G M A S G L D S P T
1 ATGCGGGTTCATCATCATCATCATGGTATGGCTAGCGGTCTTGATTCCCAACT
1      10      20      30      40      50

21 G I D F S D I T A N S F T V H W I A P R
61 GGCATTGACTTTTCTGATATTACTGCCAACTCTTTTACTGTGCACTGGATTGCTCCTCGA
61      70      80      90      100     110

41 A T I T G Y R I R H H P A H F S G R P R
121 GCCACCATCACTGGCTACAGGATCCGCCATCATCCCGCGCACTTCAGTGGGAGACCTCGA
121      130     140     150     160     170

61 E D R V P H S R N S I T L T N L T P G T
181 GAAGATCGGGTGCCCACTCTCGGAATCCATCACCCCTACCAACCTCACTCCAGGCACA
181      190     200     210     220     230

81 E Y V V S I V A L N G R E E S P P L I G
241 GAGTATGTGGTCAGCATCGTTGCTCTTAATGGCAGAGAGGAAAGTCCCCATTGATTGGC
241      250     260     270     280     290

101 Q Q S T V S D V P R D L E V V A A T P T
301 CAACAATCAACAGTTTCTGATGTTCCGAGGGACCTGGAAGTTGTTGCTGCGACCCCCACC
301      310     320     330     340     350

121 S L L I S W D A P A V T V R Y Y R I T Y
361 AGCCTACTGATCAGCTGGGATGCTCCTGCTGTCACAGTGAGATATTACAGGATCACTTAC
361      370     380     390     400     410

141 G E T G G N S P V Q E F T V P G S K S T
421 GGAGAAACAGGAGGAAATAGCCCTGTCCAGGAGTTCCTGTGCCTGGGAGCAAGTCTACA
421      430     440     450     460     470

161 A T I S G L K P G V D Y T I T V Y A V T
481 GCTACCATCAGCGGCCTTAAACCTGGAGTTGATTATACCATCACTGTGTATGCTGTCACT
481      490     500     510     520     530

181 G R G D S P A S S K P I S I N Y R T G G
541 GGCCGTGGAGACAGCCCCGCAAGCAGCAAGCCAATTTCCATTAATTACCGAACAGGTGGG
541      550     560     570     580     590

201 C
601 TGTTA
601

```

FIII9'10-GGC I2A

```

1 M R G S H H H H H H G M A S G L D S P T
1 ATGCGGGGTTCTCATCATCATCATCATGGTATGGCTAGCGGTCTTGATTCCCAACT
1          10          20          30          40          50

21 G I D F S D I T A N S F T V H W I A P R
61 GGCATTGACTTTTCTGATATTACTGCCAACTCTTTTACTGTGCACTGGATTGCTCCTCGA
61          70          80          90          100         110

41 A T I T G Y R I R H H P E H F S G R P R
121 GCCACCATCACTGGCTACAGGATCCGCCATCATCCCGAGCACTTCAGTGGGAGACCTCGA
121          130         140         150         160         170

61 E D R V P H S R N S I T L T N L T P G T
181 GAAGATCGGGTGCCCCACTCTCGGAATTCATCACCCCTCACCAACCTCACTCCAGGCACA
181          190         200         210         220         230

81 E Y V V S I V A L N G R E E S P P L A G
241 GAGTATGTGGTCAGCATCGTTGCTCTTAATGGCAGAGAGGAAAAGTCCCCCATTGGCTGGC
241          250         260         270         280         290

101 Q Q S T V S D V P R D L E V V A A T P T
301 CAACAATCAACAGTTTCTGATGTTCCGAGGGACCTGGAAGTTGTTGCTGCGACCCCCACC
301          310         320         330         340         350

121 S L L I S W D A P A V T V R Y Y R I T Y
361 AGCCTACTGATCAGCTGGGATGCTCCTGCTGTCACAGTGAGATATTACAGGATCACTTAC
361          370         380         390         400         410

141 G E T G G N S P V Q E F T V P G S K S T
421 GGAGAAACAGGAGGAAATAGCCCTGTCCAGGAGTTCACTGTGCCTGGGAGCAAGTCTACA
421          430         440         450         460         470

161 A T I S G L K P G V D Y T I T V Y A V T
481 GCTACCATCAGCGGCCTTAAACCTGGAGTTGATTATACCATCACTGTGTATGCTGTCACT
481          490         500         510         520         530

181 G R G D S P A S S K P I S I N Y R T G G
541 GGCCGTGGAGACAGCCCCGCAAGCAGCAAGCCAATATCCATTAATTACCGAACAGGTGGG
541          550         560         570         580         590

201 C *
601 TGTTAA
601

```

FIII9''10 H2P

```

1 M R G S H H H H H G M A S G L D S P T
1 ATGCGGGGTTCTCATCATCATCATGGTATGGCTAGCGGTCTTGATTCCCAACT
1      10      20      30      40      50

21 G I D F S D I T A N S F T V H W I A P R
61 GGCATTGACTTTTCTGATATTACTGCCAACTCTTTTACTGTGCACTGGATTGCTCCTCGA
61      70      80      90      100     110

41 A T I T G Y R I R H H P E H F S G R P R
121 GCCACCATCACTGGCTACAGGATCCGCCATCATCCCGAGCACTTCAGTGGGAGACCTCGA
121      130     140     150     160     170

61 E D R V P P S R N S I T L T N L T P G T
181 GAAGATCGGGTGCCGCATCTCGGAATTCATCACCCCTACCAACCTCACTCCAGGCACA
181      190     200     210     220     230

81 E Y V V S I V A L N G R E E S P P L I G
241 GAGTATGTGGTCAGCATCGTTGCTCTTAATGGCAGAGAGGAAAAGTCCCCCATTGATTGGC
241      250     260     270     280     290

101 Q Q S T V S D V P R D L E V V A A T P T
301 CAACAATCAACAGTTTCTGATGTTCCGAGGGACCTGGAAGTTGTTGCTGCGACCCCCACC
301      310     320     330     340     350

121 S L L I S W D A P A V T V R Y Y R I T Y
361 AGCCTACTGATCAGCTGGGATGCTCCTGCTGTCACAGTGAGATATTACAGGATCACTTAC
361      370     380     390     400     410

141 G E T G G N S P V Q E F T V P G S K S T
421 GGAGAAACAGGAGGAAATAGCCCTGTCCAGGAGTTCACTGTGCCTGGGAGCAAGTCTACA
421      430     440     450     460     470

161 A T I S G L K P G V D Y T I T V Y A V T
481 GCTACCATCAGCGGCCTTAAACCTGGAGTTGATTATACCATCACTGTGTATGCTGTCAC
481      490     500     510     520     530

181 G R G D S P A S S K P I S I N Y R T *
541 GGCCGTGGAGACAGCCCCGCAAGCAGCAAGCCAATTTCCATTAATTACCGAACATAA
541      550     560     570     580     590

```

FIII9''10 T2P

```

1 M R G S H H H H H G M A S G L D S P T
1 ATGCGGGGTTCTCATCATCATCATCATGGTATGGCTAGCGGTCTTGATTCCCAACT
1      10      20      30      40      50

21 G I D F S D I T A N S F T V H W I A P R
61 GGCATTGACTTTTCTGATATTACTGCCAACTCTTTTACTGTGCACTGGATTGCTCCTCGA
61      70      80      90      100     110

41 A P I T G Y R I R H H P E H F S G R P R
121 GCCCAATCACTGGCTACAGGATCCGCCATCATCCCGAGCACTTCAGTGGGAGACCTCGA
121      130     140     150     160     170

61 E D R V P H S R N S I T L T N L T P G T
181 GAAGATCGGGTGCCCACTCTCGGAATTCATCACCCCTACCAACCTCACTCCAGGCACA
181      190     200     210     220     230

81 E Y V V S I V A L N G R E E S P P L I G
241 GAGTATGTGGTCAGCATCGTTGCTCTTAATGGCAGAGAGGAAAAGTCCCCCATTGATTGGC
241      250     260     270     280     290

101 Q Q S T V S D V P R D L E V V A A T P T
301 CAACAATCAACAGTTTCTGATGTTCCGAGGGACCTGGAAGTTGTTGCTGCGACCCCCACC
301      310     320     330     340     350

121 S L L I S W D A P A V T V R Y Y R I T Y
361 AGCCTACTGATCAGCTGGGATGCTCCTGCTGTCACAGTGAGATATTACAGGATCACTTAC
361      370     380     390     400     410

141 G E T G G N S P V Q E F T V P G S K S T
421 GGAGAAACAGGAGGAAATAGCCCTGTCCAGGAGTTCACTGTGCCTGGGAGCAAGTCTACA
421      430     440     450     460     470

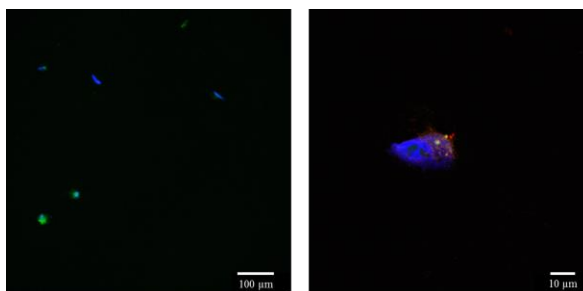
161 A T I S G L K P G V D Y T I T V Y A V T
481 GCTACCATCAGCGGCCTTAAACCTGGAGTTGATTATACCATCACTGTGTATGCTGTCACT
481      490     500     510     520     530

181 G R G D S P A S S K P I S I N Y R T *
541 GGCCGTGGAGACAGCCCCGCAAGCAGCAAGCCAATTTCCATTAATTACCGAACATAA
541      550     560     570     580     590

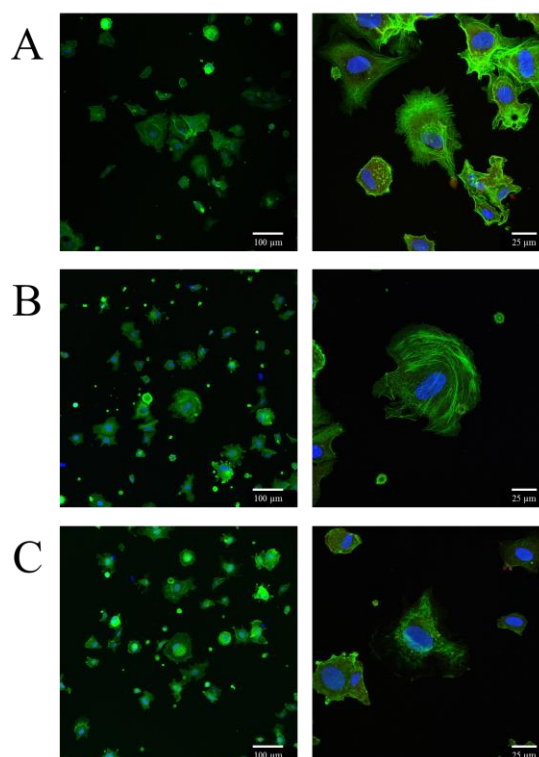
```

Appendix B

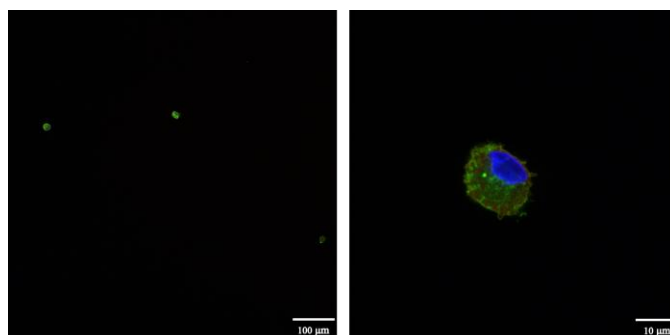
Immunofluorescence images



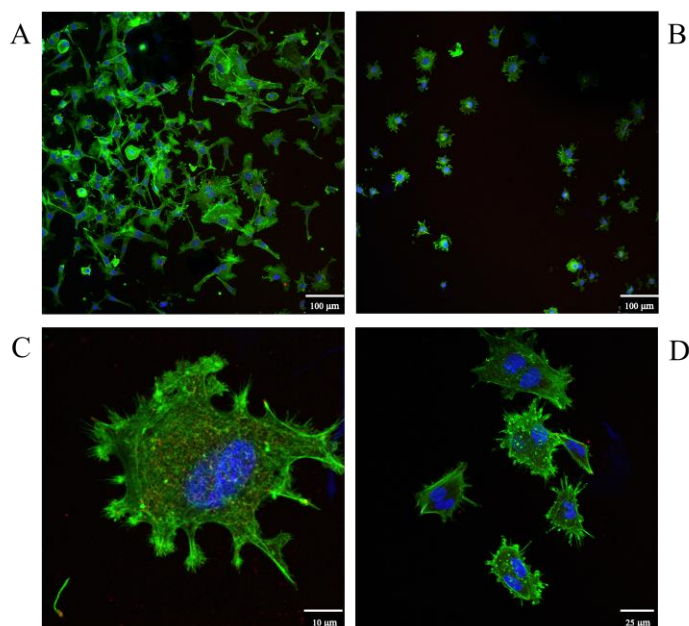
Immunofluorescence image showing BHK cell attachment onto untreated TiO_2 substrate stained for vinculin (red), actin (green), and the nuclei (blue). Images were photographed at 20x magnification (left) and 63x magnification (right).



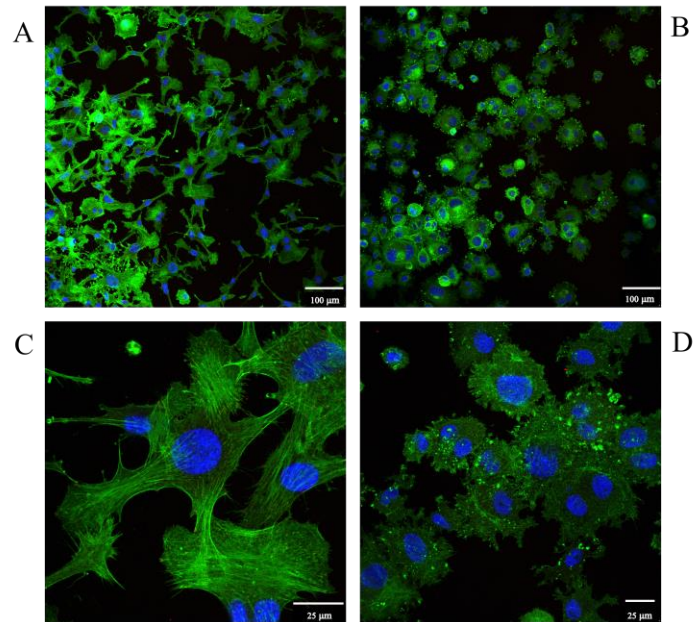
Immunofluorescence image showing BHK cell attachment onto TiO_2 substrate coated with either 100 $\mu\text{g}/\text{ml}$ FIII9-10 (A), FIII9'10 (B) or FIII9''10 H2P (C). Cells were stained for vinculin (red), actin (green), and the nuclei (blue). Images were photographed at 20x magnification (left) and 63x magnification (right).



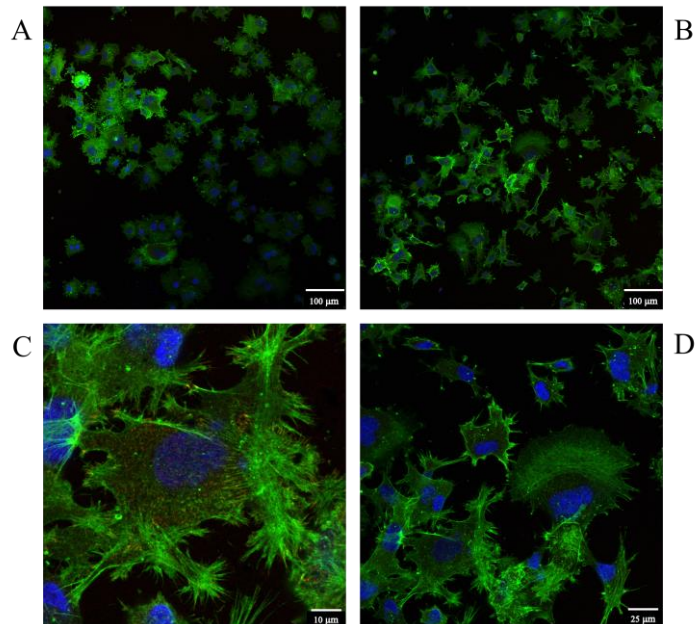
Immunofluorescence image showing BHK cell attachment onto Au/11-MUD substrate stained for vinculin (red), actin (green), and the nuclei (blue). Images were photographed at 20x magnification (left) and 63x magnification (right).



Immunofluorescence image showing BHK cell attachment onto Au/11-MUD substrate coated with FIII9' 10-GGC, stained for vinculin (red), actin (green), and the nuclei (blue). Images were photographed at 20x magnification (A and B) and 63x magnification (C and D).



Immunofluorescence image showing BHK cell attachment onto Au/11-MUD substrate coated with trimer, stained for vinculin (red), actin (green), and the nuclei (blue). Images were photographed at 20x magnification (A and B) and 63x magnification (C and D).



Immunofluorescence image showing BHK cell attachment onto Au/11-MUD substrate coated with tetramer, stained for vinculin (red), actin (green), and the nuclei (blue). Images were photographed at 20x magnification (A and B) and 63x magnification (C and D).